JAAVSO

Volume 50
Number 1
2022

The Journal of the American Association of Variable Star Observers

What Are the SRd Variables?

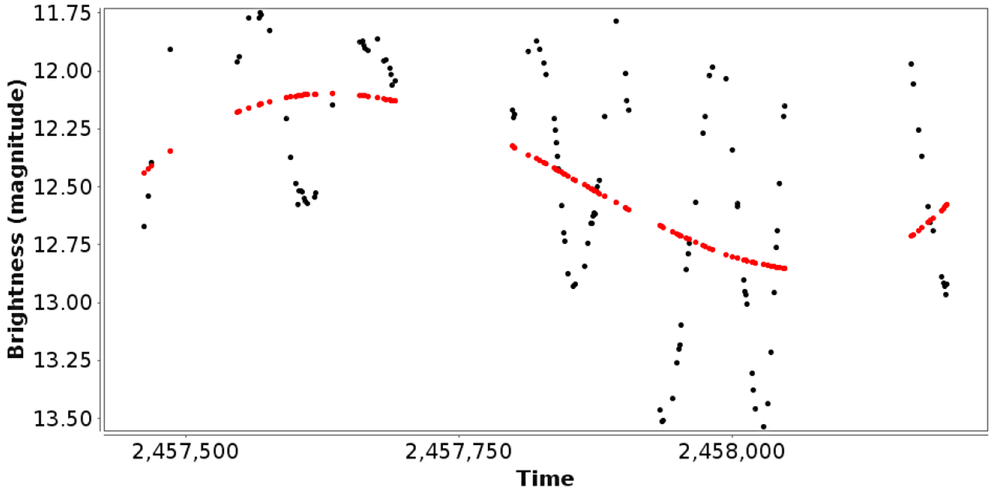

The V light curve of V3724 Sgr, from ASAS-SN data, showing a pulsation period of 81.77 days, with variable amplitude, and an LSP of about 900 days. The model (red line) is a fourth-order polynomial fit.

Also in this issue...

- Long-Term Period Behavior of the Semiregular Variable V1 and the Type II Cepheids V2 and V3 in the Globular Cluster M10
- Analyzing Transit Timing Variations of Qatar-1b
- Observation and Analysis of Qatar-1b Transit Timing Variations: No Evidence for Additional Bodies in Qatar-1
- Accuracy and Precision in Amateur Photometry

Complete table of contents inside...

The American Association of Variable Star Observers
185 Alewife Brook Parkway, Suite 410, Cambridge, MA 02138, USA

The Journal of the American Association of Variable Star Observers

Editor-in-Chief
Nancy D. Morrison
Professor of Astronomy Emerita
Department of Physics
and Astronomy
The University of Toledo,
Toledo, Ohio

Associate Editor
Elizabeth O. Waagen

Production Editor
Michael Saladyga

Editorial Board
Geoffrey C. Clayton
Louisiana State University
Baton Rouge, Louisiana

Kosmas Gazeas
University of Athens
Athens, Greece

Laszlo L. Kiss
Konkoly Observatory
Budapest, Hungary

Katrien Kolenberg
Universities of Antwerp
and of Leuven, Belgium
and Harvard-Smithsonian Center
for Astrophysics
Cambridge, Massachusetts

Kristine Larsen
Department of Geological Sciences,
Central Connecticut
State University,
New Britain, Connecticut

Vanessa McBride
IAU Office of Astronomy for
Development; South African
Astronomical Observatory;
and University of Cape Town,
South Africa

Ulisse Munari
INAF/Astronomical Observatory
of Padua
Asiago, Italy

Karen Pollard
Director, Mt. John Observatory,
University of Canterbury,
Christchurch, New Zealand

Nikolaus Vogt
Universidad de Valparaiso
Valparaiso, Chile

The Board of the American Association of Variable Star Observers
2021–2022

Interim Executive Director Kathy Spirer
President David Cowall
1st Vice President Richard Berry
2nd Vice President Sarah Austrin-Willis
Secretary Kristine Larsen
Treasurer Robert Stephens

Board Members

John Blackwell
John W. Briggs
Robert Buchheim
Dennis Conti
Joyce A. Guzik
Ken Hudson
Karen Kinemuchi
Thomas Maccarone

ISSN 0271-9053 (print)
ISSN 2380-3606 (online)

JAAVSO

The Journal of
The American Association
of Variable Star Observers

Volume 50
Number 1
2022

AAVSO
185 Alewife Brook Parkway,
Suite 410, Cambridge, MA 02138
USA

ISSN 0271-9053 (print)
ISSN 2380-3606 (online)

Publication Schedule

The Journal of the American Association of Variable Star Observers is published twice a year, June 15 (Number 1 of the volume) and December 15 (Number 2 of the volume). The submission window for inclusion in the next issue of JAAVSO closes six weeks before the publication date. A manuscript will be added to the table of contents for an issue when it has been fully accepted for publication upon successful completion of the referee process; these articles will be available online prior to the publication date. An author may not specify in which issue of JAAVSO a manuscript is to be published; accepted manuscripts will be published in the next available issue, except under extraordinary circumstances.

Page Charges

Page charges are waived for Members of the AAVSO. Publication of unsolicited manuscripts in JAAVSO requires a page charge of US $100/page for the final printed manuscript. Page charge waivers may be provided under certain circumstances.

Publication in *JAAVSO*

With the exception of abstracts of papers presented at AAVSO meetings, papers submitted to JAAVSO are peer-reviewed by individuals knowledgeable about the topic being discussed. We cannot guarantee that all submissions to JAAVSO will be published, but we encourage authors of all experience levels and in all fields related to variable star astronomy and the AAVSO to submit manuscripts. We especially encourage students and other mentees of researchers affiliated with the AAVSO to submit results of their completed research.

Subscriptions

Institutions and Libraries may subscribe to JAAVSO as part of the Complete Publications Package or as an individual subscription. Individuals may purchase printed copies of recent JAAVSO issues via Createspace. Paper copies of JAAVSO issues prior to volume 36 are available in limited quantities directly from AAVSO Headquarters; please contact the AAVSO for available issues.

Instructions for Submissions

The *Journal of the AAVSO* welcomes papers from all persons concerned with the study of variable stars and topics specifically related to variability. All manuscripts should be written in a style designed to provide clear expositions of the topic. Contributors are encouraged to submit digitized text in MS WORD, LATEX+POSTSCRIPT, or plain-text format. Manuscripts should be submitted through the JAAVSO submission portal (https://www.aavso.org/apps/jaavso/submit/) or may be mailed electronically to journal@aavso.org or submitted by postal mail to JAAVSO, 185 Alewife Brook Parkway, Suite 410, Cambridge, MA 02138, USA.

Manuscripts must be submitted according to the following guidelines, or they will be returned to the author for correction:

Manuscripts must be:
1) original, unpublished material;
2) written in English;
3) accompanied by an abstract of no more than 100 words.
4) not more than 2,500–3,000 words in length (10–12 pages double-spaced).

Figures for publication must:
1) be camera-ready or in a high-contrast, high-resolution, standard digitized image format;
2) have all coordinates labeled with division marks on all four sides;
3) be accompanied by a caption that clearly explains all symbols and significance, so that the reader can understand the figure without reference to the text.

Maximum published figure space is 4.5" by 7". When submitting original figures, be sure to allow for reduction in size by making all symbols, letters, and division marks sufficiently large.

Photographs and halftone images will be considered for publication if they directly illustrate the text.

Tables should be:
1) provided separate from the main body of the text;
2) numbered sequentially and referred to by Arabic number in the text, e.g., Table 1.

References:
1) References should relate directly to the text.
2) References should be keyed into the text with the author's last name and the year of publication, e.g., (Smith 1974; Jones 1974) or Smith (1974) and Jones (1974).
3) In the case of three or more joint authors, the text reference should be written as follows: (Smith et al. 1976).
4) All references must be listed at the end of the text in alphabetical order by the author's last name and the year of publication, according to the following format: Brown, J., and Green, E. B. 1974, *Astrophys. J.*, **200**, 765.
Thomas, K. 1982, *Phys. Rep.*, **33**, 96.
5) Abbreviations used in references should be based on recent issues of JAAVSO or the listing provided at the beginning of *Astronomy and Astrophysics Abstracts* (Springer-Verlag).

Miscellaneous:
1) Equations should be written on a separate line and given a sequential Arabic number in parentheses near the right-hand margin. Equations should be referred to in the text as, e.g., equation (1).
2) Magnitude will be assumed to be visual unless otherwise specified.
3) Manuscripts may be submitted to referees for review without obligation of publication.

Online Access

Articles published in JAAVSO, and information for authors and referees may be found online at: https://www.aavso.org/apps/jaavso/

The Journal of the American Association of Variable Star Observers
Volume 50, Number 1, 2022

Editorial

Variable Star Research

Table of Contents continued on next page

Variable Star Data

Editorial

A Constellation of Statistical Analyses

Nancy D. Morrison
Editor-in-Chief, *Journal of the AAVSO*

Department of Physics and Astronomy and Ritter Observatory, MS 113, The University of Toledo, 2801 W. Bancroft Street, Toledo OH 43606; jaavso.editor@aavso.org

Received June 9, 2022

Statistics is at the heart of variable star research. Whenever we determine a parameter of a variable star—such as its period, amplitude of variation, or time of maximum or minimum light—we use a mathematical model or a statistical analysis. Those operations return an estimate of a value (point estimate) and an estimate of its uncertainty (sometimes expressed as a confidence interval). Such a test could be as simple as the classical eyeball estimate or as complex as a wavelet analysis. Often, we accept the results of the statistical test at face value and move on to the next problem.

But how does a researcher know that the error estimate returned by a statistical test is realistic? Or even that the estimated value, with its error bars or its confidence interval, is reliable? This question has special urgency if the time series has major gaps or a low signal-to-noise ratio.

Recently, researchers in various fields—ranging from psyhchology to finance—have tried to tackle this question by crowdsourcing data analysis projects. They invited other teams of researchers to analyze a given data set, each using a different methodology. Then the project leaders compiled the results, viewing the collection of results as an approximation to the universe of possible estimates of the statistics of the problem. In an open-access comment in the 17 May issue of *Nature*, Wagenmakers *et al.* (2022) discussed the results of about a dozen formal crowdsourced projects, some of them involving over 100 independent teams. In many of those studies, some of the results by individual teams showed a range characterized by error bars that do not overlap.

I chose one of these crowdsourced studies to explore in more detail: Silberzahn *et al.* (2018). Through online advertising, those authors recruited 29 independent teams to analyze a data set on red cards given to soccer players. They aimed to test the hypothesis that dark-skinned players receive red cards more often than light-skinned players, averaging over many game situations and types of infraction.

Red cards are given for egregious bad or aggressive behavior and generally result in the player's ejection from the game. Although objective criteria for their award exist, marginal cases occur often, and the referee's judgement is important. The possible confounding variables (factors to be controlled for) are too numerous to list here. Many different assumptions about independence among variables and about systematic effects could be made. One important decision area was classification of skin tone as "light" or "dark;" Silberzahn *et al.* (2018) discuss this topic in detail. In keeping with all these complexities, the data analysis techniques differed greatly among the research teams.

In Figure 1, the studies are grouped by general methodology. The error bars are 95% confidence intervals, which are larger than the standard deviation usually used in astronomy (roughly a two-thirds confidence interval). The listing of the statistical methods is included here only to illustrate the great range of methodology involved. In statistics, the term "odds ratio" has the obvious meaning: in this case, it indicates the ratio of probability of a dark-skinned player receiving a red card, compared to that for a light-skinned player. For example, an odds ratio of 1.3 would mean that a dark-skinned player would be 1.3 times as likely to receive a red card, overall, as a light-skinned player.

It is clear from Figure 1 that the results range more widely than a single result with error bar would imply. Even though the confidence intervals mostly overlap, qualitatively different conclusions could be reached if individual results were considered in isolation. Although some of the teams' error bars give a fair representation of the overall range in the results, a few of them are exceptionally small.

How might these results apply to variable star astronomy? At first sight, our data sets are simpler than the one analyzed here. Silberzahn *et al.* (2018) admit that discrepant results are less likely in simpler problems with few measured variables, but that, even in such cases, analytical decisions may influence outcomes. Variable outcomes are more likely in case of complex data sets. Interestingly, one of those authors' examples of complex data is a longitudinal data set with missing data—exactly the case in astronomical time series.

What options are available to the individual researcher who is concerned about these problems? Silberzahn *et al.* (2018) make several suggestions. One is to crowdsource your own project: invite other researchers to analyze a well-specified data set with their own favorite methods. Those authors consider this approach to be inefficient; they spent a lot of energy on organizing their project. But they gave the analysis teams the opportunity to interact on analytical issues (without knowing each other's results), and the interaction was highly beneficial.

Another option is to re-analyze already-published data with a different technique. However, this route is subject to publication bias (Silberzahn et al. 2018 again): researchers doing the re-analysis are most likely to move to publication if their result disagrees with the original one. Here I can say that *JAAVSO* stands willing to publish re-analyses of published data, even if agreement with the original result is perfect, provided that the analytical methods are truly independent.

There are other options for sampling the universe of analytical methods. In multiverse analysis (Steegen *et al.* 2016), researchers vary the construction of the data set in all the ways they can think of and then perform a similar statistical analysis on all the versions of the analyzed data.

In the realm of statistical analysis, as opposed to data set construction, is specification curve analylsis (Simonsohn *et al.* 2020). Here a given data set is analyzed with all reasonable methods and under all reasonable sets of assumptions. As in Figure 1, the method leads to a plot of results as a function of the assumptions and analysis techniques. Cosme (2022) provides additional explanation.

In astronomy, to my knowledge, researchers employ only one or a few analytical methods to address a given research problem. If any readers know of an example in astronomy of a paper comparing results of more than three analytical methods, I would appreciate learning about it.

Meanwhile, I encourage readers to explore the uncertainties in their analyses by means of one of the techniques outlined here. If crowdsourcing, specification curve analysis, and multiverse analysis are beyond your reach, and you have access to only one or two independent analysis methods, it would be appropriate to approach your results with caution.

References

Cosme, D. 2022.[1]

Silberzahn, R., *et al.* 2018, *Adv. Methods Pr. Psychological Sci.*, **1**, 337 (https://doi.org/10.1177%2F2515245917747646).

Simonsohn, U., Simmons, J. P., and Nelson, L. D. 2020, *Nature Human Behavior*, **4**, 1208 (https://doi.org/10.1038/s41562-020-0912-z).

Steegen, S., Tuerlinckx, F., Gelman, A., and Vanpaemel. W. 2016, *Perspectives on Psychological Sci.*, **11**, 702.

Wagenmakers, E.-J., Sarafoglou, A., and Aczel, B. 2022, *Nature*, **605**, 423 (https://doi.org/10.1038/d41586-022-01332-8).

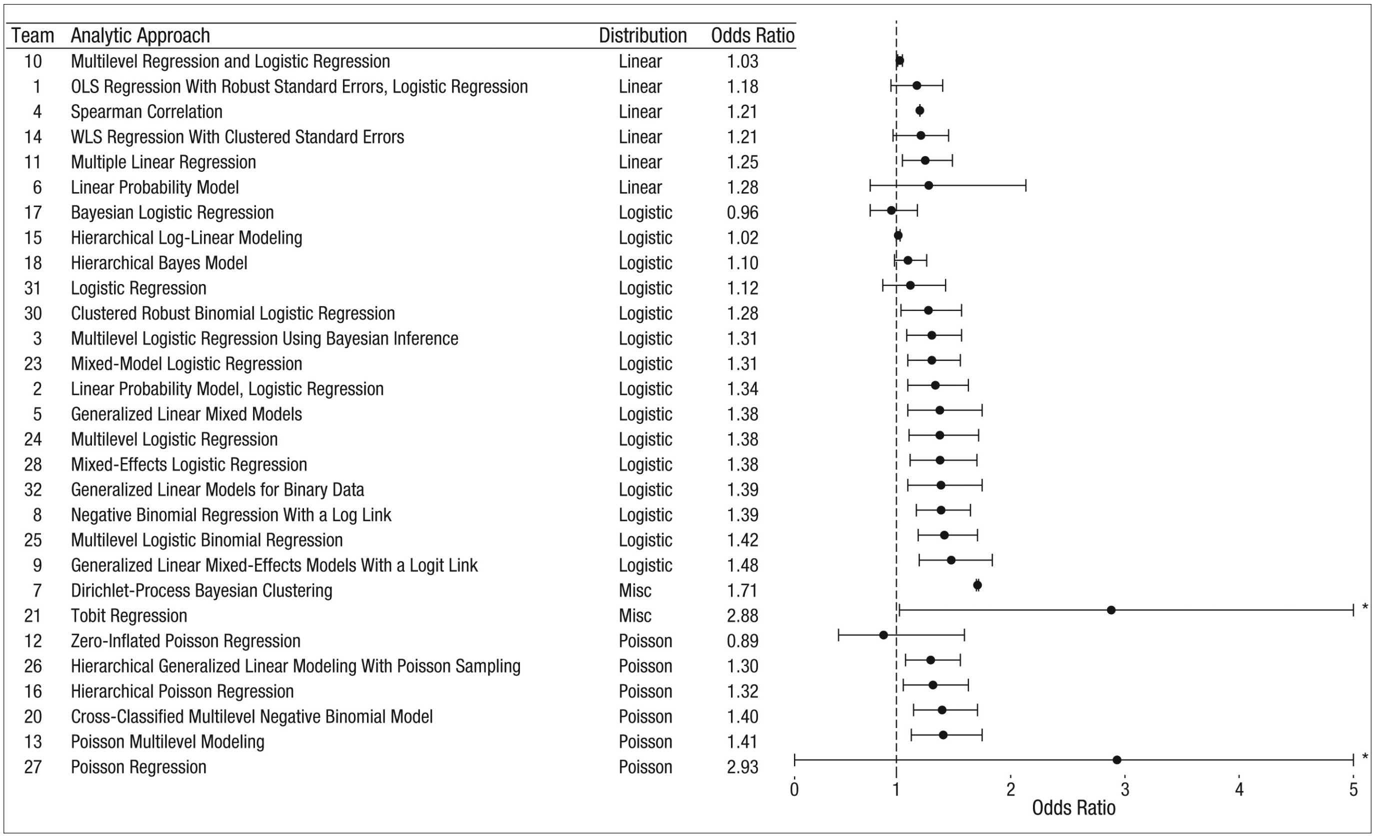

Team	Analytic Approach	Distribution	Odds Ratio
10	Multilevel Regression and Logistic Regression	Linear	1.03
1	OLS Regression With Robust Standard Errors, Logistic Regression	Linear	1.18
4	Spearman Correlation	Linear	1.21
14	WLS Regression With Clustered Standard Errors	Linear	1.21
11	Multiple Linear Regression	Linear	1.25
6	Linear Probability Model	Linear	1.28
17	Bayesian Logistic Regression	Logistic	0.96
15	Hierarchical Log-Linear Modeling	Logistic	1.02
18	Hierarchical Bayes Model	Logistic	1.10
31	Logistic Regression	Logistic	1.12
30	Clustered Robust Binomial Logistic Regression	Logistic	1.28
3	Multilevel Logistic Regression Using Bayesian Inference	Logistic	1.31
23	Mixed-Model Logistic Regression	Logistic	1.31
2	Linear Probability Model, Logistic Regression	Logistic	1.34
5	Generalized Linear Mixed Models	Logistic	1.38
24	Multilevel Logistic Regression	Logistic	1.38
28	Mixed-Effects Logistic Regression	Logistic	1.38
32	Generalized Linear Models for Binary Data	Logistic	1.39
8	Negative Binomial Regression With a Log Link	Logistic	1.39
25	Multilevel Logistic Binomial Regression	Logistic	1.42
9	Generalized Linear Mixed-Effects Models With a Logit Link	Logistic	1.48
7	Dirichlet-Process Bayesian Clustering	Misc	1.71
21	Tobit Regression	Misc	2.88
12	Zero-Inflated Poisson Regression	Poisson	0.89
26	Hierarchical Generalized Linear Modeling With Poisson Sampling	Poisson	1.30
16	Hierarchical Poisson Regression	Poisson	1.32
20	Cross-Classified Multilevel Negative Binomial Model	Poisson	1.40
13	Poisson Multilevel Modeling	Poisson	1.41
27	Poisson Regression	Poisson	2.93

Figure 1. Reproduction of Figure 3 from Silberzahn *et al*. (2018). "Odds ratio" indicates the probability of a dark-skinned player receiving a red card, divided by that for a light-skinned player. A point estimate and 95% confidence interval are shown from each of the 29 analysis teams, with similar analyses grouped together. Asterisked error bars are truncated on the right-hand side for better readability of the graph. OLS = ordinary least squares; WLS = weighted least squares; Misc = miscellaneous.

---

[1] https://dcosme.github.io/specification-curves/SCA_tutorial_inferential_presentation#1

Light Curve Analysis of Eclipsing Binary Stars LX Leo, V345 UMa, and MU Leo

Lauren Hoffman
Vince Mazzola
Vayujeet Gokhale
Truman State University, 100 E. Normal Street, Kirksville, MO, 63501; gokhale@truman.edu

Received February 18, 2021; revised March 3, May 26, 2022; accepted May 31, 2022

Abstract We present light curve analysis of three eclipsing binary stars, LX Leo, V345 UMa, and MU Leo, using data collected at the 31-inch NURO telescope at Lowell Observatory in Flagstaff, Arizona, in three filters: Bessell B, V, and R. We generate truncated twelve-term Fourier fits for the light curves to: a) confirm that LX Leo and V354 UMa are W UMa type, and MU Leo is an Algol type eclipsing binary star system and, b) quantify the light curve asymmetries exhibited by each of these systems in each filter. The asymmetries in the light curves are quantified by calculating the difference in the heights of the primary and secondary maxima (ΔI), the "Light Curve Asymmetry" (LCA), and the "O'Connell Effect Ratio" (OER). Of the systems studied here, we find that V354 UMa has the most symmetric curve and LX Leo has the most asymmetric curve. We also find that for each object, generally, the asymmetries are more pronounced in the B-filter.

1. Introduction

For the past few years, undergraduate students at Truman State University (Kirksville, Missouri) have been involved in quantifying the asymmetries in the light curves of Eclipsing Binary (EB) stars (Gardner *et al.* 2015; Akiba *et al.* 2019; Hahs *et al.* 2020). In this paper, we extend these analyses to three additional EB systems: LX Leo (P = 0.235247 d), V345 UMa (P = 0.293825 d), and MU Leo (P = 0.388442 d). All three objects were selected from a list of eclipsing binaries published by Kreiner (2004).

Following Akiba *et al.* (2019), we quantify the asymmetries in the light curves by calculating three quantities using the Fourier fits: the difference in the heights of the primary and secondary maxima (ΔI, traditionally referred to as the "O'Connell Effect," O'Connell 1951), the Light Curve Asymmetry (LCA, McCartney 1999), and the O'Connell Effect Ratio (OER). Additionally, we use Fourier fitting of the light curves to classify these EB systems into Algol, β Lyrae, or W UMa type systems.

Photometric studies of LX Leo (Gürol *et al.* 2017) and V354 UMa (Michel *et al.* 2019) have already characterized these systems as W UMa type variables. Gürol *et al.* (2017) have noticed the asymmetry in the light curve and use this asymmetry to model the system with starspots. On the basis of their light curve solution, Gürol *et al.* (2017) conclude that LX Leo is a W UMa type system with a mass ratio q = 1.89 ± 0.02. Similarly, Michel *et al.* (2019) provide a photometric solution for V354 UMa and conclude that it is also a W UMa type system with a mass ratio q = 3.623 ± 0.040. They suggest that V354 UMa has an asymmetric light curve, suggesting the presence of either star spots or dark spots. Further, Michel *et al.* 2019) also suggest that this system exhibits a variable orbital period, implying conservative mass transfer from the less massive to the more massive component.

In this paper, we are interested in quantifying the asymmetries in the light curves in the aforementioned ways (McCartney 1999), as a first step towards understanding the origins of the asymmetries. Traditionally (see Gürol *et al.* 2017, Michel *et al.* 2019, for example), these asymmetries are attributed to either "starspots" (cooler regions on one or the other star) or to "hotspots" (usually associated with mass transfer in close binary systems). Due to lack of spectroscopic data, we do not attempt to model these systems, and hence are not in a position to comment on the efficacy of either of these models. We believe that even with access to spectroscopic data, a true model of these systems is elusive unless the systems are observed over a long timeline in order to model *changes* in the light curves of these objects. To overcome this limitation, in a forthcoming publication (Knote *et al.* 2022), we are analyzing uninterrupted data from the Kepler (Prša 2011) and Transiting Exoplanet Survey Satellite (TESS) missions (Ricker *et al.* 2015) to better constrain the system parameters and hence, determine the elusive origin of these asymmetries.

In the following section, we outline the data acquisition and data reduction methods we employed. Our results and analyses are presented in section 3, followed by a discussion section summarizing our results, conclusions, and plans for the future.

2. Observations

We obtained data on three eclipsing variable stars: LX Leo (P = 0.235247), MU Leo (NSVS 7504057) (P = 0.388442), and V354 UMa (P = 0.293825), using the 2k × 2k Loral NASACam CCD attached to the 31-inch National Undergraduate Research Observatory (NURO) telescope in Flagstaff, Arizona. The data were taken on UT dates 03/20/2020, 03/14/2020, and 03/18/2020, respectively. The filters used are Bessell BVR. The images taken were processed using bias subtraction and flat fielding by constructing a master bias and master flat image using the AstroImageJ software (AIJ, v3.2, Collins *et al.* 2017). Dark subtraction was not needed due to the nitrogen-cooled camera at NURO, thus making the dark current negligible.

Differential photometry was then performed on our target stars with suitable comparison and check stars when possible using the AIJ software. We used the radial profile display utility

Table 1. Target, comparison and check star coordinates comparison star B and V magnitudes used for data from the NURO telescope.

Star	*Name*	*R.A. (J2000)*	*Dec. (J2000)*	*V*	*B*
Target	LX Leo	09 50 27072	+20 43 05.34	—	—
Comparison	TYC 1417-387-1	09 50 47.29	+20 39 01.24	11.18	11.65
Check	TYC 1417-423-1	09 49 58.99	+20 42 11.83	12.19	13.08
Target	V354 UMa	13 35 38.40	+49 14 06.12	—	—
Comparison	TYC 3466-293-1	13 35 26.02	+49 08 1910	10.27	11.21
Check	TYC 3466-294-1	13 35 06.49	+49 17 51.68	11.80	12.21
Target	MU Leo	10 24 59.90	+24 30 51.56	—	—
Comparison	TYC 1969-496-1	10 24 53.53	+24 24 41.99	10.28	11.14

Table 2. Classification of systems based on Fourier coefficients.

Target	*Filter*	a_1	a_2	a_4	$a_2\,(0.125 - a_2)$	*Classification*
LX Leo	B	0.0023 ± 0.0008	–0.2265 ± 0.0009	–0.0586 ± 0.0010	–0.0796 ± 0.0004	W UMa
	V	0.0003 ± 0.0007	–0.2211 ± 0.0008	–0.0590 ± 0.0008	–0.0765 ± 0.0004	W UMa
	R	–0.0036 ± 0.0006	–0.2155 ± 0.0006	–0.0600 ± 0.0007	–0.0734 ± 0.0003	W UMa
V354 UMa	B	0.0048 ± 0.0002	–0.0651 ± 0.0002	–0.0009 ± 0.0002	–0.01238 ± 0.00004	W UMa
	V	0.0057 ± 0.0002	–0.0617 ± 0.0002	–0.0011 ± 0.0002	–0.01151 ± 0.00004	W UMa
	R	0.0053 ± 0.0002	–0.0595 ± 0.0002	–0.0008 ± 0.0002	–0.01097 ± 0.00004	W UMa
MU Leo	B	0.0812 ± 0.0006	–0.1567 ± 0.0006	–0.0716 ± 0.0006	–0.0441 ± 0.0002	Algol
	V	0.0734 ± 0.0005	–0.1546 ± 0.0005	–0.0759 ± 0.0006	–0.0432 ± 0.0002	Algol
	R	0.0582 ± 0.0006	–0.1526 ± 0.0006	–0.0779 ± 0.0007	–0.0424 ± 0.0002	Algol

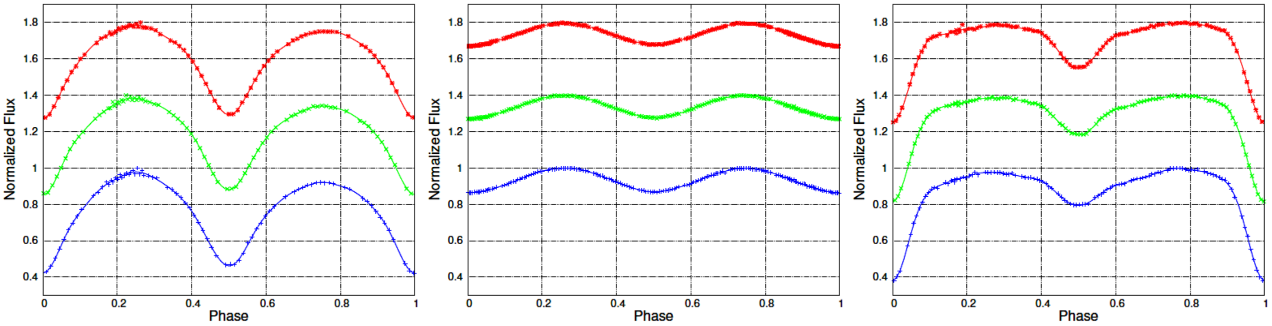

Figure 1. Normalized flux for LX Leo (left), V354 UMa (center), and MU Leo (right) in all three filters. The Fourier fits (continuous curves) are plotted along with the blue, green, and red curves corresponding to B, V, and R filters, respectively. The average error in the flux for each measurement is approximately 0.003 and 0.005 for LX Leo and V354 UMa, respectively, in all filters, and about 0.0002 for MU Leo in all filters. Error bars are not shown for the sake of clarity.

function in AIJ to determine the photometric aperture radius and the radii of the inner and outer annulus, using the method outlined in Collins *et al.* (2017) (see their Appendix A). To search for comparison and check stars, we used the SIMBAD Astronomical Database (Wenger *et al.* 2000) to find any stars in the image frame relatively close in brightness and size to our target star. We then used the cataloged B and V magnitudes of the comparison stars to determine the corresponding magnitudes of each of our target stars (Table 1). Instrumental magnitudes were used for the R-filter since the R magnitude was not listed. We also ensured that the comparison and check stars chosen showed no variability in each of the filters. All differential photometry data can be retrieved from the AAVSO International Database (Kafka 2021). These data are also available on request via email: gokhale@truman.edu and are available at http://gokhale.sites.truman.edu/asymmetries/.

3. Analysis

The analysis of the light curves in this paper closely follows the procedure outlined in Gardner *et al.* (2015), Akiba *et al.* (2019), and Hahs *et al.* (2020). We first phase-fold the time axis and ensure that the primary (deeper) eclipse always coincides with phase "0." Additionally, we calculate the normalized flux for each data point from the measured magnitudes obtained via differential photometry (Warner and Harris 2006) as:

$$I(\Phi)_{obs} = 10^{-0.4 \times (m(\Phi) - m(max))} \qquad (1)$$

where m(Φ) is the magnitude at a certain phase Φ and m(max) is the maximum magnitude observed for the object. We perform Fourier fit analyses on the light curves of each object in each filter similar to Wilsey and Beaky (2009). A truncated twelve-term Fourier fit is given by

$$\mathrm{I}(\Phi)_{\mathrm{fit}} = \mathrm{a}_0 + \sum_{n=1}^{12} (\mathrm{a}_n \cos(2\pi\, n\, \Phi) + \mathrm{b}_n \sin(2\pi\, n\, \Phi)) \qquad (2)$$

where a_0, a_n, and b_n are the Fourier coefficients of the fit, and Φ is the phase (Hoffman *et al.* 2009). The light curves of the three objects in each filter along with their Fourier fits are presented in Figure 1.

3.1. Classification

Following Akiba *et al.* (2019), the Fourier coefficients and the associated errors are extracted from the Fourier fits generated using Mathematica (Wolfram Research Co. 2019) and are tabulated in Table 2. The values of these coefficients are determined by the shape of the light curves, and hence are a quantitative measure of the geometry of the eclipsing binary (Ruciński 1973, 1993, 1997). In particular, the condition $a_4 < a_2 (0.125 - a_2)$ implies that the system is a detached system and is classified as an Algol-type system (see Akiba *et al.* 2019) for details). If this condition is not met, and additionally if $|a_1| < 0.05$, then the system is classified as a W UMa type system; otherwise it is classified as a β Lyrae type system.

For the three systems under consideration, in all three filters, the results from the Fourier coefficient method are consistent with those from qualitative visual inspection: LX Leo and V354 UMa are confirmed to be W UMa type systems, while MU Leo is of the Algol-type.

3.2. Quantifying the asymmetries in the light curves

We quantify the asymmetries in several different ways:

1. For each object, in each filter, we determine the difference in the normalized flux near the primary and secondary maxima from the data (ΔI_{ave}) and from the fit (ΔI_{fit}). Additionally, we determine $|2b_1|$ from the Fourier coefficient b_1, since this term represents the half-amplitude of the sine wave of the Fourier fit and is thus a measure of the difference between the primary and secondary maxima (Wilsey and Beaky 2009). These values are tabulated in Table 3. It is clear that V354 UMa has the smallest, if any, asymmetry in its light curve, followed by MU Leo, for which ΔI is negative. LX Leo has the greatest amount of asymmetry. Generally, ΔI is greatest in the B filter, which is consistent with the results obtained by Akiba *et al.* (2019).

2. For each object, in each filter, we determine the O'Connell Effect ratio (OER) and the Light Curve Asymmetry (LCA, McCartney 1999) using:

$$\mathrm{OER} = \frac{\int_{0.0}^{0.5} (I(\Phi)_{\mathrm{fit}} - I(0.0)_{\mathrm{fit}})d\Phi}{\int_{0.5}^{1.0} (I(\Phi)_{\mathrm{fit}} - I(0.0)_{\mathrm{fit}})d\Phi} \qquad (3)$$

and,

$$\mathrm{LCA} = \sqrt{\int_{0.0}^{0.5} \frac{(I(\Phi)_{\mathrm{fit}} - I(1.0-\Phi)_{\mathrm{fit}})^2}{I(\Phi)_{\mathrm{fit}}^2} d\Phi} \qquad (5)$$

Table 3. Quantifying the O'Connell Effect in terms of difference in maxima (see section 3.2 for details).

Target	*Filter*	$\lvert 2b_1 \rvert$	*ΔI (Fourier)*	*ΔI (Average)*
LX Leo	B	0.043 ± 0.001	0.058 ± 0.007	0.053 ± 0.001
	V	0.035 ± 0.001	0.044 ± 0.006	0.040 ± 0.001
	R	0.023 ± 0.001	0.033 ± 0.005	0.029 ± 0.001
V0354 UMa	B	0.0020 ± 0.0002	0.000 ± 0.002	0.000 ± 0.002
	V	0.0002 ± 0.0003	0.000 ± 0.002	0.000 ± 0.003
	R	0.0016 ± 0.0003	–0.001 ± 0.002	0.000 ± 0.002
MU Leo	B	0.018 ± 0.001	–0.022 ± 0.005	–0.0201 ± 0.0001
	V	0.011 ± 0.001	–0.012 ± 0.004	–0.0123 ± 0.0001
	R	0.013 ± 0.001	–0.001 ± 0.005	–0.0120 ± 0.0001

Table 4. Quantifying the O'Connell Effect in terms of OER and LCA (see section 3.2 for the definitions of the OER and LCA).

Target	*Filter*	*OER*	*LCA*
LX Leo	B	1.08 ± 0.02	0.025 ± 0.003
	V	1.07 ± 0.02	0.020 ± 0.003
	R	1.05 ± 0.02	0.014 ± 0.002
V0354 UMa	B	1.02 ± 0.02	0.003 ± 0.001
	V	1.00 ± 0.03	0.002 ± 0.001
	R	1.02 ± 0.03	0.003 ± 0.001
MU Leo	B	0.98 ± 0.01	0.021 ± 0.002
	V	0.99 ± 0.01	0.013 ± 0.002
	R	0.99 ± 0.01	0.015 ± 0.002

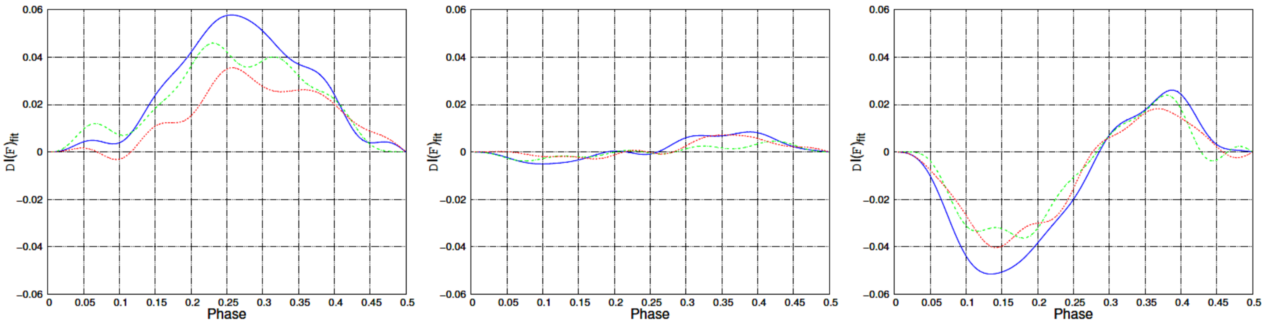

Figure 2. Difference in normalized flux between the two halves of the light curves, in the B (blue solid curve), V (green dashed), and R (red dotted) filters for LX Leo (left plot), V354 UMa (middle), and MU Leo (right). In the absence of any asymmetry, the two curves should coincide, and the solid blue curve in the bottom panel would be a flat line at "0."

The asymmetry reflected by the OER and LCA values (Table 4) are consistent with the ΔI values from Table 3. We note that V354 UMa has a very symmetric light curve, while LX Leo has a significant asymmetry as quantified by both the OER and LCA. Interestingly, MU Leo has a low OER in each filter, though the LCA is significant (see below). We do not observe any obvious trend in the amount of asymmetry as a function of filter, though generally, the OER and LCA are the greatest in the B-filter which is consistent with the results obtained by Gardner *et al.* (2015), Akiba *et al.* (2019), and Hahs *et al.* 2020). Of course, a much larger sample is necessary to derive any reliable conclusions regarding the filter-dependance of light curve asymmetries in EB light curves.

3. Additionally, we superpose the two halves of each of the light curves to generate "half-phase plots" to visually demonstrate the asymmetries. We do this by "mirroring" the light curve about the phase 0.5, and in Figure 2 we plot the difference between the flux at equivalent phases in the light curve (for example, phases $\Phi = 0.2$ and $\Phi = 0.8$). Consequently, this plot helps to indicate the phases around which the curve is most asymmetric, and where, for example, star spots may be located under the starpot model to explain these asymmetries. It is again clear that V354 UMa has a very symmetric light curve. It is interesting to note that for LX Leo, in all filters, the primary half of the light curve has a greater flux than the secondary half ($\Delta I(\Phi)_{\mathrm{fit}} > 0$). On the other hand, in MU Leo (and to some extent in V354 UMa), the contribution to the flux varies with phase - starting off with greater flux on the secondary side ($\Delta I(\Phi)_{\mathrm{fit}} > 0$ between phases 0.0–0.3, or equivalently, phases 0.7–1.0) and moving toward higher contributions from the primary side ($\Delta I(\Phi)_{\mathrm{fit}} < 0$ between phases 0.3–0.5 or phases 0.5–0.7). Thus, even though MU Leo has an OER ≈ 1, the "half-phase" plot (Figure 2) demonstrates that there is still significant asymmetry in its light curve. The "half-phase" plots are a visual demonstration of the LCA parameter, and the example of MU Leo demonstrates the advantages of quantifying the asymmetries in different ways.

4. Discussion

We have quantified the asymmetries in three short period eclipsing binary systems: LX Leo (P = 0.235247 d), V345 UMa (P = 0.293825 d), and MU Leo (P = 0.388442 d). Of these, V354 UMa exhibits the most symmetric light curve, while LX Leo is the most asymmetric. We have confirmed that LX Leo and V354 UMa are W UMa-type systems, while MU Leo is an Algol-type system. For LX Leo, the asymmetry is greatest around phase 0.25, while for MU Leo, it is greatest near phase 0.15. By visual inspection, it is clear that LX Leo has a positive O'Connell Effect (primary maxima is higher than secondary maxima) in all three filters. This bears out in the positive values of ΔI and the fact that OER > 1. For MU Leo, ΔI is negative in all filters, which is consistent with the shape of the light curve for MU Leo (Figure 1). Note also, for MU Leo, the OER $\lesssim 1$ in all three filters, showing there is slightly less flux in the primary half of the light curve than the secondary half, but overall, there is almost equal flux in the two halves. Despite this, the LCA is significant, and clear asymmetries are evident in the "half-phase plots" in Figure 2. In all three filters, the values of ΔI for V354 UMa are essentially zero implying a very small O'Connell effect. Similarly, the OER is quite small for V354 UMa, and the LCA is almost an order of magnitude smaller than the other two objects, implying an very symmetric curve for V354 UMa.

We do not discern any obvious correlation between the type of filter used and any of the asymmetry parameters we have discussed, except to note that the asymmetries seem to be more pronounced in the B-filter.

As mentioned earlier, we are currently working on several EBs from the Kepler and TESS catalogs (Knote *et al.* 2022). Our goal is to extend the work presented here to hundreds of objects, and study the time evolution of the asymmetries over several hundreds and thousands of orbital cycles. We hope to discern patterns in the changes in the asymmetries by addressing questions such as: *What are the timescales over which the asymmetries change? Are there differences in the asymmetries in over-contact, semi-detached, and detached systems? Why do the asymmetries in certain systems remain very steady, while in other systems the asymmetries vary significantly over relatively short timescales?*, and so on.

5. Acknowledgements

We have made extensive use of the tools available on the AAVSO website, in particular the VSP (Variable Star Plotter) tool to generate star charts. In addition, we have used the SIMBAD database, operated at CDS, Strasbourg, France, and NASA's Astrophysics Data System. We are thankful for the support provided by the Office of Student Research at Truman State University and the Missouri Space Grant Consortium.

References

Akiba, T., Neugarten, A., Ortmann, C., and Gokhale, V. 2019, *J. Amer. Assoc. Var. Star Obs.*, **47**, 186.

Collins, K. A., Kielkopf, J. F., Stassun, K. G., and Hessman, F. V. 2017, *Astron. J.*, **153**, 77.

Gardner, T., Hahs, G., and Gokhale, V. 2015, *J. Amer. Assoc. Var. Star Obs.*, **43**, 186.

Gürol, B., Michel, R., and Gonzalez, C. 2017, *Rev. Mex. Astron. Astrofis.*, **53**, 179.

Hahs, G., Ortmann, C., and Gokhale, V. 2020, J. *Amer. Assoc. Var. Star Obs.*, **57**, 48.

Hoffman, D. I., Harrison, T. E., and McNamara, B. J. 2009, *Astron. J.*, **138**, 466.

Kafka, S. 2021, Observations from the AAVSO International Database (https://www.aavso.org/data-download).

Knote, M. K., *et al.* 2022, *Astrophys. J., Suppl. Ser.*, accepted (https://arxiv.org/abs/2206.04142).

Kreiner, J. M. 2004, *Acta Astron.*, **54**, 207.

McCartney, S. A. 1999, Ph.D. dissertation, University of Oklahoma.

Michel, R., Xia, Q.-Q., and Higuera, J. 2019, *Res. Astron. Astrophys.*, **19**, 99 (DOI: 10.1088/1674-4527/19/7/99).

O'Connell, D. J. K. 1951, *Publ. Riverview Coll. Obs.*, **2**, 85.

Prša, A., *et al.* 2011, *Astron. J.*, **141**, 83.

Ricker G. R., *et al.* 2015, *J. Astron. Telesc. Instrum. Syst.*, **1**, 014003.

Ruciński, S. M. 1973, *Acta Astron.*, **23**, 79.

Ruciński, S. M. 1993, *Publ. Astron. Soc. Pacific*, **105**, 1433.

Ruciński, S. M. 1997, *Astron. J.*, **113**, 407.

Warner, B. D., and Harris, A. W. 2006, *A Practical Guide to Lightcurve Photometry and Analysis*, Springer, New York.

Wenger, M., *et al.* 2000, *Astron. Astrophys., Suppl. Ser.*, **143**, 9 (DOI: 10.1051/aas:2000332).

Wilsey, N. J., and Beaky M. M. 2009, in *The Society for Astronomical Sciences 28th Annual Symposium on Telescope Science*, Society for Astronomical Sciences, Rancho Cucamonga, CA, 107.

Wolfram Research Co. 2019, How to Fit Models with Measurement Errors (https://reference.wolfram.com/language/howto/FitModelsWithMeasurementErrors).

Issues in Frequency Analysis of δ Scuti Stars I—HD 39641

Bill Rea
Richmond, New Zealand; rea.william@gmail.com

Received September 28, 2021; revised January 17, April 1, 2022; accepted May 3, 2022

Abstract We examine the consequences for the frequency analysis of δ Scuti stars of using pre-whitening if the assumptions of stationarity and sinusoidal light curves were violated. We show through numerical simulation that if the assumption of stationarity is violated then very large numbers of spurious frequencies may be generated which span the entire frequency range of the analysis. We also show that if the light curve is asymmetric, even when regularly spaced, highly significant but entirely spurious frequencies are generated. We apply the results of the numerical simulations to the δ Scuti HD 39641 and show that many statistically significant frequencies are artifacts of the data analysis process. Finally, we propose a method we call restricted range frequency analysis which uses existing tools, but aims to curb the worst features of frequency analysis when assumption violations are present in the light curve.

1. Introduction

This is the first of two papers which are intended to lay out for the amateur short period variable star observing community some common problems which arise in frequency analysis in non-mathematical terms and further illustrate these through the analysis of the δ Scuti HD 39641. There is a long literature addressing this set of problems, and readers with the necessary mathematical and statistical skills to study this literature would certainly benefit from doing so. A small sampling of these papers are Deeming (1975), Lomb (1976), Scargle (1982), Mary (2005), Balona (2014a), Pascual-Granado (2018), and VanderPlas (2018). Further references can be found within the citations contained in these papers.

Throughout the long history of the American Association of Variable Star Observers (AAVSO), amateurs have observed numerous varieties of pulsating stars ranging from long period variables, such as Miras with periods ranging from hundreds to thousands of days, through to very short period variables such as ZZ Ceti with periods as short as around two minutes. Among the tools provided by the AAVSO is the VStar (Benn 2012) light curve analysis software which is often cited in articles published in this journal. There are a number of other frequency analysis tools freely available such as FAMIAS (Zima 2008) and SigSpec (Reegen 2011), described in section 2, which are the two used in this paper.

For stars pulsating in only one or two modes, in general, few problems arise with frequency analysis. However, for stars pulsating in numerous modes, such as δ Scutis, serious problems may arise in interpreting the periodogram in terms of a model of the pulsations. Conceptually, the task is to distinguish between statistically significant peaks in the periodogram which correspond to physical pulsations and statistically significant peaks which arise from some combination of the method of analysis and the spacing of the observations but do not correspond to a physical pulsation.

This problem has been known for a long time. For example, Lomb (1976) pointed out that no more than one period or, equivalently, frequency can be estimated from any one calculation of the frequency spectrum. This necessitates successively identifying periodicities and subtracting them out of the data and then recalculating the frequency spectrum from the residuals, a process usually called pre-whitening. In their textbook on asteroseismology Aerts *et al.* (2010, p. 342) state that “A pre-whitening strategy thus has to be chosen to perform the frequency analysis.”

The science of asteroseismology uses the observations of the light curve first to identify the pulsation frequencies, amplitudes, and modes and then to infer the internal structure of the star (Aerts *et al.* 2010). The so-called hybrid γ Doradus/δ Scuti pulsators are of particular asteroseismological interest because they exhibit both g- (or gravity) mode and p- (or pressure) mode pulsations. The g-mode pulsations originate and propagate deep in the interior, allowing the modelling of interior, perhaps even to the core. The p-mode pulsations originate and propagate in the outer convective layers, allowing that portion of the star also to be modelled. Thus, taken together, they may allow the asteroseismologist to model the star from its surface to its center (Goupil *et al.* 2005).

Pre-whitening, described above, when regarded as a statistical method, appears to have three underlying assumptions, namely: (1) the identified frequencies are generated by sinusoids; (2) they are stationary, in both amplitude and frequency; and (3) where multiple frequencies are present they are combined into the final light curve in an additive manner. Stationarity is defined precisely in many textbooks on time series analysis, see Bloomfield (2000, pp. 167–173) for one such definition. For our purposes it is the assumption that the frequencies, modes, and amplitudes of the pulsations do not change on the time scale spanned by the data.

While pre-whitening sounds a reasonable approach, even when all three assumptions are met, Balona (2014b) was able to show, through numerical experiments, that such a method can extract from the data large numbers of statistically significant frequencies but which do not correspond to any actual frequency in the data set. These are often referred to either as spurious or fictitious frequencies (Balona 2014b). The origins of these spurious or fictitious frequencies can be understood if we think of the pre-whitening process as adding a frequency to the data which is intended to interfere destructively with a particular frequency estimated from the data. Any errors in the estimation of the frequency, amplitude, and phase, together with the fact that the light curve of the frequency identified may not be sinusoidal in shape, will result in the intended interference not being completely destructive, and so many further frequencies are added to the residuals, which are then used to estimate another significant frequency. This is particularly problematic in the analysis of δ Scutis because their multiple active frequencies require multiple cycles of pre-whitening.

Balona (2014b) constructed simulated time series (light curves) with known frequencies and amplitudes, and reported that often frequency analysis employing pre-whitening did not recover all of the real frequencies while extracting more spurious frequencies than there were real frequencies present in the data. Balona (2014b) used stationary sinusoids which he combined additively in his simulations. As we show below, the problem is potentially much worse if any of the three assumptions are violated.

The problem of non-stationary amplitudes is well-known in δ Scuti pulsators. A number of papers report significant changes in the amplitude of one or more pulsation frequencies. For example, Bowman *et al.* (2016) studied 983 δ Scuti stars observed by *Kepler*, and reported that 61.3% exhibited amplitude modulation. If stars with amplitude modulation were subjected to a frequency analysis using pre-whitening, the consequences of this type of assumption violation needs to be taken into account, but it is likely that many serious amateurs are not fully aware of the potential problems.

These findings pose a significant problem for the analysis of δ Scuti pulsators because they are expected to have large numbers of frequencies excited requiring many cycles of pre-whitening; see Uytterhoeven *et al.* (2011) and Poretti *et al.* (2009) for examples.

While the identification of high-amplitude pulsation peaks in a δ Scuti periodogram is not an issue—they can often be identified visually without the need for sophisticated statistical analysis—this alone does not mean they are physically meaningful. Kurtz *et al.* (2015) were able to show that for slowly pulsating B-stars (SPB) combination frequencies can have amplitudes larger than the physically meaningful base frequencies which generate them.

In δ Scutis the number of modes excited is expected to increase as their pulsation amplitudes decrease, making it challenging to distinguish between physically meaningful frequencies present in the data and spurious frequencies which are an artifact of the method(s) of data analysis.

Turning now to the assumptions that the pulsations generate sinusoidal light variations, with multiple pulsations generating multiple sinusoids which are summed to form the observed light curve, it is well known from the study of Fourier series that a non-sinusoidal periodic function will require multiple sinusoids of decreasing amplitude to model it. Thus a pulsation generating an asymmetric variation in light output will be split into multiple frequencies of the form f, 2f, 3f, and so on to the maximum allowable frequency specified by the method. As we show below, these frequencies can be highly significant. These types of frequency spacings have been reported in the literature, for example see Poretti *et al.* (2009) Table 3 where their f_1 also has significant frequencies at $2f_1$ and $3f_1$. If f_1 was an asymmetric pulsation, then frequencies $2f_1$ and $3f_1$ may well be artifacts of the data analysis method, each requiring a pre-whitening cycle to model and remove it. In such a case they may be useful in trying to quantify the asymmetry but have no other physical significance.

In this paper we lay out the effect that amplitude modulation and asymmetric light curves have on frequency analysis with pre-whitening and then apply this to an analysis of the δ Scuti star HD 39641. Towards the end of the paper we mention one possible way to avoid some of the problems with frequency analysis with pre-whitening which will be examined in more detail in Paper II.

The remainder of the paper is structured as follows: section 2 presents the numerical experiments and their results; section 3 discusses the observational data and data analysis issues; section 4 presents the results from the observational data; section 5 contains the discussion; section 6 contains our conclusions and suggestions for future research.

2. Numerical experiments

The purpose of this section is to generate some fairly simple synthetic light curves of known frequency composition and which resemble, in a somewhat idealized form, changes in light curve structure observed in some δ Scutis with references to the original paper which inspired the particular simulation. The particular violations of assumptions underlying pre-whitening are noted. From these we demonstrate that many more spurious frequencies are reported by the frequency analysis than were actually present in the simulated series.

2.1. Data generation

Seven simulated time series (light curves) were generated and analyzed which examined several possible sources of amplitude or frequency modulation and light curve asymmetry. While the units of the simulated series are arbitrary, they were chosen to mimic the 2-minute (120-second) cadence observation mode of the NASA Transiting Exoplanet Survey Satellite (TESS) (Ricker *et al.* 2014) of a δ Scuti with a main pulsation frequency of 11.25 cycles d^{-1}, or a period of 128 minutes, but without the data gaps. All simulated time series or light curves consisted of 131,072 (2^{17}) data points. The sampling time was once every two minutes, which yielded 64 data points or samples per pulsation cycle. The simulated series contained no added noise. The simulated series were as follows:

1. *Stationary* Two time series with two different frequencies were generated. The main frequency of 11.25 cycles d^{-1} with amplitude 1.0 and a second frequency of 11.206226 d^{-1} with amplitude 0.5. The two series were added, yielding a series with obvious beats between the two frequencies. The resulting time series was stationary and no analytical assumptions were violated.

2. *Non-linear* The main frequency was generated as in method 1, and a second frequency with a period 45.51 days and amplitude of 0.5 was generated. The final series was produced by multiplying the two series. This violates the assumption that frequencies are combined additively.

3. *Amplitude reduction* The main frequency was generated as in method 1 and its amplitude remained constant over

45.51 days (32,768 data points, 2^{15}). The amplitude was then linearly reduced to 0.5 over the next 45.51 days, after which it remained constant until the end of the series. The assumption of a stationary amplitude was violated. This experiment was motivated by Figure 1 of Bowman *et al.* (2016).

4. *Slow rise, rapid fall* The main frequency was generated as in method 1 and was modulated by a slow increase in amplitude from 0.5 to 1.5 over 12,288 data points (17.0667 days), followed by a rapid decrease over 4,096 data points (5.6889 days), giving eight complete cycles of amplitude changes. In this simulation there were three frequencies present; the two amplitude modulation frequencies were subject to regime switching so that only two frequencies were present at any one time. The assumption of stationary amplitude and frequency was violated. This experiment was motivated by Figure 2 of Barceló Forteza *et al.* (2015).

5. *Slowly changing frequency* In this simulation the central frequency was set to 11.25 cycles d^{-1} as with the other simulations but a second frequency was used to directly modify the main frequency, which caused it to move through eight cycles between 11.20 cycles d^{-1} and 11.30 cycles d^{-1}. The assumption of stationarity of frequency was violated.

6. *Asymmetric light curve* The light curve was generated with a slow rise followed by rapid decline somewhat akin to a mirror image of a classical Cepheid light curve. This was done with two frequencies with regime switching so that only one frequency was active at any point in the series. Two variations of this were tried, one with a ratio of 3:1 (rise:fall) and the other with a ratio of 9:7. Their periodograms were obviously different but the number of significant frequencies was identical for both cases. The assumption of sinusoidal light variation was violated.

Frequency analysis was primarily carried out using two packages:

1. *SigSpec (Significance Spectrum)* (Reegen 2011) is a batch process frequency analysis tool. The user supplies the input data file and sets a range of options and parameters in an initialization file. SigSpec reads both and completes the frequency analysis without further user intervention.

2. *FAMIAS (Frequency Analysis and Mode Identification in Asteroseismology)* (Zima 2008) was also used because it is fully interactive, meaning that the user must choose the data and analysis options at each step of the analysis process. FAMIAS also stores the output of the intermediate steps so it is easy to go back to re-examine earlier periodograms and pre-whitened data sets and rerun the analysis with different options.

SigSpec uses the Lomb-Scargle periodogram (Lomb 1976; Scargle 1982) as the basis for its frequency analysis; see VanderPlas (2018) for an informative paper on this particular periodogram. See section 3.4 for further details.

2.2. Results

The results of these experiments are presented in Table 1 and Figures 1 through 3.

Table 1 reports the number of significant frequencies (sig.≥4) extracted by SigSpec (Reegen 2011) for each of the six numerical experiments described in section 2.1. The third column reports the actual number of frequencies present in the data, noting that in the "slow rise, rapid fall" that two of the three frequencies undergo regime switching so that at any particular point only two frequencies are active.

Table 1. The number of statistically significant frequencies reported by SigSpec (Reegen 2011).

Simulation Number	*Simulation Type*	*Real Frequencies*	*Reported Frequencies*
1	Stationary	2	6
2	Non-linear	2	4
3	Amplitude Reduction	1	4668
4	Amplitude Slow Rise, Rapid Fall	3	1157
5	Slowly Changing Frequency	2	13
6	Asymmetric Light Curve	2	5

In Figure 1 panels a through d the periodograms correspond to simulations 1 through 4, respectively. The spectral window was identical in all cases and is plotted in red; the periodograms are plotted in black. The frequencies 0.15 cycle d^{-1} either side of the main 11.25-cycles d^{-1} frequency were plotted. Panel a shows the two frequencies of simulation 1 were clearly resolved. Panel b, of the non-linear amplitude modulation, shows that the periodogram mimics the mode splitting caused by stellar rotation for the $l = 1$ modes. Panel c, of the amplitude reduction, shows a significant amount of power was missing from the the central peak. This was widely spread throughout the periodogram. However, the fact that the power had been spread out is not the whole explanation for the 4,668 significant frequencies reported in Table 1; see the discussion of Figure 2.

Finally, panel d with the slow rise, rapid fall amplitude modulation, mimics the mode splitting caused by stellar rotation for the $l = 2$ modes.

Figure 2 presents the frequencies extracted by SigSpec (Reegen 2011) for simulations 3 and 4 in the order in which they were extracted. While the power in the periodograms was spread out, this is not the explanation for the pattern of frequencies seen in the Figure. This was due to the pre-whitening process creating a new frequency or frequencies with each pre-whitening cycle until the process was terminated by hitting the bounds of the frequency analysis.

Figure 3 presents the full periodograms (0 to 50 cycles d^{-1}) for the two asymmetric light curves. While SigSpec reported five significant frequencies for both simulated series, it is clear that the more asymmetric light curve gave much stronger signals at 2f, 3f, and 4f. The upper bound on the frequencies was 50 cycles d^{-1}. If the upper limit had been raised, further significant frequencies would have been reported, at least for the more asymmetric curve where raising the upper frequency limit to 100 cycles d^{-1} yielded nine significant frequencies.

3. Observational data, issues, and frequency analysis

3.1. HD 39641

HD 39641 is relatively bright, low amplitude δ Scuti variable star observed in TESS' continuous viewing zone. Basic details on the star are presented in Table 2.

3.2. Data

The raw data for this paper were downloaded from the TESS Asteroseismic Science Operations Center web site on 25

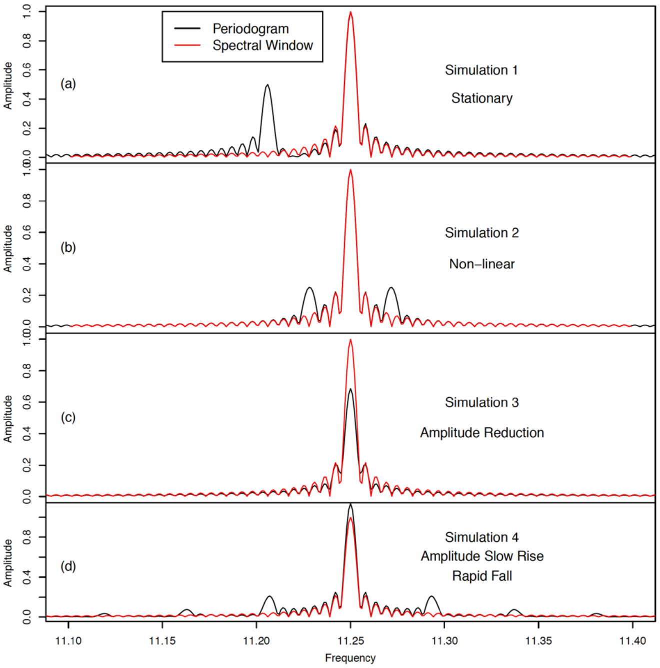

Figure 1. Panel (a) the spectral window and periodogram from simulation 1. Panel (b) the spectral window and periodogram from simulation 2. Panel (c) the spectral window and periodogram from simulation 3. Panel (d) the spectral window and periodogram from simulation 4.

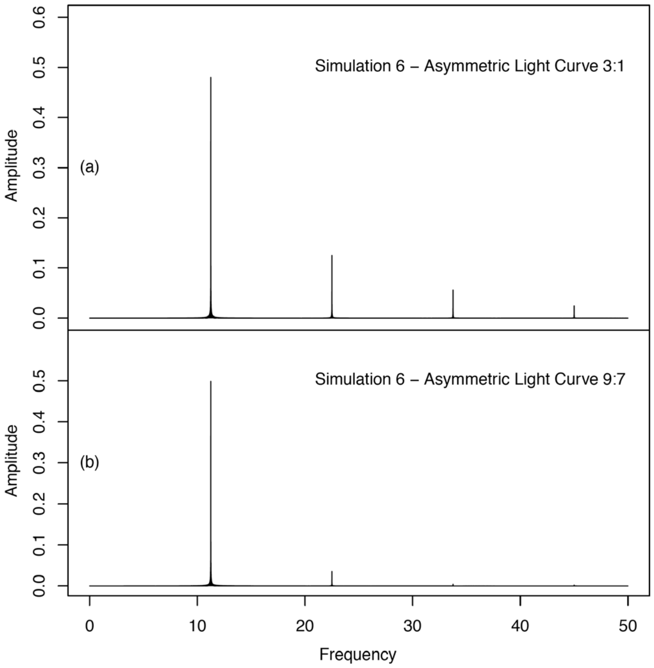

Figure 3. Panel (a) the periodogram for the 3:1 rise to fall ratio asymmetric light curve of simulation 6. Panel (b) the same for the simulation with the 9:7 rise to fall ratio asymmetric light curve.

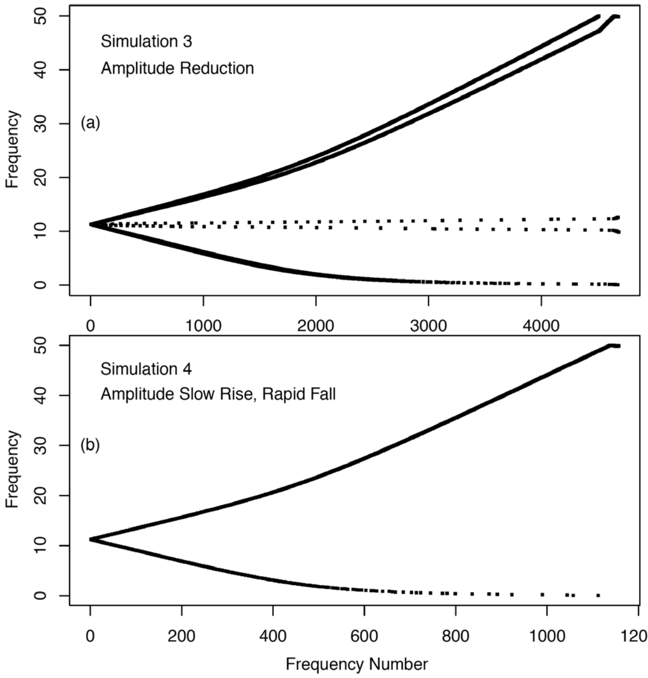

Figure 2. Panel (a) the statistically significant frequencies reported by SigSpec (Reegen 2011) for simulation 3 in the order in which they were extracted. Panel (b) the same for simulation 4.

July 2020. HD 39641 was observed by TESS in its 120-second cadence mode with a total elapsed time of approximately 357 days, which yielded 211,932 usable data points. The observing runs had significant gaps on the order of one-and-a-half days, producing 26 segments of nearly continuous data which were analyzed both separately and as a combined data set. Subsequently, a further six segments of data became available from later observations and these were downloaded on 25 Dec 2020. These were analyzed separately from the first 26 segments.

The reported corrected flux was converted to magnitudes using the value for HD 39641's magnitude in the V band as reported in SIMBAD as the mean value for each observation run. Observations were discarded if the value in the Pixel Quality Field (PQF) was non-zero or either the date or the corrected flux was recorded as not-a-number (nan). The purpose of using the V band magnitude was to align the 26 data segments from HD 39641 to prevent statistically significant but spurious low frequencies appearing in the analysis of the combined data set. There are a range of other options available for aligning the data. An approximately five-day segment of data is presented in Figure 4.

3.3. The spectral windows

A TESS sector is observed continuously for two orbits except for an approximately day-long gap when the data are downloaded to the ground. These data gaps can give rise to the presence of aliases and/or strong side lobes which must be taken account of during any frequency analysis. Figure 5 presents two views of the spectral window of the complete (357-day) data set generated by FAMIAS (Zima 2008) and the spectral window for the data from the first orbit of the TESS mission. In

Table 2. Basic stellar data for HD 39641.

Property	*Value*
R.A.	$05^h\ 49^m\ 46.689^s$
Dec.	–60° 48' 19.939"
Spectral Type (SIMBAD)	A3mA7-A8
Spectral Type (VSX)	A5mF1
Period (VSX)	0.048869 days / 70.371 min
Distance	227.8 ± 1.25 pc
Mean Mag (V)	9.3 ± 0.02
Amplitude (V)	0.015
TIC	149630117

Note: The data was drawn from the TASOC web site (https://tasoc.dk/), SIMBAD (http://simbad.u-strasbg.fr/simbad/) (Wenger et al. *2000), and the Variable Star Index (VSX, https://www.aavso.org/vsx/). The distance is from the GAIA DR2 catalogcitep (Gaia Collab. 2018). TIC is the TESS Input Catalog number.*

Table 3. The frequencies and height of the main peak relative to the alias and each of the side lobes seen in Figure 5.

Alias Frequency cycles d^{-1}	*Relative Height to Main Peak*
± 0.07392	8.1689

Side Lobe Frequency cycles d^{-1}	*Frequency Step*	*Relative Height to Main Peak*
± 0.00392	—	4.4069
± 0.00672	0.00280	6.0144
± 0.00952	0.00280	9.0188
± 0.01288	0.00336	10.8069
± 0.01792	0.00504	13.5853

Table 4. Types of statistically significan frequencies in combined data set of HD 39641.

Frequency Type	*Number*
δ Scuti	1,166
γ Doradus	297
Others	49
Total	1,512

panel (a) the main peak is approximately 8.1 times the height of the alias. Inverting the frequency difference of the alias from the peak yields 13.52 days, which closely matches Tess's 13.7-day orbital period. In panel (b) of the Figure there are five noticeable side lobes; details of these are given in Table 3. The FWHM of the central peak was 0.00336 d^{-1}, meaning that frequencies separated by less than 0.00168 d^{-1} are unlikely to be resolved. Within the individual segments the FWHM varied from segment to segment, but for comparison purposes the frequency resolution the first segment was 0.045372 d^{-1}. Panel (c) presents the spectral window from the data from the first orbit of the Sector 1 observations. The much broader frequency peak, indicating lower frequency resolution, is because the time base line of the observations is much shorter than in the combined data set.

This paper presents the analysis both of the complete data set and of each individual TESS orbit. Details of the date range and number of data points from each orbit are given in Table 5.

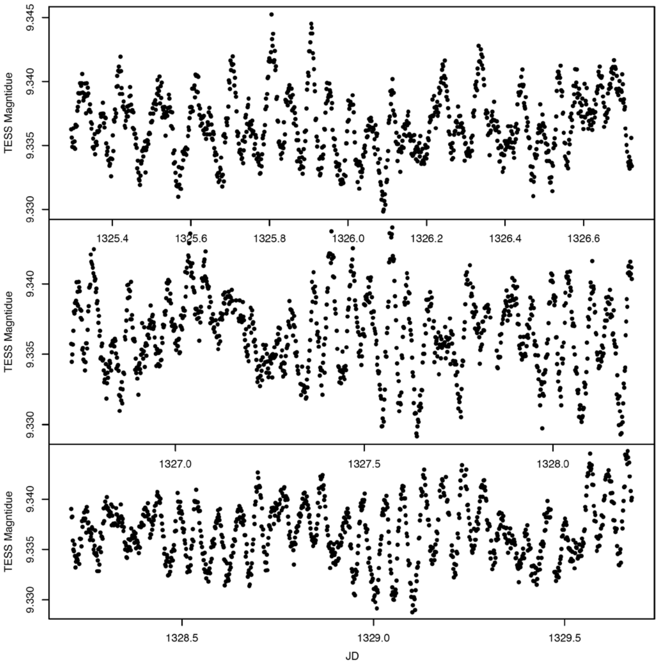

Figure 4. Approximately five days of HD 39641's light curve from the TESS data. The time axis is labelled JD and is the baricentric Julian day –2457000.

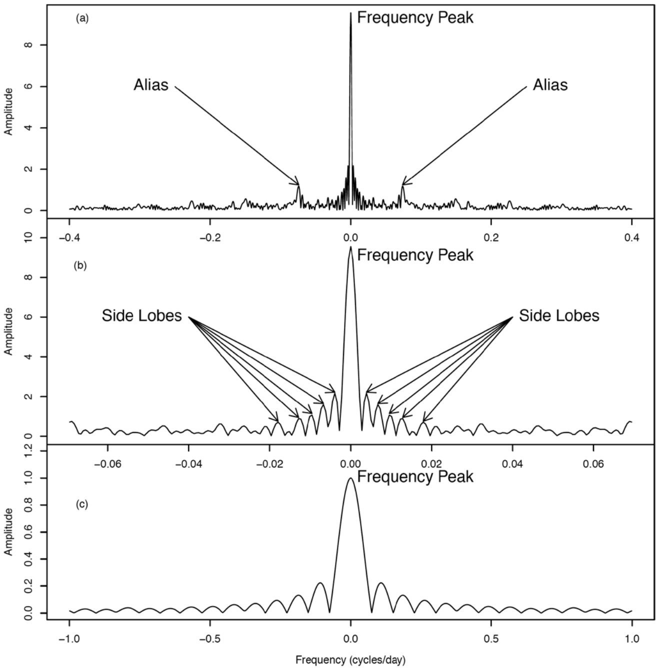

Figure 5. Panels (a) and (b) present the spectral window for the TESS data for the combined data set of HD 39641 as generated by FAMIAS (Zima 2008). Panel (a) shows the window to 0.4 cycles d^{-1} in which there is a single alias at 0:07392 cycles d^{-1}. Panel (b) shows a detail of the window to 0.07 cycles d^{-1} showing five side lobes at 0.00392, 0.00672, 0.00952, 0.01288, and 0.01792 cycles d^{-1}. Further details of the side lobes are presented in Table (3). Panel (c) presents the spectral window from the first orbit of Sector 1 of obsevations.

3.4. Frequency analysis

Similar to the simulated data, The frequency analysis was carried using FAMIAS and SigSpec, and with user-written code in Matlab (MathWorks 2019) or R (R Core Team 2019). FAMIAS had a limit of 100 frequencies which could be extracted from the data.

The default frequency range for both packages was 0 to 50 cycles d^{-1}. The minimum signal to noise ratio (SNR) used with FAMIAS was four. The minimum significance used with SigSpec was also four. These two measures are different, with an SNR of four being equivalent to a spectral significance of five.

We also carried what we are calling a "restricted range frequency analysis." While we are introducing this method in the current paper it will be the examined in some detail in a second paper. This used SigSpec's options to change the range of frequencies being analyzed and restrict this range to only encompass specific, relatively narrow, ranges. We only undertook two ranges. The first was 0.28 to 3.2 cycles d^{-1}, which is slightly wider than the traditional γ Doradus range; see Table 9.1 of Catelan and Smith (2015). This range was further subdivided into two halves, 0.28 to 1.74 and 1.74 to 3.2 cycles d^{-1}, and the results of the three analyses were combined to assess which frequencies were likely to be physically meaningful and which were like to be artifacts of the data analysis process.

The second was the 4.0 to 6.0 cycles d^{-1} range which appeared devoid of any significant pulsations in the periodogram from HD 39641's combined data set. Possible future directions for this method are discussed further in section 6.2 below.

4. Results

4.1. Observational data

Figure 6 presents a Fourier spectral analysis generated by FAMIAS (Zima 2008) of HD 39641's combined data set. The γ Doradus frequency range is marked. The vertical axis is the amplitude; this is different from the periodograms presented in Figures 8 through 11, in which the vertical axis is $\log_{10}$ (Amplitude).

An analysis of the combined data set was undertaken with SigSpec (Reegen 2011). 1,512 statistically significant frequencies were reported. A summary of their types is given in Table 4. Frequency of $f \geq 3$ cycles d^{-1} were classified as δ Scuti types, $0.3 \leq f < 3$ where classified as γ Doradus types and $f < 0.3$ cycles d^{-1} were classified as other.

Each observing run was also analyzed. Details of the date range, number of usable and unusable data points, numbers of statistically significant frequencies, and their types are reported in Table 5. It can be seen that some orbits within some sectors had a large number of usable data points. The row for JD 1410–1423 shows 2,073 unusable data points, a consequence of a continuous period of approximately 2.7 days in which all fields, apart from the PQF, were recorded as nan. The raw data for JD 1558.28–1568.47 had an approximately half-day period with non-zero PQF values.

Figure 7 presents a plot of the frequencies below 30 cycles d^{-1} in the order in which SigSpec (Reegen 2011) extracted them.

Table 5. A summary of the frequency analysis of the 32 sub-periods of the TESS data for HD 39641.

Date Range	*Usable Data Points*	*Unusable Data Points*	*Frequencies*			
			δ Sct	*γ Dor*	*Others*	*Total*
1325.30–1338.52	9223	300	96	19	1	116
1339.66–1353.18	8875	857	94	21	2	117
1354.11–1367.15	9225	167	89	19	3	111
1368.20–1381.51	9090	207	93	18	2	113
1385.95–1395.44	6683	152	74	14	2	90
1396.64–1406.21	6767	127	78	14	1	93
1410.90–1423.51	7005	2073	69	13	3	85
1424.56–1436.84	8784	60	84	20	3	107
1437.99–1450.19	8746	35	84	17	2	103
1451.56–1463.94	8888	28	84	17	1	102
1468.27–1477.02	6263	37	67	14	1	82
1478.12–1490.04	8561	26	88	18	2	108
1491.63–1503.04	8190	23	90	19	2	111
1504.71–1516.09	8168	26	87	17	2	106
1517.40–1529.07	8379	29	87	16	3	106
1535.00–1542.00	5019	19	58	10	1	69
1544.88–1555.54	7653	22	81	16	0	97
1558.28–1568.47	6935	403	69	16	1	86
1571.06–1581.78	7695	28	77	16	2	95
1584.74–1595.68	7852	29	81	16	1	98
1599.85–1609.69	6989	100	74	15	2	91
1612.37–1623.89	8268	31	82	15	3	100
1624.96–1639.00	9894	213	90	20	2	112
1640.04–1652.89	9207	48	89	17	4	110
1653.92–1667.69	9767	148	96	20	4	120
1668.63–1682.36	9812	75	96	21	3	120
2036.28–2048.13	8521	11	88	18	2	108
2049.15–2060.64	8258	14	86	17	0	103
2061.85–2071.57	6988	16	78	12	2	92
2075.16–2085.54	7386	91	69	17	2	88
2115.89–2127.43	8295	18	80	19	2	101
2130.21–2141.82	8329	30	81	16	2	99

Note: The date range is reported to two decimal places for formatting reasons, TESS dates are precise to eight decimal places.

Figure 8 presents the evolution of the periodogram of HD 39641 over the 26 orbits of the combined data set in the γ Doradus frequency range. Plotting the periodograms in this manner allows us to examine change in the active frequencies over time. Some, such as the strong peak at approximately 2.71 cycles d^{-1}, are relatively stable, whereas others, such as the more complicated peak near 2.3 d^{-1}, may show changes in frequency, amplitude, and splitting of an apparent single frequency into two or more frequencies followed by their recombining. When looking for deviations from a sinusoid which may have given rise to a cascade of spurious frequencies, such as can be seen in Figure 7, the 2.3 d^{-1} frequency is a clear candidate.

Figure 9 presents the evolution of the periodogram of HD 39641 over the 26 orbits of the combined data set over the 9 to 12 cycles d^{-1} part of the δ Scuti frequency range. Similar to what was seen in Figure 8, the two strongest frequencies vary across time, sometimes splitting into two distinct frequencies. As observed in the numerical simulations, such behavior can give rise to many spurious frequencies during analysis.

Figures 10 and 11 present the evolution of the periodogram of HD 39641 over the 26 orbits of the combined data set over

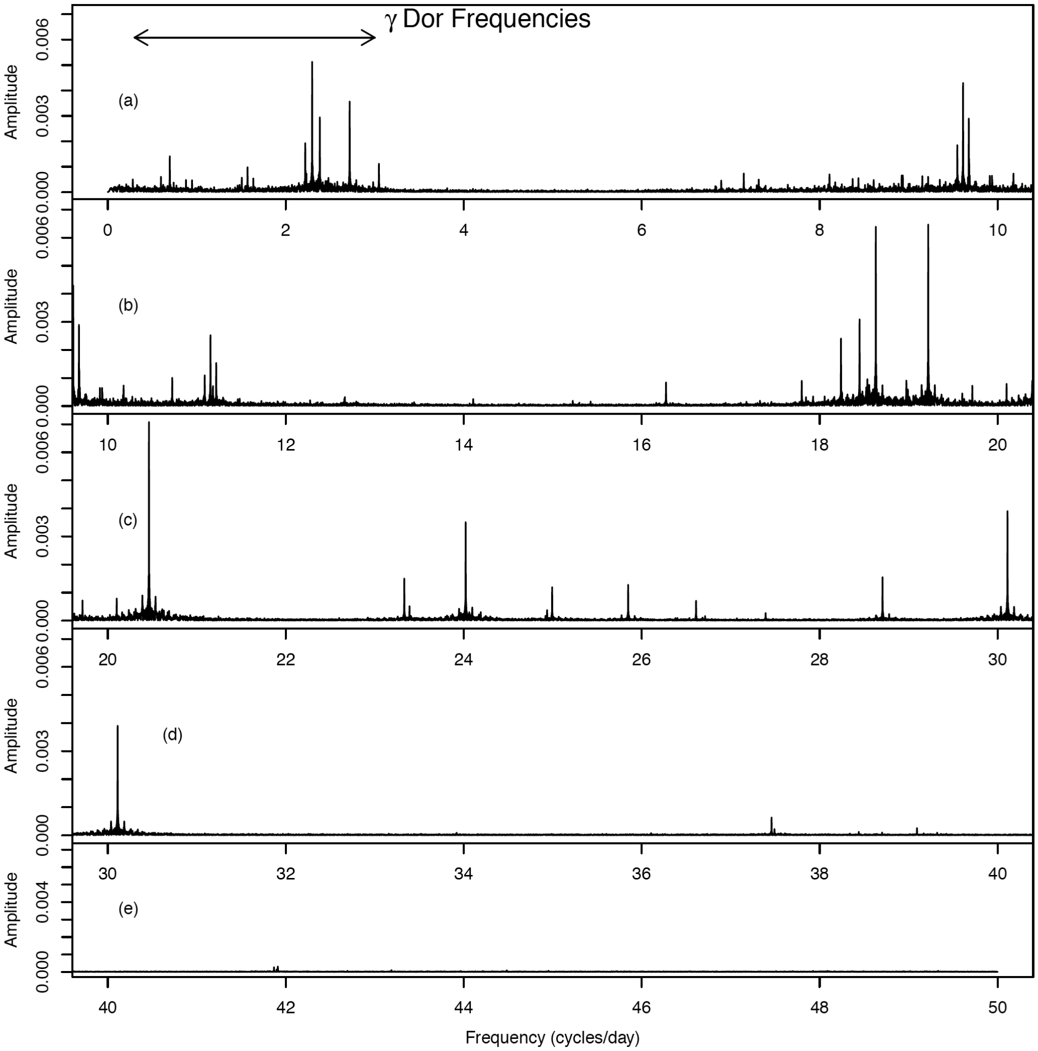

Figure 6. The Fourier spectral analysis of HD 39641's combined data set broken into five segments of frequencies. The range γ Doradus frequencies are marked in panel (a), the remainder of the frequencies in panel (a) and the frequencies in panels (b)–(e) are considered to be δ Scuti frequencies.

the 17.5 to 21 cycles d^{-1} and 23 to 31 cycles d^{-1} respectively. In contrast to both Figure 8 and Figure 9, the three strongest frequencies are stable both in amplitude and frequency. However, from this we cannot determine if these pulsations generate a sinusoidal light curve.

A search was made for highly significant frequencies (sig. ≥ 100), of which there were 84, which may be generating cascades of significant frequencies of the form $kf, k=1,2,...,$ due to asymmetries in their contributions to the light curve. There were 13 such groups of frequencies and Table 6 reports the results of this search.

Figure 12 presents four details of the periodogram in Figure 6 where four sets of triplets were observed.

4.2. Restricted range frequency analysis

SigSpec (Reegen 2011), in common with many other frequency analysis tools, had the option of changing the range of frequencies being analyzed. Because it was clear from the results in the previous section that spurious frequencies were contaminating all of the frequency space, we restricted the range of frequencies as described above. We undertook two restricted range frequency analyses. The first was in the range 0.28 to 3.2 cycles d^{-1}, typical of the g-mode pulsations of γ Doradus stars. The periodogram of HD 39641's combined data set together with the periodogram of the residuals after the analysis was run are presented in Figure 13.

From the unrestricted analysis of the combined data set, there were 315 significant frequencies reported in the slightly enlarged γ Doradus range. This can be compared to the 48 significant frequencies from the restricted range frequency analysis.

In the second range, 4 to 6 cycles d^{-1}, the full frequency analysis yielded 59 significant frequencies, whereas the restricted range analysis yielded none. With no frequencies modelled and removed the periodogram was unchanged before and after the analysis.

5. Discussion

The results of the numerical experiments in section 2.2 clearly show that some types of non-stationarity pose a major problem for frequency analysis of δ Scuti stars using pre-

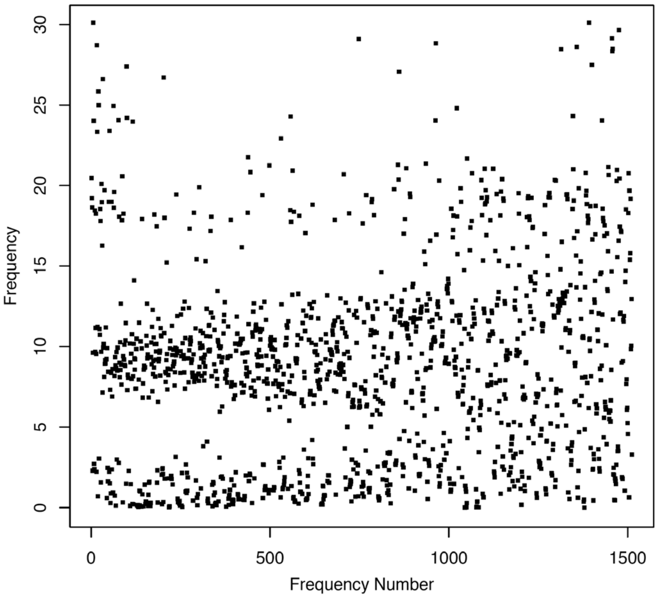

Figure 7. The statistically signicant frequencies as reported by SigSpec (Reegen 2011) in the order in which SigSpec extracted them.

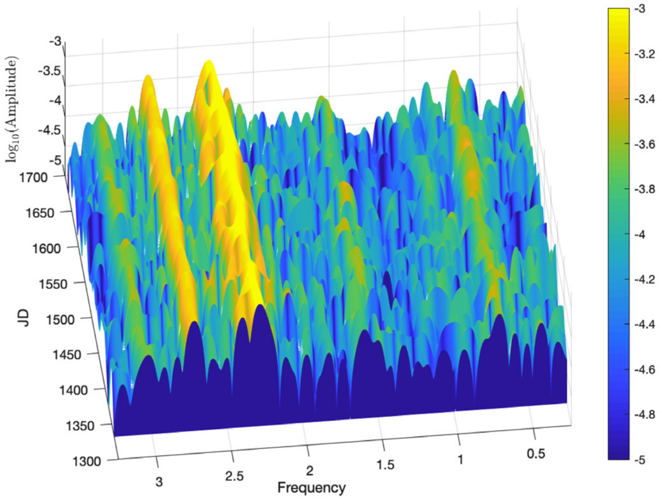

Figure 8. The evolution of the periodogram from the 26 data segments for the γ Doradus frequency range. The colorbar units are in $\log_{10}$ (Amplitude).

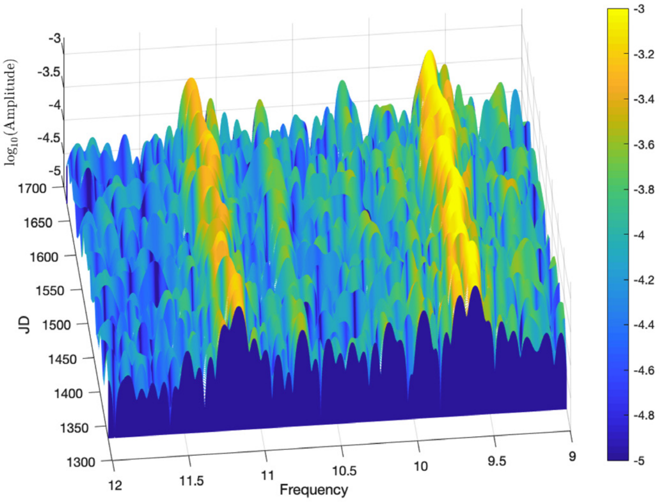

Figure 9. The evolution of the periodogram from the 26 data segments for part of the δ Scuti range of 9 to 12 cycles d^{-1}. The color bar units are in $\log_{10}$ (Amplitude).

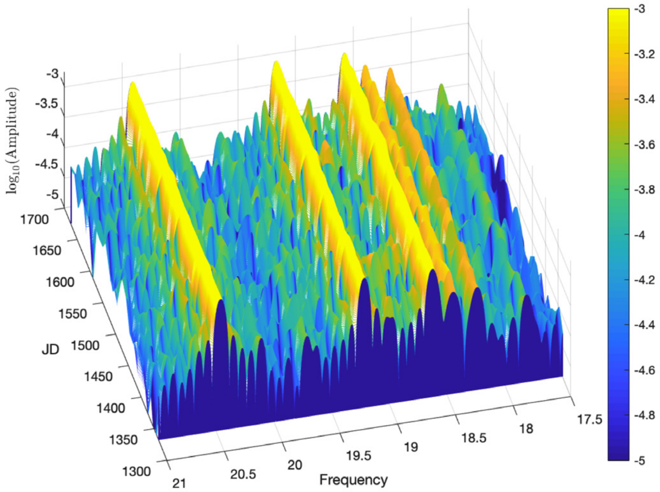

Figure 10. The evolution of the periodogram from the 26 data segments for the δ Scuti range of 17.5 to 21 cycles d^{-1}. The colorbar units are in $\log_{10}$ (Amplitude).

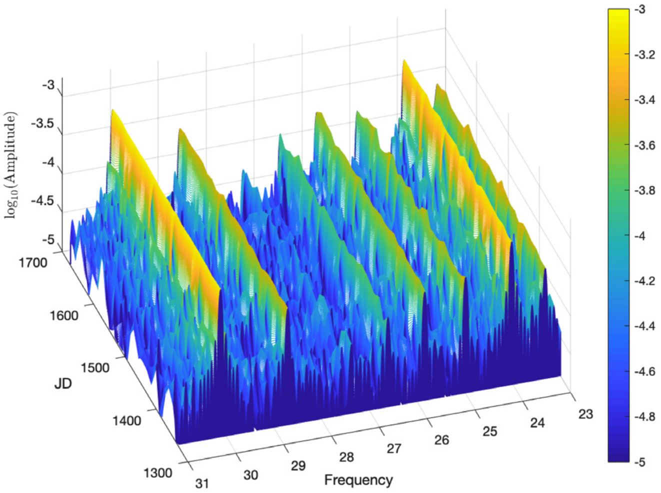

Figure 11. The evolution of the periodogram from the 26 data segments for the δ Scuti range of 23 to 31 cycles d^{-1}. The colorbar units are in $\log_{10}$ (Amplitude).

whitening. The two numerical experiments which yielded the largest number of statistically significant frequencies were motivated by results of the analysis of actual δ Scutis reported in the literature. If the reported amplitude modulation is not the result of very slow beating of otherwise stable frequencies, they have the potential to contaminate the entire frequency range with very large numbers of spurious frequencies.

If an apparent amplitude modulation is caused by two narrowly separated, but otherwise stable, frequencies then these frequencies will be able to be resolved with a long enough time series. However, similar to Balona (2014b), more spurious frequencies were reported than there were actual frequencies in the data in this case. Moreover, one of the spurious frequencies had a significance approximately equal to the two real frequencies (22,778.8 and 28,327.8 for the two real frequencies and 26,420.8 for the first spurious frequency). The likely consequence would be that in a frequency analysis of a real star we would be unable to conclude the frequency was an artifact of data analysis from checking the significances alone. In this case the periodogram was sufficiently simple, and hence sufficiently easy to interpret, that a researcher would be able to correctly conclude that only two physically meaningful frequencies were present by examining the periodogram at the locations of the reported significant frequencies.

Grigahcène *et al.* (2010), in their Figure 2, showed that for hybrid γ Doradus/δ Scuti stars the γ Doradus and δ Scuti frequency ranges should not overlap. It is clear even from a cursory examination of the periodogram of HD 39641's data, see Figure 6, that there is nothing other than noise in the periodogram between approximately 3.5 and 6.5 cycles d^{-1}. This matches the theoretically predicted gap. A detailed examination of the 26 individual periodograms which compose the subsets of HD 39641's combined data set showed no stable peaks across time within this range. However, when a frequency analysis was run using SigSpec (Reegen 2011) using the frequency range of 0 to 50 cycles d^{-1}, 105 significant frequencies were reported within the 3.5–6.5 cycles d^{-1} range. As Poretti *et al.* (2009) note, this range of frequencies is lower than the fundamental radial mode, to which one must add that they are also above the theoretical range of g-mode frequencies. This leaves no immediately obvious physical explanation for their origins.

Figure 7 shows that the frequency gap did not become appreciably filled in until some time after the 500th frequency was extracted. The gradual "fanning out" of significant frequencies, initially from the range 6–12 cycles d^{-1} into both higher and lower frequencies, was similar to that seen in Figure 2 from the numerical experiments. Also, there was a "fanning out" of frequencies from the γ Doradus range into the gap. The implication is that at least some, if not all, of these statistically significant frequencies are simply artifacts of the data analysis process and do not represent physically meaningful pulsations.

The "fanning out" of the significant frequencies from the γ Doradus and 6–12 cycles d^{-1} ranges seen in Figure 7 stands in contrast to the 18–21 cycles d^{-1} or 23–31 cycles d^{-1} regions (see Figures 10 and 11) where there were a number of very significant frequencies, including the three most significant in HD 39641's combined data set. But the evidence for the gradual "fanning out" of significant frequencies like that seen in the two lower ranges is much less. This could be explained if one or more frequencies in the γ Doradus and 6–12 cycles d^{-1} ranges (see Figures 8 and 9) were unstable either in amplitude or frequency, or both, but the higher frequencies were stable. Put another way, if there were assumption violations in the two lower ranges, but not in the higher ranges, then this could account for both presence of the spurious frequencies and the manner in which they appear in Figure 7.

The Figures 8 through 11, just referred to, seek to answer this question. These are plots of the evolution of the periodogram over the 26 segments forming HD 39641's combined data set in four different frequency ranges. Although SigSpec reported 33 frequencies with significance ≥ 100 from the combined data set in the 6–12 cycles d^{-1} range, it was clear through examining the 3-d plot and using Matlab's (MathWorks 2019) rotation tool that all frequencies which could be identified visually were unstable in either frequency or amplitude or both. In Figure 9 the two strongest frequencies clearly change over time and occasionally split into two distinct frequencies, behaviors which will generate spurious frequencies during analysis.

A similar situation exists in the γ Doradus frequency region (Figure 8). It did have a very wide peak covering the 2.25 to 2.50 cycles d^{-1} region which clearly split into two distinct frequencies five times, each time rejoining. Because the number of usable data points varied by almost a factor of two in the 26 individual segments, we checked whether this was just an artifact of a larger number of data points giving better resolution. This does not appear to be an explanation for the observed behavior.

These observations of the lower frequency ranges were in contrast to the higher frequency ranges of Figures 10 and 11. In these Figures the frequencies which could be identified visually were noticeably more stable in both frequency and amplitude. In Figure 7 these two higher frequency regions did not appear to generate large numbers of frequencies which then "fan out" from their region of origin.

In light of the numerical experiments, it is a reasonable conclusion that there were sufficiently large violations of the underlying assumptions of the frequency analysis that the two lower frequency regions generated large numbers of spurious frequencies, hence filled in the clear gap between the top of the γ Doradus frequency range and the bottom of δ Scuti range.

Similar comments could be applied to the frequency range 12–16.5 cycles d^{-1}, where there are only eight frequency peaks in the periodogram of HD 39641's combined data set (Figure 6). A careful examination of the evolution of the 26 periodograms revealed only one stable structure at 16.27343 cycles d^{-1}. The remaining seven peaks were discernable, but all of them had periods in which their amplitudes dropped sufficiently low that they were not statistically significant. However, that frequency region was gradually filled in as frequencies "fanned out" from the top of the 6 to 12 cycles d^{-1} region, eventually giving 116 significant frequencies in this region. It was difficult to tell if there was any appreciable fanning out from the 18 cycles d^{-1} and higher region because, if there was, it did not begin to occur until somewhere about the 800th significant frequency. SigSpec reported 158 significant frequencies in this "gap," of which 120 had significances under 10 and hence were very likely to be spurious.

Table 6 presents a series of frequencies of the form kf, k=1,2,.... If one or more of these were a cascade of frequencies generated by an asymmetric light curve we would expect that there to be a monotonic decline in amplitude and significance. However, with 1,512 significant frequencies, the problem of either a chance alignment with another spurious frequency or one of the kf frequencies merging with a physically meaningful frequency the expected pattern would be disrupted. Of the frequencies listed only frequency 6, namely 0.946136 cycles d^{-1}, fully follows the expected pattern, concluding with a frequency (3.783453), which lies between the top of the γ Doradus and the bottom of the δ Scuti frequencies and has no known physical explanation.

A restricted range frequency analysis was performed. Restricting the range of frequencies to be modelled does two things: first, it prevents spurious frequencies from the parts of the frequency range outside the range being analyzed from contaminating the analysis, and secondly, it prevents spurious frequencies from the range being modelled from contaminating other frequency ranges. The basic problem of the violation the

Table 6. The highly significant frequencies (sig ≥ 100) which also had further significant frequencies at integer multiples of the base frequency.

N	f	2f	3f	4f	5f	6f	7f	8f
1	0.1303333 (125.15)	0.2616298 (15.18)	0.3888451 (53.22)	0.5227608 (21.12)	0.6477295 (6.56)	0.7813393 (12.83)	0.9148378 (31.63)	1.0436858 (63.41)
2	0.2815179 (248.75)	0.5615032 (21.20)						
3	0.5978526 (338.17)	1.1946123 (28.75)	1.7930717 (39.98)	2.3907837 (41.58)	2.9911594 (7.26)	3.5832385 (5.09)		
4	0.7403535 (148.27)	1.4815043 (81.11)	2.2191678 (1850.16)	2.9650469 (7.93)				
5	0.8787684 (246.30)	1.7575015 (9.29)						
6	0.9461362 (215.54)	1.8932267 (7.02)	2.8406652 (6.87)	3.7834527 (4.70)				
7	2.9822269 (119.0364)	5.9655588 (7.67)	8.9486721 (12.96)					
8	3.0469668 (885.64)	6.0950020 (4.53)	9.1414396 (12.30)	12.1840934 (8.95)				
9	8.5106303 (120.28)	17.0202440 (4.61)						
10	8.9220928 (378.06)	17.8442241 (6.37)						
11	9.1540018 (385.72)	18.3077848 (18.27)						
12	9.6114526 (4671.35)	19.2218557 (6.13)	28.8358362 (7.51)					
13	19.2199717 (6589.14)	38.4399206 (20.07)						

Note: The figures in brackets below each frequency are the significance as reported by SigSpec *(Reegen 2011).*

underlying statistical assumptions remained, but the hope was that some of the grossest features created by these violations could be usefully reduced.

The results indicate this is a worthwhile strategy which is investigated further in a second paper. The complete elimination of all 59 spurious frequencies in the 4 to 6 cycle d^{-1} range was particularly notable. Within this range there is nothing but noise, so no assumption violations were present. The reduction from 315 to 48 in the number of statistically significant frequencies in the γ Doradus range and the fact that there appeared to be nothing but noise in the periodogram of the residuals (see Figure 13) was also encouraging.

6. Conclusions and future research

6.1. Conclusions

Much of the promise which the study of δ Scutis holds for asteroseismology had not been realized. The evidence presented here confirms existing literature which argues that part of the problem is that the methods of data analysis in common use include pre-whitening as an integral part of their analysis and hence yield large numbers of statistically significant but physically meaningless frequencies. We have confirmed the reported result of Balona (2014b) that even if all assumptions are met, pre-whitening still generates numerous spurious frequencies. Further, we have shown that if one or more assumptions are violated the problem can be dramatically worse.

Given that the spurious frequencies generated by pre-whitening are not necessarily of low significance, meaning the problem cannot be solved simply by raising the significance threshold, it is necessary to check all reported frequencies against the periodogram of a data set, to determine whether they are likely to be real or spurious. The use of restricted range frequency analysis has the potential to significantly reduce the number of frequencies which need to be checked against the periodogram and will be investigated in more detail in a second paper.

If a light curve spans sufficient time to meaningfully split the data into non-overlapping subperiods, closely examining the evolution of the periodogram over time can yield additional insights not obtainable from treating the data as a single data set.

The fact that there are four triplets with almost identical frequency differences in HD 39641's periodogram strongly suggests that they are the result of rotation. However, the fact that they were not always present in the periodograms of the subperiods needs further research. Other δ Scutis with reported triplets should provide a good source of data to work with.

6.2. Future research

It is particularly troubling that mode splitting by stellar rotation can be convincingly mimicked by amplitude modulation. Further research is needed to find a method to distinguish between these two cases.

A curious finding was that in the lower frequency regions, namely the γ Doradus range and the 6–12 cycles d^{-1} region of the δ Scuti range, most of the frequencies were unstable, whereas above about 16 cycles d^{-1} they were largely stable. Further δ Scutis need to be studied to determine if this is a common feature among this class of variables.

The use of restricted frequency range analysis still has the same underlying assumptions as doing an unrestricted frequency

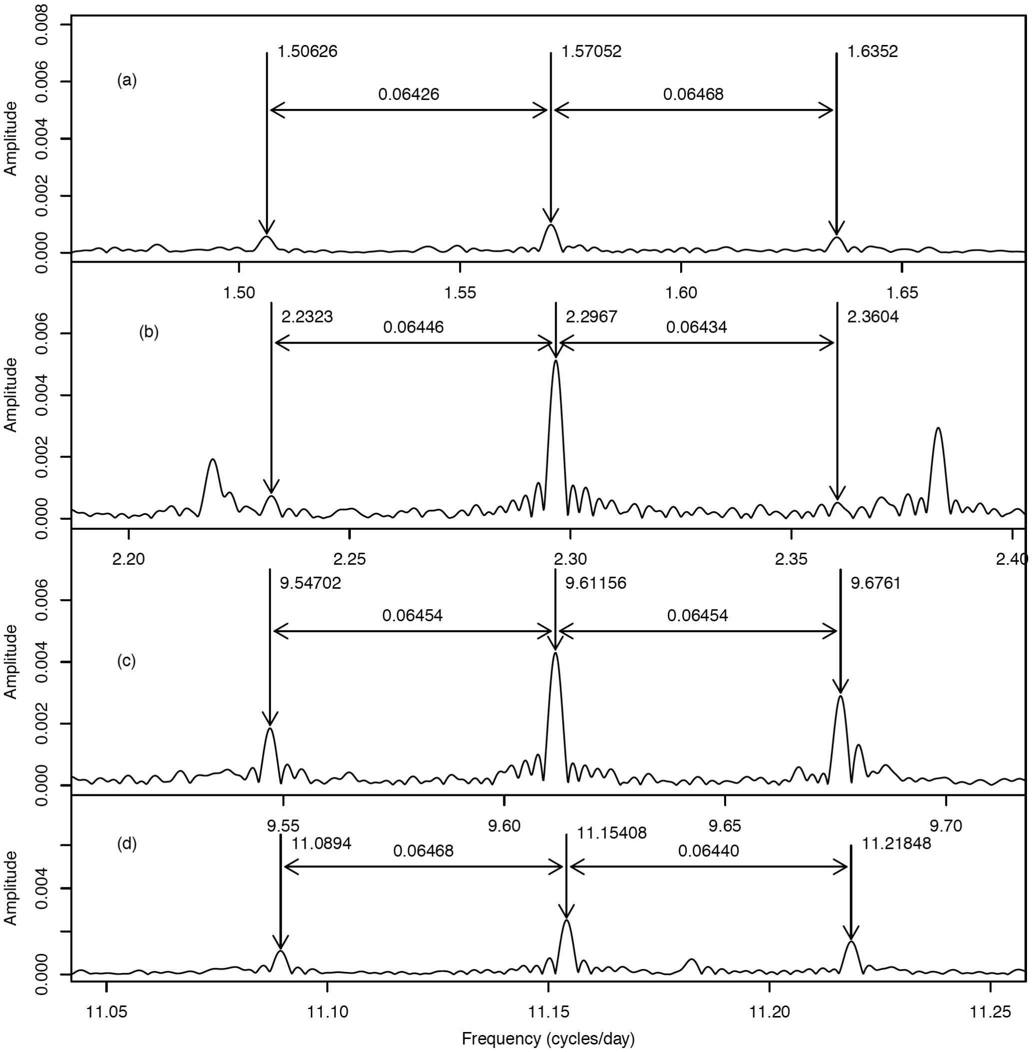

Figure 12. The Fourier spectral analysis of HD 39641's combined data revealed four sets of triplets. Panel (a) shows the rst set of triplets in the γ Doradus range. Panel (b) shows the second set of triplets in the γ Doradus range. Panel (c) which the first set of triplets in the lower part of the δ Scuti range while panel (d) also shows another set of triplets in the lower part of the δ Scuti range.

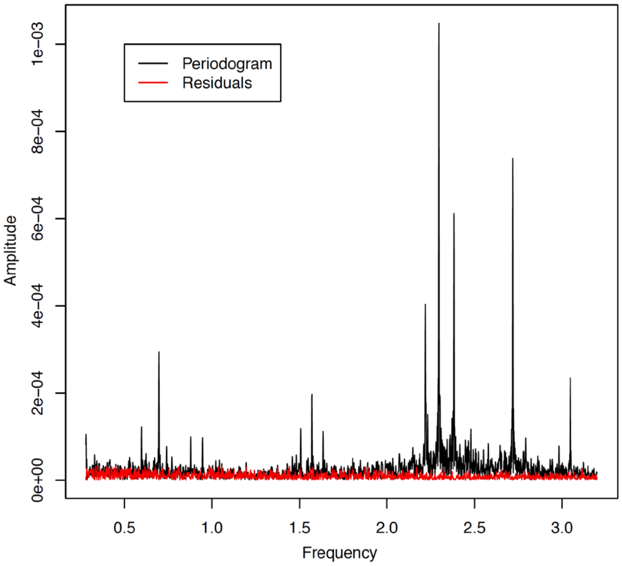

Figure 13. A detail of The Fourier spectral analysis of HD 39641's combined data set before (black) and the residuals after (red) a frequency analysis by SigSpec (Reegen 2011) with the frequency range restricted to 0.28 to 3.2 cycles d^{-1}.

analysis where the entire frequency analysis is done at one time. However, it has the potential to curb some of the worst consequences of assumption violations, such as the spreading of spurious frequencies across the entire frequency range being analyzed. This is addressed in greater detail in Paper II.

7. Acknowledgements

The author would like to thank the editor and an anonymous referee for valuable comments which helped to improve the paper.

The author would like to thank NASA for making the data from its Transiting Exoplanet Survey Satellite freely available and the TESS Asteroseismic Science Operations Center for operating their particular database (TASOC) of TESS photometry data.

The author would like to thank the American Association of Variable Star Observers for maintaining and making freely available the Variable Star Index (VSX).

This research has made use of the SIMBAD database, operated at CDS, Strasbourg, France.

References

Aerts, C., Christensen-Dalsgaard, J., and Kurtz, D. 2010, *Asteroseismology*, Springer, Dordrecht.

Balona, L. A. 2014a, *Mon. Not. Roy. Astron. Soc.*, **437**, 1476.

Balona, L. A. 2014b, *Mon. Not. Roy. Astron. Soc.*, **439**, 3453.

Barceló Forteza, S., Michel, E., Roca Cortés, T., and García, R. A. 2015, *Astron. Astrophys.*, **579**, A133.

Benn, D. 2012, *J. Amer. Assoc. Var. Star Obs.*, **40**, 852.

Bloomfield, P. 2000, *Fourier Analysis of Time Series: An Introduction*, 2nd ed., Wiley, New York.

Bowman, D. M., Kurtz, D. W., Breger, M., Murphy, S. J., and Holdsworth, D. L. 2016, *Mon. Not. Roy. Astron. Soc.*, **460**, 1970.

Catelan, M., and Smith, H. A. 2015, *Pulsating Stars*, Wiley-VCH, Weinheim, Germany.

Deeming, T. 1975, *Astrophys. Space Sci.*, **36**, 137.

Gaia Collaboration, *et al.* 2018, *Astron. Astrophys.*, **616A**, 1.

Goupil, M.-J., Dupret, M. A., Samadi, R., Boehm, T., Alecian, E., Suarez, J. C., Lebtreton, Y., and Catala, C. 2005, *J. Astrophys. Astron.*, **26**, 249.

Grigahcène, A., *et al.* 2010, *Astrophys. J., Lett.*, **713**, L192.

Kurtz, D. W., Shibahashi, H., Murphy, S. J., Bedding, T. R., and Bowman, D. M. 2015, *Mon. Not. Roy. Astron. Soc.*, **450**, 3015.

Lomb, N. R. 1976, *Astrophys. Space Sci.*, **39**, 447.

Mary, D. L. 2005, *J. Astrophys. Astron.*, **26**, 283.

MathWorks. 2019, MATLAB programming and numeric computing platform, ver. 9.6.00, The MathWorks Inc., Natick, MA (https://www.mathworks.com/products/matlab.html).

Pascual-Granado, J., Suárez, J. C., Garrido, R., Moya, A., García Hernández, A., Rodón, J. R., and Lares-Martiz, M. 2018, *Astron. Astrophys.*, **614**, A40.

Poretti, E., *et al.* 2009, *Astron. Astrophys.*, **506**, 85.

R Core Team. 2019, R: A Language and Environment for Statistical Computing, R Foundation for Statistical Computing, Vienna, Austria (https://www.R-project.org).

Reegen, P. 2011, *Commun. Asteroseismology*, **163**, 3.

Ricker, G. R. *et al.* 2014, *Proc. SPIE*, **9143**, id. 914320.

Scargle, J. D. 1982, *Astrophys. J.*, **263**, 835.

Uytterhoeven, K., *et al.* 2011, *Astron. Astrophys.*, **534**, A125.

VanderPlas, J. T. 2018, *Astrophys. J., Suppl. Ser.*, **236**, 16.

Wenger, M., *et al.*, 2000, *Astron. Astrophys., Suppl. Ser.*, **143**, 9.

Zima, W. 2008, *Commun. Asteroseismology*, **155**, 17.

Analyzing Transit Timing Variations of Qatar-1b

Elise Yang
Saint Francis High School, 1885 Miramonte Avenue, Mountain View, CA 94040; elisemkyang@gmail.com

Daniel Mendoza
Saint Francis High School, 1885 Miramonte Avenue, Mountain View, CA 94040; danieldoza2003@gmail.com

Pablo A. Mendoza
University of California, Davis, 1 Shields Avenue, Davis, CA 95616; andresdoza.11@gmail.com

Vani Pandian
Louisiana School for Math, Science, and the Arts, 715 University Parkway, Natchitoches, LA 71457; vp5564@princeton.edu

Kaushik Tota
Saint Francis High School, 1885 Miramonte Avenue, Mountain View, CA 94040; kaushi.tota@gmail.com

Paige Yeung
Stanford Online High School, 415 Broadway Academy Hall, Floor 2, 8853, Redwood City, CA 94063; paige.yeung@gmail.com

Received June 5, 2021; revised January 7, 2022; accepted January 17, 2022

Abstract This study investigates 13 transits of Qatar-1b from archival data collected using 6-inch telescopes in the MicroObservatory network. The purpose of this transit analysis was to update transit midpoints of Qatar-1b to maintain the ephemeris. Additionally, the study sought to uncover trends in the transit data, which could provide more information about the exoplanet. In order to achieve this goal, the EXOplanet Transit Interpretation Code (EXOTIC) pipeline was used to process these transits and generate light curves, which were contributed to the American Association of Variable Star Observers (AAVSO) Exoplanet Database. The analysis of the data did not indicate the presence of other planets in the system. This study contributes observations of the star system Qatar-1b and supports the current ephemeris of this planet.

1. Introduction

Exoplanet transit photometry takes advantage of the fact that if an exoplanet passes in front of a star relative to Earth's line of sight, there will be a dip in the brightness that will result in a characteristic curve (Deeg and Alonso 2018). This is described by the equation

$$\Delta F \approx (R_p / R_s)^2 = k^2 \quad (1)$$

where ΔF is the change in flux, R_p is the radius of the planet, R_s is the radius of the host star, and k is the ratio of the two radii. Thus, by measuring the percentage of light that is blocked by a transiting planet, the radius of an exoplanet relative to its host star can be determined. In addition, the shape of the curve and the period with which it repeats allows determination of many more characteristics of the planet, the orbit, and the host star.

Observations of confirmed transiting exoplanets can help refine the ephemerides of targets used for detailed spectroscopic characterization (Zellem *et al.* 2020). When its transits are not observed for an extended period of time, a planet's mid-transit time uncertainty increases, and recovering its ephemeris becomes more difficult. A network of smaller telescopes can be used to observe bright, high-priority targets, which allows larger telescopes to allocate their observing time to the dimmer, smaller targets for which they are optimized. The NASA Exoplanet Watch program facilitates citizen scientists conducting research on bright exoplanet targets (brighter than 12 magnitude) using small telescopes, and collates their results in the AAVSO Exoplanet Database (Zellem *et al.* 2020). Such observations not only help to maintain the ephemerides of these exoplanets, but also facilitate analysis that require a large pool of measurements.

One example of a type of analysis that can be done with a pool of transit mid-point measurements is to search for transit timing variations (TTVs) (Zellem *et al.* 2020). TTVs can be used to detect additional exoplanets in the system, because their gravitational influence causes the planet under study to transit slightly earlier or later than expected. Thus, if the difference between the expected and observed midpoints of a planet exhibits a patterned variation, this can be analyzed to identify and characterize the perturber. However, such variations occur only within systems that contain massive, tightly packed planets, and they can only be detected with a sufficiently large collection of data (Cortés-Zuleta *et al.* 2020). Such a collection is currently accumulating in the AAVSO Exoplanet Database. Exoplanet Watch will reduce these data via a common pipeline to update their ephemerides and identify TTV's.

This study analyzes 13 transits from the planet Qatar-1b, which is characterized as a "hot Jupiter" (Alsubai *et al.* 2011). Hot Jupiters are a class of exoplanets characterized by large radius, high temperature, and short orbital period as a result of their being located close to their primary star (e.g. within 0.1 AU), with a mass similar to that of Jupiter. The short orbital period (~1.43 d) and deep transit depth (~2.1%) of Qatar-1b allows for frequent opportunities to observe the planet's transit using small telescopes (Collins *et al.* 2017a).

Previous studies have indicated no evidence of additional planets in the Qatar-1 system (Collins *et al.* 2017a). In Collins *et al.* (2017a), it was found that Qatar-1b transit times were well modeled by the ephemeris with transit midpoint $T_0 = 2456234.10321800 \pm 0.00006071$ and period $P = 1.4200242 \pm 0.0000002173$.

2. Instruments used

The MicroObservatory Robotic Telescope Network is a network of 6-inch telescopes operated by the Harvard-Smithsonian Center for Astrophysics (Sadler *et al.* 2001). This network allows teachers across the U.S. to provide their students access to use the telescopes over the World Wide Web. With this access, students can easily take and analyze images. Students can also adjust many of the settings, such as field of view and exposure times.

Data for this study were collected using the MicroObservatory telescope Cecilia, located at the Fred Lawrence Whipple Observatory on Mount Hopkins, Arizona. The unfiltered images were taken using a KAF-1400 ME camera that has a CCD image sensor, at a focal length of 560mm, and an exposure time of 60 seconds. Exoplanet transit data have been collected by Cecilia since 2011 and are ongoing. Observations made on 13 dates between 17 May 2011 and 09 June 2014 were analyzed. The observations have been uploaded to the AAVSO Exoplanet Database under observer code YELA.

3. Data reduction and light curves

The EXOplanet Transit Interpretation Code (EXOTIC) pipeline is a PYTHON-based tool for reducing transit data. It takes raw fits files or a pre-reduced photometric time series as input. To use it, the user first identifies a comparison star or stars. A comparison star should be close to the target star so that its light is affected by Earth's atmosphere in the same way, well-separated from other stars, not saturated or too dim, not variable, and similar in color to the target star. AstroImageJ (Collins *et al.* 2017a) was used to identify suitable comparison stars. Figure 1 indicates comparison stars found through this method.

EXOTIC performed dark field subtraction using darks taken the same night as the science images. Additionally, instrument specifications along with parameters from the NASA Exoplanet Archive (NEA), shown in Table 1, were used to compute priors for EXOTIC's Markov Chain Monte Carlo (MCMC) fitting algorithm. Note that the latest versions of EXOTIC use dynamic nested sampling, which is similar to MCMC but more efficient. The NEA parameters input as priors were a mid-transit time of 2456234.10321800 days, a mid-transit time uncertainty of ±0.00006071 day, and a period of 1.42002420 ± 0.00000022 days (Collins *et al.* 2017a).

EXOTIC analyzes the image files by first performing multi-object optimal aperture photometry (Zellem *et al.* 2020). It takes the pixel coordinates of a target star and a comparison star as input, and tracks the location of the target star relative to the comparison star through the series of images. The MCMC fits the raw photometric data with a model light curve and a function accounting for airmass to calculate the transit midpoint and its uncertainty.

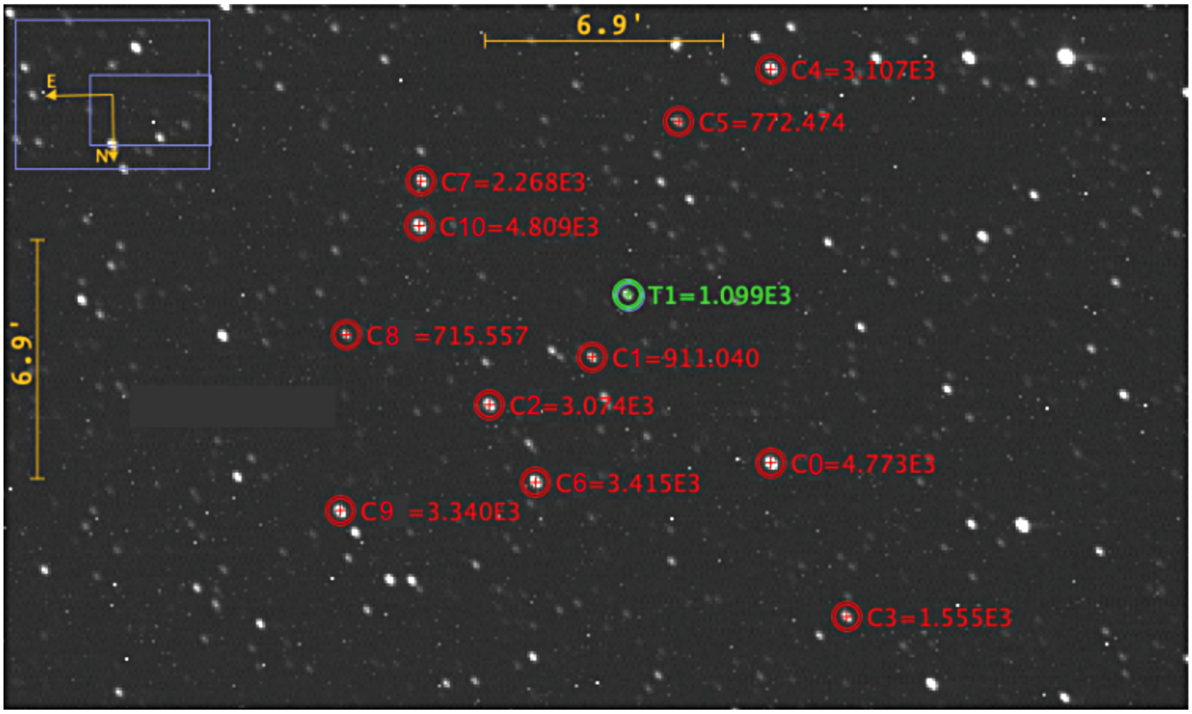

Figure 1. Qatar-1b starfield with labeled comparison stars.

Table 1. Input parameters queried from the NASA Exoplanet Archive used for the fits files by EXOTIC.

Parameter	*Value*
Target Star R.A.	$20^h\ 13^m\ 31.6^{5s}$
Target Star Dec.	+65° 09' 44.39"
Planet Name	Qatar-1b
Host Start Name	Qatar-1
Orbital Period (days)	1.42002420
Orbital Period Uncertainty	± 0.00000022
Published Mid-Transit Time (BJD-UTC)	2456234.10321800
Mid-Transit Time Uncertainty	0.00006071
Planet to Stellar Radius (R_p/R_s)	0.14629
R_p/R_s (+) Uncertainty	+0.00063
R_p/R_s (–) Uncertainty	–0.00064
Ratio of Distance to Stellar Radius (a/R_S)	6.247
a/R_S (+) Uncertainty	+0.067
a/R_S (–) Uncertainty	–0.065
Orbital Inclination i (deg)	84.08
i (deg) (+) Uncertainty	+0.16
i (deg) (–) Uncertainty	–0.15
Orbital Eccentricity (0 if null)	0
Star Effective Temperature (K)	4910.0000
K (+) Uncertainty	+135.9410
K (–) Uncertainty	–80.7669
Star Metallicity ([M/H])	0.2
Star Metallicity Uncertainty	0.1
Star Surface Gravity (log(g))	4.5724800
Star Surface Gravity (+) Uncertainty	+0.0674466
Star Surface Gravity (–) Uncertainty	–0.0982458

The fits files of Qatar-1b were run through EXOTIC to produce light curves for each of the thirty-seven observation dates on which images were acquired by Cecilia. The light curves were classified into four categories: good light curve, poor light curve, partial light curve, and technical issue. "Good light curves" were the light curves where there was a clear dip, and the transit depth looked close to its expected value of approximately 2.1%. The good light curves, shown in Figure 3, were used for analysis; in total, thirteen of the thirty-seven dates yielded good light curves. "Poor light curves" describes light curves in which no dip or no notable dip was observed. Two of the thirty-seven dates analyzed yielded poor light curves. "Partial light curves" showed a clear dip, but did not capture the entire transit of the exoplanet; two of the thirty-seven dates analyzed yielded partial light curves. "Technical issues" describes cases in which fitting errors or poor weather led to a light curve not being output or being unclear, so that data could not be collected. These issues can be caused by cloudy weather (shown in Figure 2), an external light source, a star getting too close to the edge of the field of view, an inadequate comparison star, and rain. Twenty of the thirty-seven dates analyzed yielded technical issues. Examples of each of these types of light curves can be seen in Figure 4.

4. Results

For each successful light curve fit, EXOTIC estimated values for the residual scatter, observed transit midpoint, and transit midpoint uncertainty using the BJD time system. With the observed transit midpoint, the expected transit midpoint can be calculated using the formula:

$$T = T_0 + E \cdot P \tag{2}$$

where E is the epoch, P is the orbital period, T_0 is the optimal transit time in a zero epoch (picked as the first transit date from the reduced data so that all the following transit dates have positive E values), and T is the transit time at the given epoch.

Table 2 shows these values, where each row is a successful transit using the comparison star that yielded the lowest residual scatter percentage. Observed minus Calculated (O–C) values are found by subtracting the midpoint found by Equation 2 using the period derived by Collins *et al.* (2017a) from the midpoint fit by EXOTIC (T_{obs}). The O–C uncertainty values were determined using the equation:

$$\Delta(O–C) = \sqrt{\Delta T_{obs}^2 + E^2 \cdot \Delta P^2 + 2 \cdot E \cdot \Delta P \cdot \Delta T_0 + \Delta T_0^2} \tag{3}$$

which is Equation 3 from Zellem *et al.* (2020).

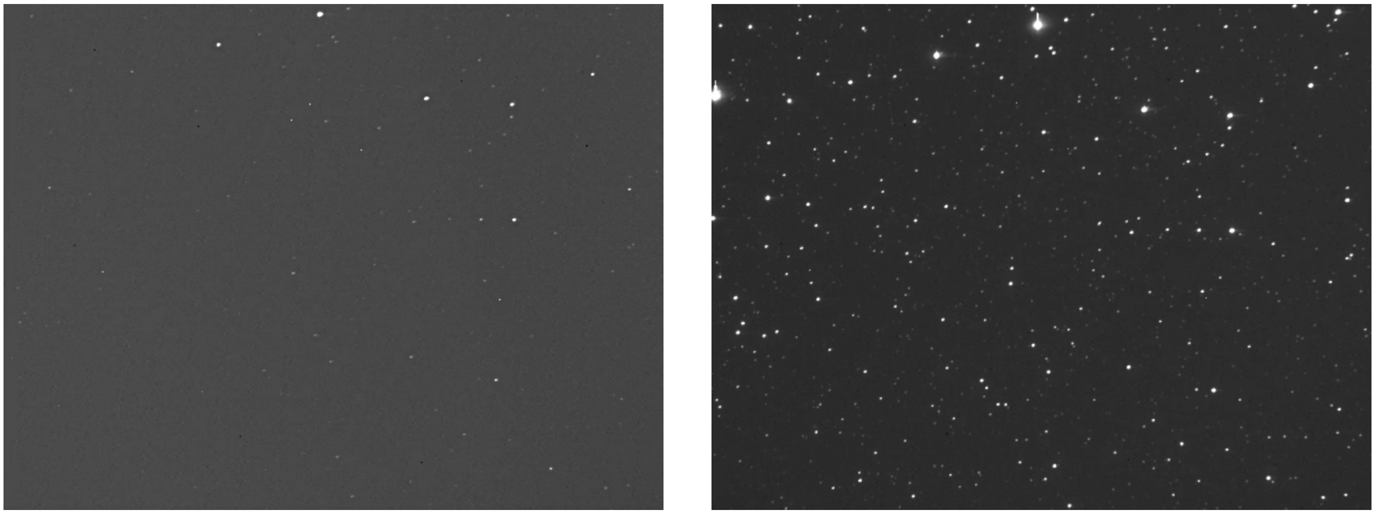

Figure 2. Image showing poor weather (left) versus image showing clear weather (right).

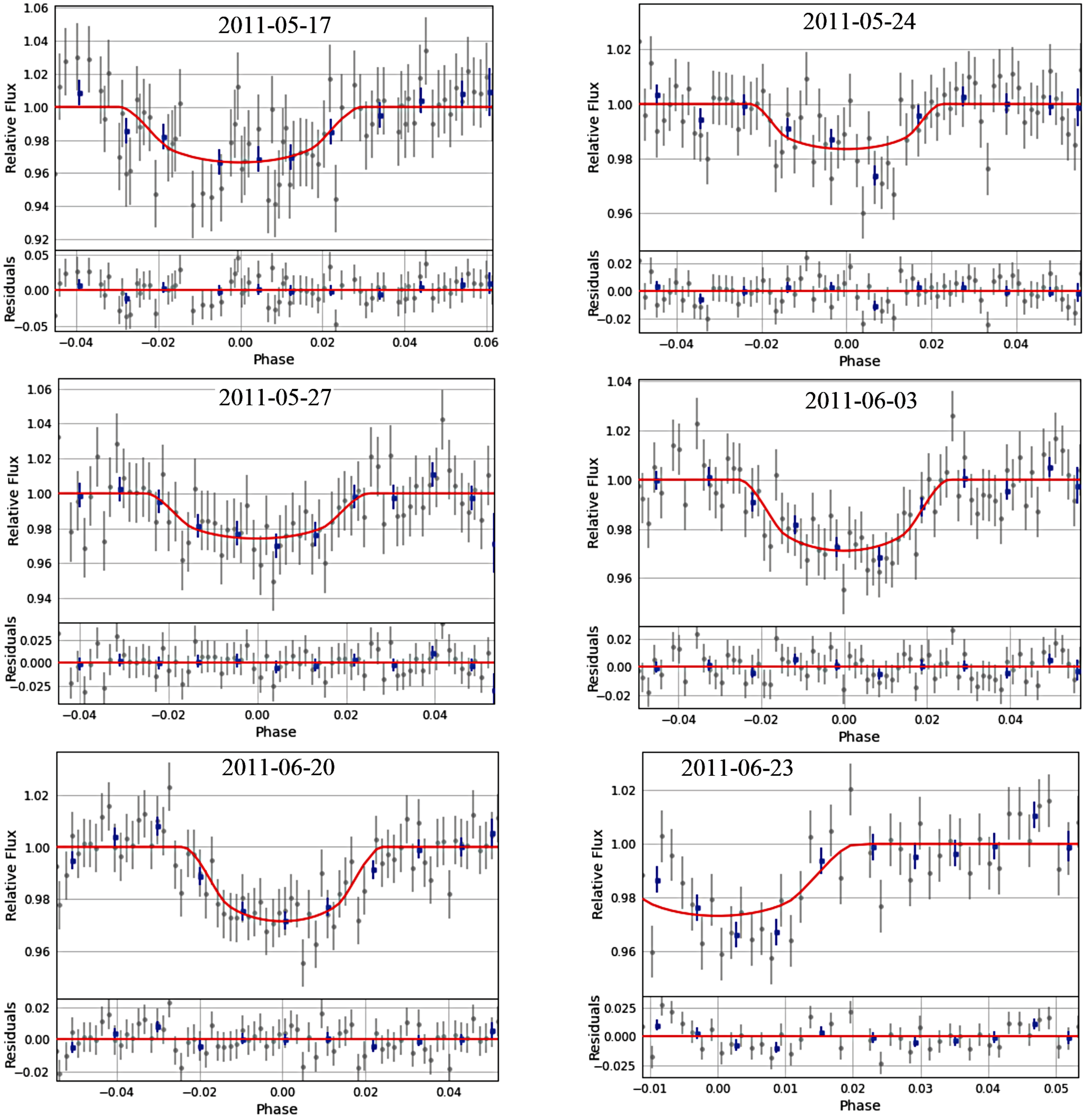

Figure 3. Successful light curve fits by EXOTIC for the transits of Qatar-1b on 17 May, 24 May, May 27, 03 June, 20 June, 23 June of 2011; 18 September, 02 October, 05 October of 2012; 05 October, 12 October, 22 October of 2013; and 09 June of 2014. After an EXOTIC update on 09 July 2020, the color of the outputted light curves changed from black to gray (observe the difference between 2011-06-03 and 2011-06-24). (Figure continued on next page).

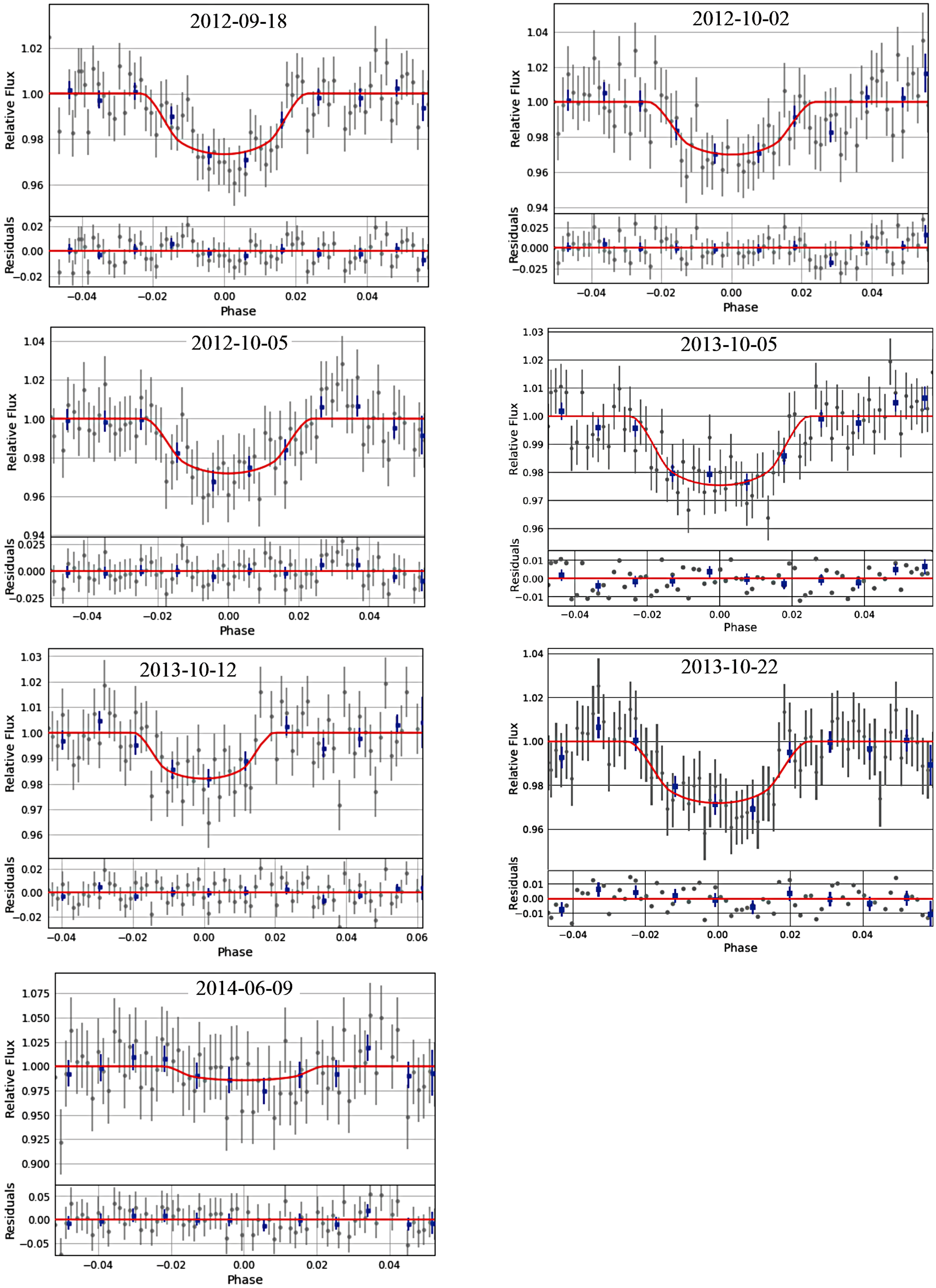

Figure 3. Successful light curve fits by EXOTIC for the transits of Qatar-1b (cont.)

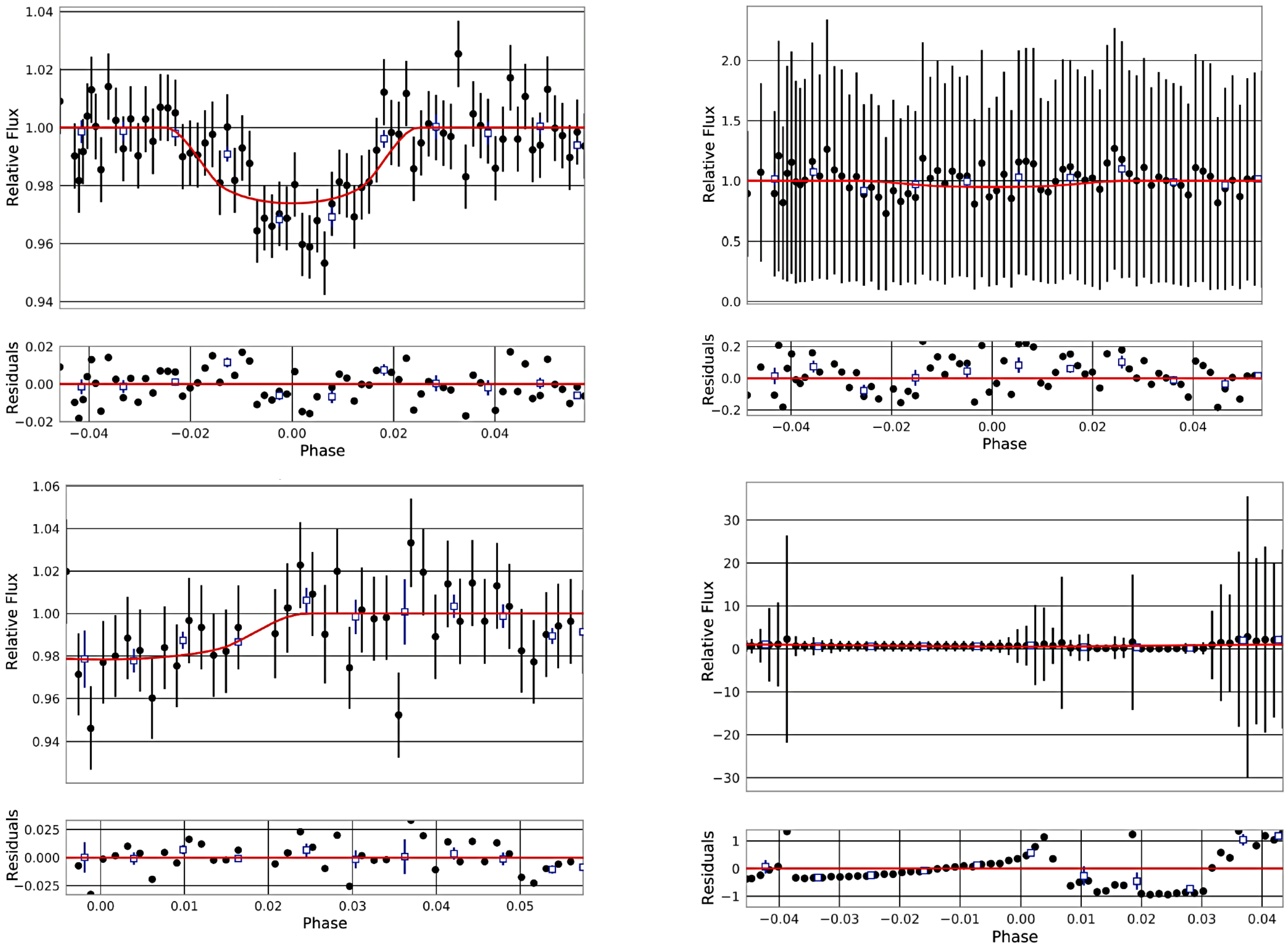

Figure 4. Top left: Good light curve from images taken on 09 June 2014. Top right: Poor light curve from images taken on 26 July 2012. Bottom left: Partial light curve from images taken on 08 September 2019. Bottom right: Technical issue from images taken on 21 September 2016.

Table 2. Transit midpoints (BJD time system) from EXOTIC and calculated O–C and O–C error values.

Date (yyyy-mm-dd)	*Residual Scatter (%)*	*Observed Transit Midpoint*	*Transit Midpoint Uncertainty*	*Expected Transit Midpoint*	*O–C (min)*	*O–C Uncertainty (min)*
2011-05-17	1.69	2455698.7537	0.0031	2455698.7541	–0.57	4.46
2011-05-24	0.99	2455705.8512	0.0029	2455705.8542	–4.34	14.26
2011-05-27	1.47	2455708.6955	0.0036	2455708.6943	1.78	5.18
2011-06-03	0.97	2455715.7906	0.002	2455715.7944	–5.45	2.88
2011-06-20	0.86	2455732.8377	0.0018	2455732.8347	4.36	2.59
2011-06-23	1.24	2455735.6722	0.003	2455735.6747	–3.63	4.32
2012-09-18	0.94	2456188.6631	0.0018	2456188.6624	0.95	2.60
2012-10-02	1.42	2456202.8646	0.0027	2456202.8627	2.76	3.89
2012-10-05	1.08	2456205.7046	0.0028	2456205.7027	2.69	4.04
2013-10-05	2.65	2456205.7090	0.0034	2456205.7027	9.02	4.90
2013-10-12	0.97	2456577.7466	0.0015	2456577.7491	–3.56	2.18
2013-10-22	0.95	2456587.6890	0.00196	2456587.6892	–0.39	2.84
2014-06-09	2.50	2456817.7326	0.00035	2456817.7332	–0.83	0.61

An O–C diagram plots each O–C value as a function of epoch. If the observed transit midpoint always matches the calculated transit midpoint, the diagram will show a horizontal line, signifying that there is no difference between the observations and the model. If the line is slanted, then the predicted period may have significant error, indicating that the ephemeris needs to be updated. If there is a sinusoidal curve in the diagram, this may be a TTV indicating other bodies in the system.

In order to determine whether the ephemeris is up-to-date, a chi-squared test of the observed transit midpoint and the expected transit midpoint (see Table 2) was performed. A chi-squared test demonstrates whether the observed data fits the model created by the previous data well. If the chi-squared test value is not close to zero, the model of expected values as computed using previous transit data needs to be updated (Kane *et al.* 2009). The chi-squared test value computed using the

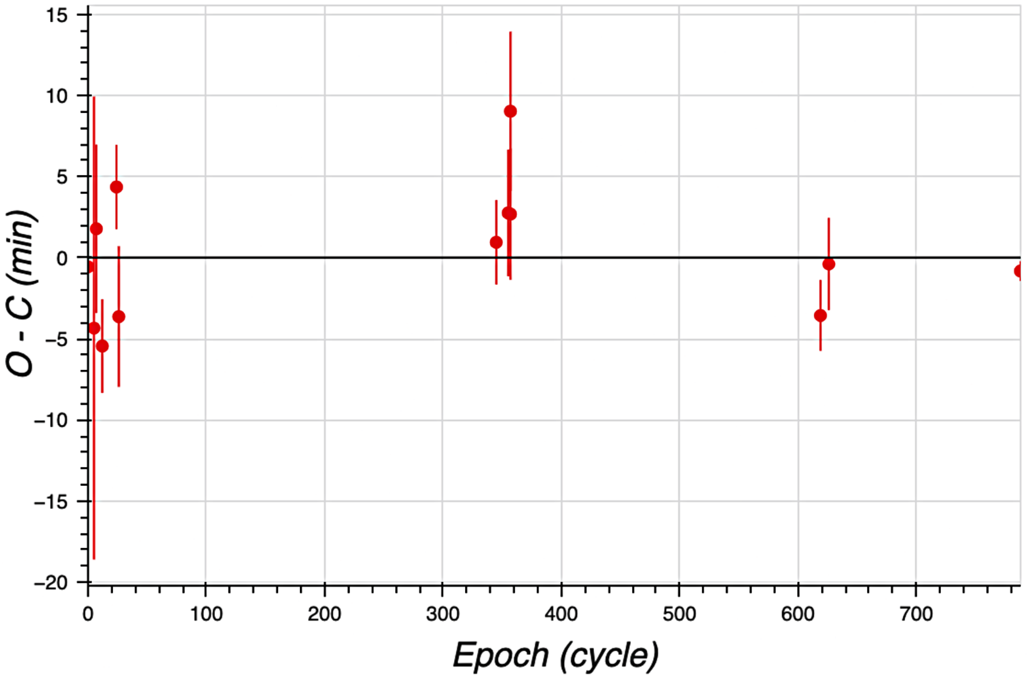

Figure 5. O–C plot from the reduction of Qatar-1b transit data in EXOTIC.

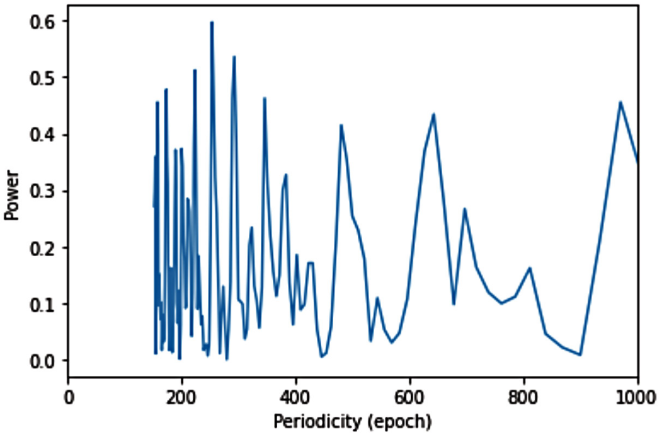

Figure 6. Lomb-Scargle periodogram for the O-C values.

observed transit midpoints was 0.114. This value is compared to the critical value for a 0.05 significance level with n−1, or 11, degrees of freedom, which is 19.675. The test value is much smaller than the critical value, so these data support the validity of the current ephemeris.

A Lomb-Scargle graph in Figure 5 was created to check if there is any periodicity of the variations from the predicted transit midpoints. The graph is unlikely to show visible results with fewer than 50 data points, unless there was a very strong signal. The graph demonstrates a visualization of the temporally unevenly sampled data. It represents an estimate of the Fourier power at a given epoch value, which aids in the determining of periodicity in the data which would be impossible to discern with the naked eye. Ideally, in the event of another body existing within the Qatar-1b system, the Lomb-Scargle periodogram would be expected to display a singular clear spike, indicating that there is a clear period in the data, supporting periodicity and suggesting the existence of another body in the system. However, the periodogram in Figure 6 does not suggest that another body exists in the Qatar-1b system. This is due to the expression of many uneven spikes in the periodogram, which indicate a lack of periodicity (VanderPlas 2018).

5. Conclusion

This study contributes observations and reductions of observations of the planet Qatar-1b using small telescopes in the MicroObservatory network to help maintain the ephemeris and check for other planets in the system. Analysis of the O-C values shows that the period does not show evidence of periodicity or a slope in the O-C results, so our data support the current ephemeris (Collins *et al.* 2017b). From this analysis of TTVs in Qatar-1b, evidence of more planets in the system was not found. This lack of significant TTVs is consistent with the findings presented in Collins *et al.* (2017b).

6. Acknowledgements

This research has made use of the astropy.io.fits PYTHON module.

Data from the Harvard-Smithsonian Institute for Astrophysics MicroObservatory telescope network was incorporated. Special thanks to Frank Sienkiewicz for making the data available.

This publication makes use of the EXOTIC data reduction package from Exoplanet Watch, a citizen science project managed by NASA's Jet Propulsion Laboratory on behalf of NASA's Universe of Learning. This work is supported by NASA under award number NNX16AC65A to the Space Telescope Science Institute.

Additionally, this research used the imaging software AstroImageJ. We would like to formally thank the creators of AstroImageJ along with the NASA Exoplanet Watch team and the American Association of Variable Star Observers for making this research possible. We would also like to thank Henry Heiberger, Harry Heiberger, Quennie Nguyen, Katie Kolodner, Damian Musk, and David Crair for contributing transit data to our research.

We would like to thank Kalée Tock, Ryan Caputo, Quinn Perian, Elliott Chalcraft, and Peyton Robertson for hosting the Exoplanet Research Workshop, which greatly assisted us in the research process. We would especially like to thank Kalée Tock, Martin Fowler, and Michael Fitzgerald for reviewing this paper and guiding the writing process.

References

Alsubai, K. A., *et al.* 2011, *Mon. Not. Roy. Astron. Soc.*, **417**, 709.

Collins, K. A., Kielkopf, J. F., and Stassun, K. G. 2017a, *Astron. J.*, **153**, 78 (DOI:10.3847/1538-3881/153/2/78).

Collins, K. A., Kielkopf, J. F., Stassun, K. G., and Hessman, F. V. 2017b, *Astron. J.*, **153**, 77 (DOI:10.3847/1538-3881/153/2/77).

Cortés-Zuleta, P., Rojo, P., Wang, S., Hinse, T. C., Hoyer, S., Sanhueza, B., Correa-Amaro, P., and Albornoz, J. 2020, *Astron. Astrophys.*, **636A**, 98 (DOI:10.1051/0004-6361/201936279).

Deeg, H. J., and Alonso, R. 2018, in *Handbook of Exoplanets*, Springer International Publishing AG, Berlin, 633.

Kane, S. R., Mahadevan, S., von Braun, K., Laughlin, G., and Ciardi, D. R. 2009, *Publ. Astron. Soc. Pacific*, **121**, 1386.

Sadler, P. M., *et al.* 2001, *J. Sci. Education Technol.*, **10**, 39 (DOI:10.1023/A:1016668526933).

VanderPlas, J. T. 2018, *Astrophys. J., Suppl. Ser.*, **236**, 16 (DOI:10.3847/1538-4365/aab766).

Zellem, R. T., *et al.* 2020, *Publ. Astron. Soc. Pacific*, **132**, 054401.

Distance Determination of RR Lyrae Stars AE Leo, AT Vir, and HY Com

Cody Soper
Christopher Tenenbaum
Adam Lounsbery
Jarred Rheiner
David Klassen (ORCID 0000-0001-6142-1982)
Department of Physics and Astronomy, Rowan University, Glassboro, NJ; soperc46@students.rowan.edu

Received June 21, 2021; revised April 11, 2022; accepted April 19, 2022

Abstract We present the results of our observations and analyses of three RR Lyrae variable stars: AT Vir, HY Com, and AE Leo, in order to test period-luminosity relationships derived from stellar models. We have measured the periods of these stars to be 0.52359, 0.44898, and 0.63021 days, respectively, closely matching previous work. Period-Luminosity-Metallicity (PLM) relationships were used to calculate new distance values which averaged 1331 ± 41 pc, 957 ± 49 pc, and 2480 ± 76 pc for AT Vir, HY Com, and AE Leo, respectively. These measurements are compared with Gaia distances calculated from EDR3 parallax angles. Our results appear to generally support the PLM relationship with distance differences less than 2σ.

1. Introduction

RR Lyrae stars are low–mass, horizontal branch, pulsating variable stars with periods of less than a day. Longmore *et al.* (1986) observed that there exist period-luminosity (PL) relationships that can allow us to measure the distance to globular clusters where these stars are known to exist. However, a relation was only found in the K band. Later, work by Catelan *et al.* (2004) established theoretical relations for the absolute magnitudes in I, J, H, K, and V, and later Cáceres and Catelan (2008) established further theoretical relations in i' and z. Confirmation of these relations can help in the general overall understanding of RR Lyrae stars.

In our study, observations of known RR Lyrae stars AT Vir, HY Com, and AE Leo are made in B, V , i', and z filters over several periods. From here we use the established period-luminosity relations and metallicities of our stars found in the literature to calculate their distances. Our goal is to compare these results to Gaia parallax distance measurements and test the P-L relations.

2. Observations and methods

Our three observed stars, AT Vir, HY Com, and AE Leo, were chosen from a list of RR Lyrae variable stars whose distance has been measured by Gaia and was provided by the Our Solar Siblings project team (OSS) (Fitzgerald *et al.* 2018). Through the OSS, we received access to Las Cumbres Observatories' (LCO) (Brown *et al.* 2013) international system of 0.4-meter robotic telescopes. With these telescopes, Images of our stars were collected in B, V , i', and z filters.

As these stars are short period variables, and we want to collect images robotically over time, we first collected test images for each of them with estimated exposure times and then used the aperture tool in AstroImageJ (Collins *et al.* 2017) to ensure counts would be within an acceptable range (source−sky of 10–500 thousand counts) that would neither saturate the frame nor be so faint as to have low signal-to-noise. These final exposure times used for our observations are presented in Table 1.

Table 1. Filters and exposure times used.

Filter	*λ (Å)*	*Δλ (Å)*	*Exposure Time (s)* *AT Vir*	*HY Com*	*AE Leo*
B	4361	890	30	20	36
V	5448	840	30	20	36
i'	7540	1290	30	20	36
z	8700	1040	90	45	60

Once viable exposure times were found, we scheduled 84 observations in B, V , i', and z filters for each of our three stars, with images requested every 3 hours. As these stars all should have periods of less than a day, this cadence should ensure good coverage for several periods Of these 84 scheduled observations, 66 were successful; some were lost due to weather or scheduling clashes with other programs. The collected images were then processed through the OSS Pipeline (Fitzgerald 2018), which reduces cosmic rays, standardizes file names, and performs six different photometric measurements on all stars in the frame. For our purposes, we were able to obtain reliable results using the Source Extractor (SExtractor) photometry method (Bertin and Arnouts 1996) and therefore this was the only method of the six that we used. The SExtractor method is an automated process that makes a catalog of all of the stars in a given image after analyzing the image by estimating the background, thresholding, deblending, filtering, photometry on each source, and finally separating stars/galaxies.

The resulting photometry files were processed using the Astrosource package (Fitzgerald *et al.* 2021) to calculate phased light curves as well as average magnitudes, amplitudes, and periods for our observed stars. Calibration of our comparison stars were done by crossmatching to the APASS catalog (Henden *et al.* 2016) for B and V filters, and Skymapper DR1.1 (Wolf *et al.* 2018) for i' and z filters. The package does this by means of the Phase Dispersion Minimization (PDM) method (Stellingwerf 1978), which uses a least–squares fitting technique that seeks to minimize the dispersion of the data from our images at constant phase, and String Length (SL) method (Lafler and Kinman 1965), which is another least–squares approach that uses trial periods to calculate the best fit for the period. Other needed information, such as interstellar reddening and metallicity, were found in the literature and used in tandem with our results from Astrosource to calculate the distance to our stars.

Metallicity, reported as [Fe/H], was converted to logZ for use in the period-luminosity relation. The metallicity of our stars was found using the VizieR catalog (Ochsenbein *et al.* 2000) for links to primary sources and tabulations of those results. The conversions were done using the equations presented by Catelan *et al.* (2004) and are reprinted here in Equations 1 and 2. They note that $f_\alpha = 10^{[\alpha/\mathrm{Fe}]}$, a scaling factor to account for enhancement of α-elements (Salaris *et al.* 1993); it is assumed that $[\alpha/\mathrm{Fe}] \approx 0.3$.

$$[\mathrm{M/H}] = [\mathrm{Fe/H}] + \log(0.638\, f_\alpha + 0.362) \tag{1}$$

$$\log Z = [\mathrm{M/H}] - 1.765 \tag{2}$$

The value from Equation 2 is then used in the PLM relations for the V , i', and z bands in Equations 3, 4, and 5 below. These equations were first theorized for V by Catelan *et al.* (2004), and then later for i' and z by Cáceres and Catelan (2008).

$$M_V = 2.288 + 0.882 \log Z + 0.108 (\log Z)^2 \tag{3}$$

$$M_i = 0.908 - 1.035 \log P + 0.220 \log Z \tag{4}$$

$$M_z = 0.839 - 1.295 \log P + 0.211 \log Z \tag{5}$$

When calculating the distance of our star, we also had to take into consideration the extinction factor due to interstellar dust for each star. Reddening values, E(B−V), found in the NASA/IPAC Infrared Science Archive (Desai *et al.* 2018) were originally calculated for our stars by Schlafly and Finkbeiner (2011). These were then be used to calculate the extinction, A, for each of our filters based on Cardelli *et al.* (1989) as shown in Equations 6, 7, and 8 below.

$$A_V = E[B-V] \times R \times 1 \tag{6}$$

$$A_i = E[B-V] \times R \times 0.68319 \tag{7}$$

$$A_z = E[B-V] \times R \times 0.49264 \tag{8}$$

where R = 3.1 is a standard value for the galaxy and A_V, A_i, and A_z are the extinction corrections for the V, i', and z bands, respectively. The values of M and A for each of our filters can then finally be used with the average apparent magnitude, m, of our star calculated by Astrosource to obtain the distance of our star in parsecs, D, using:

$$D = 10^{(m-M-A+5)/5} \tag{9}$$

The distance calculated can then be compared to the distance measured by Gaia as reported in Gaia EDR3 (Gaia Collab. *et al.* 2021). Table 2 shows these Gaia distances and other general information discussed above for our selected stars.

3. Results

We present the results of our work in the tables and figures below. Table 2 gives basic information on each star found in the literature. Tables 3–8 and Figures 1–6 are the various results for each star in turn: AT Vir, HY Com, and AE Leo. We include: the plot for period likelihood (Figures 1, 3, 5), the phased light curves using the period with highest likelihood in each filter (Figures 2, 4, 6), the periods and "middle magnitudes" in each filter (Tables 3, 5, 7), and the calculated extinction, measured apparent magnitude, calculated absolute magnitude, and calculated distance in each filter (Tables 4, 6, 8).

Given that the period likelihood for each star is equivalent within uncertainty for all filters and across both methods, the period likelihood plot will only be presented for the i' filter using the PDM method for each of our stars as representative of our results and to save space. The center of the first peak is chosen as the most likely period.

Similarly, phased light curves for each of our stars will only be presented using the most likely period from the PDM method, as they are equivalent within uncertainty to curves produced by the SL method.

Note that "middle magnitude" is calculated as the average of the brightest and dimmest magnitude in the calibrated series and is not a mathematical mean over the entire set of measurements. Since we cannot be sure we have adequately sampled the possible brightness values, a standard mean could suffer from bias. By taking the middle value we avoid that.

The uncertainty errors on the light curves are due to the photometry process itself. They are strongly influenced by signal-to-noise (S/N) based on integration time, number of comparison field stars in the image, and potential drops in S/N due to variation in sky conditions with a fixed integration time across the observing period. As the observing requests for each of the three stars were done independently, sky conditions for any run of images can vary between them significantly.

Table 2. General information and Gaia distances.

Star	*Type*	*R.A. (deg.)*	*Dec (deg.).*	*[Fe/H]*	*E(B−V)*	*ϖ (mas)*
AT Vir	RRab	193.7936	−05.45923	−1.87 ± 0.10	0.0314 ± 0.0012	0.7579 ± 0.0401
HY Com	RRc	98.73142	−45.30863	−1.75 ± 0.02	0.0237 ± 0.0004	0.9616 ± 0.0189
AE Leo	RRab/bl	171.55094	17.6609	−1.71 ± 0.11	0.0200 ± 0.0009	0.3706 ± 0.0188

Note: Metallicities for AT Vir and HY Com are from Crestani et al. *(2021), and AE Leo is from Layden (1994). Error for AT Vir was set to a standard value by the authors due to an insufficient number of measurements to calculate it. Gaia parallax angles from EDR3 (Gaia Collaboration* et al. *2021) reported at VizieR.*

Table 3. Calculated period, middle magnitude, and amplitude of AT Vir.

	Period Calculations			
Filter	*PDM*	*SL*	*Middle Magnitude*	*Amplitude*
B	0.5065 ± 0.0069	0.5254 ± 0.009	11.471 ± 0.071	1.673
V	0.5254 ± 0.0058	0.5254 ± 0.0069	11.266 ± 0.106	1.322
i'	0.5263 ± 0.0115	0.5254 ± 0.0083	11.227 ± 0.019	1.209
z	0.5276 ± 0.0079	0.5268 ± 0.0115	11.040 ± 0.034	0.803

Table 4. Calculated distance of AT Vir.

Filter	*Extinction*	*m*	*M*	*Distance (pc)*
V	0.097	11.266	0.741	1339 ± 110
i'	0.067	11.227	0.638	1390 ± 51
z	0.048	11.04	0.665	1265 ± 49
Average				1331 ± 41

Table 5. Calculated period, middle magnitude, and amplitude of HY Com.

	Period Calculations			
Filter	*PDM*	*SL*	*Middle Magnitude*	*Amplitude*
B	0.4491 ± 0.0044	0.4485 ± 0.005	10.846 ± 0.038	0.702
V	0.4492 ± 0.0039	0.4492 ± 0.0049	10.550 ± 0.032	0.474
i'	0.4491 ± 0.0048	0.4485 ± 0.005	10.395 ± 0.015	0.330
z	0.4491 ± 0.0042	0.4491 ± 0.005	10.215 ± 0.070	0.319

Table 6. Calculated distance of HY Com.

Filter	*Extinction*	*m*	*M*	*Distance (pc)*
V	0.073	10.55	0.616	965 ± 39
i'	0.05	10.365	0.477	971 ± 90
z	0.036	10.215	0.492	935 ± 49
Average				957 ± 49

Table 7. Calculated period, middle magnitude, and amplitude of AE Leo.

	Period Calculations			
Filter	*PDM*	*SL*	*Middle Magnitude*	*Amplitude*
B	0.6295 ± 0.022	0.6261 ± 0.0225	12.920 ± 0.034	1.391
V	0.6327 ± 0.0188	0.6282 ± 0.0198	12.498 ± 0.025	1.235
i'	0.6295 ± 0.0214	0.6366 ± 0.0221	12.719 ± 0.030	0.674
z	0.6295 ± 0.0256	0.6295 ± 0.0256	12.166 ± 0.088	0.626

Table 8. Calculated distance of AE Leo.

FilterExtinction		m	M	Distance (pc)
V	0.062	12.5	0.56	2372 ± 107
i'	0.042	12.93	0.4	2856 ± 131
z	0.031	12.17	0.41	2213 ± 76
Average				2480 ± 76

The near-infrared z-band will be the most susceptible to these sorts of variations, being near a water vapor band, which accounts for that filter generally having larger error bars.

In Table 9 we present a summary of our average distances for each star computed from a straight arithmetic mean of the per-filter results. Gaia distances computed from parallaxes, a difference, and relative difference are also presented. The relative difference is the ratio of the absolute difference to the uncertainty in our average value and represents a goodness-of-match and overall are less than 2 in the worst cases. Our comparisons are done to a simple ϖ distance calculation as well as to the distance results from a more comprehensive study by Bailer-Jones *et al.* (2021) that includes direction-dependent priors and various color-magnitude corrections. Our results are, on average, better fits to these.

4. Discussion

Overall the errors in our period calculations are less than 2%—calculated by taking the full-width-at-halfmax of the first peak in the graphs in Figures 1, 3, and 5—and therefore only affects ıble 10 below presents a comparison of our calculated periods to those calculated in other studies. We found that the period we calculated is equivalent within our uncertainties. Note that the error on the literature average is a simple standard deviation of the values found and makes no attempt to weight them based on their reported uncertainties.

Table 9. Distance comparisons—differences and relative differences.

	AT Vir	*HY Com*	*AE Leo*
This study	1331 ± 41	957 ± 49	2480 ± 76
Gaia (1 / [omega])	1319 ± 70	1040 ± 20	2698 ± 137
Δr	12	83	218
Δr / max(σ)	0.2	1.7	1.6
Gaia (bj)	1251 ± 66	1012 ± 17	2516 ± 115
Δr	80	55	36
Δr / max(σ)	1.2	1.1	0.3

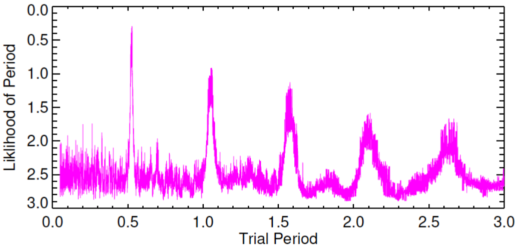

Figure 1. Period likelihood of AT Vir.

Table 10. Period comparisons.

	AT Vir	*HY Com*	*AE Leo*
This Work	0.52359 ± 0.00854	0.44898 ± 0.00472	0.63021 ± 0.02218
Kafka 2021 (AAVSO)	0.52577	0.44859	0.62667
Samus *et al.* 2017 (GCVS)	0.52579	—	0.62672
Alfonso-Garzón *et al.* (2012)	0.52578	—	—
Kovács (2005)	0.52578	—	—
Kunder *et al.* (2010)	0.52979	—	—
Bramich *et al.* (2014)	—	—	0.62672
Percy and Tan (2013)	—	0.449	—
Wils (2008)	—	0.44862	—
Literature Average	0.52658 ± 0.0018	0.44874 ± 0.0002	0.62671 ± 0.0001
ΔP	0.00299	0.00024	0.0035
ΔP / σ	0.4	0.05	0.2

Note: For relative differences, σ used is from this work.

Interstellar reddening and extinction values found in the literature had as much as a 5% error, and thus accounted for an error in our distance calculation of approximately 0.2%. Because of how small this uncertainty is compared to those of the apparent and absolute magnitude, we conclude that reddening most likely did not play a large a role in the final uncertainty of our distance measurement. The larger concern with the reddening used is how appropriate the particular values we had found are for our study. We see in other similar studies that the value found in literature for reddening for other RR Lyrae stars has proved to be a very important issue as it is not well known (Uzpen and Slater 2020).

Another error that is cause for high uncertainty is that of the average magnitude from our light curves. In our study we found the error in the measurement for the middle magnitude to be as great as 1%, which in return is cause for as great as 5% uncertainty in the final distance. To limit this error, time was spent to obtain exposure times that would produce observations that did not collect too little or too much light from our source; we still found that some of our images were too dim and therefore unable to be used. To limit the error in the apparent magnitude of our star within our light curve, we chose to have astrosource only use 90% of our images when calculating our period and producing our light curves. Although discarding 10% of our images proved to produce viable results for HY Com and AT Vir, we found that for AE Leo, some of our images not only came back too dim, but also some had too few comparison stars, and therefore we discarded 20% of the returned images so we could produce better light curves and mitigate the error in the measured apparent magnitude. Because of this, we can see in our light curves, as shown in Figures 2, 4, and 6, that the curve is not filled out completely; this is especially the case with AT Vir and AE Leo, our RRab type stars, where there is little information on our light curves during the sharp increase in magnitude.

Being that the observations of our star were only carried out throughout the duration of approximately 20 days, it is reasonable to assume that if more images were collected over

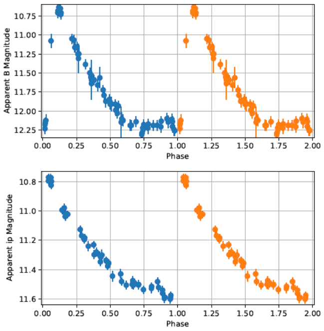

Figure 2. Phased light curves of AT Vir in B, V , i', and z filters respectively from left to right, top to bottom. A sharp peak can be seen for each curve, which is a quality known to be seen in RRab type stars.

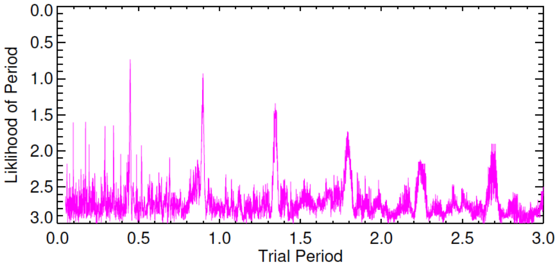

Figure 3. Period likelihood of HY Com.

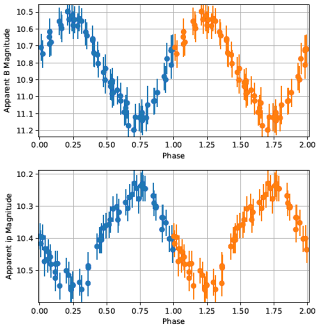

Figure 4. Phased light curves of HY Com in B, V , i', and z filters respectively from left to right, top to bottom. A more sinusoidal curve can be seen for this RRc type star.

a larger period of time, errors in apparent magnitude and period of our star would be reduced. This would allow a light curve of greater quality to be produced as more images can be taken during the sharp increase in magnitude portion of the phase of RRab type stars. Because of this loss, the apparent magnitude used in our study is the average between the minimum and maximum magnitude in effort to mitigate our uncertainty—taking the average of the entire light curve would be biased due to missing information.

It is worth noting that the overall errors for AT Vir and HY Com are comparable between our study, the simple ϖ method, and the Bailer-Jones *et al.* (2021) method. Similarly, all methods have the highest errors for AE Leo; this makes sense as it is the farthest, and dimmest, of the three stars and it exhibits the Blazhko effect (Szabó 2014) that causes the amplitude of the variability to vary. In our work we have assumed this will not affect the overall calculation of the middle-magnitude "average", but it does add more noise.

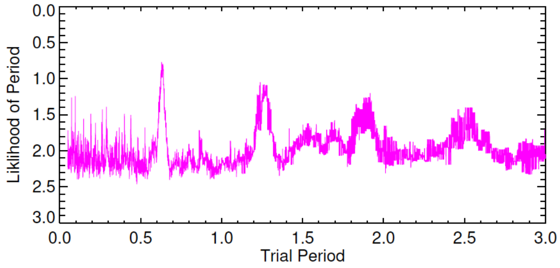

Figure 5. Period likelihood of AE Leo.

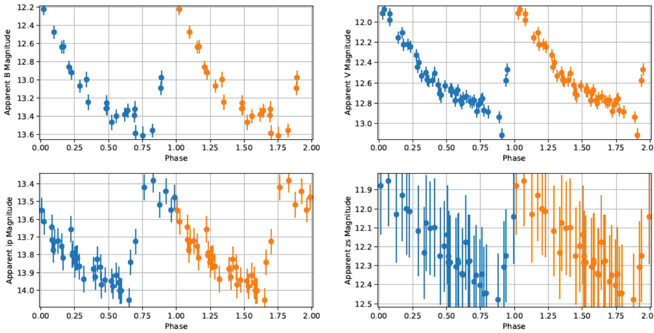

Figure 6. Phased light curves of AE Leo in B, V , i', and z filters respectively from left to right, top to bottom. Notice the light curve for this RRab type star is not as tight as that of AT Vir due to the Blazhko effect (Szabó, 2014; Layden, 1997). In this study the Blazhko effect can be ignored as only the amplitude changes while the middle magnitude is relatively constant.

5. Conclusion

Our work has determined the periods of AT Vir, HY Com, and AE Leo to be 0.524 ± 0.008, 0.449 ± 0.005, and 0.630 ± 0.022 day, respectively. Distances using PLM relationships (Catelan *et al.* 2004; Cáceres and Catelan 2008) yielded average distances to our stars of 1331 ± 41, 957 ± 49, and 2480 ± 76 pc, respectively. These distance calculations are equivalent, within 1.2σ, to the Gaia calculated distances of Bailer-Jones *et al.* (2021). In general this appears to support the PLM relationship method.

6. Acknowledgements

This work has made use of data from the AAVSO Photometric All Sky Survey (APASS; Henden *et al.* 2016).

This work has made use of data from the European Space Agency (ESA) mission Gaia (https://www.cosmos.esa.int/gaia), processed by the Gaia Data Processing and Analysis Consortium (DPAC, https://www.cosmos.esa.int/web/gaia/dpac/consortium). Funding for the DPAC has been provided by national institutions, in particular the institutions participating in the Gaia Multilateral Agreement.

This research has made use of the SIMBAD database, VizieR catalogue, and "Aladin sky atlas" developed and operated at CDS, Strasbourg, France.

We acknowledge with thanks the variable star observations from the AAVSO International Database contributed by observers worldwide and used in this research.

This research has made use of the NASA/IPAC Infrared Science Archive, which is funded by the National Aeronautics and Space Administration and operated by the California Institute of Technology.

We also give a special thanks to Las Cumbres Observatory global telescope network and especially the support of Michael Fitzgerald and the entire Our Solar Siblings staff without whom none of this would have been possible

References

Alfonso-Garzón, J., Domingo, A., Mas-Hesse, J. M., and Giménez, A. 2012, *Astron. Astrophys.*, **548**, A79.

Bailer-Jones, C. A. L., Rybizki, J., Fouesneau, M., Demleitner, M., and Andrae, R. 2021, *Astron. J.*, **161**, 147.

Bertin, E., and Arnouts, S. 1996, *Astron. Astrophys., Suppl. Ser.*, **117**, 393.

Bramich, D. M., Alsubai, K. A., Arellano Ferro, A., Parley, N. R., Collier Cameron, A., Horne, K., and West, R. G. 2014, *Inf. Bull. Var. Stars*, No. 6106, 1.

Brown, T. M., *et al.* 2013, *Publ. Astron. Soc. Pacific*, **125**, 1031.

Cáceres, C., and Catelan, M. 2008, *Astrophys. J., Suppl. Ser.*, **179**, 242.

Cardelli, J. A., Clayton, G. C., and Mathis, J. S. 1989, *Astrophys. J.*, **345**, 245.

Catelan, M., Pritzl, B. J., and Smith, H. A. 2004, *Astrophys. J., Suppl. Ser.*, **154**, 633.

Collins, K. A., Kielkopf, J. F., Stassun, K. G., and Hessman, F. V. 2017, *Astron. J.*, **153**, 77.

Crestani, J., *et al.* 2021, *Astrophys. J.*, **914**, 10.

Desai, V., Rebull, L. M., and IRSA Team. 2018, in *American Astronomical Society Meeting Abstracts*, No. 232, 214.01.

Fitzgerald, M. T. 2018, *Robotic Telesc. Student Res. Education Proc.*, **1**, 347.

Fitzgerald, M. T., Gomez, E., Salimpour, S., Singleton, J., and Wibowo, R. W. 2021, *J. Open Source Software*, **6**, 2641.

Fitzgerald, M. T., McKinnon, D. H., Danaia, L., Cutts, R., Salimpour, S., and Sacchi, M. 2018, *Robotic Telesc. Student Res. Education Proc.*, **1**, 221.

Gaia Collaboration, *et al.* 2021, *Astron. Astrophys.*, **649A**, 1.

Henden, A. A., Templeton, M., Terrell, D., Smith, T. C., Levine, S., and Welch, D. 2016, AAVSO Photometric All Sky Survey (APASS) DR9 (Henden+, 2016). VizieR Online Data Catalog, II/336.

Kafka, S. 2021, Observations from the AAVSO International Database (https://www.aavso.org).

Kovács, G. 2005, *Astron. Astrophys.*, **438**, 227.

Kunder, A., Chaboyer, B., and Layden, A. 2010, *Astron. J.*, **139**, 415.

Lafler, J., and Kinman, T. D. 1965, *Astrophys. J., Suppl. Ser.*, **11**, 216.

Layden, A. C. 1994, *Astron. J.*, **108**, 1016.

Layden, A. C. 1997, *Publ. Astron. Soc. Pacific*, **109**, 524.

Longmore, A. J., Fernley, J. A., and Jameson, R. F. 1986, *Mon. Not. Roy. Astron. Soc.*, **220**, 279.

Ochsenbein, F., Bauer, P., and Marcout, J. 2000, *Astron. Astrophys., Suppl. Ser.*, **143**, 23.

Percy, J. R., and Tan, P. J. 2013, *J. Amer. Assoc. Var. Star Obs.*, **41**, 75.

Salaris, M., Chieffi, A., and Straniero, O. 1993, *Astrophys. J.*, **414**, 580.

Samus, N. N., Kazarovets, E. V., Durlevich, O. V., Kireeva, N. N., and Pastukhova, E. N. 2017, *Astron. Rep.*, **61**, 80, *General Catalogue of Variable Stars: Version GCVS 5.1* (http://www.sai.msu.su/gcvs/gcvs/index.htm).

Schlafly, E. F., and Finkbeiner, D. P. 2011, *Astrophys. J.*, **737**, 103.

Stellingwerf, R. F. 1978, *Astrophys. J.*, **224**, 953.

Szabó, R. 2014, in *Precision Asteroseismology*, eds. J. A. Guzik, W. J. Chaplin, G. Handler, A. Pigulski, IAU Symp. 301, 241.

Uzpen, B., and Slater, T. F. 2020, *Astron. Theory Obs. Methods*, **1**, 54.

Wils, P. 2008, *Perem. Zvezdy*, **28**, 1.

Wolf, C., *et al.* 2018, *Publ. Astron. Soc. Australia*, **35**, e010.

Updates to Pulsator Periods in NGC 3201

Avni Bansal
Paul Hamrick
Kalée Tock
Stanford Online High School, 415 Broadway Academy Hall, Floor 2, 8853, Redwood City, CA 94063; avnibansal2004@gmail.com; paulahamrick@gmail.com; kaleeg@stanford.edu

Received July 1, 2021; revised February 9, March 7, 2022; accepted March 7, 2022

Abstract The periods for RR Lyrae variables in NGC 3201 were calculated using the "string length method" in order to update or verify their periods. We confirm the published periods for 54 RR Lyraes in the cluster and offer eight period updates. We also identify the possibility that there is a non-linear CCD brightness response across different telescope cameras of the same specifications, which can result in pseudo-pulsations when multiple telescopes are used to image the cluster. Finally, we observe that in cases where two stars are very close together, source extractor photometry often only discerns one of the stars. Although point spread function photometry is more likely to discern both, it introduces challenges in identifying which star is which. The use of both photometric algorithms in tandem can help to untangle ambiguities.

1. Introduction

1.1. Pulsators

Pulsators are stars that periodically expand and contract in the process of maintaining hydrostatic equilibrium. Two classes of variables, RR Lyraes, and Cepheids, are used as standard candles for measuring large distances because their pulsation period and luminosity are related (Dall'Ora *et al.* 2006). For Cepheids, the period-luminosity relationship is pronounced and occurs across multiple wavelengths. For RR Lyraes, the period-luminosity relationship is more subtle and metallicity-dependent and occurs primarily at infrared wavelengths (Lee 1992). With those caveats, once the period of such a variable is known, its luminosity is also known. The luminosity can be compared to the apparent brightness to determine the pulsator's distance.

In addition to improving distance measurements, accurate pulsator period measurements improve theoretical period-metallicity relationships in globular clusters. This is especially relevant to RR Lyrae stars as discussed above. Because period-luminosity-metallicity relationships are so important, we sought to independently calculate the periods of previously identified RR Lyrae stars in the globular cluster NGC 3201. The objective was to verify or update older period measurements.

1.2. Previous observations of NGC 3201

Periods for pulsators in NGC 3201 were first calculated in 1941 (Wright 1941). At that time, the cluster had 86 known pulsators. In that study, NGC 3201 was imaged using astronomical plates at the Boyden Station of Harvard Observatory near Arequipa, Peru. The periods were calculated manually from the plate data. The study succeeded in finding periods for all but 18 of the variables identified. These variables were either too close to other stars or had pulsation amplitudes too small to detect.

Since 1941, the search for new variables has continued in tandem with efforts to calculate ever more accurate periods for them. Initially, all analyses of NGC 3201 were photographic investigations. Photoelectric photometry such as the investigation of 47 Tuc conducted at Siding Spring Observatory by Menzies (1973) became more common in the latter part of the century. A photoelectric photometer measures the brightness of a star based on the current produced when light falls onto a light-sensitive cathode. Every time a photon hits the cathode, an electric pulse is generated. The number of these signals per second indicates the star's brightness, and using the frequency of pulses to measure brightness is known as pulse-counting photometry. Photographic data must undergo significant processing for brightnesses to be determined, while photoelectric photometry directly measures variations in brightness, so photoelectric methods soon replaced photographic methods as the standard measurement technique. For NGC 3201, the upgrade from photographic methods to photoelectric methods led to the discovery of nine new variables (Lee 1992).

As CCDs became more common, more discoveries were made about the stars of NGC 3201. Piersimoni *et al.* developed a model for the differential reddening of NGC 3201 in 2002 (Piersimoni *et al.* 2002), which was refined by Kravtsov *et al.* in 2009 (Kravtsov *et al.* 2009). CCDs led to the discovery of the first SX Phoenicis variables in NGC 3201, which are both dimmer and have lower amplitude pulsations than RR Lyrae stars (Mazur *et al.* 2003). Furthermore, some of the variables identified in the pre-CCD era were shown to be non-variable through CCD studies.

Layden and Sarjedini (2003) conducted the most comprehensive search for RR Lyraes in NGC 3201 to date. They searched for pulsators in their time-series BVI photometry data using three independent methods: the string length method, Lomb-Scargle, and their own template-finding method. The latter method entailed studying older light curves to make templates with the characteristic shapes of RR Lyraes and then fitting observed data points to these templates.

The periods of the 160 currently-known variables in NGC 3201 are listed in the Clement catalog (Clement *et al.* 2001). Using the catalog's naming convention, the periods for stars V1 to V100 mostly come from Layden and Sarajedini (2003). They found reliable periods for most variables, with a few exceptions. V6, V12, V19, V20, V27-V30, V36, and V45 either had uncertain phases, uncertain periods, or had too few or no data points at their minimum or maximum brightness. In addition, V8, V10, V37, V38, V51, and V76 were suspected of having the Blazhko effect. The Blazhko effect refers to periodic variations in the amplitude and phase of pulsation observed in RR Lyraes. The cause of the Blazhko effect is unclear, although several theories have been proposed (Smolec and Moskalik 2012).

A later study in 2014 (Arellano Ferro *et al.* 2014) used independently collected data as well as Layden and Sarajedini data to confirm the periods of V8, V12, V28, V36-V38, V45, and V76. They also confirmed that V28 was a Blazkho, and identified V18, V25, V50, and V73 as Blazkhos as well. V101–V143 are either SX Phoenicis (SXP), Beta-Lyrae type Eclipsing binaries (EB), or Algol type Eclipsing binaries (EA). It is currently uncertain whether V144–V160 are variables, and if so, what their classification is.

Since NGC 3201 is known to have some stars that exhibit the Blazhko effect, studying the periods of the stars over time can help to refine models of Blazhko period and amplitude changes over time. Furthermore, frequent recalculation of the period makes possible the identification of new Blazkhos. This is one of the reasons we have chosen to recalculate the periods of variables in NGC 3201. In addition, this study can improve the certainty in periods of variables whose periods we confirm.

1.3. Period-finding algorithm

This study uses a string-length method (Dworetsky 1983) algorithm that has been implemented by the authors. The period-finding method used here is an example of methods collectively known as Phase Dispersion Minimization (PDM), which reduces the range of values at a given phase of the light curve by minimizing a “cost function” of their scatter. VanderPlas (2018) gives a summary of several other commonly-used algorithms for characterizing periodicity in unevenly-sampled time-series data, including Fourier methods, phase-folding, least-squares, and Bayesian approaches. However, any of these would necessitate feeding the time-series data into an existing “black-box” Python module. Also, the most commonly used of these methods, Lomb-Scargle, is optimized for sinusoidal data sets, and RR Lyrae pulsations are not sinusoidal in shape (VanderPlas 2018). Because PDM is conceptually straightforward enough to code ourselves from scratch, because it is well-suited to periodic data of any type, and because using it did not necessitate purchasing auxiliary software, it was chosen for this project. Details of our implementation are discussed further in section 2.5.

2. Procedure

2.1. Target selection

The globular cluster NGC 3201 was selected for three reasons. Firstly, it has several RR Lyraes with known periods, so we were able to compare our period estimates with previous ones. Secondly, NGC 3201 was visible while images for this study were being collected (February and March 2021). Lastly, a majority of its RR Lyrae stars have an apparent magnitude lower than magnitude 17, so the 0.4-m telescopes of the Las Cumbres Observatory were able to image them clearly.

2.2. Instruments used

The instruments used were the Las Cumbres Observatory (LCO) telescopes in Cerro Tololo, Chile, in Siding Spring, Australia, in Sutherland, South Africa, and in Fort Davis, Texas (Brown *et al.* 2013). Each telescope has identical specifications, being 0.4 meter in aperture with a Meade 16-inch (40-cm) tube and three-element optics, mounted in LCO equatorial C-ring mounting. The optics are a primary, secondary, and Corrector plate (Meade) with an LCO focus mechanism driving corrector plate/secondary. The instruments on the telescopes also have identical specifications. The cameras are SBIG STL6303, which have a 19.5' × 29.5' field of view and a pixel scale of 0.591. The images were taken with two of the eight filters provided by the Las Cumbres Observatory: Bessel-V and SDSS-ip, where SDSS stands for Sloan Digital Sky Survey (SDSS; Blanton *et al.* 2017). The Bessel V images were taken with an exposure time of 240 seconds and the SDSS-ip images were taken with an exposure time of 150 seconds. Images were taken through both filters at each epoch.

2.3. Image reduction

First, NGC 3201 was imaged in the V and ip filters. Images were taken with a cadence of approximately 3 hours between February 19 and February 27, 2021, and March 16 and March 23, 2021. Each image was plate solved and calibrated by LCO’s BANZAI pipeline. BANZAI calibration involves subtraction of a master dark multiplied by the corresponding image exposure time and then divided by a master flat. The full calibration procedure is described in McCully *et al.* (2018). Following this, the images were fed to the Our Solar Siblings (OSS) pipeline, which transformed their original Julian Date timestamps to Barycentric Julian dates, computed from the latitude, longitude, elevation of the corresponding LCO telescope, along with the R.A. and Dec. of the target. The OSS pipeline performed six different photometric extraction algorithms on the images (Fitzgerald 2018). Of these six, the Point Spread eXtractor (psx) and Source Extractor (sex) photometries were used (Bertin and Arnouts 1996). Psx was used because it is a point spread function fitting photometry (Hamrick *et al.* 2021). Point spread function fitting photometry can be effective at pinpointing the magnitudes of stars in crowded fields such as that of NGC 3201 (Heasley 1999). Sex photometry was used because using two different photometric algorithms lowers the likelihood of being misled by blended pairs.

2.4. Reference star selection

After photometric reduction, reference stars were chosen. Initially, a list of reference stars was generated using the autocal function, which is part of the astrosource python module (Fitzgerald *et al.* 2021). One reference among those identified by the software was selected, and all the known pulsators in NGC 3201 were then calibrated against it. However, when we calculated periods using stars that were calibrated in this way, we found that a large fraction of periods were close to one day or half a day. This was puzzling for two reasons. Firstly, older period estimates for the RR Lyraes in NGC 3201 range from 0.1 to 0.6 day instead of being concentrated around half a day or a day. Secondly, it is highly unlikely that most of the RR Lyraes in NGC 3201 have periods of such similar fractions of a day.

The similarity of the periods suggested the following hypothesis: the periodicity may be an aliasing effect, arising as an artifact of which Las Cumbres Observatory telescope is being used at different times during the night. For example, if the target is the highest for the telescope in Tenerife around 9 P.M. UTC but highest for Texas around 6 A.M. UTC, then most of the early evening observations will be taken in Tenerife while most of the late evening–early morning (UTC) observations will be taken in Texas.

Although the reference star we had used to calibrate magnitudes is meant to control for different imaging circumstances, if the reference is much brighter or dimmer than the target, then non-linearity in the camera's response to photons might come into play. Specifically, consider the example where the reference star is much brighter than the target, and the Tenerife camera responds to that difference in a slightly different way than the Texas camera does, despite the identical specifications of the two instruments. In this case, we might see a pseudo-pulsation which is an artifact of which camera took the images rather than a pulsation of the star itself, and the period of the pseudo-pulsation would be close to 1 day or a multiple thereof.

To control for this, we selected multiple reference stars based on several criteria. First, each reference star had to appear in the Gaia and APASS catalogs (Gaia Collab. 2016, 2018; Henden *et al.* 2016). Second, the calibrated magnitude of each reference star had to have a standard deviation of less than 0.03 magnitude with respect to at least five check stars across the entire image series. Finally, the reference star had to appear in every time-series image photometry file. One criterion that we chose not to factor in was the color of the reference star since the differential CCD response of the instruments used was based on magnitude only. In addition to this, the color of an RR Lyrae star often changes as it pulsates, making the best color reference star tricky to pin down.

Once the reference stars that met these criteria were identified, each known pulsator was calibrated against the reference star that was closest to it in magnitude. Because the magnitudes of the target and pulsator were near-identical, the differential brightness response of the cameras was no longer a factor. This careful selection of reference stars successfully eliminated the pseudo-pulsations with periods of half a day or a day. The nonlinearity was reported to LCO and was traced by the LCO science team to a differential accumulation of dust on the optics between instruments. The reference stars identified for psx photometry, V-filter images are shown in Figure 1. These include two of the AAVSO-recommended comparison stars shown in Figure 2 and Table 1: 000-BPD-811 and 000-BPD-812.

2.5. Period-finding using string length

We wrote Python code, which we will call "GENIE," to calculate the pulsation periods. GENIE takes each star's time-

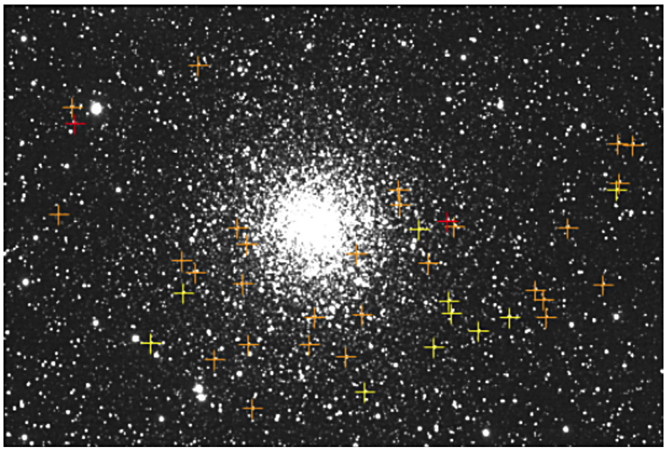

Figure 1. Reference stars found in psx V filter, labeled with colors corresponding to spectral type. Red stars have APASS B–V magnitudes greater than 1.3, orange stars have APASS B–V magnitudes between 0.9 and 1.3, and yellow stars have APASS B–V magnitudes between 0.3 and 0.9 (APASS; Henden *et al.* 2016).

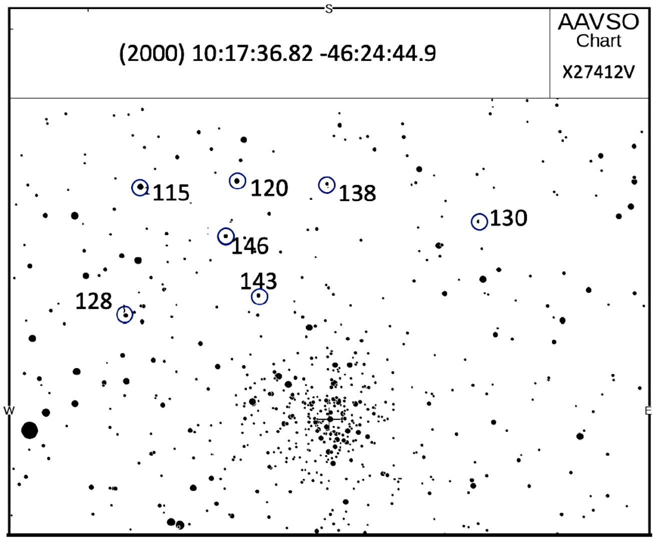

Figure 2. AAVSO recommended comparison stars from the Variable Star Plotter, chart X27412V. Of these, the stars labeled 138 and 143 (AUID 000-BPD-811 and AUID 000-BPD-812) were also identified as appropriate reference stars within our data set according to the criteria outlined above. See Table 1.

Table 1. AAVSO recommended comparison stars from the Variable Star Plotter, chart X27412V (shown in Figure 2).

AUID	*R.A. (°)*	*Dec. (°)*	*Label*	*V*	*B–V*
Epoch 2021-02-01 (2021.08767)–2021-03-23 (2021.22466)					
000-BPD-807	154.18971	–46.59292	115	11.483	0.559
000-BPD-808	154.29900	–46.59750	120	12.017	0.593
000-BPD-809	154.17329	–46.49244	128	12.833	0.771
000-BPD-810	154.57425	–46.56581	130	12.993	0.930
000-BPD-811	154.40138	–46.59531	138	13.760	0.009
000-BPD-812	154.31262	–46.51139	143	14.261	0.706
000-BPD-813	154.28625	–46.55450	146	14.575	0.824

Note: Of these, the stars labeled 138 and 143 (AUID 000-BPD-811 and AUID 000-BPD-812) were also identified as appropriate reference stars within our data set according to the criteria outlined above.

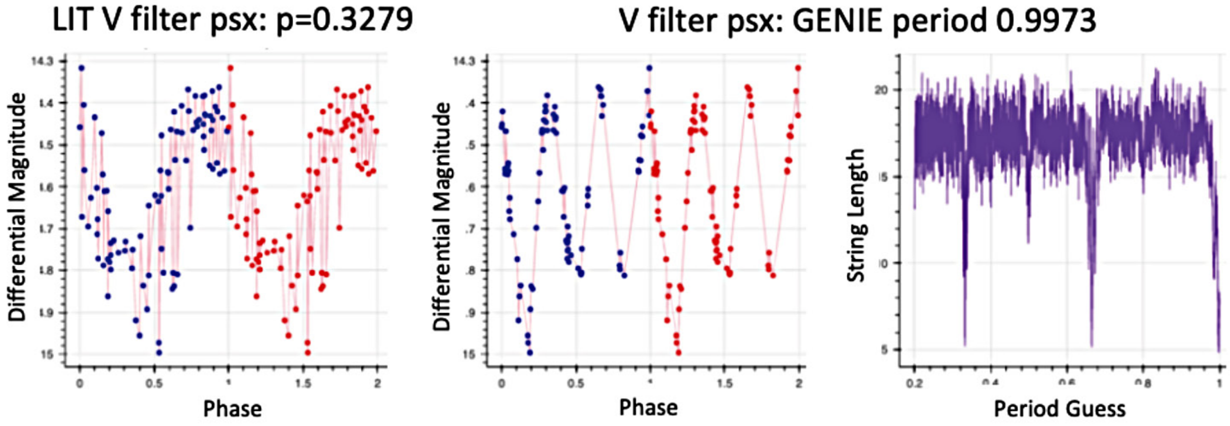

Figure 3. V67, or ASASSN-V J101700.89-462635.3: two phases of the light curve folded over the literature period (left), two phases of the light curve folded over the GENIE period (center), and the corresponding string-length plot (right).

series photometry data in the V and ip filters and folds them over periods ranging from 0.1 to 1 day, at 0.001-day increments. For each fold, a "string length" is computed for the plot of magnitude versus time (Dworetsky 1983). The string length is defined as follows: if one were to take a string and overlay it on the light curve, the string length is the length of that string on the graph. The shortest string length will correspond to the "smoothest" or most continuous light curve. Thus, whichever period yielded the shortest string length became our period estimate/GENIE period.

A plot of string length versus period is analogous to an inverted power spectrum. Manual analysis of these plots helped to catch cases where the string length was deceptive. For example, if the string length plot showed multiple minima, corresponding to harmonic oscillations, then the best period identified by the code might be a multiple of the true period. Alternatively, if the string length plot did not show a clear minimum, then it is unlikely that the brightness plot would show a clear pulsation when folded over the code-identified period.

After determining the GENIE period, light curves were plotted by folding over both the literature period and the GENIE period. Upon examination of the light curves, we visually determined which period between the GENIE period and the literature period yielded a clearer pulsation pattern. Because of the idiomatic nature of this test, estimating the error of the period presents difficulties. One technique involves taking the width of the string length plot 5% or 50% of the way up from its minimum value (Altunin *et al.* 2020; VanderPlas 2018). However, this technique is problematic because the noise in the string length plot makes the position of the plot's baseline difficult to pin down, and further ambiguity is introduced by the local minima that occur near multiples or fractions of the correct period. Therefore, a conservative estimate is to assign error bars to our GENIE periods whose width encompasses the corresponding literature period for the star.

3. Results

3.1. Nomenclature of the stars

The stars are referred to by their Clement catalog names, augmented where available by their AUIDs, and their listings in the ASAS-SN catalog, WISE catalog, and WASP catalog (Jayasinghe *et al.* 2021; Greer *et al.* 2017; Wright *et al.* 2010; Clement *et al.* 2001).

3.2. Periods found

One limitation of most period-finding methods is that multiples and fractions of the actual period (harmonics) also fit the data quite well. This is because folding the light curve over multiples of the actual period also yields a relatively clean curve. In some cases, the string length of the light curve folded over a multiple of the actual period may be slightly shorter than that of the actual period. An example of this is shown in Figure 3.

In Figure 3, all three multiples of the pulsator's period are represented by minima of approximately the same depth in the string length plot at right. However, visual confirmation of multiple pulses in the light curve invalidates the longer periods. Period-finding methods may sometimes identify multiples of the correct period, as ours did for this system, because any behavior that is periodic over a time x is also periodic over whole number multiples of x.

Another initial anomaly in the first run of the GENIE code was that a large proportion of pulsators apparently had periods of close to a day or half a day. As discussed in section 2, Procedure, the artificial pulsation was likely induced by a non-linear CCD brightness response across different LCO cameras. Thus GENIE initially found that 28% of pulsators seemed to have a period over 0.9 day. After reference stars were selected as described above and filtered for similarity in brightness to each pulsator target, the artificial pulsations went away. This suggests that our rigorous reference star selection procedure reduced the likelihood that the reference was significantly brighter or dimmer than its corresponding target.

After making these corrections, the known RR Lyrae pulsators in the cluster became clearly evident, and their light curves are shown in Appendix A. In addition, we identified eight pulsators for which the GENIE period yielded significantly cleaner light curves than the literature period did. These are tabulated in Table 2 and shown in Figure 4. The literature periods and pulsator classes quoted in Table 1 were taken from the Clement catalog (Clement *et al.* 2001). This catalog cited Layden and Sarajedini (2003) as the source for the literature periods.

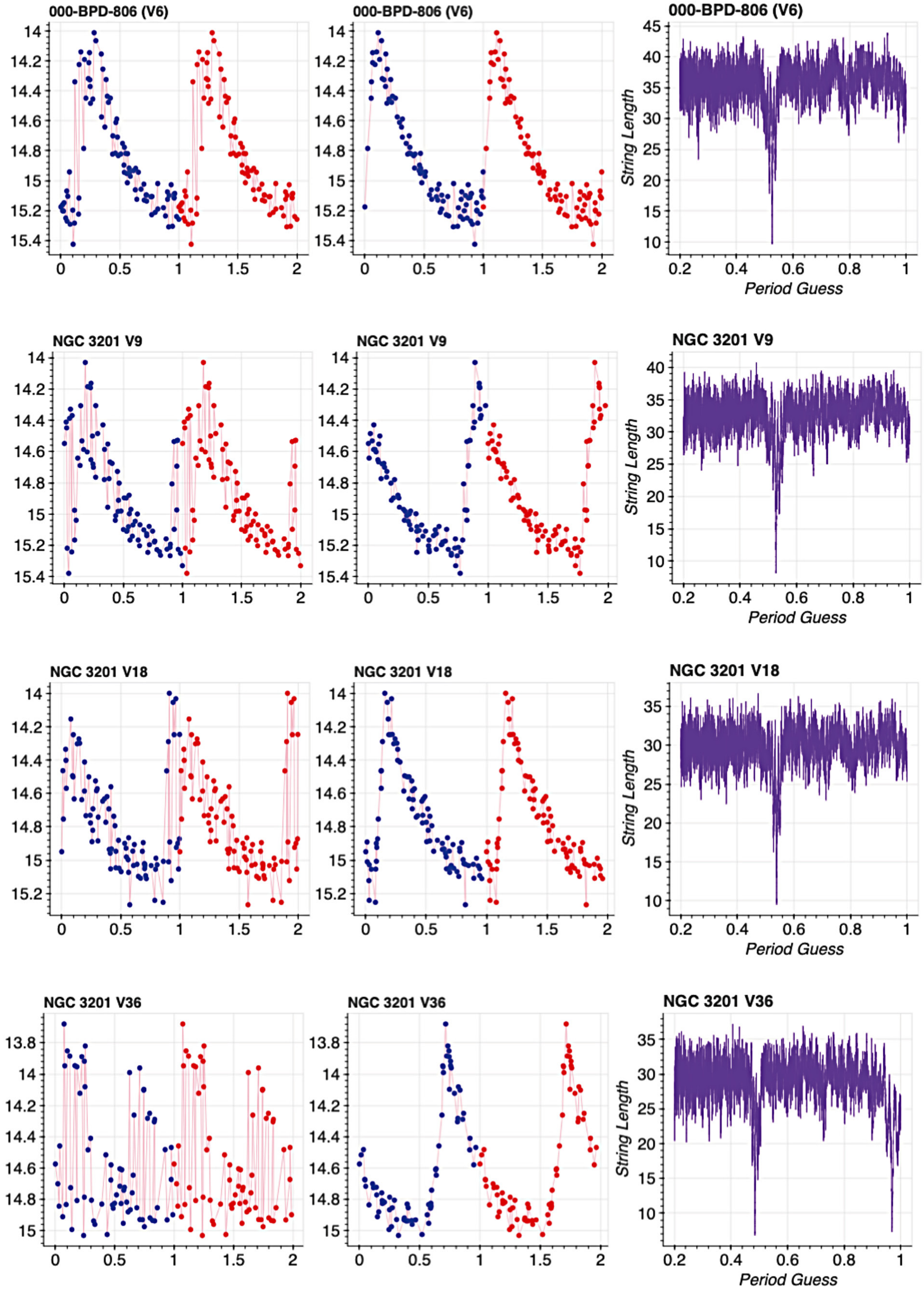

Figure 4. Left: Calibrated magnitude versus phase folded over the literature period from Table 1. Middle: Calibrated magnitude versus phases folded over the GENIE period from Table 1. Right: String length plot. (Figure continued on next page.)

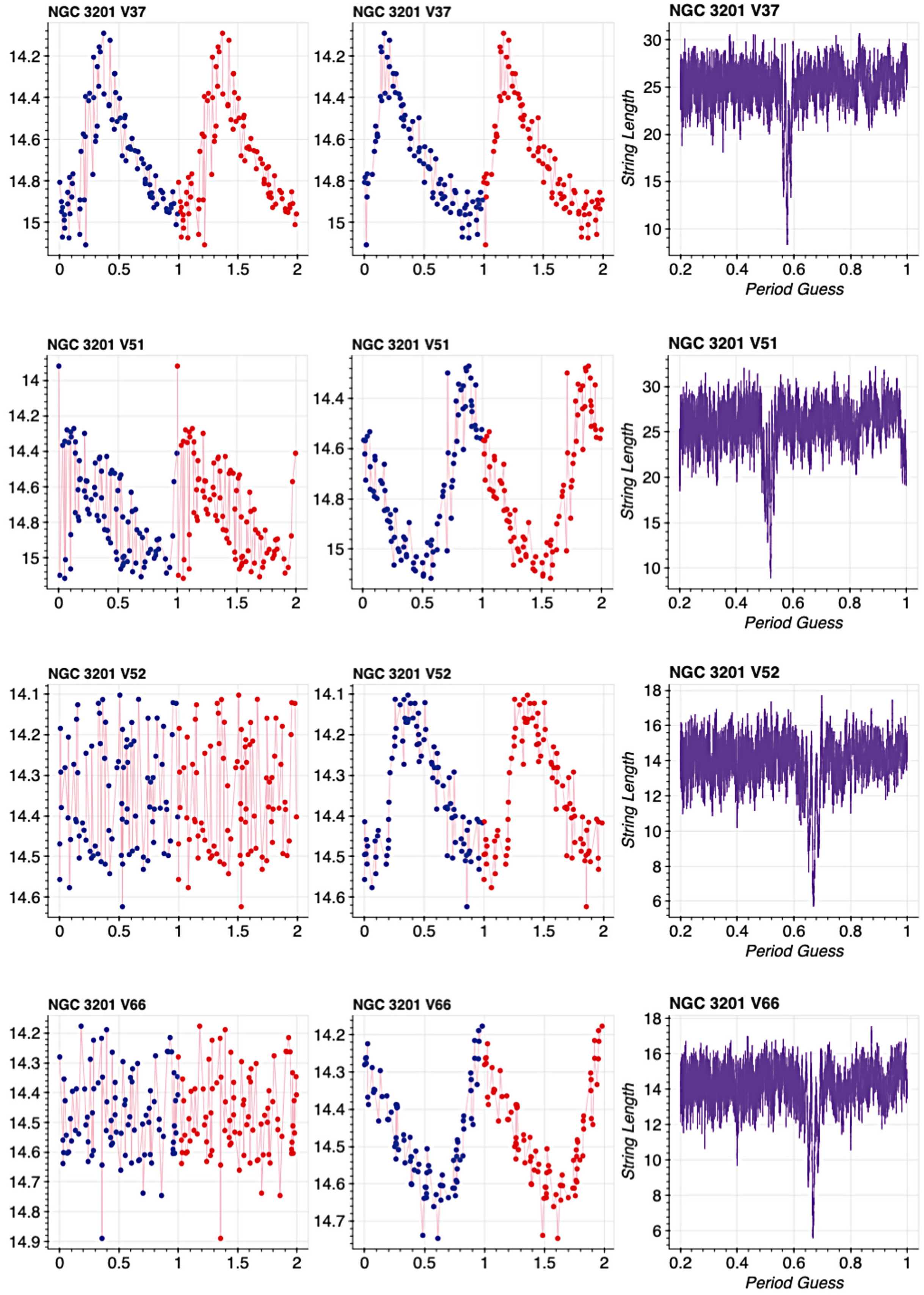
NGC 3201 V37

NGC 3201 V37

NGC 3201 V37

NGC 3201 V51

NGC 3201 V51

NGC 3201 V51

NGC 3201 V52

NGC 3201 V52

NGC 3201 V52

NGC 3201 V66

NGC 3201 V66

NGC 3201 V66

Figure 4 (cont.). Left: Calibrated magnitude versus phase folded over the literature period from Table 1. Middle: Calibrated magnitude versus phases folded over the GENIE period from Table 1. Right: String length plot.

Table 2. The position, class, literature period, and GENIE period for updated pulsators.

Clement Catalog Name	*R.A. (°)*	*Dec. (°)*	*Clement Catalog Pulsator Class*	*GENIE Period*	*Layden (2003) Period*
Epoch 2021-02-01 (2021.08767)–2021-03-23 (2021.22466)					
000–BPD–806 (NGC 3201 V6)	154.35875	–46.45063	RR0	0.5263	0.5253
NGC 3201 V9	154.38457	–46.43683	RR0	0.5271	0.5254
NGC 3201 V18	154.41408	–46.41839	RR0	0.5389	0.5404
NGC 3201 V36	154.36265	–46.41464	RR0	0.4844	0.4796
NGC 3201 V37	154.37793	–46.43212	RR0	0.5766	0.5751
NGC 3201 V51	154.32363	–46.41839	RR0	0.5214	0.5186
NGC 3201 V52	154.40958	–46.63284	RR1	0.6691	0.38
NGC 3201 V66	154.24627	–46.33007	RR2	0.6675	0.284

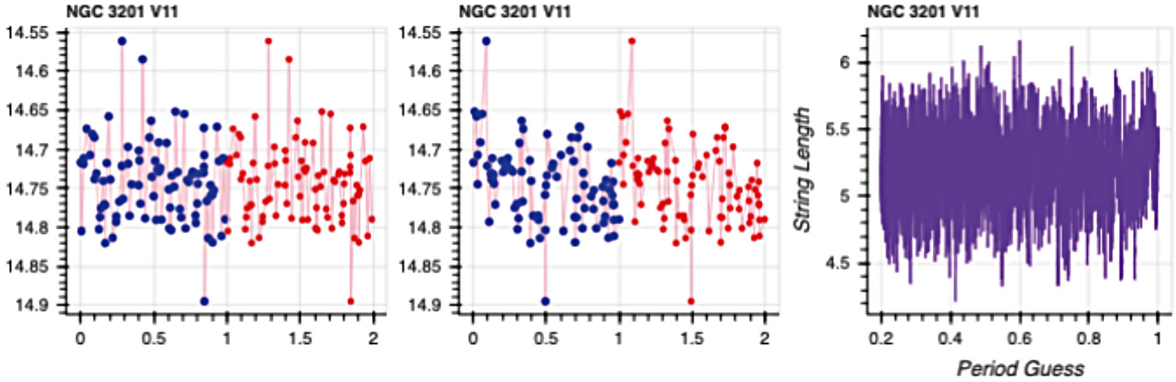

Figure 5. NGC 3201 V11. Left: Calibrated magnitude versus phase folded over the literature period from Table 1. Middle: Calibrated magnitude versus phases folded over the GENIE period from Table 1. Right: String length plot.

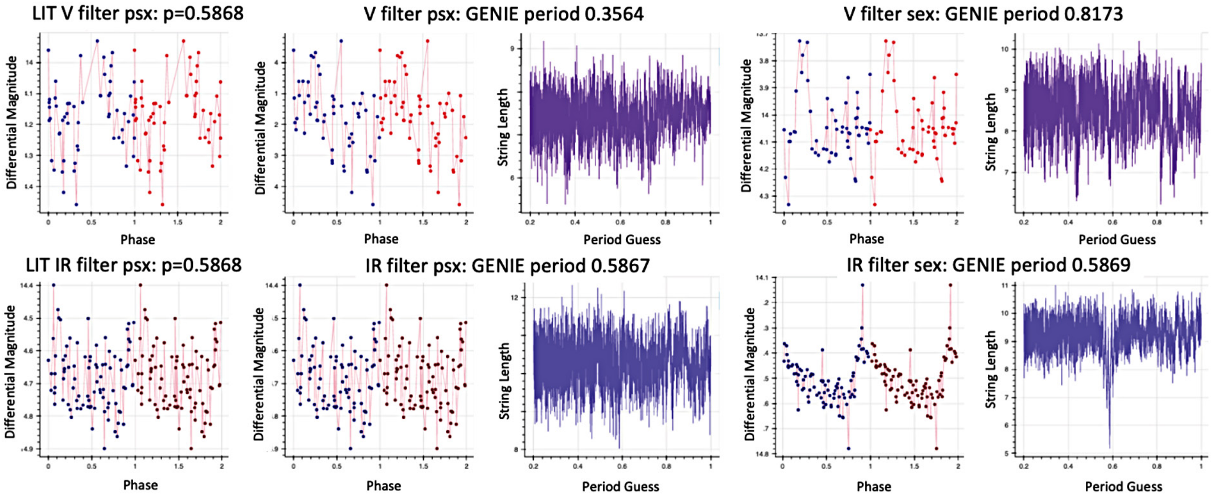

Figure 6. NGC 3201 V23, pulsator for which only the sex IP light curve is clearly pulsing.

Table 3. Photometry file for psx V photometry file (Bertin and Arnouts 1996), with three stars very close together.

R.A. (°)	*Dec. (°)*	*Pixel X*	*Pixel Y*	*ADU Count X*	*ADU Count Y*	*Error X*	*Error Y*
Epoch 2021-02-01 (2021.08767)–2021-03-23 (2021.22466)							
154.3863432	–46.4291925	1602.9081	927.7031	41177.74	316.8156	7.614074^{-6}	3.741641^{-6}
154.3803840	–46.4232605	1565.3450	901.5863	40363.49	315.9283	6.314095^{-6}	3.153824^{-6}
154.3860066	–46.4255095	1579.5896	926.3909	90200.72	392.6851	3.316372^{-6}	3.998483^{-6}

In each case, a visual comparison was made between the light curve folded over the literature period and the light curve folded over the GENIE period for both V and ip filters, in both psx and sex photometry. For simplicity, we display the literature and GENIE period for only V filter, psx photometry in the plots of Figure 4. Note that the last two light curves represent RR Lyrae stars of type RR1 and RR2, respectively, according to their Clement catalog classifications. They have a pulse profile with a correspondingly different shape than the sharp sawtooth light curve characteristic of an RR0.

The discrepancies between the GENIE period and literature periods in Table 1 have unclear origins. Typical changes in RR Lyrae periods are on the scale of 0.2 or 0.5 day every one million years, but the changes found here are significantly more. However, previous articles have found much greater discrepancies than predicted as well (Neilson *et al.* 2016). The reason for these discrepancies is presently unknown. We note that the most drastic differences (V52 and V66) correspond to stars for which no amplitude or magnitude is listed in the Clement catalog and that V6 and V36 were stars for which Layden and Sarajedini did not find reliable periods, as discussed previously. Also of note is the fact that V18 is one of the stars highlighted in the introduction as a suspected Blazhko (Arellano Ferro *et al.* 2014).

Analogous plots to those shown in Figure 4 were also generated for psx photometry in the ip filter, sex photometry in the V filter, and sex photometry in the ip filter. The GENIE periods were almost or exactly identical to those found above, and the GENIE period light curves compared similarly to the literature period light curves as for psx photometry in the V filter. Therefore, these 72 additional plots are not shown.

The fact that GENIE found the same period as the literature value for 50 of the stars in Appendix A, and that folding over the GENIE period sharpens and smooths the light curves in Figure 4, improves confidence in the string-length period-finding method. For V52 and V66, although the GENIE period is much larger than the literature period by almost a full multiple, we are confident that the GENIE period is valid because there is only one dip in the string length plot and the light curve shows a clear pulse. However, it should be noted that these stars are type RR1 and RR2 rather than RR0. RR1s and RR2s typically have shorter periods of about 0.3 day. Hence the GENIE period of approximately double that is surprising. Further investigation may reveal that these stars should be reclassified, possibly to RR0s.

In addition to offering some updates, we also draw attention to some special cases. For the NGC 3201 V11 pulsator, neither the GENIE period nor the literature period yielded a light curve that appeared to be pulsing, as shown in Figure 5. We hypothesize that this star may have been incorrectly identified in our images. In this case, the plots below may pertain to an entirely different star.

Another special case is NGC 3201 V23, for which pulsation was only evident in the sex ip-filter light curve. This is shown in Figure 6.

One hypothesis is that in some filters and photometries, stars that are close together are being blended. As shown in Table 3, there are three stars with an R.A. starting with 154.38 and Dec. starting with –46.42 in the psx V photometry. Figure 7 shows this region of the crowded starfield, along with a surface plot of ADU count as a function of x and y pixel coordinates. Since the stars are so close together, it can be challenging to pick out which star is which. GENIE's criterion was to find the closest star to the Gaia coordinates relative to the image plate solution within 2 arcseconds, which may be inadequate. If the incorrect star is identified as the pulsator in some images, the pulse may be obscured.

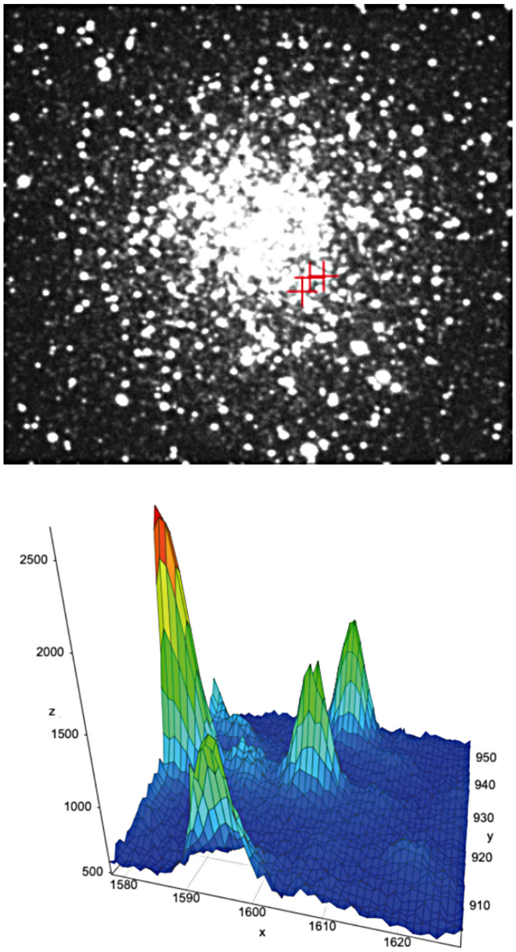

Figure 7. Region surrounding the three stars highlighted in Table 3, as seen on the image (top) and as a surface in three dimensions (bottom).

The figures above imply that sex V may be showing one of the non-pulsators while sex ip shows the pulsator. When stars are very close together, sex photometry likely finds either the brightest one only or a blend of multiple stars. Perhaps the non-pulsator is brighter in the V filter, but the pulsator is brighter in the ip filter.

Another item to note is that our methods failed to find accurate periods for SX Phoenicis (SXP) pulsators. Although some of our SXP light curves show some evidence of pulsation when folded over the literature period, there is no sharp dip in the string length plots. This is likely because the SXP pulsators are very dim, having magnitudes close to 17, which is near the limit of what the Las Cumbres 0.4-m telescopes can observe. Secondly, SXPs usually have pulsations of less than 0.3 magnitude (Aerts 2010). Thus the SXP pulse often does not rise above the noise floor for our images, and the string length

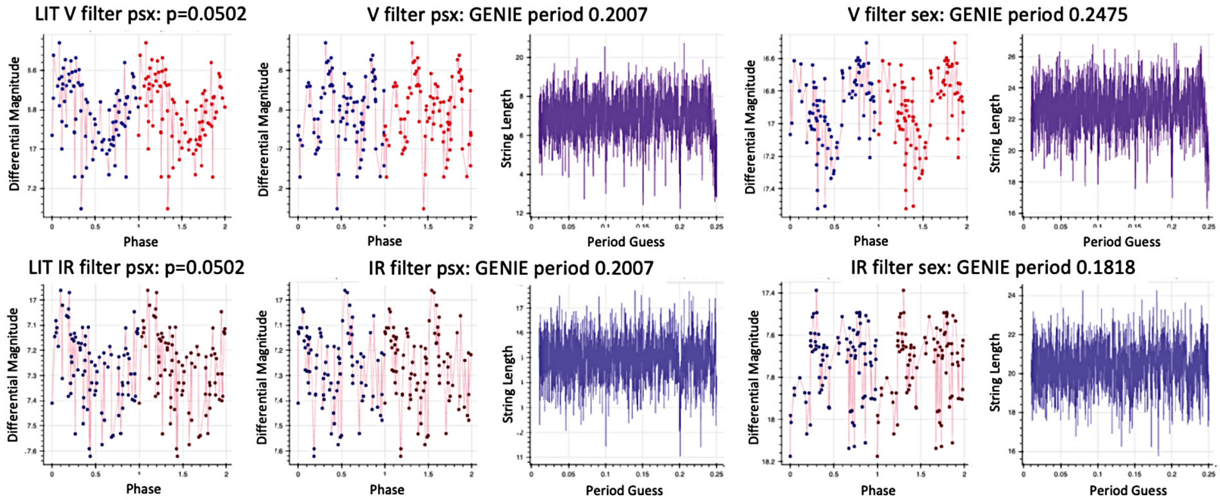

Figure 8. Light curves and string length plot for SXP pulsator NGC 3201 V110.

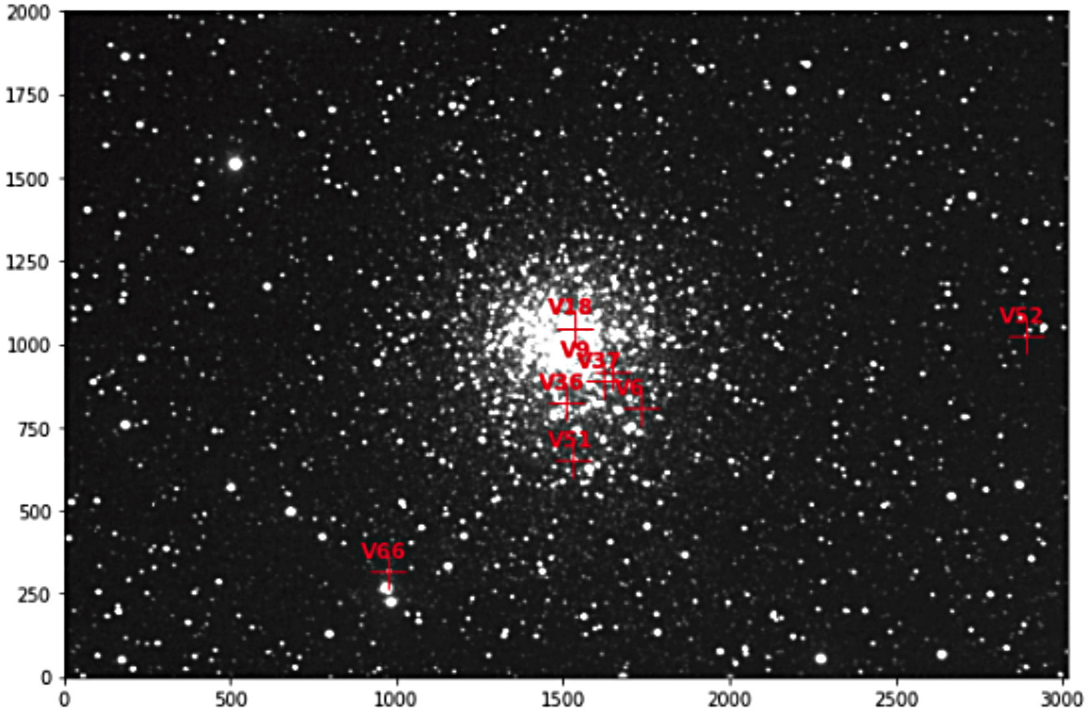

Figure 9. The pulsators whose periods are updated by this study include NGC 3201 V6 (000-BPD-806), V9, V18, V36, V37, V51, V52, and V66.

method may not be appropriate for such cases. When folded over the literature period, we did see evidence of one SXP pulsation, shown in the plots for NGC 3201 V110 in Figure 8. The literature period and classification as an SXP for V110 were also obtained from the Clement catalog (Clement *et al.* 2001). The Clement catalog cites Mazur *et al.* (2003) as the source for this pulsator's period.

3.3. Distribution of data and results

Sharing data with the scientific community makes more extensive studies possible. The AAVSO maintains several databases for the purpose of facilitating the storing and sharing of data pertinent to variable stars. At present, these databases are set up to tie each observation to a particular observing site, which is problematic for the LCO Global Telescope network. Although the 0.4-m LCO telescopes have identical specifications, they are located at multiple sites all over the world. It is not possible to submit observations taken by multiple telescopes within the same data file being uploaded via WebObs to the AAVSO International Database, and separating the observations by telescope is impractical given the large number of images in this study. That said, the images and photometry are all freely accessible on Google Drive from the links in Appendix A, or by corresponding with the study authors.

The authors are exploring uploading the photometry to the AAVSO International Database.

4. Conclusions

Our GENIE code for finding periods using the string-length method appears to be sound. 54 of the periods of pulsators in NGC 3201 were confirmed, and the periods of the eight pulsators highlighted above were updated. The positions within the cluster of the stars whose period updates are presented are shown in Figure 9.

Secondly, we caution that a non-linear CCD brightness response across different cameras is possible, even when these cameras have the same specifications. This can result in pseudo-pulsations. However, this can be overcome by ensuring that the reference and the pulsator stars are of near-identical brightness.

Thirdly, we point out that using two or more different photometries minimizes the chances of being misled by blended stars, because at least one of the photometries may be able to isolate close stars instead of blending them.

5. Acknowledgements

This work makes use of observations taken by the 0.4-m telescopes of Las Cumbres Observatory Global Telescope Network located in Cerro Tololo, Chile, in Siding Spring, Australia, in Sutherland, South Africa, and in Fort Davis, Texas, reduced using the Our Solar Siblings Pipeline. This research was made possible through the use of the AAVSO Photometric All-Sky Survey (APASS), funded by the Robert Martin Ayers Sciences Fund, and the International Variable Star Index, maintained by the AAVSO.

The authors would particularly like to thank Daniel Zaharevitz for his Python coding help, as he was the original author of a script that we adapted to visualize the positions of particular stars within the cluster. We would also like to thank Chuck Cynamon for his assistance in generating an AAVSO sequence for the NGC 3201 field, and requesting AUIDs for many of our targets. In addition, Michael Fitzgerald was an invaluable source of help and advice, especially regarding the operation of the LCO telescopes and the possible nonlinearity of the CCD sensor.

References

Aerts, C., Christensen-Dalsgaard, J., and Kurtz, D. W. 2010, Asteroseismology, Springer Science+Business Media B.V., Berlin (DOI: 10.1007/978-1-4020-5803-5).

Altunin, I., Caputo, R., and Tock, K. 2020, *Astron. Theory Obs. Methods*, **1**, 1 (DOI: 10.32374/atom.2020.1.1).

Arellano Ferro, A., Ahumada, J. A., Calderón, J. H., and Kains, N. 2014, *Rev. Mex. Astron. Astrofís.*, **50**, 3 (arXiv:1406.2635).

Bertin, E., and Arnouts, S. 1996, *Astron. Astrophys., Suppl. Ser.*, **117**, 393 (DOI: 10.1051/aas:1996164).

Blanton, M. R., *et al.* 2017, *Astron. J.*, **154**, 28 (Sloan Digital Sky Survey IV, https://www.sdss.org/).

Brown, T. M., *et al.* 2013, *Publ. Astron. Soc. Pacific*, **125**, 1031 (DOI: 10.1086/673168).

Clement, C. M., *et al.* 2001, *Astron. J.*, **122**, 2587 (DOI: 10.1086/323719).

Dall'Ora, M., *et al.* 2006, *Mem. Soc. Astron. Ital.*, **77**, 214 (arXiv:astro-ph/0601237).

Dworetsky, M. M. 1983, *Mon. Not. Roy. Astron. Soc.*, **203**, 917 (DOI: 10.1093/mnras/203.4.917).

Fitzgerald, M. 2018, *Robotic Telesc. Student Res. Education Proc.*, **1**, 347 (DOI: 10.32374/rtsre.2017.033).

Fitzgerald, M., Gomez, E., Salimpour, S., Singleton, J., and Wibowo, R. 2021, *J. Open Source Software*, **6**, 2641 (DOI: 10.21105/joss.02641).

Gaia Collaboration, *et al.* 2016, *Astron. Astrophys.*, **595A**, 1.

Gaia Collaboration, *et al.* 2018, *Astron. Astrophys.*, **616A**, 1.

Greer, P. A., Payne, S. G., Norton, A. J., Maxted, P. F. L., Smalley, B., West, R. G., Wheatley, P. J., and Kolb, U. C. 2017, *Astron. Astrophys.*, **607A**, 11 (DOI: 10.1051/0004-6361/201630296).

Hamrick, P., Bansal, A., and Tock, K. 2021, *J. Amer. Assoc. Var. Star Obs.*, **49**, 192.

Heasley, J. N. 1999, in *Precision CCD Photometry*, eds. E. R. Craine, D. L. Crawford, R. A. Tucker, ASP Conf. Ser. 189, Astronomical Society of the Pacific, San Francisco, 56.

Henden, A. A., Templeton, M., Terrell, D., Smith, T. C., Levine, S., and Welch, D. 2016, VizieR Online Data Catalog: AAVSO Photometric All Sky Survey (APASS) DR9, II/336.

Jayasinghe, T., *et al.* 2021, *Mon. Not. Roy. Astron. Soc.*, **503**, 200. (DOI: 10.1093/mnras/stab114).

Kravtsov, V., Alcaíno, G., Marconi, G., and Alvarado, F. 2009, *Astron. Astrophys.*, **497**, 371 (DOI: 10.1051/0004-6361/200810555).

Layden, A. C., and Sarajedini, A. 2003, *Astron. J.*, **125**, 208 (DOI: 10.1086/344948).

Lee, Y.-W. 1992, *Mem. Soc. Astron. Ital.*, **63**, 331.

Mazur, B., Krzemiński, W., and Thompson, I. B. 2003, *Mon. Not. Roy. Astron. Soc.*, **340**, 1205.

McCully, C., Volgenau, N. H., Harbeck, D.-R., Lister, T. A., Saunders, E. S., Turner M. L., Siiverd, R. J., and Bowman, M. 2018, *Proc. SPIE*, id. 107070K (https://arxiv.org/pdf/1811.04163.pdf).

Menzies, J. 1973, *Mon. Not. Roy. Astron. Soc.*, **163**, 323 (DOI: 10.1093/mnras/163.3.323).

Neilson, H. R., Percy, J. R., and Smith, H. A. 2016, *J. Amer. Assoc. Var. Star Obs.*, **44**, 179.

Piersimoni, A. M., Bono, G., and Ripepi, V. 2002, *Astron. J.*, **124**, 1528.

Smolec, R., and Moskalik, P. 2012, *Mon. Not. Roy. Astron. Soc.*, **426**, 108 (DOI: 10.1111/j.1365-2966.2012.21678.x).

VanderPlas, J. T. 2018, *Astrophys. J., Suppl. Ser.*, **236**, 16 (DOI: 10.3847/1538-4365/aab766).

Wright, F. W. 1941, *Bull. Harvard Coll. Obs.*, No. 915, 2.

Wright, E. L., *et al.* 2010, *Astron. J.*, **140**, 1868. (DOI: 10.1088/0004-6256/140/6/1868).

Appendix A

We confirm the periods of the 54 RR Lyrae pulsators in NGC 3201, listed by their Clements Catalog variable names in Table A1 and shown in Figure A1. These include 50 stars for which GENIE code found a period less than 0.001 day different from the literature value. In addition, we include one star (NGC 3201 V80) whose light curve folded over the literature period (0.5887 day) was cleaner than when folded over the GENIE period (0.5901 day), and one star (NGC 3201 V76) for which neither the literature period nor the GENIE period was decidedly cleaner. Finally, we include two stars for which folding over the literature period produced a clean light curve but GENIE found a multiple of the period. These are NGC 3201 V16 (ASASSN-V J101718.47-462836.5) and NGC 3201 V67 (ASASSN-V J101700.89-462635.3). Thus, in total, we confirm the periods of 54 stars.

Three of the stars in this "confirmed" list are suspected Blazhko stars: NGC 3201 V25 (ASASSN-V J101746.15-462152.1), NGC 3201 V28, and NGC 3201 V73 (ASASSN-V J101725.20-462315.1). These are noted in Table A1.

A list of stars that were not positively identified in at least 50 of our images of the cluster is shown in Table A2. Stars that were outside the field of view of our images are noted.

Links to the original images along with the OSS photometry appear in Table A3.

In Table A4, all 64 of the RR Lyrae stars identified in our images are listed by their Clements Catalog names and alternative designations where available. Of these, 54 of the periods were confirmed (Table A1), eight of the periods were updated (Main Study Table 1), and two of the stars did not display a clear pulse (V11 and V23, shown in Main Study Figures 5 and 6).

Table A1. NGC 3201 stars whose periods are confirmed by this study, with suspected Blazhko stars indicated.

NGC 3201 Star		
1	25 Blazhko susp.	47
2	26	48
3	27	49
4	28 Blazhko susp.	55
5	29	56
7	30	57
8	31	58
10	32	59
13	34	67
14	35	71
15	38	73 Blazhko susp.
16	39	76
17	40	78
19	41	80
20	42	83
21	43	84
22	44	98
24	46	100

Table A2. NGC 3201 stars that were not positively identified in the images for this study, which suspected Blazhko stars and stars that were outside the image FOV indicated.

NGC 3201 Star			
12		77	
33		79	
45		81	
50	Blazhko susp.	82	
53–54	Outside FOV	85–89	Outside FOV
60–64	Outside FOV	90	
65		91	Outside FOV
68–69	Outside FOV	92	
70		93–96	Outside FOV
72		97	
74		99	
75			

Table A3. Repository of images and photometry used for this study.

Available through Google Drive		
Images		https://tinyurl.com/NGC3201images
Photometry	V psx	https://tinyurl.com/NGC3201Vpsx
	V sex	https://tinyurl.com/NGC3201Vsex
	ip psx	https://tinyurl.com/NGC3201ipsx
	ip sex	https://tinyurl.com/NGC3201isex
Available through the AAVSO ftp public datasets site (photometry only)		
ftp://ftp.aavso.org/public/datasets/J50.1-Bansal-NGC3201/small_phot_files-20220329T185408Z-001.zip		
ftp://ftp.aavso.org/public/datasets/J50.1-Bansal-NGC3201/NGC3201_sex_V-20220329T185526Z-001.zip		
ftp://ftp.aavso.org/public/datasets/J50.1-Bansal-NGC3201/NGC3201_psx_ip-20220329T185836Z-001.zip		
ftp://ftp.aavso.org/public/datasets/J50.1-Bansal-NGC3201/NGC3201_sex_ip-20220329T190205Z-001.zip		

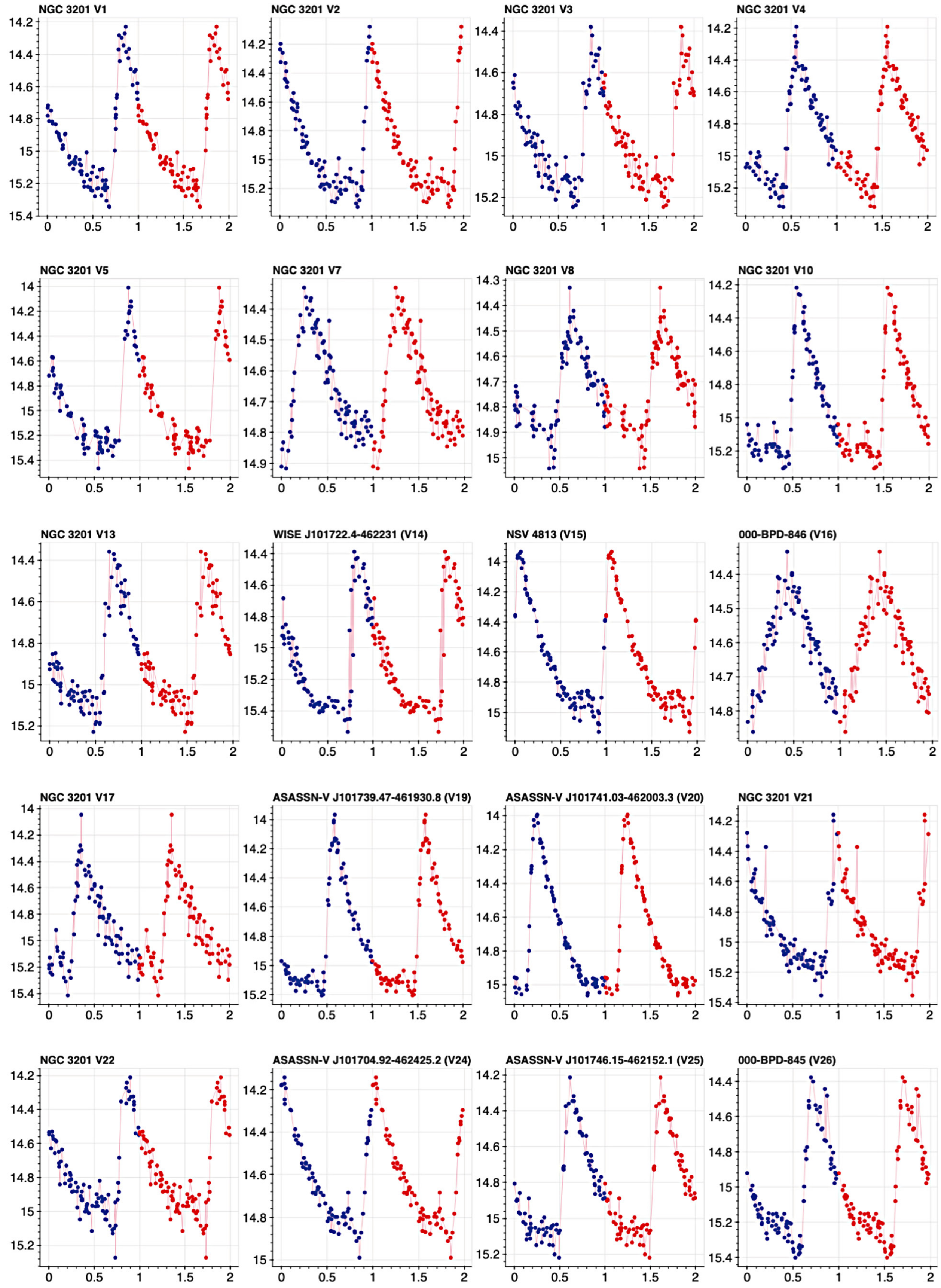

Figure A1. Light curves of 54 RR Lyrae variable stars whose literature periods are confirmed by this study. (Figure continued on following pages.)

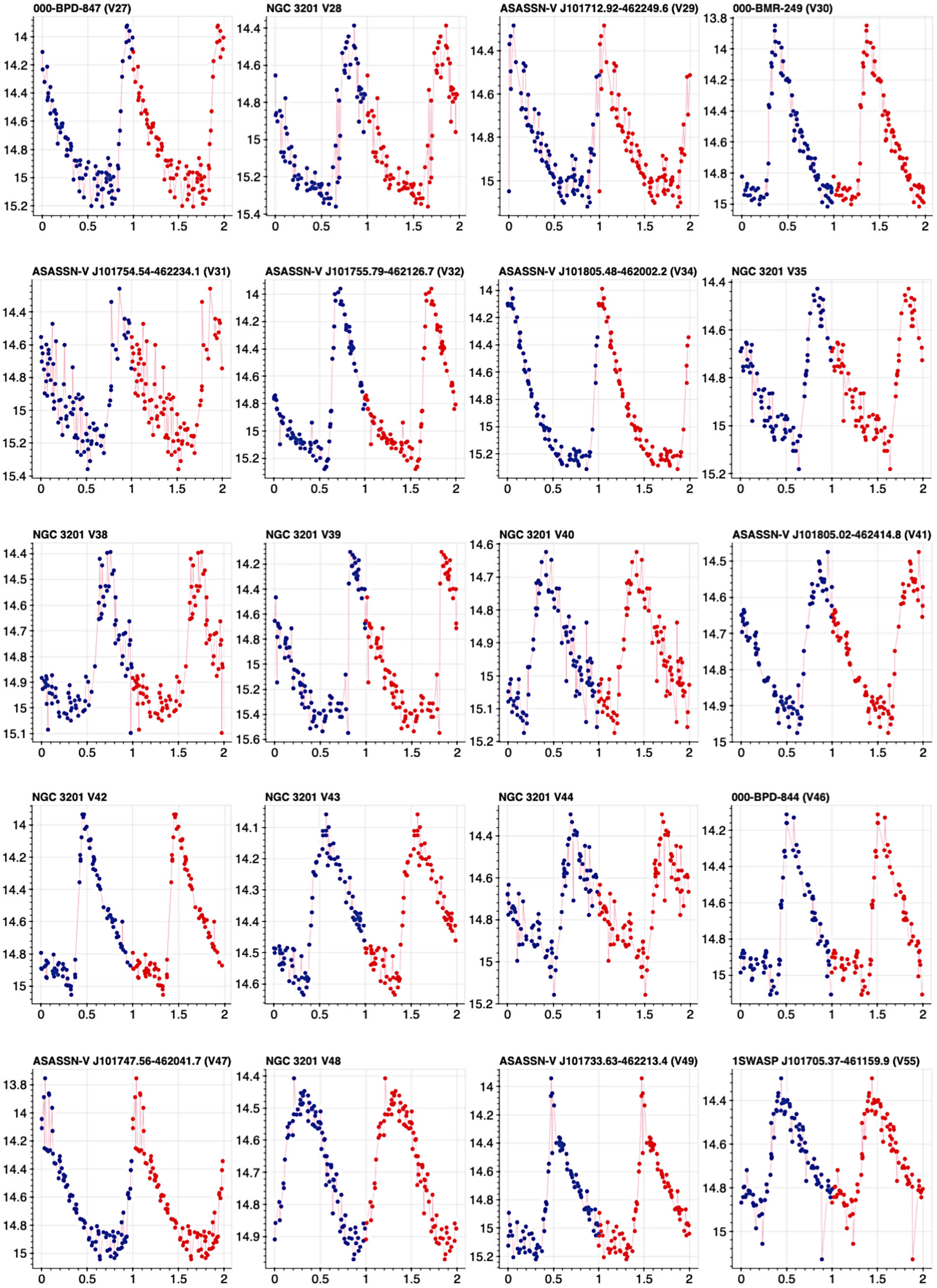

Figure A1. Light curves of 54 RR Lyrae variable stars whose literature periods are confirmed by this study (cont.). (Figure continued on next page.)

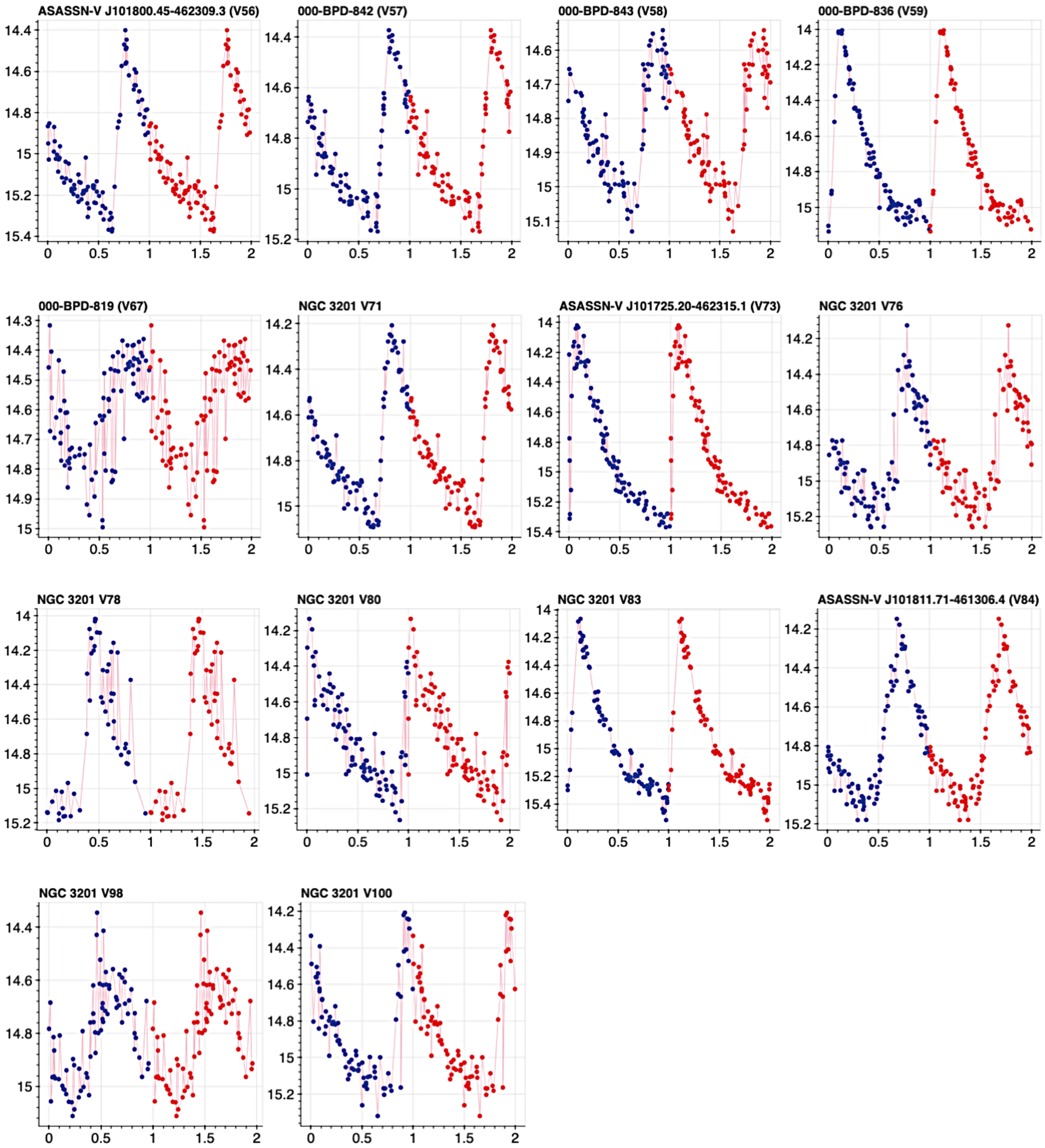

Figure A1. Light curves of 54 RR Lyrae variable stars whose literature periods are confirmed by this study (cont.).

Table A4. All 64 of the RR Lyrae stars identified in the images of this study.

Number	*Name*	*AUID*	*R.A. (°)*	*Dec. (°)*	*Type*	*Publ. Mag.*	*Publ. Ampl.*	*Publ. Period*	*Genie Best Period*	*Notes*
Epoch 2021-02-01 (2021.08767)–2021-03-23 (2021.22466)										
1	NGC 3201 V1	000-BPD-806	154.42844	–46.44382	RR0	14.81	0.92	0.6048	0.6049	
2	NGC 3201 V2		154.41666	–46.44385	RR0	14.8	1.07	0.5326	0.5327	
3	NGC 3201 V3		154.47705	–46.42376	RR0	14.91	0.8	0.5994	0.5993	
4	NGC 3201 V4		154.46677	–46.41124	RR0	14.8	1.02	0.63	0.6303	
5	NGC 3201 V5		154.42208	–46.41844	RR0	14.73	0.94	0.5013	0.5011	
6	ASASSN-V J101726.09-462702.3		154.35875	–46.45063	RR0	14.74	0.9	0.5253	0.5263	updated in this study
7	NGC 3201 V7		154.36872	–46.46352	RR0	14.69	0.67	0.6303	0.6301	
8	NGC 3201 V8		154.37817	–46.4387	RR0	14.74	0.73	0.6286	0.6286	
9	NGC 3201 V9		154.38457	–46.43683	RR0	14.82	0.96	0.5254	0.5271	updated in this study
10	NGC 3201 V10		154.33394	–46.34726	RR0	14.84	0.88	0.5352	0.5352	
11	NGC 3201 V11		154.36483	–46.38211	RR1	14.79	0.58	0.2991	0.4146	no clear pulse
13	NGC 3201 V13		154.34185	–46.38644	RR0	14.85	0.88	0.5748	0.5753	
14	WISE J101722.4-462231		154.34349	–46.3754	RR0	14.99	1.13	0.5089	0.5093	
16	ASASSN-V J101718.47-462836.5	000-BPD-846	154.327	–46.47683	RR1	14.62	0.63	0.2634	0.5269	multiple pulses
17	NGC 3201 V17		154.40963	–46.41867	RR0	14.76	0.92	0.5658	0.5655	
18	NGC 3201 V18		154.41408	–46.41839	RR0	14.74	1.05	0.5404	0.5389	Blazhko, updated in this study
19	ASASSN-V J101739.47-461930.8		154.4145	–46.32524	RR0	14.73	0.92	0.525	0.5251	
20	ASASSN-V J101741.03-462003.3		154.42092	–46.33431	RR0	14.68	1.07	0.5291	0.5289	
21	NGC 3201 V021		154.44267	–46.37483	RR0	14.83	0.73	0.5668	0.5667	
22	NGC 3201 V22		154.36528	–46.42723	RR0	14.75	0.86	0.6058	0.606	
23	NGC 3201 V23		154.38604	–46.42521	RR0	14.8	0.77	0.5868	0.3564	no clear pulse
24	ASASSN-V J101704.92-462425.2		154.27053	–46.40702	RR0	14.65	0.76	0.589	0.5889	
25	ASASSN-V J101746.15-462152.1		154.44235	–46.36448	RR0	14.73	1.05	0.5147	0.5145	Blazhko
26	ASASSN-V J101758.09-462701.8	000-BPD-845	154.49208	–46.45049	RR0	14.91	0.92	0.569	0.569	
27	ASASSN-V J101742.79-463001.0	000-BPD-847	154.42842	–46.50035	RR0	14.76	1.21	0.4843	0.4843	
28	NGC 3201 V28		154.43131	–46.42512	RR0	14.87	0.86	0.5795	0.5786	Blazhko
29	ASASSN-V J101712.92-462249.6		154.30387	–46.38046	RR0	14.78	0.68	0.5291	0.5298	
30	NGC 3201 V30	000-BMR-249	154.29131	–46.33731	RR0	14.6	0.87	0.5159	0.5161	
31	ASASSN-V J101754.54-462234.1		154.47734	–46.37615	RR0	14.9	1.26	0.5191	0.5191	
32	ASASSN-V J101755.79-462126.7		154.48248	–46.35742	RR0	14.73	1.24	0.5612	0.5611	
34	ASASSN-V J101805.48-462002.2		154.52289	–46.33397	RR0	14.75	1.27	0.4679	0.4679	
35	NGC 3201 V35		154.40129	–46.37867	RR0	14.75	0.63	0.6155	0.6156	
36	NGC 3201 V36		154.36265	–46.41464	RR0	14.73	1.26	0.4796	0.4844	updated in this study
37	NGC 3201 V37		154.37793	–46.43212	RR0	14.74	1.05	0.5751	0.5766	updated in this study
38	NGC 3201 V38		154.38092	–46.42806	RR0	14.81	0.81	0.5094	0.5093	
39	NGC 3201 V39		154.42186	–46.39713	RR0	14.81	1.2	0.4829	0.4833	
40	NGC 3201 V40		154.36674	–46.3933	RR0	14.84	0.58	0.6437	0.644	
41	ASASSN-V J101805.02-462414.8		154.52097	–46.40411	RR0	14.81	0.45	0.665	0.6648	
42	NGC 3201 V42		154.28616	–46.3578	RR0	14.61	1.22	0.5382	0.5381	
43	NGC 3201 V43		154.25569	–46.40719	RR0	14.65	0.5	0.6761	0.6765	
44	NGC 3201 V44		154.41703	–46.39355	RR0	14.76	0.62	0.6107	0.6106	
46	1SWASP J101657.56-463212.1	000-BMR-249	154.24628	–46.55113	RR0	14.74	0.98	0.5432	0.5432	
47	ASASSN-V J101747.56-462041.7		154.44823	–46.34493	RR0	14.65	0.89	0.5212	0.521	
48	NGC 3201 V48		154.3056	–46.408	RR1	14.68	0.65	0.3413	0.3413	
49	ASASSN-V J101733.63-462213.4		154.39018	–46.3704	RR0	14.72	1.04	0.581	0.5813	
51	NGC 3201 V51		154.32363	–46.41839	RR0	14.72	1.16	0.5186	0.5214	updated in this study
52	NGC 3201 V52		154.40958	–46.63284	RR1	—	—	0.38	0.6691	updated in this study
55	1SWASP J101705.37-461159.9		154.27246	–46.20005	RR0	14.57	0.55	0.6041	0.6048	
56	ASASSN-V J101800.45-462309.3		154.50307	–46.38613	RR0	14.89	0.79	0.5903	0.5905	
57	ASASSN-V J101804.87-462554.6	000-BPD-842	154.52035	–46.43183	RR0	14.83	0.71	0.5934	0.5935	
58	ASASSN-V J101810.58-462604.6	000-BPD-843	154.54413	–46.43462	RR0	14.7	0.72	0.622	0.6229	
59	1SWASP J101651.71-462523.2	000-BPD-836	154.20851	–46.43049	RR0	14.66	1.08	0.5177	0.5179	
66	NGC 3201 V66	000-BPD-819	154.24627	–46.33007	RR2	—	—	0.284	0.6675	updated in this study
67	ASASSN-V J101700.89-462635.3		154.25376	–46.44314	RR1	14.69	0.39	0.3279	0.9973	multiple pulses
71	NGC 3201 V71		154.3307	–46.44347	RR0	14.7	0.78	0.6012	0.6013	
73	ASASSN-V J101725.20-462315.1		154.35504	–46.38753	RR0	14.76	1.24	0.5195	0.5199	Blazhko
76	NGC 3201 V76		154.38039	–46.42321	RR0	14.81	0.66	0.5267	0.5254	
78	NGC 3201 V78		154.40374	–46.45109	RR0	14.85	1	0.5139	0.5137	
80	NGC 3201 V80		154.4295	–46.40467	RR0	14.8	0.59	0.5887	0.5901	* see note
83	NGC 3201 V83		154.47821	–46.36511	RR0	14.78	1.23	0.5452	0.5452	
84	ASASSN-V J101811.71-461306.4		154.54879	–46.2185	RR0	14.8	0.94	0.5137	0.5137	
98	NGC 3201 V98		154.35666	–46.42184	RR1	14.78	0.43	0.3363	0.3356	
100	NGC 3201 V100		154.40067	–46.4078	RR0	14.77	1.02	0.5485	0.5489	

** GENIE period different but light curve not cleaner.*

Bouncing against the Yellow Void—Exploring the Outbursts of ρ Cassiopeiae from Visual Observations

Grigoris Maravelias (ORCID 0000-0002-0891-7564)
IAASARS, National Observatory of Athens, GR-15236, Penteli, Greece; Institute of Astrophysics, FORTH, GR-71110, Heraklion, Greece; and Hellenic Amateur Astronomy Association, GR-10676, Athens, Greece; maravelias@noa.gr

Michaela Kraus (ORCID 0000-0002-4502-6330)
Astronomical Institute, Czech Academy of Sciences, Fričova 298, 251 65 Ondřejov, Czech Republic

Received August 26, 2021; revised December 20, 2021; accepted December 21, 2021

Abstract Massive stars are rare but of paramount importance for their immediate environment and their host galaxies. They lose mass from their birth through strong stellar winds up to the spectacular end of their lives as supernovae. The mass loss changes as they evolve and in some phases it becomes episodic or displays outburst activity. One such phase is the Yellow Hypergiant, in which they experience outbursts due to their pulsations and atmosphere instabilities. This is depicted in photometry as a decrease in their apparent magnitude. The object ρ Cassiopeiae (ρ Cas) is a bright and well known variable star that has experienced four major outbursts over the last century, with the most recent one detected in 2013. We derived the light curves from both visual and digital observations and we show that with some processing and a small correction (~0.2 mag) for the visual the two curves match. This highlights the importance of visual observations both because of the accuracy we can obtain and because they fully cover the historic activity (only the last two of the four outbursts are well covered by digital observations) with a homogeneous approach. By fitting the outburst profiles from visual observations we derive the duration of each outburst. We notice a decreasing trend in the duration, as well as shorter intervals between the outbursts. This activity indicates that ρ Cas may be preparing to pass to the next evolutionary phase.

1. Introduction

Massive stars are very rare: “for every 20 $M_\odot$ star in the Milky Way there are roughly a hundred thousand solar-type stars; for every 100 $M_\odot$ star there should be over a million solar-type stars” (Massey 2003). However, these stars have a significant impact on their immediate environment as well as their host galaxies. They lose mass through their intense stellar winds and they end their lives through spectacular supernovae. This continuous mass loss transfers energy and momentum to the interstellar medium, and it enhances it with material that has been produced in their cores as they evolve. Currently, we are not certain about exactly how a massive star evolves from a main sequence star to more evolved phases and in between them, although we have uncovered many of their properties. (There are a few groups in the world dealing with the details of stellar evolution and their results do not always agree (Martins and Palacios 2013).) The main factors that influence stellar evolution and the final stage of (single) massive stars are metallicity, rotation, and mass loss (Ekstrom *et al.* 2012; Georgy *et al.* 2013; Smith 2014). Moreover, the presence of a companion, which seems to be the rule rather than the exception in massive stars (~50–70% in binary systems; Sana *et al.* 2012, 2013; Dunstall *et al.* 2015), substantially affects the evolution though strong interaction and mass exchange. The mass loss changes with the evolutionary phase and in some cases even episodic and/or outburst activity is observed. Examples of such activity are Wolf-Rayet stars, the Luminous Blue Variables, the B[e] Supergiants, the Yellow Hypergiants (YHGs), and the Red Supergiants (RSGs). In most of these cases a complex circumstellar environment is formed, which can be observed as shells, nebulae, or disks (for example, IRC+10420; Tiffany *et al.* 2010).

As the stars evolve beyond the main sequence (ending their hydrogen burning at their cores) they move towards the right part of the Hertzsprung-Russel Diagram (HRD) to the RSGs (burning Helium at their cores). Depending on their mass, rotation, and internal mixing, they may end up as RSGs or, for stars with initial mass range of ~20–40 $M_\odot$, they can even move back again close to their initial position on the HRD, forming a “blue loop.” In those cases, there is a region in the HRD (~11000–7000 K) in which an apparent lack of sources is noticeable. This has been labelled “Yellow Void” (de Jager 1998), a temperature regime in which instabilities can occur within the highly inflated envelopes of these objects that might lead, under certain conditions, to eruptions and mass ejections leading to circumstellar shells or envelopes. During such an outburst the released material obscures the hot atmosphere of the star, which looks fainter and cooler in total. This process may repeat many times up to the point that the largest fraction of the atmosphere is lost and the star is found in a hotter and more stable phase. Then it has passed through the Yellow Void and it appears on the other side as a blue supergiant (Aret *et al.* 2017; Davies *et al.* 2007).

One such star is ρ Cassiopeiae (ρ Cas; (J2000.0) R.A. 23^h 54^m 23.03^s, Dec. +57° 29' 57.8"), which is a very bright star (V ~ 4.6 mag) easily spotted in the constellation Cassiopeia. It is a variable star with a modulation determined by multiple long periods (Percy *et al.* 2000) and it has exhibited four outbursts, with magnitude drops over 1 magnitude in 1945–1947 and 2000–2001, and ~0.6 magnitude in 1985–1986 and 2013–2014 (see Kraus *et al.* 2019 and Lobel *et al.* 2003 for an overview).

In Kraus *et al.* (2019) the light curve of CCD photometry obtained from a single observer covering the whole outburst and additional data from the Bright Star Monitor of the American Association of Variable Star Observers (AAVSO) was used in correlation with spectroscopic observations. In this work, we extend the photometric analysis by using all available digital data, as well as visual observations, which could be found in the AAVSO International Database for the particular outburst. In addition, we explore the whole light curve (from both visual and digital as obtained from a variety of techniques) to study the outburst activity in total.

Such an investigation requires the longest light curves possible (century long). Ideally these would consist of excellent quality data obtained with the same instrumentation and observing strategy. However, technology changes significantly over this time span and calibration of the different techniques is mandatory to derive robust conclusions. Therefore, we examine the visual observations (that provide the largest coverage) and compare them to the digital ones.

2. Data collection and analysis

We used observations spanning the activity between (March) 1941 and (June) 2021, splitting them into two sets: (a) visual observations (magnitude estimates using naked eye or visually using binoculars or small telescope); (b) digital observations. The second set is a collection from various instrumentation (photoelectric photometers, CCD and DSLR cameras), all of which have been reported to the standard Johnson V filter. In general, there can be systematic differences between the various techniques and between observers. However, in the current approach we selected the best observations (marked as non-discrepant by the AAVSO) which simplifies the analysis, as we avoid dealing with these systematics. We also used digital observations retrieved from Leiker and Hoff (1987) and Zsoldos and Percy (1991) for reasons that will become clear later on.

In the visual approach observers are using standard charts (i.e. selected comparison stars) that help to reduce systematic differences. However, even in this case the magnitude estimate is based on the perception ability of each individual. Therefore, there is a significant spread of the reported values even for the same epochs (nights). However, with some proper statistical treatment we can obtain a more accurate result. To address that and in order to exclude any short-term variability, we smoothed all data by using a moving average with a window of 30 days (the number was derived by visual inspection of the resulting light curves). Then we grouped the smoothed data into 20-day bins (a typical required frequency of visual observations for long period variables), from which we derive a mean value and its corresponding standard deviation. Finally, we kept only those observations within one standard deviation from the mean value. Starting from 53,560 visual observations—from 772 unique observers (We removed eleven observations with upper limits, i.e. values indicated with the "<" symbol as "fainter than.")—we kept 34,604 (~65%). Using those we re-estimate the mean values and the standard deviations (as errors) at each 20-day bin (1,448 points in total). From these data we obtain the (green) light curve, as shown in Figure 1, where individual visual observations are shown as gray points (the green shaded area corresponds to the 1σ error). This includes all visual observations in the last 80 years, from 03 March 1941, to 01 June 2021 (there are about 20 observations omitted before and after these dates).

In Kraus *et al.* (2019) measurements from the AAVSO's Bright Star Monitor (https://www.aavso.org/bright-star-monitor-section) (514 observations) and from one specific observer (W. Vollmann; AAVSO code VOL; 243 points), who covered the whole 2013 outburst, were used. In this work, we expanded the coverage of the 2013 outburst with more observations. We also considered all available observations around the outbursts (except for the 1946 outburst, for which this technology was simply not available) and up to June 2021. In order to improve the coverage of the 1986 outburst the AAVSO data were supplemented by 67 and 83 observations by Leiker and Hoff (1987) and Zsoldos and Percy (1991), respectively. (There are a few more digital observations since the 1960s and prior to this outburst (for example, Brodskaya (1966); Landolt (1973); and Arellano Ferro (1985), but since these data only sample dates outside the outburst, we refrained from adding them into the current work.)

Even though they originate from different systems and sensors, the reported magnitudes are given in the standard photometric V filter, providing us with a relatively homogeneous sample. The digital set consists of 2,208 measurements in total (2,058 from 59 AAVSO unique observers, and 150 from the two papers). A fraction of these data (~10%, 222 observations) do not include an error measurement. To estimate it we used a mean error derived from the rest of the 1986 observations using two approaches: (a) a simple average value at 0.014 mag; (b) a median value at 0.006 mag. Although the latter is a reasonable error routinely reported in such observations (especially in the more recent CCD and DSLR observations) we opted to use the former value, which is a more conservative approach. The digital observations with their corresponding errors are shown as black x-points in Figure 1.

3. Results and discussion

3.1. Visual vs. digital observations

In Panel A of Figure 1 we present the independently extracted light curves from visual (with a –0.2-magnitude offset) and digital observations. We highlight the four major outbursts that the star has experienced over the last century (henceforth indicated as 1946, 1986, 2000, and 2013).

A small offset in the visual light curve is necessary in order for the visual light curve better to match the digital one. Then, they become almost identical as is better shown in the zoom in Panel B of Figure 1, where we focus on the last two outbursts, 2000 and 2013 (and where the visual and digital coverage maximizes). This is consistent with the offset of 0.3 magnitude found by Percy *et al.* (1985). (They define this offset as the conversion factor between the visual band and the photometric V filter the parameter: $e = (V–Vis) / \Delta(B–V) \sim 0.25$ mag, where $\Delta(B–V)$ is the difference of the color index for ρ Cas $(B–V = 1.3)$ with the average color index of comparison/reference stars $(B–V = 0.1.)$ In our case and due to the pre-processing of the visual observations a slightly smaller offset is enough to match the two curves. Although for the most part the two curves are identical, there are some small noteworthy differences:

1. Although supplementing the dataset with more digital observations for the 1986 outburst, we notice that the minimum is still not properly sampled. However, there is a fairly good agreement between digital and visual observations during the recovering phase, with the former pointing to a brighter magnitude than the latter (visual observations have been smoothed, so digital ones are more sensitive to the cyclic behavior).

2. There is a difference in the minimum values of the 2000 outburst (mJD ~ 21775—where mJD corresponds to the day from the initial x-axis coordinate set at JD −2430057) and of the 2013 event (mJD ~ 26550).

3. Digital observations appear fainter than the visual ones at mJD ~ 22800 and ~23200 with offsets of ~0.3 mag, and at mJD ~24736 and ~24976 with offset of ~0.1 mag.

4. Visual observations appear fainter than the digital ones at mJD ~ 26100 with an offset of ~0.1 mag.

5. There is a mismatch between mJD ~ 26640–27200. It is possible that these differences, and especially those at the minima, may be attributed to color changes of ρ Cas that are perceived differently between the visual observers (which see all the visual spectrum) and the digital sensors equipped with the photometric filters. Further investigation of the reasons behind this requires a complete set of multi-color observations at these epochs which is not easily available and it is beyond the scope of this paper (an opacity imposed effect based on a gradient in the temperature is discussed in van Genderen *et al.* (2019)).

In general, we can conclude that even though the visual approach may seem (and it is) simplistic, when enough data are available they can provide accurate results, almost identical to the ones obtained by digital means, which are more precise but at the expense of more complicated procedures.

3.2. Cyclic and outburst activity

Even from a visual inspection of the light curves in Figure 1 we can easily spot the cyclic activity of ρ Cas outside the outbursts. These periods are of the order of a few hundred days (~300 d, ~500 d, and ~800 d; (Percy *et al.* 2000)). In Panel C of Figure 1 we show a zoom-in of the light curve centered around the 2013 outburst, where we highlight the aforementioned periods. The magnitude drops as measured from the visual and the digital curve are ~0.4 mag and ~0.6 mag, respectively, with an averaged value of 0.5 mag. The profile of the outburst is characterized by a sudden drop in the magnitude (due to the intense release of the material) and a gradual return to the normal state (as the material expands further).

As the 2013 outburst was the fourth one recorded in the history of ρ Cas and came a few years after the 2000 one, we were motivated to explore the outburst activity with time. For this we opted to use only the visual observations for the following reasons: (a) good match between the visual and digital observations; (b) there are no digital observations for the 1946 and 1986 outbursts, while different equipment for digital observations has been used over the years; (c) they provide a homogeneous approach as the method has not changed over the years.

For each outburst we first determined a baseline magnitude derived by taking the median from (smoothed) observations about 1,000 days before the start and after the end of each outburst (start/end dates were determined visually). Then, for each outburst profile we plot the difference of the smoothed values with the baseline magnitude (see Figure 2), in order to bring all profiles to the same scale and to erase a possible long-term variability of several thousand days that seems to be present (see Panel A of Figure 1). However, with this approach we do not remove the cyclic behavior. Obviously, during phases of quiescence the star undergoes cyclic expansion and contraction of its envelope, which sometimes ends up in an outburst. Due to the high luminosity over mass ratio of ρ Cas it is plausible that these outbursts could be triggered by pulsational, so-called strange mode, instabilities excited in the extended tenuous envelope. (A current theoretical investigation for the stellar parameters of ρ Cas confirms the occurrence of very strong strange mode instabilities in this object (Glatzel *et al.* in preparation).) After the outburst, the star needs to settle to a new equilibrium state before starting the next variability cycle, which can have a different length than the one prior to the outburst. But while the outbursts happen during a phase of expansion, hence dimming, the outburst itself cannot be considered as being part of an underlying pulsation cycle. Therefore, it is not reasonable to subtract a strict pulsation variability from the light curve underneath the outburst, and we opted for the simplest approach of fitting a Gaussian function to the observed profiles.

For the fitting process we changed the window of the smoothing to 15 days, as this provides more points for fitting without affecting the end result much. The free parameters were the amplitude, the standard deviation (σ), and the mean that corresponds to the minimum date of the outburst. In Figure 2 we show the final fits obtained for each outburst while in Table 1 we present the derived parameters, along with their corresponding goodness-of-fit as defined from the $\chi^2_{\rm red}$. We approximated the total duration for each outburst by taking the Full Width at 10% of the Maximum (FWTM), calculated as $\mathrm{FWTM} = 4.29193 \times \sigma$.

The values of $\chi^2_{\rm red}$ are not optimal for two reasons: (a) a Gaussian profile is not the most appropriate model as the outbursts are not symmetrical; (b) the errors related to the observations are probably overestimated (since they correspond to the spread of the visual estimates). Although their mean values can track the true activity of the star the large spread leads to significant errors that propagate through the fitting to the final estimates of each outburst duration.

Nevertheless, the actual derived numbers for the duration and the amplitudes are consistent with the values from previous works. For the 2000 and 2013 outbursts, durations of ~477 d and ~300 d, and amplitudes of ~1 mag and ~0.55 mag, are quoted by Lobel *et al.* (2003) and Kraus *et al.* (2019). It is also worth noting that the depth of the 2013 outburst is the shallowest of all, which results simultaneously in the highest uncertainties. Concurrently, the 1946 outburst is the longest and deepest outburst observed so far.

In Figure 3 we plot the duration of each outburst (dots) with time. What is evident from this plot is that the outbursts seem to become shorter with time. This decreasing trend is also shown

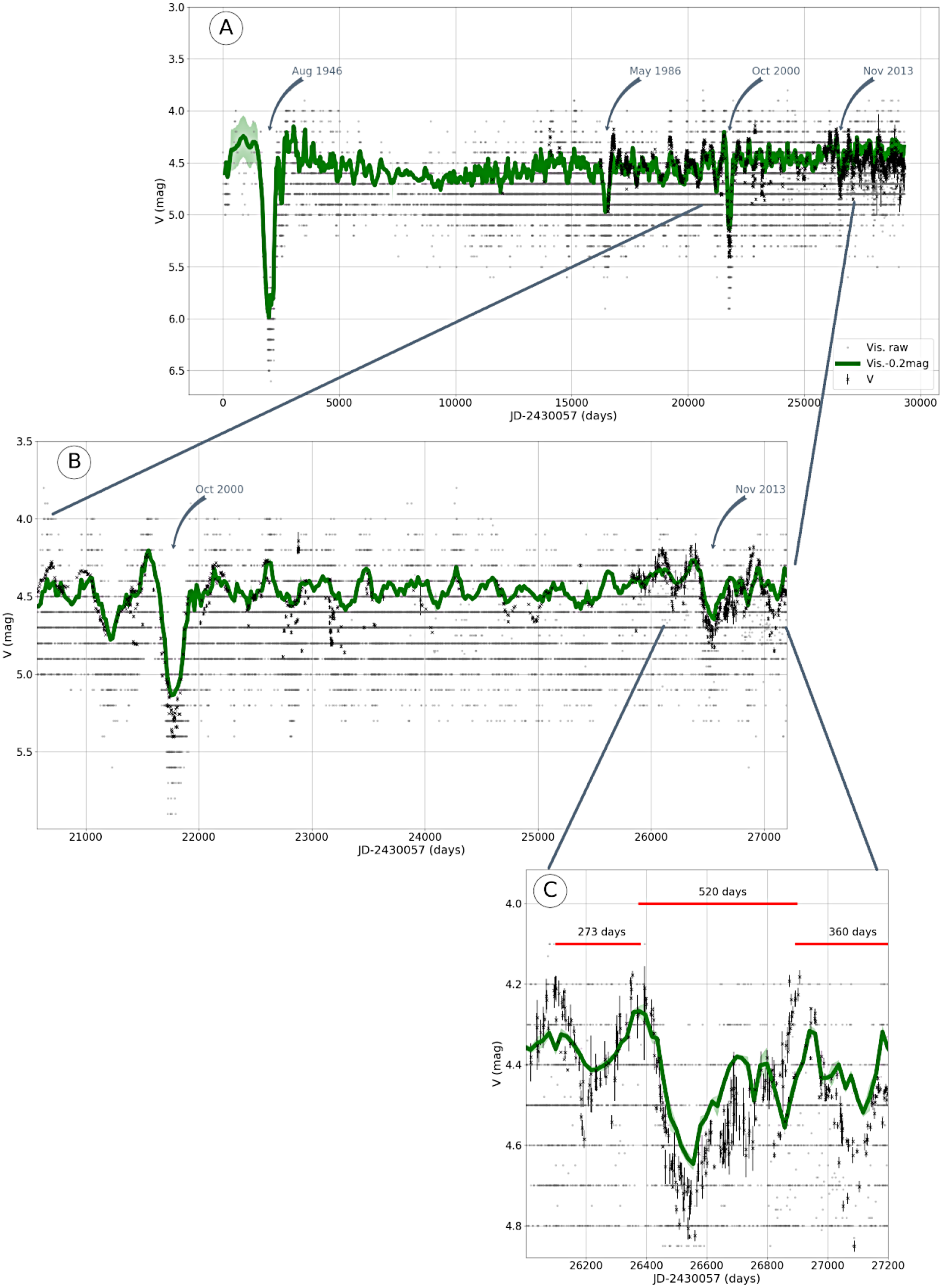

Figure 1. Panel A: The light curve of ρ Cas for the period 1941–2021 (x-axis in Julian Dates – 2430057, corresponding to the initial date). The green line corresponds to the (processed) visual observations (with raw observations shown as gray points) and the shaded area to the 1σ error, while digital observations are shown as black dots. After a minor correction of –0.2 mag for the visual light curve the shape of the two curves is almost identical. Panel B: Zoom-in of the two major outbursts in November 2000 and 2013. Panel C: Zoom-in of the 2013 outburst with various periods (of ~300–800 days; (Percy *et al.* 2000) highlighted (see section 2 for more details).

Table 1. Outburst properties and statistics.

Outburst Label	*Amplitude (mag)*	σ *(days)*	*JD of Minimum (days)*	*Date of Minimum (DD/MM/YYYY)*	*d.o.f.**	χ^2_{red}	*Duration (days)*
1946	1.69 ± 0.27	187 ± 36	2432048 ± 35	15/08/1946	53	1.37	800 ± 154
1986	0.42 ± 0.36	102 ± 99	2446539 ± 98	18/04/1986	36	0.06	437 ± 426
2000	0.71 ± 0.45	63 ± 45	2451840 ± 46	22/10/2000	38	0.26	270 ± 196
2013	0.29 ± 0.50	50 ± 118	2456603 ± 118	7/11/2013	21	0.13	214 ± 509

**d.o.f. is the number of smoothed magnitude values per outburst minus the three free parameters.*

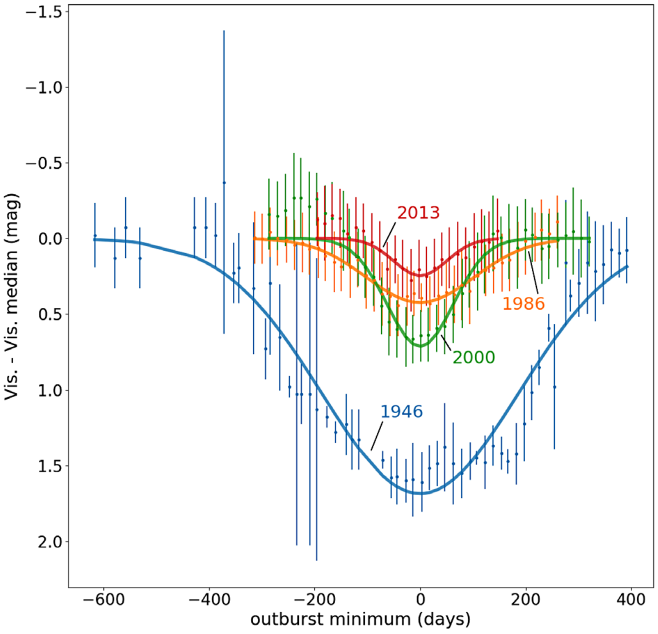

Figure 2. Gaussian fits (lines) of the four outbursts of ρ Cas. The points and the errors correspond to the moving-average processing of the visual observations for each outburst. All outbursts have been centered on their date of minimum (as identified from the fitting process) so that the x-axis refers to days from outburst minimum. The magnitudes have been normalized with respect to median Vis. magnitude derived from about 1,000 days before the start and after the end of each outburst.

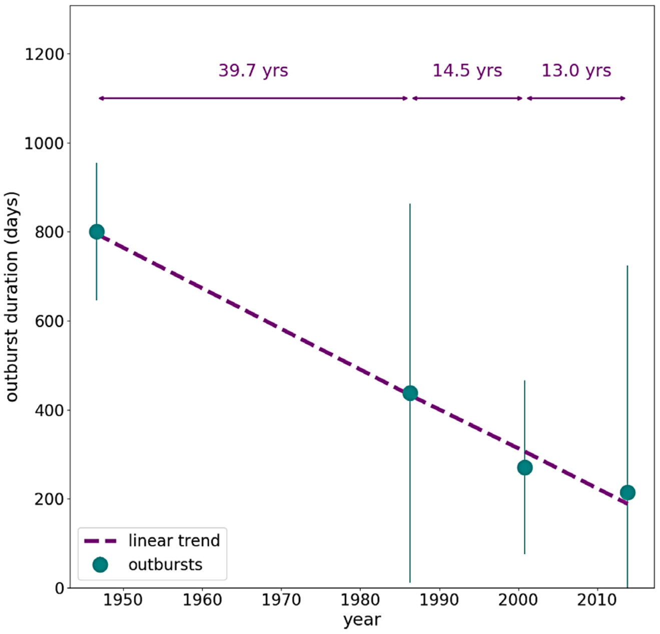

Figure 3. The duration of each outburst (dots) with time (using the minimum dates as identified from the fitting process). There is a trend of shorter outbursts with time (linear model indicated with the violet dashed line). They also seem to occur more frequently, as it is indicated by the time difference between the outbursts (violet arrows).

with a simple linear fit model (violet dashed line). The slope from this model suggests a shortening trend of approximately –10 days/year. Simultaneously, there is a, relatively, increase in the frequency of these outbursts that occurred at about 40, 15, and 13 years. It seems as if ρ Cas is actively "hitting" against the Yellow Void, and possibly preparing to pass through (Lobel *et al.* 2003; Aret *et al.* 2017). Although the trend is definitely true some caution should be used with respect to potential extrapolations, based on the model limitations described previously.

As of the moment of writing this article, there is no indication of another outburst yet. We are "only" eight years since the last outburst, therefore it is more than interesting to keep monitoring the activity of ρ Cas in order to catch another one in the (possible) near future. (Such a campaign has been initiated by Ernst Pollmann, see *AAVSO Alert Notice 746* (Waagen 2021).)

4. Summary

ρ Cas is one of the brightest and most easily spotted Yellow Hypergiants, with a large set of observations dating back almost a century. Its having experienced four major outbursts with the latest one in 2013, only 13 years after the 2000 one, we were motivated to investigate the outburst activity. Only visual observations completely cover the first two outbursts (1946 and 1986). After some processing of the raw visual observations we show that they are a good match (with a small offset of ~0.2 mag) to the digital ones (as shown for the 2000 and 2013 outbursts). Given this result we fit the visual curves for all outbursts to derive their durations and amplitudes. The result is a decreasing trend in duration, i.e. the outbursts become shorter and more frequent. This behavior strengthens the argument that ρ Cas is bouncing against the Yellow Void and it is probably preparing to pass through it and transit to a new phase (such as a B[e] supergiant).

5. Acknowledgements

GM acknowledges funding support from the European Research Council (ERC) under the European Union's Horizon 2020 research and innovation program (Grant agreement No. 772086), and MK from the Czech Science Foundation (GAČR 20-00150S). The Astronomical Institute Ondřejov is supported by the project RVO:67985815. We thank Alceste Bonanos for providing feedback on the manuscript. We acknowledge with thanks the variable star observations from the AAVSO International Database contributed by observers worldwide and used in this research. This research has made use of NASA's Astrophysics Data System.

Facility: AAVSO

Software: NumPy (Harris *et al.* 2020), Matplotlib (Hunter 2007), Astropy (Astropy Collaboration *et al*. 2013).

References

Arellano Ferro, A. 1985, *Mon. Not. Roy. Astron. Soc.*, **216**, 571 (DOI: 10.1093/mnras/216.3.571).

Aret, A., Kraus, M., Kolka, I., and Maravelias, G. 2017, in *Stars: From Collapse to Collapse*, eds. Y. Y. Balega, D. O. Kudryavtsev, I. I. Romanyuk, I. A. Yakunin, ASP Conf. Ser 510 (https://arxiv.org/abs/1611.06044), Astronomical Society of the Pacific, San Francisco, 162.

Astropy Collaboration, *et al.* 2013, *Astron. Astrophys.*, **558A**, 33 (DOI: 10.1051/0004-6361/201322068).

Brodskaya, É. S. 1966, *Soviet Ast.*, **10**, 186.

Davies, B., Oudmaijer, R. D., and Sahu, K. C. 2007, *Astrophys. J.*, **671**, 2059 (DOI: 10.1086/523692).

de Jager, C. 1998, *Astron. Astrophys. Rev.*, **8**, 145 (DOI: 10.1007/s001590050009).

Dunstall, P. R., *et al.* 2015, *Astron. Astrophys.*, **580A**, 93 (DOI: 10.1051/0004-6361/201526192).

Ekström, S., *et al.* 2012, *Astron. Astrophys.*, **537A**, 146 (DOI: 10.1051/0004-6361/201117751).

Georgy, C., Ekström, S., Granada, A., Meynet, G., Mowlavi, N., Eggenberger, P., and Maeder, A. 2013, *Astron. Astrophys.*, **553A**, 24 (DOI: 10.1051/0004-6361/201220558).

Harris, C. R., *et al.* 2020, *Nature*, **585**, 357 (DOI: 10.1038/s41586-020-2649-2).

Hunter, J. D. 2007, *Comput. Sci. Eng.*, **9**, 90.

Kraus, M., Kolka, I., Aret, A., Nickeler, D. H., Maravelias, G., Eenmäe, T., Lobel, A., and Klochkova, V. G. 2019, *Mon. Not. Roy. Astron. Soc.*, **483**, 3792 (DOI: 10.1093/mnras/sty3375).

Landolt, A. U. 1973, *Publ. Astron. Soc. Pacific*, **85**, 606 (DOI: 10.1086/129512).

Leiker, P. S., and Hoff, D. B. 1987, *Inf. Bull. Var. Stars*, 3020, 1.

Lobel, A., *et al.* 2003, *Astrophys. J.*, **583**, 923 (DOI: 10.1086/345503).

Martins, F., and Palacios, A. 2013, *Astron. Astrophys.*, **560A**, 16 (DOI: 10.1051/0004-6361/201322480).

Massey, P. 2003, *Annu. Rev. Astron. Astrophys.*, **41**, 15 (DOI: 10.1146/annurev.astro.41.071601.170033).

Percy, J. R., Fabro, V. A., and Keith, D. W. 1985, *J. Amer. Assoc. Var. Star Obs.*, **14**, 1.

Percy, J. R., Kolin, D. L., and Henry, G. W. 2000, *Publ. Astron. Soc. Pacific*, **112**, 363 (DOI: 10.1086/316541).

Sana, H., *et al.* 2012, *Science*, **337**, 444 (DOI: 10.1126/science.1223344).

Sana, H., *et al.* 2013, *Astron. Astrophys.*, **550A**, 107 (DOI: 10.1051/0004-6361/201219621).

Smith, N. 2014, *Annu. Rev. Astron. Astrophys.*, **52**, 487 (DOI: 10.1146/annurev-astro-081913-040025).

Tiffany, C., Humphreys, R. M., Jones, T. J., and Davidson, K. 2010, *Astron. J.*, **140**, 339 (DOI: 10.1088/0004-6256/140/2/339).

van Genderen, A. M., Lobel, A., Nieuwenhuijzen, H., Henry, G. W., de Jager, C., Blown, E., Di Scala, G., and van Ballegoij, E. J. 2019, *Astron. Astrophys.*, **631A**, 48 (DOI: 10.1051/0004-6361/201834358).

Waagen, E. O. 2021, *AAVSO Alert Notice 746* (June 18; (https://www.aavso.org/aavso-alert-notice-746).

Zsoldos, E., and Percy, J. R. 1991, *Astron. Astrophys.*, **246**, 441.

BViz Photometry of the RR Lyrae Star RU Ceti

Jadon Fickle
Michael L. Allen (ORCID 0000-0002-6047-3315)
Department of Physics and Astronomy, Washington State University, Pullman, WA 99164-2814;
jadon.fickle@wsu.edu; mlfa@wsu.edu

Received September 1, 2021; revised April 14, 2022; accepted April 19, 2022

Abstract The RR Lyrae star RU Cet was observed between October 26 and November 23, 2020. The observations were taken in the B, V, ip, and zs filters, with the telescope images being analyzed using various aperture photometry methods. The period of variation for RU Cet was found to be 0.585 ± 0.020 day. Theoretical period-luminosity-metallicity relations in the V, ip, and zs filters were used to compute the distance. These distances were 1641 ± 77 parsecs in the V filter, 1621 ± 58 parsecs in the ip filter, and 1645 ± 48 parsecs in the zs filter, for a weighted average of 1636 ± 33 parsecs. The Gaia EDR3 value is 1699 +83 / –75 parsecs. The photometric distances are consistent with the parallax determination despite peculiar variations in RU Cet's light curve.

1. Introduction

This research was undertaken as part of OurSolarSiblings' (OSS) education effort to make observational astronomical research more straightforward for students and teachers via a collaboration led by Michael Fitzgerald (Fitzgerald 2018). One goal of this ongoing effort was to use observations to test the theoretical RR Lyrae period-luminosity (PL) relationship in the infrared ip and zs filters given by Cáceres and Catelan (2008) and in the Johnson V filter given by Cáceres and Catelan (2008). We compare against parallax measurements.

RR Lyrae stars are fundamental mode pulsating stars that belong to the horizontal branch. They are often used as standard candles to determine distances within the Milky Way, due to the period-luminosity relations. Empirically derived PL, and period-luminosity-metallicity (PLZ), relations exist for many colors, e.g., Neeley *et al.* (2019), and Cusano *et al.* (2021). These relations exhibit some scatter, thus limiting their precision when used as standard candles, especially for field stars. The RR Lyrae-type star covered in this paper is RU Cet.

RU Cet (Figure 1) is classified as an RRab type variable star in the AAVSO Variable Star Index (Watson *et al.* 2006). This can be seen in the nature of the light curve itself, presented in section 3, as RRab light curves are consistently defined by a quick rise to maximum light followed by a gradual decline.

One of the earlier reports of a potential Blazhko effect comes from Kovacs (2005). RU Cet was reported as a RRab star with "weak" Blazhko effects. Kolenberg *et al.* performed work to determine the Blazhko period of RU Cet (Kolenberg *et al.* 2008). Both of these papers made use of the All Sky Automated Survey (ASAS) database in order to have data over a long enough range of time to test for the presence of a Blazhko effect and thus a Blazhko period. In the present study, data were not taken over a wide enough range of time to consider the Blazhko nature of this star.

We will cover how we set up our observations of RU Cet, and discuss what happened to the observations before we received them (section 2) via the data pipelines set up by Las Cumbres Observatory (LCO) and OurSolarSiblings (OSS). Then, we will discuss how we analyzed the observations to

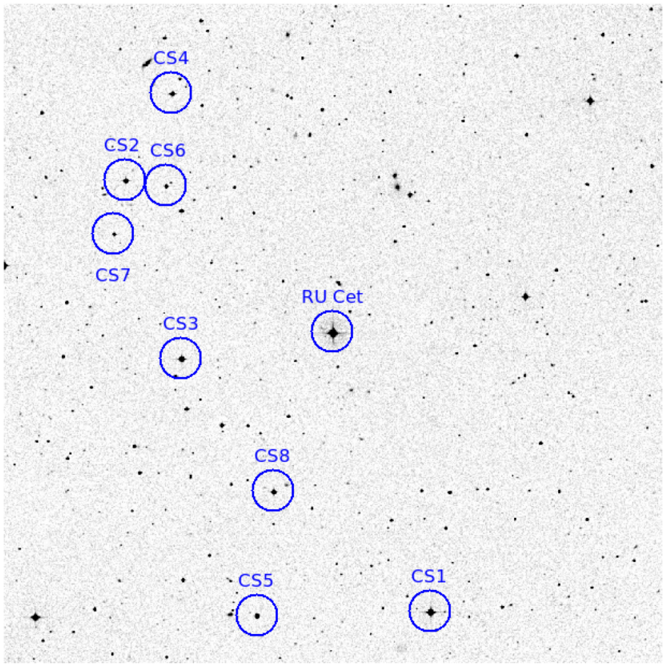

Figure 1. Inverted starfield of observation for RU Cet. Eight comparison stars were used in the data analysis. The image is 25 × 25 arcminutes. North is up and east is to the left. Image is from the DSS and processed using SAOImageDS9.

Table 1. Basic properties of RU Cet.

Property	*Value*	*Reference*
R.A. (J2000)	15.16803563°	Bailer-Jones *et al.* (2021) (Gaia EDR3)
Dec. (J2000)	-15.95777516°	Bailer-Jones *et al.* (2021)
Sp type	kA3p	Graham and Slettebak (1973)
Variable type	RRab	Watson *et al.* (2006) (VSX)
Distance	1699 + 83 / –75 parsecs	Bailer-Jones *et al.* (2021)
[Fe/H]	–1.33	Kovacs (2005)
	–1.39	Sandage (1993)
	–1.51	Preston et al. (1991)
	–1.6	Chiba and Yoshii (1998)
	–1.6	Layden (1994)
	–1.6	Layden *et al.* (1996)
	–1.66	Feast *et al.* (2008)

determine information about RU Cet (section 3), specifically its period and distance from Earth.

2. Observations

RU Cet was observed between October 26 and November 23, 2020. The star was observed in the Johnson-Cousins B and V (e.g., Bessel 1993), SDSS ip (Fukugita *et al.* 1996), and Pan-STARRS zs (Tonry *et al.* 2012) filters with the Las Cumbres Observatory network of robotic telescopes. The LCO comprises several 2-meter, 1-meter, and 0.4-meter aperture telescopes. Table 2 lists the location and number of observations captured at each location of RU Cet.

All of the observations of RU Cet were performed using the 0.4-meter series of telescopes. Each was equipped with a SBIG STL-6303 CCD camera of format 3k × 2k pixels, with a pixel size of 0.571 arcsec and a field of view of 29.2 × 19.5 arcmin. Observation cadence was approximately once every four hours, weather permitting. Accounting for poor weather and observation windows expiring, a total of 79 observations of RU Cet were recovered.

Integration times were chosen to achieve a signal-to-noise (S/N) of about 300 on the target star. This is the equivalent of about 100,000 photons integrated. This photon count is where the CCD camera is responding linearly to photon flux and well below the saturation limit. This can be considered the "sweet spot" of the detector, where the noise in the image is attenuated by the true counts from the source, but the image is not overexposed. These integration times were computed to be 100 seconds in B, 41 seconds in V, 39 seconds in ip, and 144 seconds in zs. All images recovered were usable.

Table 2. Telescope locations and number of observations performed by each telescope.

Telescope Location	*LCO Telescope Label*	*Number of Observations*
SAAO, Sutherland, South Aftica	kb84	32
CTIO, Region IV, Chile	kb26	12
Haleakala Observatory, Maui, USA	kb82	11
Siding Spring Observatory, NSW, Australia	kb56	7
Siding Spring Observatory, NSW, Australia	kb24	7
CTIO, Region IV, Chile	kb29	6
Haleakala Observatory, Maui, USA	kb27	2
McDonald Observatory, Texas, USA	kb92	1
Teide Observatory, Tenerife, Spain	kb98	1

Note: CTIO—Cerro Tololo Inter-American Observatory; SAAO—South African Astronomical Observatory.

The LCO's BANZAI data pipeline (Brown *et al.* 2013) took the raw images from the telescope and corrected them using flat, bias, and dark images that were taken nightly. Reduction to the magnitude system was then performed automatically by the OurSolarSiblings (OSS) data pipeline (Fitzgerald 2018). This pipeline performs many functions, but the ones that were immediately relevant to this paper were as follows: the pipeline performed photometric calculations on the images through six different methods. These were the Source Extractor Aperture (SEX) and Source Extractor Kron (SEK) (Bertin and Arnouts 1996), Aperture Photometry Tool (APT) (Laher *et al.* 2012a, 2012b), Dominion Astrophysical Observatory Photometry (DAO) (Stetson 1987), DoPHOT (DOP) (Schechter *et al.* 1993; Alonso-Garciá *et al.* 2012), and PSFEx (PSX) (Bertin 2011). The results of these methods were then organized into photometry catalogue files comparing the R.A. and Dec. with the x-y pixel location and the number of counts detected at that location and its error.

The next step was to search the image for potential comparison stars using various catalogues. These catalogues were: APASS DR1 for the B and V filters (Henden *et al.* 2009, 2016)), Skymapper 1.1 for the ip filter (Wolf *et al.* 2018), and Pan-STARRS DR1 for the zs filter (Magnier *et al.* 2020; Flewelling *et al.* 2020). Calibration stars were chosen by the ASTROSOURCE package (Fitzgerald *et al.* 2021). ASTROSOURCE is a tool designed to interpret the output of the OSS pipeline. It first determines comparison stars of a sufficient signal-to-noise ratio across the whole data set for a specific filter. It then analyzes these potential stars to determine which have the least variable magnitudes across the data set. Using the stars with known magnitudes, listed in Table 3, ASTROSOURCE calibrates the stars that fulfil the above criteria to determine their magnitudes. These are then used to produce a differential magnitude light curve for the observed variable star, RU Cet.

The full list of calibration stars and their locations is given in Table 3. For this paper the light curve produced by the SEK method was chosen because it produced the light curve with the lowest amount of scatter to the eye. The SEK method has been used by many using the LCO telescopes to research RR Lyrae stars through the OurSolarSiblings RR Lyrae research course (Fitzgerald 2021). The SEK method can determine the apparent

Table 3. List of calibrator stars and calibrated magnitudes from the surveys listed in the text.

Calibration Star	*R.A. (degrees)*	*Dec. (degrees)*	*Filters*	*B Magnitude*	*V Magnitude*	*ip Magnitude*	*zs Magnitude*
CS1	15.1034613	–16.134187	B	12.465 ± 0.02	—	—	—
CS2	15.3044044	–15.861488	B, V, ip, zs	14.268 ± 0.03	13.631 ± 0.01	13.276 ± 0.006	12.2732 ± 0.0065
CS3	15.267423	–15.9739347	B, V, ip	13.518 ± 0.018	12.97 ± 0.019	12.681 ± 0.09	—
CS4	15.2740296	–15.8059527	B, V, ip	14.322 ± 0.02	13.459 ± 0.019	12.874 ± 0.004	—
CS5	15.2180487	–16.1363677	B, V, ip	14.241 ± 0.027	13.612 ± 0.034	13.295 ± 0.003	—
CS6	15.2773297	–15.8654621	ip, zs	—	—	13.243 ± 0.003	13.0735 ± 0099
CS7	15.3122939	–15.8950456	ip	—	—	14.181 ± 0.005	—
CS8	15.2069684	–16.0582662	V	—	13.471 ± 0.009	—	—

Note: R.A. and Dec. are provided in ICRS degree format. CS1 is also identified as TYC 5848-2346-1.

Table 4. Results derived in this work.

Measurement	*Units*	*Filter*			
		B	*V*	*ip*	*zs*
Average magnitude	Magnitude	12.006 ± 0.002	11.690 ± 0.001	11.535 ± 0.002	11.583 ± 0.002
Pstring	Days	0.588 ± 0.016	0.586 ± 0.025	0.588 ± 0.023	0.584 ± 0.0295
PPDM	Days	0.586 ± 0.015	0.585 ± 0.019	0.584 ± 0.014	0.584 ± 0.019
Magnitude range	Magnitude	1.413208	1.05476277	0.8153254	0.70325996

Note: Average magnitude is the error-weighted average apparent magnitude. Magnitude range is the difference between the data minimum and maximum magnitudes. P stands for period. String refers to the string length minimization method and PDM refers to the phase dispersion method.

magnitude of stars and galaxies with consistency (Bertin and Arnouts 1996). Accurately determining the magnitude of our observed star and comparison stars is important to determining the distance to our star, and will be elaborated further in section 3. In total, the following numbers of measurements of magnitude were recovered in the SEK method from the images: 33 in the B filter, 34 in the V filter, 35 in the ip filter, and 32 in the zs filter.

3. Results

In this section we first discuss the derivation of the period, average apparent magnitude, and metallicity of RU Cet. These quantities are then applied to compute the distance to the star. We consider first the derivation of the period.

Period finding and light curves were produced by ASTROSOURCE. Two methods of period finding are implemented, being the string length minimization method (Dworetsky 1983) and the phase dispersion method (Stellingwerf 1978). These are both standard methods, having the advantage that they are model-independent. No assumption is made of the form of the underlying function, only that there is a repeating signal, in this case a period. Altunin *et al.* (2020) developed a method to automate these processes across data sets, and this method is incorporated into the ASTROSOURCE program. We report the period averaged from eight derived periods. We present folded light curves (Figures 2–5) only for periods derived from the PDM method for each filter.

We next address the question of whether the light curve is adequately sampled to derive a convincing distance estimate. Our light curves are not sampled as densely as we would have wished, due in part to the steep rise of RU Cet. Notably, a single datum defines the brightest magnitude. The data set is complete enough for our purpose, as demonstrated in the next three paragraphs where we compare our periods and magnitudes with those from other studies.

The period of RU Cet was determined through averaging the eight period values presented in Table 4. This was an unweighted average. The result, 0.585 ± 0.020 day, is in good agreement with those of other authors. Two examples: from the All Sky Automated Survey (ASAS) Szczygiel *et al.* (2009) derive a period of 0.5862844 d, and from the Catalina Sky Survey (CSS) Drake *et al.* (2013) derive a period of 0.5862768 d.

The average apparent magnitude, from which our distances are determined, was determined for each filter as an error-weighted average of measured magnitudes, m_j,

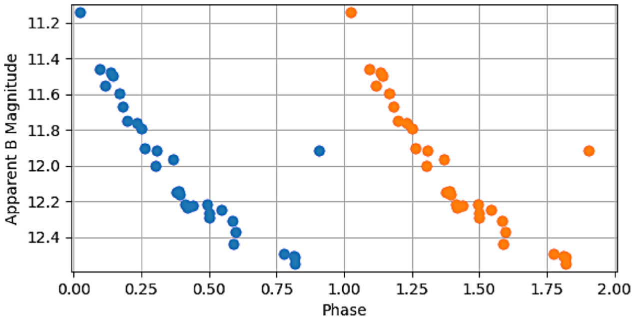

Figure 2. Folded lightcurve in the B filter with the PDM method applied.

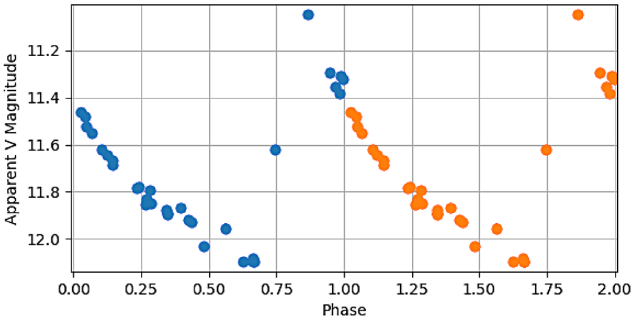

Figure 3. Folded lightcurve in the V filter with the PDM method applied.

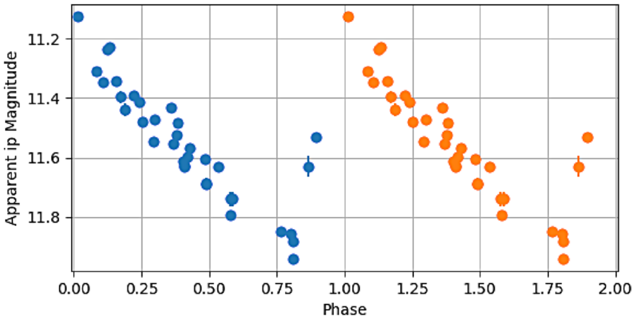

Figure 4. Folded lightcurve in the ip filter with the PDM method applied.

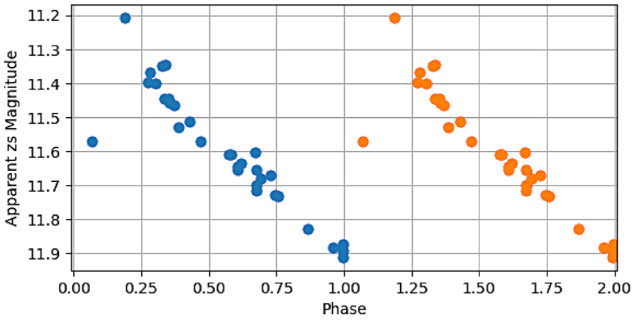

Figure 5. Folded lightcurve in the zs filter with the PDM method applied.

$$\text{Average magnitude} = \frac{\Sigma \, m_j / \sigma_j^2}{\Sigma \, 1 / \sigma_j^2} \tag{1}$$

In the V-band, we observed a magnitude range of 11.045–12.099, an average magnitude of 11.690 ± 0.001, and an amplitude of 0.527. As a check on our weighted average we also computed an average magnitude by integrating the phased light curves. We used the trapezoid rule. The trapezoid averages were statistically indistinguishable from the weighted averages. Our average magnitude values correspond well with those of other authors. For example, citing again the ASAS analysis, Szczygiel *et al.* (2009) list a magnitude range of 11.101–12.034, an average magnitude of 11.689, and an amplitude of 0.465 mag. Our average V-magnitude is statistically identical to that of ASAS. We use the average apparent magnitude to determine a photometric distance.

RU Cet exhibits variations in both magnitude range and period. Variations in period are best-studied. The Groupe Europeen d'Observations Stellaires (GEOS) RR Lyrae database (Le Borgne *et al.* 2007) maintains a list of times of maxima of a large group of RR Lyrae field stars, including RU Cet. The most recent ephemeris for this star was published by Vandenbroere *et al.* (2014). They reported a period derived from observations of 97 maxima between 1890 and 2012, being 0.58628706 with a standard deviation of 0.1787 day. The brightest points recorded on our light curves were collected near JD 2459153.87; the GEOS database records a maximum near JD 2459153.84. Our observation is about 40 minutes after maximum, or about 5% of the period. The true brightest magnitude could be a tenth of a magnitude brighter than our observed value in V, a few hundredths of a magnitude in the infrared filters. This error then would be the largest error in our analysis.

We consider here the question of metallicity. Measured [Fe/H] values are summarized in Table 1. We adopted a value for [Fe/H] of –1.5 ± 0.2, a midpoint between the lowest and highest values from the literature. This quantity is converted to a metals/hydrogen ratio [M/H] via (Salaris *et al.* 1993):

$$[\mathrm{M/H}] = [\mathrm{Fe/H}] + \log\,(0.638 \times 10^{0.3} + 0.362) \tag{2}$$

We then applied a conversion to log(Z) via (Catelan *et al.* (2004) and Cáceres and Catelan (2008)):

$$\log \mathrm{Z} = [\mathrm{M/H}] - 1.765 \tag{3}$$

Absolute magnitudes for RU Cet were obtained using the following relations (the M_V-metallicity relation comes from Catelan *et al.* (2004), while the M_i- and M_z-metallicity relations come from Cáceres and Catelan (2008)):

$$M_v = 2.288 + 0.882 \log \mathrm{Z} + 0.108\,(\log \mathrm{Z})^2 \tag{4}$$

$$M_i = 0.908 - 1.035 \log \mathrm{P} + 0.220 \log \mathrm{Z} \tag{5}$$

$$M_z = 0.839 - 1.295 \log \mathrm{P} + 0.211 \log \mathrm{Z} \tag{6}$$

In these equations, M is the absolute magnitude of the source star, P is the period (days), and Z is the metallicity.

Solving for the absolute magnitudes allows us to compare them to the apparent magnitudes, derived from the observations using the photometry methods described in section 2. The equation used to compare the two is:

$$\mathrm{d} = 10^{\frac{m - M - A + 5}{5}} \tag{7}$$

Here, m is the average apparent magnitude, derived through the photometric methods described in section 2. The large M is absolute magnitude, derived through the theoretical equations listed above. The A is the value for interstellar extinction. We solved for distance, d, and extinction, A, simultaneously thus: we chose the value of color excess, E(B–V), that minimized the standard deviation computed from three distance values d_V, d_{ip}, and d_{zs}, i.e., the distance derived in each of the V, ip, and zs filers using extinctions A_V, A_{ip}, and A_{zs}. We used the standard relations for extinction, e.g.,

$$R_v = \frac{A_v}{E(B-V)} \tag{8}$$

with $R_V = 3.1$. We derived a color excess of E(B–V) = 0.004 mag. An estimate of the maximum extinction along the line of sight to RU Cet is provided by Schlafly and Finkbeiner (2011) via online query of the NASA/IPAC Infrared Science Archive. Their value is E(B–V) = 0.0207 mag, a bit larger than our value. Given the patchiness of extinction and the high galactic coordinates of RU Cet (b = 78°, l = 134°) the extinction is plausibly very small.

Calculating a weighted average of the distances in the different filters given above, we obtain an average distance of 1636 ± 33 parsecs to RU Cet. The Gaia Early Data Release 3 (EDR3) distance value for RU Cet is 1699 +83 / –75 parsecs (median of the photogeometric distance; Bailer-Jones *et al.* (2021)). The differences between the calculated values here and the Gaia EDR3 value are of order 1 to 2 standard deviations.

4. Conclusion

This research used observations of the RR Lyrae star RU Cet to test the infrared period-luminosity-metallicity (PLZ) relationships put forward by Catelan *et al.* (2004) and Cáceres and Catelan (2008). The period was determined to be 0.585 ± 0.020 days. The distance to RU Cet was determined to be 1633 ± 33 pc. The difference between the PLZ value and the Gaia EDR3 value is 66 parsecs, which is between 1 and 2 times the uncertainties. The PLZ method thus yields consistent results. This consistency is reassuring given the changing period of RU Cet.

Suggestions for future work would include inventing and testing further refinements to the PLZ relations, continued regular monitoring of RU Cet for changes in period and magnitude range, and a better estimate of the interstellar extinction.

5. Acknowledgements

Thank you to Michael Fitzgerald for his help in setting up the OurSolarSiblings RR Lyrae research course, as well as the work put into developing an efficient data pipeline and software to make the research process incredibly easy to apply and understand.

We also thank the referee for many helpful suggestions upon the manuscript.

This research has made use of the SIMBAD database, operated at CDS, Strasbourg, France.

This research has made use of the International Variable Star Index (VSX) database, operated at AAVSO, Cambridge, Massachusetts, USA.

This work has made use of data from the European Space Agency (ESA) mission Gaia (https://www.cosmos.esa.int/gaia), processed by the Gaia Data Processing and Analysis Consortium (DPAC, https://www.cosmos.esa.int/web/gaia/dpac/consortium). Funding for the DPAC has been provided by national institutions, in particular the institutions participating in the Gaia Multilateral Agreement.

The DSS image is based on photographic data obtained using The UK Schmidt Telescope. The UK Schmidt Telescope was operated by the Royal Observatory Edinburgh, with funding from the UK Science and Engineering Research Council, until 1988 June, and thereafter by the Anglo-Australian Observatory. Original plate material is copyright © the Royal Observatory Edinburgh and the Anglo-Australian Observatory. The plates were processed into the present compressed digital form with their permission. The Digitized Sky Survey was produced at the Space Telescope Science Institute under US Government grant NAG W-2166.

This research has made use of SAOImageDS9, developed by Smithsonian Astrophysical Observatory.

This research has made use of the NASA/IPAC Infrared Science Archive, which is funded by the National Aeronautics and Space Administration and operated by the California Institute of Technology.

References

Alonso-García, J., Mateo, M., Sen, B., Banerjee, M., Catelan, M., Minniti, D., and von Braun, K. 2012, *Astron. J.*, **143**, 70 (DOI: 10.1088/0004-6256/143/3/70).

Altunin, I., Caputo, R., and Tock, K. 2020, *Astron. Theory Obs. Methods*, **1**, 1 (DOI: 10.32374/atom.2020.1.1).

Bailer-Jones, C. A. L., Rybizki, J., Fouesneau, M., Demleitner, M., and Andrae, R. 2021, *Astron. J.*, **161**, 147 (DOI: 10.3847/1538-3881/abd806).

Bertin, E. 2011, in *Astronomical Data Analysis Software and Systems XX*, eds. I. N. Evans, A. Accomazzi, D. J. Mink, A. H. Rots, ASP Conf. Ser. 442, Astronomical Society of the Pacific, San Francisco, 435.

Bertin, E., and Arnouts, S. 1996, *Astron. Astrophys., Suppl. Ser.*, **117**, 393 (DOI: 10.1051/aas:1996164).

Bessell, M. S. 1993, in *Stellar photometry - Current techniques and Future Developments*, eds. C. J. Butler, I. Elliott, IAU Colloq. 136, Cambridge Univ. Press, Cambridge, 22.

Brown, T. M., *et al.* 2013, *Publ. Astron. Soc. Pacific*, **125**, 1031 (DOI: 10.1086/673168).

Cáceres, C., and Catelan, M. 2008, *Astrophys. J., Suppl. Ser.*, **179**, 242 (DOI: 10.1086/591231).

Catelan, M., Pritzl, Barton J., and Smith, H. A. 2004, *Astrophys. J., Suppl. Ser.*, **154**, 633 (DOI: 10.1086/422916).

Chiba, M., and Yoshii, Y. 1998, *Astron. J.*, **115**, 168 (DOI: 10.1086/300177).

Cusano, F., *et al.* 2021, *Mon. Not. Roy. Astron. Soc.*, **504**, 1 (DOI: 10.1093/mnras/stab901).

Drake, A. J., *et al.* 2013, *Astrophys. J.*, **763**, 32 (DOI: 10.1088/0004-637X/763/1/32).

Dworetsky, M. M. 1983, *Mon. Not. Roy. Astron. Soc.*, **203**, 917 (DOI: 10.1093/mnras/203.4.917).

Feast, M. W., Laney, C. D., Kinman, T. D., van Leeuwen, F., and Whitelock, P. A. 2008, *Mon. Not. Roy. Astron. Soc.*, **386**, 2115 (DOI: 10.1111/j.1365-2966.2008.13181.x).

Fitzgerald, M. 2018, *Robotic Telesc. Student Res. Education Proc.*, **1**, 343 (DOI: 10.32374/rtsre.2017.033).

Fitzgerald, M. 2021, private communication.

Fitzgerald, M., Gomez, E., Salimpour, S., Singleton, J., and Wibowo, R. 2021, *J. Open Source Software*, **6** (DOI: 10.21105/joss.02641

Flewelling, H. A., *et al.* 2020, *Astrophys. J., Suppl. Ser.*, **251**, 7 (DOI: 10.3847/1538-4365/abb82d).

Fukugita, M., Ichikawa, T., Gunn, J. E., Doi, M., Shimasaku, K., and Schneider, D. P. 1996, *Astron. J.*, **111**, 1748 (DOI: 10.1086/117915).

Graham, J. A., and Slettebak, A. 1973, *Astron. J.*, **78**, 295 (DOI: 10.1086/111416

Henden, A. A., Templeton, M., Terrell, D., Smith, T. C., Levine, S., and Welch, D. 2016, VizieR Online Data Catalog: AAVSO Photometric All Sky Survey (APASS) DR9, II/336.

Henden, A., Welch, D., Terrell, D., and Levine, S. 2009, *Bull. Amer. Astron. Soc.*, **41**, 669.

Kolenberg, K., Guggenberger, E., and Medupe, T. 2008, *Commun. Asteroseismology*, **153**, 67 (DOI: 10.1553/cia 153s67).

Kovács, G. 2005, *Astron. Astrophys.*, **438**, 227 (DOI: 10.1051/0004-6361:20052742).

Laher, R. R., Gorjian, V., Rebull, L. M., Masci, F. J., Fowler, J. W., Helou, G., Kulkarni, S. R., and Law, N. M. 2012a, *Publ. Astron. Soc. Pacific*, **124**, 737 (DOI: 10.1086/666883).

Laher, R. R., *et al.* 2012b, *Publ. Astron. Soc. Pacific*, **124**, 764 (DOI: 10.1086/666507).

Layden, A. C. 1994, *Astron. J.*, **108**, 1016 (DOI: 10.1086/117132).

Layden, A. C., Hanson, R. B., Hawley, S. L., Klemola, A. R., and Hanley, C. J. 1996, *Astron. J.*, **112**, 2110 (DOI: 10.1086/118167).

Le Borgne, J. F., *et al.* 2007, *Astron. Astrophys.*, **476**, 307, 283 (DOI: 10.1051/0004-6361:20077957).

Magnier, E. A., *et al.* 2020, *Astrophys. J., Suppl. Ser.*, **251**, 3 (DOI: 10.3847/1538-4365/abb829).

Neeley, J. R., *et al.* 2019, *Mon. Not. Roy. Astron. Soc.*, **490**, 4254 (DOI: 10.1093/mnras/stz2814).

Preston, G. W., Shectman, S. A., and Beers, T. C. 1991, *Astrophys. J.*, **375**, 121 (DOI: 10.1086/170175).

Salaris, M., Chieffi, A., and Straniero, O. 1993, *Astrophys. J.*, **414**, 580 (DOI: 10.1086/173105).

Sandage, A. 1993, *Astron. J.*, **106**, 687 (DOI: 10.1086/116675).

Schechter, P. L., Mateo, M., and Saha, A. 1993, *Publ. Astron. Soc. Pacific*, **105**, 1342 (DOI: 10.1086/133316).

Schlafly, E. F., and Finkbeiner, D. P. 2011, *Astrophys. J.*, **299** 737, 103 (DOI: 10.1088/0004-637X/737/2/103).

Stellingwerf, R. F. 1978, *Astrophys. J.*, **224**, 953 (DOI: 10.1086/156444).

Stetson, P. B. 1987, *Publ. Astron. Soc. Pacific*, **99**, 191 (DOI: 10.1086/131977).

Szczygiel , D. M., Pojmański, G., and Pilecki, B. 2009, *Acta Astron.*, **59**, 137 (https://arxiv.org/abs/0906.2199).

Tonry, J. L., *et al.* 2012, *Astrophys. J.*, **750**, 99 (DOI: 10.1088/0004-637X/750/2/99).

Vandenbroere, J., Le Borgne, J.-F., and Boninsegna, R. 2014, *GEOS Circ. RR53* (July), 1 (http://geos.upv.es/index.php/publications/func-startdown/1519/).

Watson, C. L., Henden, A. A., and Price, A. 2006, in *The Society for Astronomical Sciences 25th Annual Symposium on Telescope Science*, Society for Astronomical Sciences, Rancho Cucamonga, CA, 47.

Wolf, C., *et al.* 2018, *Publ. Astron. Soc. Australia*, **35**, e010 (DOI: 10.1017/pasa.2018.5).

CCD Photometry, Light Curve Deconvolution, Period Analysis, and Evolutionary Status of the HADS Variable V417 Boötis

Kevin B. Alton
Desert Blooms Observatory, 70 Summit Avenue, Cedar Knolls, NJ 07927; kbalton@optonline.net

W. Allen Gilchrist, Jr.
Stonecrest Observatory, 104 Deer Ridge Drive, Fort Davis, TX 79734; gilchrist.allen@ymail.com

Received September 29, 2021; revised November 3, 2021; accepted December 1, 2021

Abstract CCD-derived photometric B- and V-magnitude data were acquired from V417 Boo, an intrinsic variable classically defined as a High Amplitude δ Scuti (HADS) star. Deconvolution of precise time-series light curve data was accomplished using discrete Fourier transformation and revealed a fundamental mode (f_0) of oscillation at ~11.5408 d^{-1} along with three other partial harmonics ($2f_0$–$4f_0$). No other statistically significant frequencies were resolved following successive pre-whitening of each residual signal. An assessment of potential period changes over time was performed using five new times of maximum (ToMx) light produced from the present study along with 34 other ToMx values mined from the AAVSO VSX archives. These results indicate that no substantive change in the fundamental period of oscillation or amplitude (V-mag) has likely occurred over the past 11 years. Finally, an investigation with PARSEC models for generating stellar tracks and isochrones provided valuable insight into the evolutionary status and physical nature of V417 Boo.

1. Introduction

Amongst the most common A- and F-type stars which exhibit variability are the multi-periodic δ Scuti-like (hereafter δ Sct) pulsating stars. These intrinsic variables occupy a narrow space at the intersection of the classical instability strip, pre-main sequence, and main sequence (MS) on the Hertzsprung-Russell diagram. Therein they represent a transition from the high-amplitude radial pulsators, such as Cepheid variables, and non-radial multi-periodic pulsators (Breger 2000). Main sequence δ Sct stars typically range from spectral type F2 to A2 (Rodríguez and Breger 2001) which correspond to effective temperatures varying between 6300 and 8600 K (Uytterhoeven *et al.* 2011). Hotter δ Sct stars generally have shorter pulsation periods (i.e. higher pulsation mode frequencies) than cooler δ Sct stars.

Pulsations in δ Sct stars are excited by the κ-mechanism operating in the He II partial ionization zone (T ~ 50000 K) which produce low-order pressure (p) modes akin to acoustic waves (Cox 1963; Chevalier 1971). These can produce radial pulsations which evoke symmetrical changes in stellar size and/or non-radial pulsations that give rise to asymmetric changes in shape but not volume. Although shorter periods (< 30 min) have been observed (Holdsworth *et al.* 2014) in some A-type stars, the fundamental radial pulsations of Galactic δ Sct variables with near solar metallicity typically range between 0.05 to 0.25 d. Masses vary from ~ 1.2 $M_\odot$ to ~ 2.5 $M_\odot$, so they are more luminous and larger than our Sun.

The luminosity classes for δ Sct variables generally range from III (normal giants) to V (MS stars). δ Sct variables with moderate (40 km s^{-1}) to rapid (250 km s^{-1}) rotational velocities (v sin i) generally have small light curve amplitudes (ΔV ~ 0.01–0.03 mag) composed of a multitude of pulsation frequencies, most of them nonradial. Stars with slow rotational velocities (< 30 km s^{-1}) tend to be radial pulsators and have light curve amplitudes (V-mag) in excess of 0.20–0.30 mag. The latter characteristics define a δ Sct subgroup called High-Amplitude δ Scuti stars (HADS).

Although HADS stars represent a very small fraction (< 1%) of all δ Sct variables (Lee *et al.* 2008), they are attractive targets for the budding photometrist in possession of a modestly sized telescope and CCD camera. Given their comparatively short pulsation periods (< 0.2 d), high modulation amplitude (> 0.2 mag), and luminosity (> 10 $L_\odot$) an entire light curve (LC) can be completed in just a few imaging sessions. HADS variables commonly oscillate via low-order single or double radial pulsation modes (Poretti 2003a, 2003b; Niu *et al.* 2013, 2017). A high percentage (~ 40%) are double pulsators showing simultaneous pulsations in the fundamental and the first overtone mode with amplitudes generally higher in the fundamental mode (McNamara 2000). It should be noted, however, that non-radial pulsations have also been detected with the HADS variable V974 Oph (Poretti 2003a, 2003b). HADS stars have historically been divided according to metallicity relative to our Sun ([Fe/H] = 0 dex). Members of the metal-poor ([Fe/H] << 0) group are called SX Phe stars, based on the eponymous prototype SX Phoenicis. Ostensibly they have shorter periods (0.02 < P < 0.125 d) and lower masses (~ 1.0–1.3 $M_\odot$) than their sibling HADS variables possessing near solar metal abundance. SX Phe stars frequently dwell in globular clusters (GC), ancient collections of Population II stars. Therein, the majority of SX Phe variables are classified as blue straggler stars, paradoxically appearing much younger than their GC cohorts. Despite previous claims to the contrary, Balona and Nemec (2012) make a strong case that it is not possible to differentiate between δ Sct and field SX Phe variables based on pulsation amplitude, the number of pulsation modes, period, or even metallicity (Garg *et al.* 2010). They further argue that the evolutionary status of each star is the only way to distinguish between these two classes. Much more sensitive space telescopes like NASA's Kepler (Gilliland *et al.* 2010; Guzik 2021; Yang *et al.* 2021), the European Space Agency's

CoRoT (Baglin 2003), the Canadian Microvariability and Oscillations of STars [MOST] (Walker *et al.* 2003), and the Transiting Exoplanet Survey Satellite, TESS (Ricker *et al.* 2015; Bedding *et al.* 2020) have detected a rich supply of HADS stars using highly precise photometry. New discoveries from Kepler and TESS have begun to blur the traditional line of distinction between HADS and SX Phe type variables.

An additional classification scheme for δ Scuti stars was recently proposed by Qian *et al.* (2018). Therein two distinct groups of δ Scuti stars were uncovered from the Large Sky Area Multi-Object Fiber Spectroscopic Telescope (LAMOST) survey (Zhao *et al.* 2012) that fundamentally differed in effective temperature. One group was identified as normal δ Scuti stars (NDSTs) when T_{eff} ranged between 6700–8500 K while the other was considered as unusual and cool variable stars (UCVs) with T_{eff} values less than 6700 K. A more restrictive fundamental pulsation range (0.09–0.22 d) coupled with being slightly metal-poor ([Fe/H] = –0.25–0.0) further differentiates the UCVs from the NDST group. Furthermore, once the UCV stars were excluded from consideration, empirically based temperature-period, log g-period, and metallicity-period relationships could be developed for NDSTs.

One of the most important astronomical events in history occurred when Henrietta Leavitt discovered a period-luminosity (P-L) relationship between 25 Cepheid variables in the Small Magellanic Cloud (Leavitt and Pickering 1912). Since then pulsating stars have served as standard candles for estimating cosmic distances to individual stars, clusters, and galaxies. Over time this P-L relationship has been refined owing to differences between metal-rich (Population~ I) and metal-poor (Population II) Cepheids (Baade 1956).

A more modern refinement of the P-L relationship for δ Sct variables was reported by McNamara (2011), albeit with Hipparcos parallaxes and not the more accurate values determined by the Gaia Mission (Lindegren *et al.* 2016; Gaia Collab. *et al.* 2018). Nonetheless this empirically-derived expression (McNamara 2011) appears to correspond reasonably well to the main ridge of Gaia DR2 derived P-L relationship for δ Sct variables determined by Ziaali *et al.* (2019). The most recent investigation that resulted in the derivation of P-L relationships for δ Sct stars oscillating in the fundamental (adopted herein) as well as first through third overtones was reported by Poro *et al.* (2021).

The variability of V417 Boo (= NSVS 5189969) was first detected during the ROTSE-I survey between 1999 and 2000 (Akerlof *et al.* 2000; Woźniak *et al.* 2004). Accordingly, Hoffman *et al.* (2009) classified this star as a short period (P = 0.08665 d) δ Sct variable following an evaluation of unfiltered photometric data from the ROTSE-I Survey. Photometric (V-mag) data from V417 Boo (CSS J154137.0+515924) were also acquired during the Catalina Sky Survey (Drake *et al.* 2009) and the All-Sky Automated Survey for SuperNovae (ASAS-SN) (Shappee *et al.* 2014; Jayasinghe *et al.* 2021). Herein we report the first two-color photometric study on V417 Boo which uses discrete Fourier transformation to assess the fundamental pulsation modes along with secular analyses to establish whether there have been any obvious changes in magnitude and pulsation period.

2. Observations and data reduction

2.1. Photometry

Precise time-series images were acquired at Stonecrest Observatory (SO, USA: 103.9767 W, 30.6167 N) with an SBIG ST10-XME CCD camera installed at the secondary focus of a 0.3-m Ritchey Chretien telescope. This instrument produces an image scale of 1.15 arcsec/pixel (bin = 2 × 2) and a field of view (FOV) of 21' × 14'. Image acquisition (B: 120-s; V: 50-s) was performed using TheSkyX Pro Version 10.5.0 (Software Bisque 2019) which controlled an Astro-Physics AP-1200 GTO German equatorial mount. The CCD-camera was equipped with B and V filters manufactured to match the Johnson-Cousins Bessell specification. Dark subtraction, flat correction, and registration of all images collected at SO were performed with ImagesPlus Ver. 6.5 (Unsold 2000). Instrumental readings were reduced to catalog-based magnitudes using the APASS star fields (Henden *et al.* 2009, 2010, 2011; Smith *et al.* 2011) built into MPO Canopus v10.8.5.0 (Minor Planet Observer 2010). LCs for V417 Boo were generated using an ensemble of five non-varying comparison stars. The identity, J2000 coordinates, and APASS color indices (B–V) for these stars are provided in Table 1; a corresponding FOV image is rendered in Figure 1. Only data from images taken above 30° altitude (airmass < 2.0) were included; considering the proximity of all program stars, differential atmospheric extinction was ignored. During each imaging session comparison stars typically stayed within ± 0.009 mag for both passbands.

3. Results and discussion

3.1. Photometry and ephemerides

Photometric values in B (n = 231) and V (n = 249) passbands were separately processed to produce LCs acquired between 28 April (JD 2459332.71243) and 26 May 2021 (JD 2459360.90958) (Figure 2). Period determinations were initially performed using Peranso v2.5 (Vanmunster 2011) by applying periodic orthogonals (Schwarzenberg-Czerny 1996) to fit observations and analysis of variance (ANOVA) to assess fit quality. In this case a similar period solution for each passband (0.086649 ± 0.000002 d) was obtained. Separately folding the sparsely sampled CSS and ASAS-SN survey data with those (V-mag) acquired at SO yielded a period at 0.086648 ± 0.000008 d and 0.086649 ± 0.000002 d, respectively (Figure 3). New ToMx light values were estimated using the polynomial extremum fit utility featured in Peranso (Paunzen and Vanmunster 2016). There was no obvious color dependency on the SO timings such as those reported for other δ Sct variables (Elst 1978); therefore, corresponding B and V data were averaged (Table 2) at each time of maximum (ToMx). New maxima from SO (5) along with published results starting in 2010 (Table 2) and values (34) derived from the AAVSO International Variable Star Index (VSX; Watson *et al.* 2014) archive were used to establish whether there were any pulse timing differences (PTD) between the observed and predicted fundamental period of oscillation. The reference epoch (15 April 2020, VSX) was initially defined by the following linear ephemeris (Equation 1):

Table 1. Astrometric coordinates (J2000), V-magnitude and color indices (B–V) for V417 Boo and five comparison stars (1–5) used during this photometric study.

FOV Identification	*Star Identification*	*R. A. (J2000) h m s*	*Dec. (J2000) deg ' "*	*APASSa V-mag.*	*APASS[a] (B-V)*
T	V417 Boo	15 41 36.994	+51 59 24.99	13.017	0.324
1	GSC 03489-00958	15 41 12.732	+52 02 29.66	11.832	0.843
2	GSC 03489-00854	15 41 46.077	+52 03 48.99	12.302	0.731
3	GSC 03489-01407	15 42 03.317	+52 02 55.97	11.045	1.193
4	GSC 03489-01132	15 42 27.265	+52 03 50.33	11.635	0.841
5	GSC 03489-01298	15 41 34.504	+51 56 00.86	14.175	0.775

a. V-magnitude and (B–V) for comparison stars derived from APASS database described by Henden et al. *(2009, 2010, 2011) and Smith* et al. *(2010), as well as on the AAVSO web site (https://www.aavso.org/apass).*

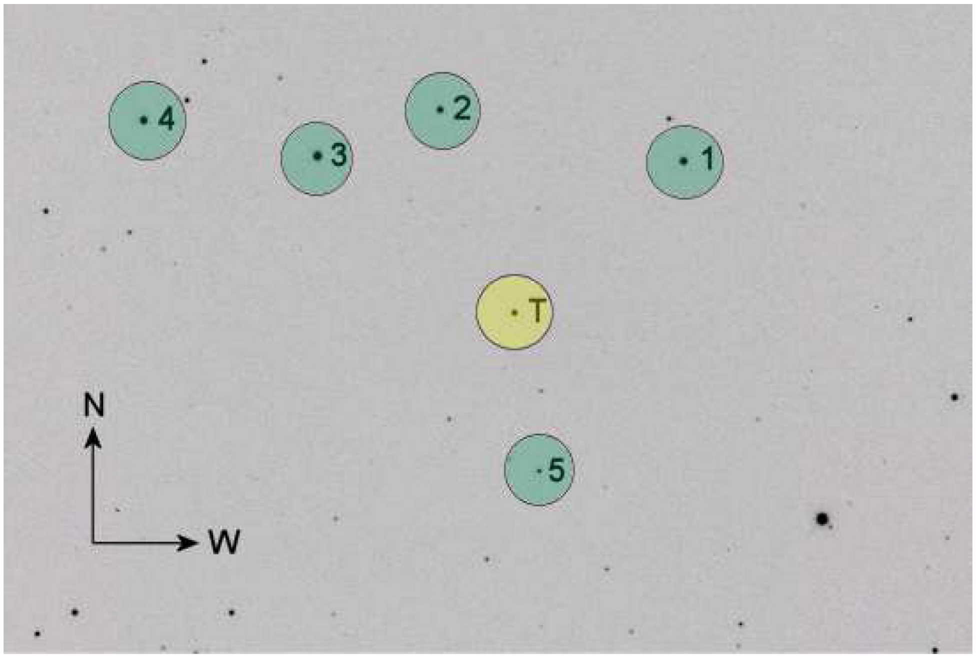

Figure 1. V417 Boo (T) along with the five comparison stars (1–5) used to reduce time-series images to APASS-catalog based magnitudes.

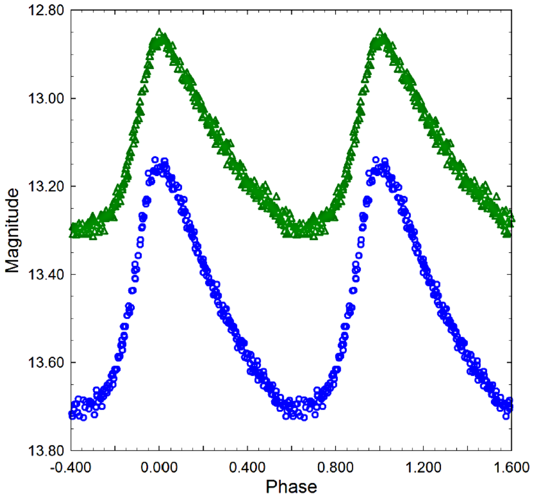

Figure 2. Period folded (0.086640 d) LCs for V417 Boo produced from photometric data obtained between 28 April and 26 May 2021 at SO. LCs shown at the top (V) and bottom (B) represent catalog-based (APASS) magnitudes determined using MPO Canopus.

$$\text{Max (HJD)} = 2458955.406 + 0.08664937\ E. \qquad (1)$$

As shown in Figure 4, secular changes in pulsation period can potentially be uncovered by plotting the PTD residuals vs. epoch (or cycle number). Thus far, this relationship is basically described by a straight line and suggests that little or no change to the period has occurred since 2010. The updated ephemeris (Equation 2) based on maximum light timing data available through May 2021 is as follows:

$$\text{Max (HJD)} = 2459360.83902\ (9) + 0.08664937\ (1)\ E, \quad (2)$$

where the times of maxima are in Heliocentric Julian Dates (HJD), and E is an integral cycle number chosen so that E = 0 represents the most recent maximum measurement.

These results, along with nearly superimposable period-folded LCs from SO, CSS, and ASAS-SN (Figure 3), further support that the fundamental pulsation period has not substantively changed since 2010 nor has the V-mag amplitude changed significantly over the same period of time.

Table 2. Differences between the times-of-maximum light (HJD) predicted from the updated linear ephemeris (Equation 2) and those observed for V417 Boo between 2010 and 2021.

HJD 2400000+	*Epoch (Cycle No.)*	*PTD*[a]	*Reference*[b]
55334.4160	–46468	–0.00023	1
55334.5016	–46467	–0.00128	1
55713.3338	–42095	–0.00011	2
55713.4204	–42094	–0.00016	2
55729.3637	–41910	–0.00035	2
55729.4504	–41909	–0.00030	2
55729.5369	–41908	–0.00045	2
56075.4428	–37916	0.00118	3
56075.5293	–37915	0.00103	3
56349.8601	–34749	–0.00007	4
56349.9467	–34748	–0.00011	4
56385.3868	–34339	0.00039	4
56385.4731	–34338	0.00004	4
56730.5108	–30356	–0.00004	5
56730.5976	–30355	0.00012	5
56730.6841	–30354	–0.00003	5
56793.5048	–29629	–0.00013	5
56793.5918	–29628	0.00023	5
57071.4758	–26421	–0.00028	6
57071.5630	–26420	0.00027	6
57514.4277	–21309	–0.00001	6
57803.5761	–17972	–0.00049	6
57803.6627	–17971	–0.00060	6
57828.5314	–17684	–0.00019	6
57828.6177	–17683	–0.00052	6
58173.6559	–13701	–0.00013	6
58246.3552	–12862	0.00036	6
58246.4411	–12861	–0.00037	6
58247.4816	–12849	0.00024	6
58474.6756	–10227	–0.00039	6
58523.6323	–9662	–0.00052	6
58523.7193	–9661	–0.00019	6
58654.5594	–8151	–0.00068	6
58694.4190	–7691	0.00023	6
58715.3880	–7449	0.00007	6
58747.3613	–7080	–0.00022	6
58917.5421	–5116	0.00127	6
58950.3813	–4737	0.00029	6
58950.5537	–4735	–0.00055	6
58955.4073	–4679	0.00067	6
58958.6992	–4641	–0.00013	6
58958.6994	–4641	0.00005	6
58958.7855	–4640	–0.00042	6
58958.7857	–4640	–0.00023	6
58968.7509	–4525	0.00026	6
59270.6370	–1041	–0.00008	6
59302.5245	–673	0.00050	6
59302.6101	–672	–0.00054	6
59327.4792	–385	0.00016	6
59332.7644	–324	–0.00026	7
59334.4114	–305	0.00041	6
59339.6967	–244	0.00007	7
59342.3830	–213	0.00028	6
59342.4696	–212	0.00021	6
59344.7227	–186	0.00043	7
59353.9069	–80	–0.00014	7
59360.8389	0	–0.00017	7

a. PTD = Time difference between observed fundamental pulsation time–of–maximum and that calculated using the reference ephemeris (Equation 2).
b. 1. Wils et al. *(2011); 2. Wils* et al. *(2012); 3. Wils* et al. *(2013); 4. Wils* et al. *(2014); 5. Wils* et al. *(2015); 6. AAVSO–VSX (Watson* et al. *2014); 7. This study.*

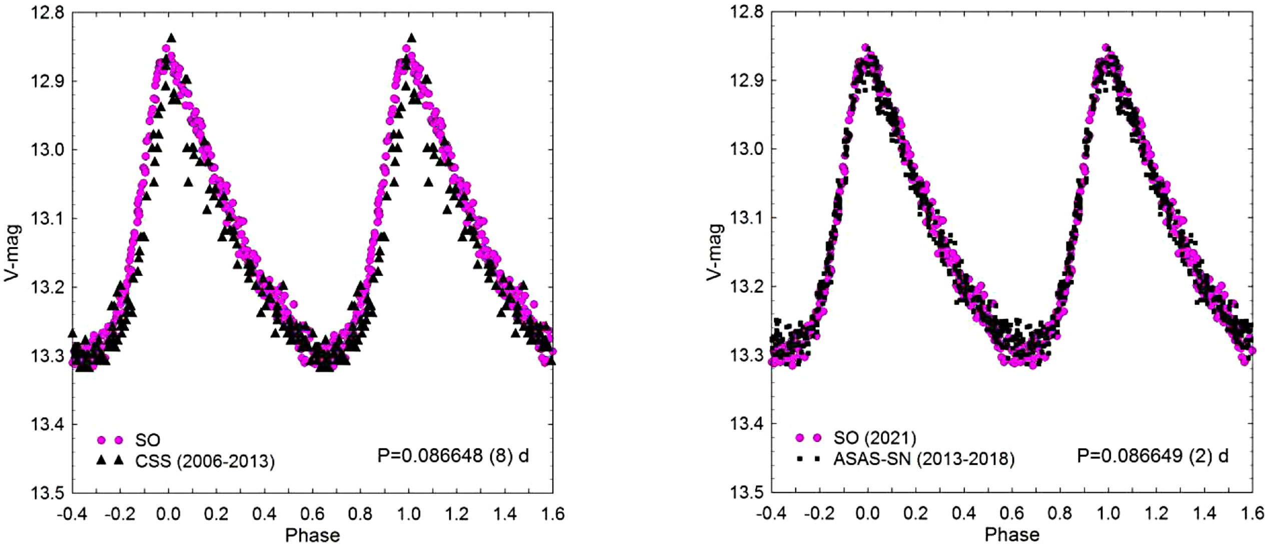

Figure 3. Period-folded LCs for V417 Boo produced from precise photometric V-magnitude data obtained at SO (2021) along with sparsely sampled data from the CSS (2006–2013) and ASAS-SN (2013–2018) surveys. CSS and ASAS-SN magnitudes were offset to conform with the APASS-derived values from SO.

Table 3. Fundamental frequency (f_0) and corresponding partial harmonics ($2f_0$–$4f_0$) detected following DFT analysis of time-series photometric data (B and V) from V417 Boo.

	Frequency (d^{-1})	*Frequency Error*	*Amplitude (mag)*	*Amplitude Error*	*Phase*	*Phase Error*	*S/N*
f_0-B	11.54078	0.00009	0.24961	0.00121	0.66076	0.00066	140.7
f_0-V	11.54084	0.00009	0.19006	0.00110	0.94685	0.30980	103.8
$2f_0$-B	23.08167	0.00030	0.07345	0.00149	0.60829	0.00273	59.6
$2f_0$-V	23.08168	0.00030	0.05988	0.00106	0.03210	0.28679	37.6
$3f_0$-B	34.62231	0.00077	0.02968	0.00159	0.17567	0.00783	20.4
$3f_0$-V	34.62314	0.00079	0.02260	0.00114	0.89959	0.32002	17.8
$4f_0$-B	46.16234	0.03573	0.01290	0.00238	0.55778	0.10054	8.2
$4f_0$-V	46.16235	0.00125	0.01350	0.00113	0.08956	0.31381	8.8

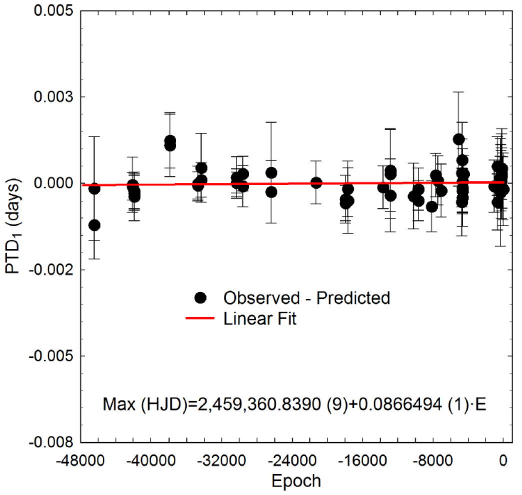

Figure 4. Straight line fit (PTD vs. epoch) suggesting that little or no change to the fundamental mode of oscillation for V417 Boo had occurred between 2010 and 2021.

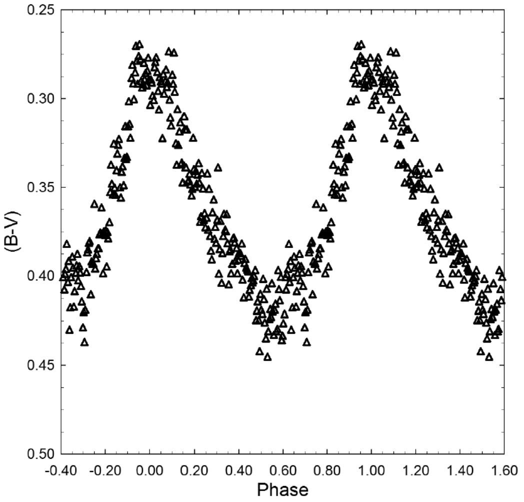

Figure 5. V417 Boo LCs illustrating significant change in color index (0.28 < (B–V) < 0.41) as maximum light slowly descends to minimum light. This effect is most closely associated with a decrease in the effective surface temperature during minimum light.

3.2. Light curve behavior

Characteristically, light curves from HADS variables are asymmetrical with a faster ascent from minimum to maximum light than the decline back to minimum brightness. V417 Boo appears to be a textbook example in this regard (Figure 2). The largest difference between maximum and minimum light is observed in the blue passband (ΔB-mag = 0.55), followed by V (ΔV-mag = 0.47). This behavior is typical for pulsating F- to A-type stars. It follows when the B- and V-mag LCs are binned into equal phase intervals and then subtracted from one another, the emerging LC (B–V) exhibits significant reddening during minimum light (Figure 5). In this case color excess (B–V) ranges between 0.28 and 0.41 mag. Estimates for interstellar extinction (A_V) vary widely depending on the model selected (Amôres and Lépine 2005, 2007; Schlegel *et al.* 1998; Schlafly and Finkbeiner 2011). Access to these data is greatly facilitated via the GALextin website at http://www.galextin.org/. The median reddening value (E(B–V) = 0.0361 ± 0.0119 mag) corresponds to an intrinsic color index $(B–V)_0$ for V417 Boo that varies between 0.191 ± 0.028 at maximum light and 0.372 ± 0.032 mag at minimum brightness. Based on the corrected (Torres 2010) polynomial transformation equations derived by Flower (1996), the mean effective temperature (T_{eff}) was estimated to be 7310 ± 223 K, with a minimum T_{eff} of ~6859 ± 151 K and a maximum T_{eff} of ~7814 ± 171 K. These results based strictly on B–V photometry at SO are in good agreement with the Johnson-Cousins transformations (Warner 2007) from 2MASS (Skrutskie *et al.* 2006). When transformed, J- and K-band data from 2MASS predict a T_{eff} value of 7673 ± 315 K. A low resolution UV-vis spectrum has been reported by LAMOST DR5 (Zhao *et al.* 2012; Wang *et al.* 2019) that is consistent with an A7V classification for V417 Boo (T_{eff} = 7608 ± 54 K). We adopted the median value (7640 ± 181 K) derived from our LCs, 2MASS, LAMOST DR5, and Gaia DR2. According to Qian *et al.* (2018), V417 Boo would be considered a NDST rather than a UCV since T_{eff} is between 6700 and 8500 K, while the fundamental pulsation period is less than 0.09 d.

3.3. Light curve analysis by discrete Fourier transformation

LC deconvolution was performed with Period04 (Lenz and Breger 2005) wherein discrete Fourier transformation (DFT) was used to extract the fundamental pulsating frequency (spectral window = 100 d^{-1}). Pre-whitening steps which successively remove the previous most intense signals were employed to tease out other potential oscillations from the residuals. Only those frequencies with a S/N ≥ 6 (Baran *et al.* 2014) in each passband are presented in Table 3. In all cases, uncertainties in frequency, amplitude, and phase were estimated by the Monte Carlo simulation (n = 400) routine built into Period04.

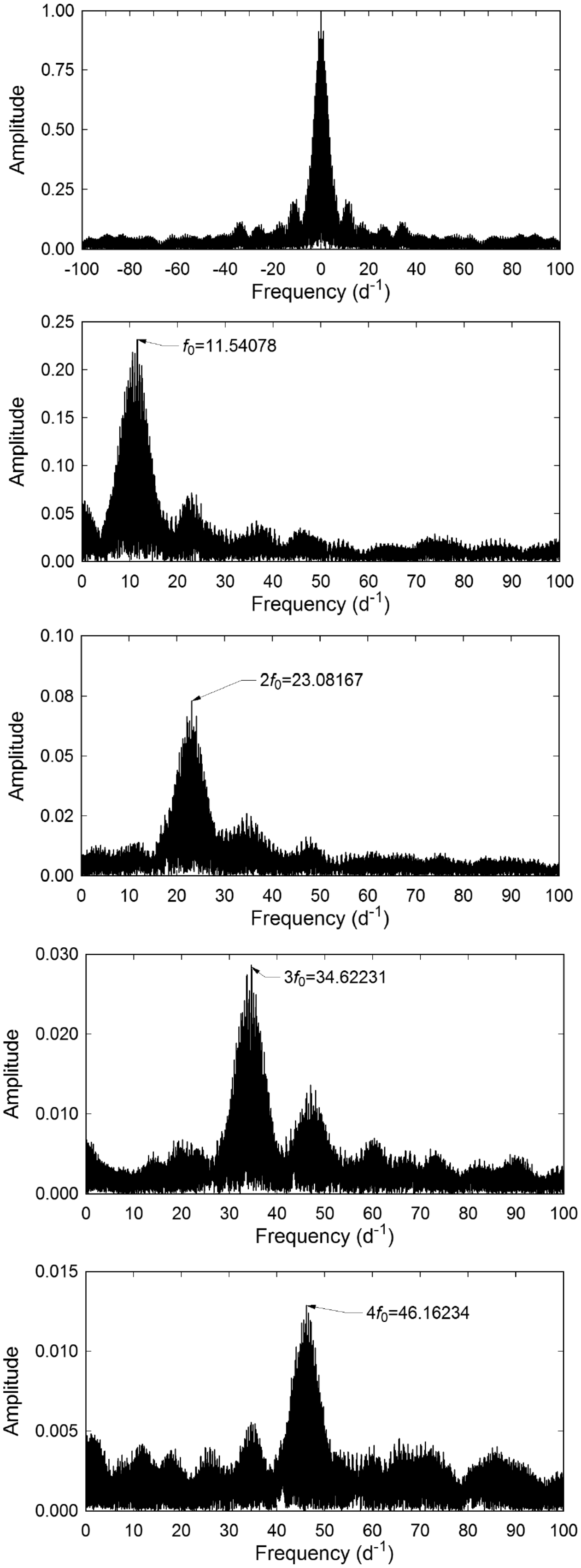

Figure 6. B-magnitude spectral window (top) and all significant pulsation frequencies following DFT analysis of photometric data from V417 Boo acquired in 2021 at SO. The amplitude spectra illustrate the fundamental (f_0) frequency and its highest partial harmonic ($4f_0$) which was clearly detected (S/N ≥ 8) following prewhitening.

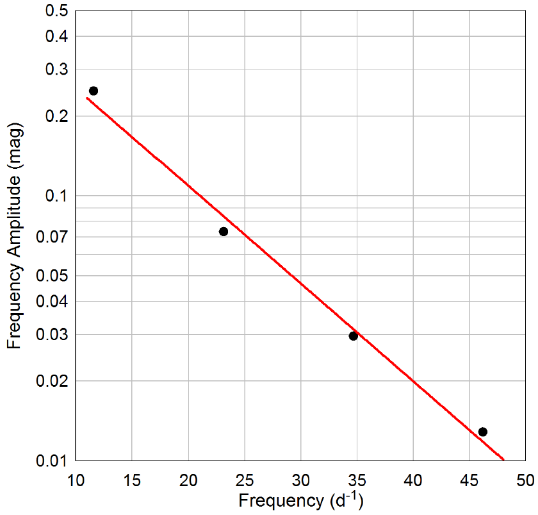

Figure 7. Amplitude decay of the fundamental (f_0) pulsation period and its corresponding partial harmonics ($2f_0$–$4f_0$) observed in the B-passband.

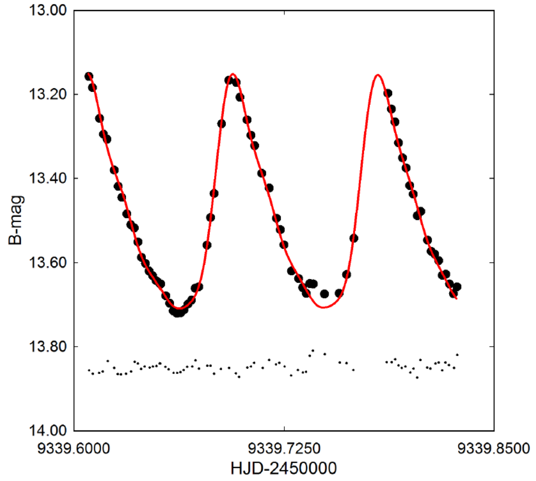

Figure 8. Representative fit of B-mag time-series data (05 May 2021) based on elements derived from DFT. Model fit residuals at bottom are offset by constant amount to compress y-axis scale.

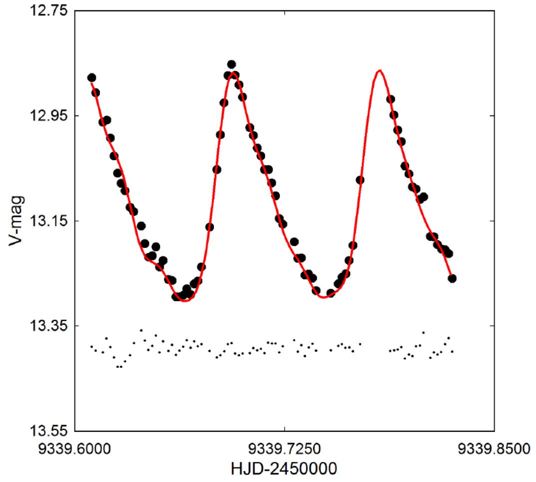

Figure 9. Representative fit of V-magitude time-series data (05 May 2021) based on elements derived from DFT. Model fit residuals at bottom are offset by constant amount to compress y-axis scale.

Our results strongly suggest that V417 Boo is a monoperiodic radial pulsator; changes in stellar size during each pulsation cycle are therefore symmetrical. The spectral window and amplitude spectra derived from the B-passband data are illustrated in Figure 6; others from V-passband are not included since they are essentially redundant with respect to detected frequencies. As would be expected, the fundamental pulsation period ($f_0 \simeq 11.5408\,d^{-1}$ has the greatest amplitude. Successive pre-whitening steps uncovered statistically significant partial harmonics out as far as $4f_0$. The amplitude decay appears to be exponential as a function of harmonic order (Figure 7), a behavior that has been observed with other HADS variables such as VX Hya (Templeton *et al.* 2009) and RR Gem (Jurcsik *et al.* 2005). Although no other independent pulsation modes were detected during this short campaign, it is acknowledged that a longer baseline in time from multiple sites would be required to validate this claim (Breger 2000). Representative LC fits to B- and V-mag time-series data (05 May 2021) following DFT analysis are respectively illustrated in Figures 8 and 9.

3.4. Global parameters

Absolute visual magnitude (M_V) was estimated (1.800 ± 0.015) after substituting the pulsation period ($P = 0.08664937$ d) into Equation 3, the P-L relationship reported by Poro *et al.* (2021) for δ Scuti stars oscillating in a fundamental radial mode:

$$M_V = (-3.200 \pm 0.010) \log(P) - (1.599 \pm 0.010). \quad (3)$$

Thereafter applying known values for m, ($V_{avg} = 13.112 \pm 0.031$), $A_V = 0.1119 \pm 0.0370$), and M_V, the reddening-corrected distance modulus (Equation 4):

$$d(pc) = 10^{(m - M_V - A_V + 5)/5}, \quad (4)$$

produced an estimated distance (1737 ± 40 pc) to V417 Boo. This value is within 4.5% of the Gaia DR2 determination of distance ($1663^{+79.2}_{-72.4}$ pc) calculated from parallax using the Bailer-Jones bias correction (Bailer-Jones 2015). As it turns out V417 Boo is in a region of the Milky Way (Gal. coord. (J2000): l = 82.8255; b = 49.7338) where corrections for interstellar extinction ($A_V = 0.1119$) should be included. This is an important distinction when comparing our results to those reported in Gaia DR2 wherein interstellar extinction (A_G) is assumed to be zero. Accordingly the luminosity and radius were determined (Table 4) as follows where $V_{avg} = 13.112 \pm 0.031$, $A_V = 0.1119 \pm 0.037$, $M_V = 1.783$, and $BC_V = 0.0312$. Luminosity ($L_* = 14.52 \pm 0.20\,L_\odot$) was calculated according to Equation 5:

$$\frac{L_*}{L_\odot} = 10^{((M_{bol\odot} - M_{bol*})/2.5)}, \quad (5)$$

where $M_{bol\odot} = 4.74$ and $M_{bol*} = 1.835$. Finally, the radius of V417 Boo in solar units ($R_* = 2.18 \pm 0.02$) was estimated using the well-known relationship (Equation 6) where:

$$\frac{L_*}{L_\odot} = \left(\frac{R_*}{R_\odot}\right)^2 \left(\frac{T_*}{T_\odot}\right)^4. \quad (6)$$

Table 4. Global stellar parameters for V417 Boo using empirically derived values and those predicted from the PARSEC model where Z = 0.020.

Parameter	*SO*	*PARSEC*
Mean T_{eff}[K]	7640 ± 181	7640 ± 181
Luminosity [$L_\odot$]	14.52 ± 0.20	14.52 ± 0.20
Mass [$M_\odot$]	1.87 ± 0.01	1.82 ± 0.02
Radius [$R_\odot$]	2.18 ± 0.02	2.21 ± 0.01
rho [g/cm3]	0.256 ± 0.006	0.238 ± 0.003
log g [cgs]	4.034 ± 0.042	4.010 ± 0.012
Q [d]	0.037 ± 0.002	0.036 ± 0.001

Stellar radius was independently estimated from an empirically derived period-radius (P-R) relationship (Equation 7) reported by Laney *et al.* (2003) for HADS stars and classical Cepheids:

$$\log(R_*) = a + b \cdot \log(P) + c, \quad (7)$$

where $a = 1.106 \pm 0.012$, $b = 0.725 \pm 0.010$, and $c = 0.029 \pm 0.024$. In this case the value for R_* ($2.32 \pm 0.36\,R_\odot$) was 13.8% higher than value obtained from observations at SO ($2.18 \pm 0.02\,R_\odot$).

Unlike the mass derived from the Keplerian motion of binary stars, the mass of a single isolated field star is very difficult to determine accurately. We adopted a model using MS stars in detached binary systems (Eker *et al.* 2018) which established a mass-luminosity relationship ($1.05 < M/M_\odot \leq 2.40$) according to the following equation:

$$\log(L) = 4.329(\pm 0.087) \cdot \log(M) - 0.010(\pm 0.019), \quad (8)$$

whereby a mass value in solar units ($1.865 \pm 0.014\,M_\odot$) was calculated. Other derived values for density ($\rho_\odot$), surface gravity (log g), and pulsation constant (Q) are also included in Table 4 along with those estimated from evolutionary modeling (section 3.5). Stellar density (ρ_*) in solar units (g/cm³) was calculated according to Equation 9:

$$\rho_* = \frac{3 \cdot G \cdot M_* \cdot m_\odot}{4\pi(R_* \cdot r_\odot)^3}. \quad (9)$$

where G = the gravitational constant ($6.67408 \cdot 10^{-8}\,cm \cdot g^{-1} \cdot sec^{-2}$), $m_\odot$ = solar mass (g), $r_\odot$ = solar radius (cm), M_* is the mass, and R_* the radius of V417 Boo in solar units. Using the same algebraic assignments, surface gravity (log g) was determined by the following expression:

$$\log g = \log\left(\frac{M_* \cdot m_\odot \cdot G}{(R_* \cdot r_\odot)^2}\right). \quad (10)$$

When attempting to characterize p-mode pulsations (radial) it is helpful to introduce the concept of a pulsation constant (Q). The dynamical time that it takes a p-mode acoustic wave to internally traverse a star is related to its size but more accurately the mean density. This is defined by the period-density relationship:

$$Q = P\sqrt{\bar{\rho}_*/\bar{\rho}_\odot}. \quad (11)$$

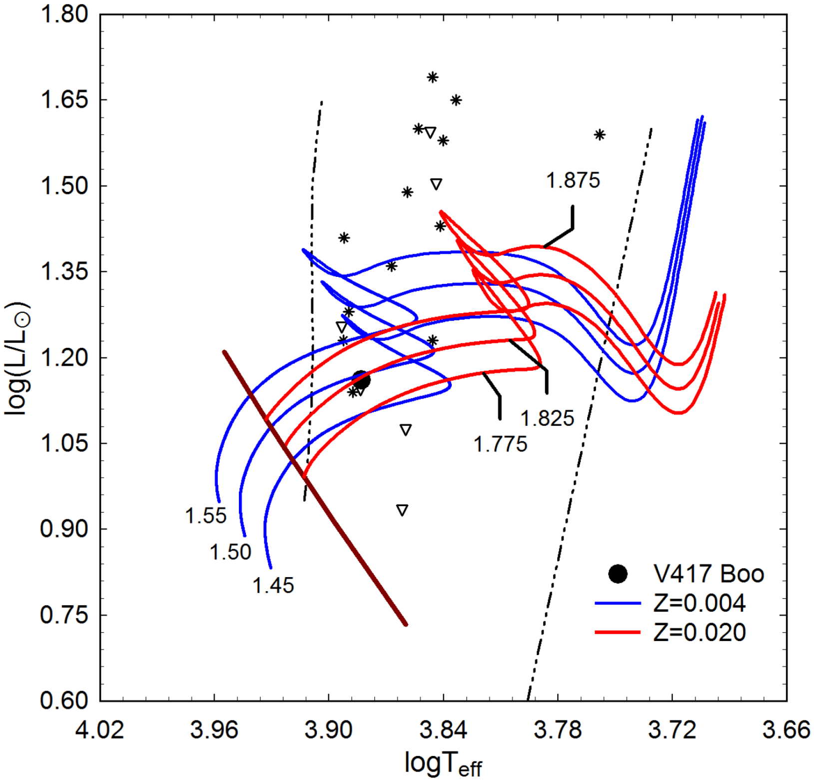

Figiure 10. Evolutionary tracks (red solid line: Z = 0.020 at 1.775, 1.825, and 1.875 $M_\odot$ and blue line: Z = 0.004 at 1.45, 1.50, and 1.55 $M_\odot$) derived from PARSEC models (Bressan *et al.* 2012). The position of V417 Boo (●) is shown relative to ZAMS (thick maroon line) and within the theoretical instability strip (dashed lines) for radial low-p mode pulsators. Asterisks denote the positions of known HADS stars while open triangles (▽) indicate the position of SX Phe stars (Balona 2018).

where P is the pulsation period (d) and $\bar{\rho}_*$ and $\bar{\rho}_\odot$ are the mean densities of the target star and Sun, respectively. The mean density of an isolated field star like V417 Boo can not be determined without great difficulty. However, it can be expressed in terms (Equation 12) of other measurable stellar parameters where:

$$\log(Q) = -6.545 + \log(P) + 0.5\log(g) + 0.1M_{bol} + \log(T_{eff}). \quad (12)$$

The full derivation of this expression is provided by Breger (1990). The resulting Q values (Table 4) derived from observations at SO are consistent with theory (Q = 0.032 d) and the distribution of Q-values (0.03–0.04 d) from fundamental radial pulsations observed with other δ Sct variables (Breger 1979; Joshi and Joshi 2015; Antonello and Pastori 1981).

Finally, we attempted to get a comparative sense of how the physical size, temperature, and brightness of V417 Boo changes over the course of a single 2.08-hour pulsation. As shown in Figure 5 there is a significant change in color index (B–V) as maximum light descends to minimum light. Intrinsic color reveals that at maximum light, where $(B-V)_0 = 0.192 \pm 0.028$, the corresponding effective temperature is 7814 ± 171 K, whereas at minimum light ($(B-V)_0 = 0.372 \pm 0.032$) the estimated effective temperature is 6859 ± 151 K. Between these two extremes the putative rise in temperature (+956 K) would correspond to a 1.4-fold increase in luminosity with a relatively small decrease (9.4%) in radius. This rather crude estimate for changes in stellar radius would be best performed using the Baade-Wesselink method developed by Wesselink (1946), should radial velocity data over an entire oscillation cycle become available for this system.

3.5. Evolutionary status of V417 Boo

We can attempt to describe the evolutionary status of this variable using our estimates for luminosity and effective temperature. These values are plotted in the theoretical Hertzsprung-Russell diagram (HRD) shown in Figure 10. Here, the thick solid line gives the Zero Age Main Sequence (ZAMS) position for stars with solar metallicity (Z = 0.020) while two broken lines nearly perpendicular to the ZAMS delimit the blue and red edges of the theoretical instability strip for radial low-p modes (Xiong *et al.* 2016). The positions of several known (Balona 2018) δ Scuti (*) and SX Phe types (▽) are marked. The solid black circle indicates the position of V417 Boo using the SO-derived parameters and corresponding error estimates provided in Table 4. To determine the mass and age of V417 Boo from theoretical evolutionary tracks, its metallicity, Z, the total amount of metals by mass, needs to be known. Unfortunately, a high resolution spectrum is not available for this star so no direct measurement of Z exists. Nonetheless, we can try to estimate its value indirectly. A useful calculation:

$$z = d \cdot \sin(b), \quad (13)$$

where d is distance in pc (1663) and b is the Galactic latitude (49.7338°) places V417 Boo nearly 1267 pc above the Galactic plane in thick disk territory and not the halo, an area generally occupied by older metal-poor stars. We can therefore assume that V417 Boo approaches solar metallicity, or at most a few times lower, which also corresponds to the metallicity of metal-rich globular clusters classified as Oosterhoff type I.

A definitive measure for total solar metallicity, Z, remains elusive despite the fact that the Sun is our closest star. Values obtained over the last few decades range between 0.012 and 0.020, including one derived by Asplund *et al.* (2009) where $Z_{\odot} = 0.0142$. However, von Steiger and Zurbuchen (2016) challenged this result after obtaining a value of $Z_{\odot} = 0.0196 \pm 0.0014$ based on the chemical composition of solar wind. Soon thereafter, Serenelli *et al.* (2016) showed that their analysis of the solar wind was in serious disagreement with observables from the basic solar model so it cannot be representative of the solar interior. Obviously, a precise value for $Z_{\odot}$ still remains an open question (Vagnozzi 2019). Nonetheless, we plot two series of PARSEC evolutionary models (Bressan *et al.* 2012) in Figure 10 wherein red solid lines show the models with $Z = 0.020$ and blue solid lines define the models with $Z = 0.004$. The latter models would correspond to a decrease in metallicity by a factor of 3 to 5, depending on the reference solar metallicity. Assuming $Z = 0.020$, it can be shown by linear interpolation from the closest isochrone ($1.825 M_{\odot}$) that V417 Boo has a mass of $1.82 \pm 0.02\ M_{\odot}$. As depicted in Figure 10, the isochrone defined by a MS star with mass $1.825\ M_{\odot}$ ranges in age from $1.01 \cdot 10^8$ to $1.64 \cdot 10^9$ yr, wherein V417 Boo falls at 0.95 ± 0.10 Gyr. Each isochrone model contains predictions about changes in T_{eff}, $L_{\odot}$, and $R_{\odot}$ with time. The observed luminosity and effective temperature of V417 Boo lies within a range of predicted values where $R_{\odot} = 2.21 \pm 0.01$. Alternatively, a metal-poor ($Z = 0.004$) star would likely be somewhat smaller ($R_{\odot} = 2.15 \pm 0.03$), less massive ($M_{\odot} = 1.51 \pm 0.07$), and older ($1.71 \pm 0.01$ Gyr). V417 Boo lies well within the instability strip among the other known HADS stars. Uncertainty in the determination of mass will hopefully improve should high resolution spectroscopic data become available for V417 Boo in the future.

4. Conclusions

This first two-color (B and V) CCD study of V417 Boo has produced 39 new times of maximum which, along with other published values, lead to an updated linear ephemeris. Potential changes in the pulsation period assessed using the observed and predicted times of maximum suggest that since 2010 no significant change has occurred. Deconvolution of time-series photometric data by discrete Fourier transformation indicates that V417 Boo is a monoperiodic radial pulsator ($f_0 \simeq 11.5408\ d^{-1}$) which also oscillates in at least three other partial harmonics ($2f_0$–$4f_0$). A low resolution spectrum suggested an A7V classification, which was consistent with the adopted median effective temperature (7640 ± 181 K). These results, along with the distance estimate (1737 ± 40 pc), agreed reasonably well with the same findings (1663^{-72}_{+79} pc) provided by Gaia DR2. The pulsation period (0.0866494 d), oscillation mode (radial), V_{mag} amplitude (0.45 mag), and LC morphology are all consistent with the defining characteristics of a HADS variable. Furthermore, evolutionary tracks from the PARSEC model which assume near solar abundance ($Z = 0.020$) for V417 Boo are best matched by a MS star with a mass of $1.82 \pm 0.02\ M_{\odot}$ and radius of $2.21\ R_{\odot}$. These results are consistent with an independent mass estimate, $1.87 \pm 0.01\ M_{\odot}$, derived from an empirical mass-luminosity relationship (Eker *et al.* 2018). It would appear that the estimated mass of V417 Boo (1.80–$1.90\ M_{\odot}$) exceeds the generally accepted threshold ($M < 1.3\ M_{\odot}$) for SX Phe stars (McNamara 2011).

5. Acknowledgements

This research has made use of the SIMBAD database operated at Centre de Données astronomiques de Strasbourg, France. Time of maximum light data from the *Information Bulletin on Variable Stars* (IBVS) website (https://konkoly.hu/IBVS/IBVS.html) proved invaluable to the assessment of potential period changes experienced by this variable star. In addition, the International Variable Star Index maintained by the AAVSO, the All-Sky Automated Survey for Supernovae, and the Catalina Sky Survey (CSDR1) maintained at CalTech were mined for critical information. This work also presents results from the European Space Agency (ESA) space mission Gaia. Gaia data are being processed by the Gaia Data Processing and Analysis Consortium (DPAC). Funding for the DPAC is provided by national institutions, in particular the institutions participating in the Gaia MultiLateral Agreement (MLA). The Gaia mission website is https://www.cosmos.esa.int/gaia. The Gaia archive website is https://archives.esac.esa.int/gaia. The use of public data from LAMOST is also acknowledged. Guoshoujing Telescope (the Large Sky Area Multi-Object Fiber Spectroscopic Telescope LAMOST) is a National Major Scientific Project built by the Chinese Academy of Sciences. Funding for the project has been provided by the National Development and Reform Commission. LAMOST is operated and managed by the National Astronomical Observatories, Chinese Academy of Sciences. The diligence and dedication shown by all associated with these organizations is very much appreciated. We gratefully acknowledge the careful review and helpful commentary provided by an anonymous referee and Editor Morrison.

References

Akerlof, C., *et al.* 2000, *Astron. J.*, **119**, 1901.

Amôres, E. B. and Lépine, J. R. D. 2005, *Astron. J.*, **130**, 659.

Amôres, E. B. and Lépine, J. R. D. 2007, Astron. J., 133, 1519.

Antonello, E., and Pastori, L. 1981, *Publ. Astron. Soc. Pacific*, **93**, 237.

Asplund, M., Grevesse, N., Sauval, A. J., and Scott, P. 2009, *Annu. Rev. Astron. Astrophys.*, **47**, 481.

Baade, W. 1956, *Publ. Astron. Soc. Pacific*, **68**, 5.

Baglin, A. 2003, *Adv. Space Res.*, **31**, 345.

Bailer-Jones, C. A. L. 2015, *Publ. Astron. Soc. Pacific*, **127**, 994.

Balona, L. A. 2018, *Mon. Not. Roy. Astron. Soc.*, **479**, 183.

Balona, L. A., and Nemec, J. M. 2012, *Mon. Not. Roy. Astron. Soc.*, **426**, 2413.

Baran, A. S., Koen, C., and Porkrzywka, B. 2014, *Mon. Not. Roy. Astron. Soc.*, **448**, L16.

Bedding, T. R., *et al.* 2020, *Nature*, **581**, 147.

Breger, M. 1979, *Publ. Astron. Soc. Pacific*, **91**, 5.

Breger, M. 1990, *Delta Scuti Newsl.*, **2**, 13.

Breger, M. 2000, *Baltic Astron.*, **9**, 149.

Bressan, A., Marigo, P., Girardi, L., Salasnich, B., Dal Cero, C., Rubele, S., and Nanni, A. 2012, *Mon. Not. Roy. Astron. Soc.*, **427**, 127.

Gaia Collaboration, *et al.* 2018, *Astron. Astrophys.*, **616A**, 1.

Chevalier, C. 1971, *Astron. Astrophys.*, **14**, 24.

Cox, J. P. 1963, *Astrophys. J.*, **138**, 487.

Drake, A. J., *et al.* 2009, *Astrophys. J.*, **696**, 870.

Eker, Z., *et al.* 2018, *Mon. Not. Roy. Astron. Soc.*, **479**, 5491.

Elst, E. W. 1978, *Inf. Bull. Var. Stars*, No. 1442, 1.

Flower, P. J. 1996, *Astrophys. J.*, **469**, 355.

Garg, A., *et al.* 2010, *Astron. J.*, **140**, 328.

Gilliland, R. L., *et al.* 2010, *Publ. Astron. Soc. Pacific*, **122**, 131.

Guzik, J. A. 2021, *Frontiers Astron. Space Sci.*, **8**, 653558 (DOI: 10.3389/fspas.2021.653558).

Henden, A. A., Welch, D. L., Terrell, D., and Levine, S. E. 2009, *Bull. Amer. Astron. Soc.*, **41**, 669.

Henden, A. A., Terrell, D., Welch, D., and Smith, T. C. 2010, *Bull. Amer. Astron. Soc.*, **42**, 515.

Henden, A. A., Levine, S. E., Terrell, D., Smith, T. C., and Welch, D. L. 2011, *Bull. Amer. Astron. Soc.*, **43**, 2011.

Holdsworth, D. L., *et al.* 2014, *Mon. Not. Roy. Astron. Soc.*, **439**, 2078.

Hoffman, D. I., Harrison, T. E., and McNamara, B. J. 2009, *Astron. J.*, **138**, 466.

Jayasinghe, T., *et al.* 2021, *Mon. Not. Roy. Astron. Soc.*, **503**, 200.

Joshi, S., and Joshi, Y. C 2015, *J. Astrophys. Astron.*, **36**, 33.

Jurcsik, J., *et al.* 2005, *Astron. Astrophys.*, **430**, 1049.

Kukarkin, B. V., Parenago, P. P., Efremov, Yu. N., and Kholopov, P. N. 1951, *The Catalogue of the Stars of Suspected Variability*, Academy of Sciences, Moscow.

Laney, C. D., Joner, M., and Rodriguez, E. 2003, in *Interplay of Periodic, Cyclic and Stochastic Variability in Selected Areas of the H-R Diagram*, ed. C. Sterken, Astron. Soc. Pacific Conf. Ser. 292, Astronomical Society of the Pacific, San Francisco, 203.

Leavitt, H. S., and Pickering, E. C. 1912, *Circ. Harvard Coll. Obs.*, No. 173, 1.

Lee, Y.-H., Kim, S. S., Shin, J. Lee, J., and Jin, H. 2008, *Pub. Astron. Soc. Japan*, **60**, 551.

Lenz, P., and Breger, M. 2005, *Commun. Asteroseismology*, **146**, 53.

Lindegren, L., *et al.* 2016, *Astron. Astrophys.*, **595A**, 4.

Minor Planet Observer. 2010, MPO Software Suite (http://www.minorplanetobserver.com), BDW Publishing, Colorado Springs.

McNamara, D. H. 2000, in *Delta Scuti and Related Stars*, eds. M. Breger, M. Montgomery, Astron. Soc. Pacific Conf. Ser., 210, Astronomical Society of the Pacific, San Francisco, 373.

McNamara, D. H. 2011, *Astron. J.*, **142**, 110.

Nemec, J. M., Balona, L. A., Murphy, S. J., Kinemuchi, K., and Jeon, Y.-B. 2017, *Mon. Not. Roy. Astron. Soc.*, **466**, 1290.

Niu, J.-S., Fu, J.-N., and Zong, W.-K. 2013, *Res. Astron. Astrophys.*, **13**, 1181.

Niu, J.-S., *et al.* 2017, *Mon. Not. Roy. Astron. Soc.*, **467**, 3122.

Paunzen, E., and Vanmunster, T. 2016, *Astron. Nachr.*, **337**, 239.

Poretti, E. 2003a, *Astron. Astrophys.*, **409**, 1031.

Poretti, E. 2003b, in *Interplay of Periodic, Cyclic and Stochastic Variability in Selected Areas of the H-R Diagram*, ed. C. Sterken, ASP Conf. Ser. 292, Astronomical Society of the Pacific, San Francisco, 145.

Poro, A., *et al.* 2021, *Publ. Astron. Soc. Pacific*, **133**, 084201.

Qian, S.-B., Li, L.-J., He, J.-J., Zhang, J., Zhu, L.-Y., and Han, Z.-T. 2018, *Mon. Not. Roy. Astron. Soc.*, **475**, 478. [2018 not 2017]

Ricker, G. R., *et al.* 2015, *J. Astron. Telesc, Instrum. Syst.*, **1**, 014003.

Rodríguez E. and Breger M. 2001, *Astron. Astrophys.*, **366**, 178.

Schlafly, E. F., and Finkbeiner, D. P. 2011, *Astrophys. J.*, **737**, 103.

Schlegel, D. J., Finkbeiner, D. P., and Davis, M. 1998, *Astrophys. J.*, **500**, 525.

Schwarzenberg-Czerny, A. 1996, *Astrophys. J.*, **460L**, 107.

Serenelli, A., Scott, P., Villante, F. L., Vincent, A. C., Asplund, M., Basu, S., Grevesse, N., and Peña-Garay, C. 2016, *Mon. Not. Roy. Astron. Soc.*, **463**, 2.

Shappee, B. J., *et al.* 2014, *Astrophys. J.*, **788**, 48.

Skrutskie, M. F., *et al.* 2006, *Astron. J.*, **131**, 1163.

Smith, T. C., Henden, A. A., and Starkey, D. R. 2011, in *The Society for Astronomical Sciences 30th Annual Symposium on Telescope Science*, Society for Astronomical Sciences, Rancho Cucamonga, CA, 121.

Software Bisque. 2019, TheSkyX professional edition 10.5.0 (https://www.bisque.com).

Templeton, M. R., Samolyk, G., Dvorak, S., Poklar, R., Butterworth, N., and Gerner, H. 2009, *Publ. Astron. Soc. Pacific*, **121**, 1076.

Torres, G. 2010, *Astron. J.*, **140**, 1158.

Unsold, M. 2000, ImagesPlus Ver. 6.5 (http://www.mlunsold.com/ILOrdering.html).

Uytterhoeven K., *et al.* 2011, *Astron. Astrophys.*, **534A**, 125.

Vagnozzi, S. 2019, *Atoms*, **7**, 41.

Vanmunster, T. 2011, light curve and period analysis software, Peranso v.2.50 (https://www.cbabelgium.com/peranso).

von Steiger, R., and Zurbuchen, T. H. 2016, *Astrophys. J.*, **816**, 13.

Walker, G., *et al.* 2003, *Publ. Astron. Soc. Pacific*, **115**, 1023.

Wang, R., *et al.* 2019, *Pub. Astron. Soc. Pacific*, **131**, 024505.

Warner, B. D. 2007, *Minor Planet Bull.*, **34**, 113.

Watson, C., Henden, A. A., and Price, C. A. 2014, AAVSO International Variable Star Index VSX (Watson+, 2006–2014; https://www.aavso.org/vsx).

Wesselink, W. J. 1946, *Bull. Astron. Inst. Netherlands*, **10**, 91.

Wils, P., *et al.* 2011, *Inf. Bull. Var. Stars*, No. 5977, 1.

Wils, P., *et al.* 2012, *Inf. Bull. Var. Stars*, No. 6015, 1.

Wils, P., *et al.* 2013, *Inf. Bull. Var. Stars*, No. 6049, 1.

Wils, P., *et al.* 2014, *Inf. Bull. Var. Stars*, No. 6122, 1.

Wils, P., *et al.* 2015, *Inf. Bull. Var. Stars*, No. 6150, 1.

Woźniak, P. R., *et al.* 2004, *Astron. J.*, **127**, 2436.

Xiong, D. R., Deng, L., Zhang, C., and Wang, K. 2016, *Mon. Not. Roy. Astron. Soc.*, **457**, 3163.

Yang, T.-Z, Sun, X.-Y., Zuo, Z.-Y. and Liu, H.-W. 2021, *Astron. J.*, 161, 27.

Zacharias, N., *et al.* 2010, *Astron. J.*, **139**, 2184.

Zhao, G., Zhao, Y.-H., Chu, Y.-Q., Jing, Y.-P., and Deng, L.-C. 2012, *Res. Astron. Astrophys.*, **12**, 723.

Ziaali, E., Bedding, T. R., Murphy, S. J., Van Reeth, T., and Hey, D. R. 2019, *Mon. Not. Roy. Astron. Soc.*, **486**, 4348.

Accuracy and Precision in Amateur Photometry

Edward O. Wiley
Live Oaks Observatory, Stellar Skies, Pontotoc, TX; ewiley@suddenlink.net

Kenneth Menzies
Tigh Speuran Observatory, Framingham, MA; kenmenstar@gmail.com

Received December 5, 2021; revised February 5, 2022; accepted February 7, 2022

Abstract Photometric accuracy and photometric precision were determined using the average magnitude and standard deviation of 7 to 10 images of 63 Landolt stars taken from 11 Northern Landolt fields by two amateur observers using CCD sensors in B, V, and I_c. Similar measures were taken for two of these Landolt fields using a CMOS sensor from the AAVSO Bright Star Monitoring NH2 observatory. A series of analyses were performed on observed average magnitudes compared to known Landolt magnitudes of the pooled data under different treatments that included both transformed and untransformed analyses under both single comparison star and ensemble treatments using observed minus known magnitude values (O–K analysis). A variety of non-parametric tests of magnitudes resulting from different treatments using absolute O–K values was used to assess the statistical differences between treatments. Regression analysis using untransformed (“raw”) O–K values and B–V color indexes for each star were used to assess the differences between transformed and untransformed treatments for each filter and test for any statistical differences. Correlation analysis was used to assess the relationship between accuracy and precision. In most cases, transformed magnitudes are statistically more accurate than untransformed magnitudes. Even when there is no statistical difference in median values between transformed and untransformed results there is a statistically significant difference in the regression analysis indicating that transformation improves accuracy for the data as a whole in each filter. There were no statistical differences between the 16-bit CCD results and the 12-bit CMOS results for the two fields analyzed. Both were capable of a median accuracy of 0.02 magnitude or less, which is similar to the accuracies of the same APASS secondary standard stars in four of the fields included in the study. We detected no statistical difference between using a single versus small ensemble of comparison stars but prefer ensembles for reasons given. Precision is not correlated with accuracy nor need it be for some studies.

1. Introduction

Amateur photometrists desire their measurements to be both accurate and precise. But what does this mean? Photometric magnitudes reported to AAVSO are generally reported with uncertainty values, either derived from signal-to-noise estimates or standard deviation of the target star (if slowly varying), a check star of similar magnitude, or an ensemble. These estimates are certainly a measure of uncertainty of submitted observations, but how do they relate to the accuracy of the observations? To carefully assess uncertainty, we need to clearly separate accuracy (i.e., systematic error) and precision (i.e., random error).

Mandel (1964) outlines two concepts of accuracy: (1) accuracy relative to a value accepted as the “real” value, or (2) a value assigned to be true by consensus (or agreement). The value of the speed of light in a vacuum is an example of (1). A value assigned by expert consensus, as in the value of the meter, is an example of (2). Landolt standard stars (LSS) are an example of magnitude values assigned by expert opinion (2). Therefore, the difference between a measured magnitude of a Landolt star and the Landolt standard magnitude will provide a measure of accuracy within the accepted value of the uncertainty of the Landolt standard magnitude.

Precision is harder to define. To Mandel, it is easier to define imprecision: “Given a well described experimental procedure for measuring a particular characteristic of a chemical or physical system, and given such a system, we can define imprecision as the amount of scatter exhibited by the results obtained by repeated application of the process to that system” (Mandel 1964, p. 103). For example, if you repeatably measure the brightness of a slowly changing variable or a check star, then the standard deviation will provide a measure of imprecision. In photometry, imprecision is often referred to as a measurement of uncertainty. In general, it is meant to describe the distributional scatter of point source measures in a (hopefully) Gaussian set of observed magnitudes.

Papers in the literature with discussions of accuracy and precision fall into two categories. In the professional literature the concern is accurate measurement of flux by careful control of image acquisition and processing under known conditions (e. g., Stubbs and Tonry 2006). When Stubbs and Tonry (2006) use the term accuracy, they refer to the accuracy of uncertainty values of flux measurements. In a similar vein more applicable to amateurs are papers outlining best practices in photometry that are likely to improve precision (e.g., Newberry 1999; Koppelmann 2005). Sonnett *et al.* (2013, p. 446) define a measure of photometric accuracy as the Root Mean Square (RMS) residual of a magnitude estimate from a light curve model. An assessment of fit with other observations to a light curve model has merit in identifying outliers, but our understanding of models is that they are never true; their function is to predict future observations. Thus, they do not fulfill the accepted concepts outlined by Mandel. We propose to address accuracy and imprecision on the level of amateur photometry directly by addressing the Mandel criterion, comparing a result to a known standard.

Our main objective is to access photometric accuracy using differential aperture photometric techniques with typical amateur equipment and protocols. In doing so we hope to provide protocols for other amateurs to access their accuracy by imaging Landolt (or other) standard star fields. The ability to produce reasonably accurate results using standard stars gives confidence that measures of variable stars are also reasonably accurate in spite of the fact that no one can access the true accuracy of a variable at any given time of observation.

We assess accuracy using observed and known BVI_c magnitude values of Landolt Standard Stars (LSS) by comparing their known accepted magnitudes (K) against their observed magnitudes (O) using O–K analysis, a variant of O–C analysis using the known magnitude rather than a magnitude computed from a model. Magnitudes reported by Landolt (2013) were derived by repeated measures over several nights. The uncertainties reported are "mean errors of means," and not directly comparable to uncertainties of a single nightly measure or the standard deviation of a series of measures. Thus, to directly compare our accuracy with the Landolt standard would require observations over multiple nights, a research method not likely to be employed by amateur photometrists. However, Landolt (1983, p. 450) provides a method to calculate the "mean error for a single observation" by multiplying the square root of the number of nights the star was observed by the mean error of means. We performed these calculations on one field comprising all the stars of SA20 for B, V, and I_c magnitudes. Johnson V single observation error ranged from 0.001 to 0.011 magnitude: B from 0.001 to 0.011 magnitude, and I_c from 0.002 to 0.018 magnitude. These ranges are accuracy ranges, not precision ranges as the mean-of-means magnitude is taken as the known standard value. We conclude that any magnitude that we might measure, that is within 0.01 O–K, would be considered very accurate.

We evaluate various data reduction approaches for accuracy of magnitude estimates under transformed and untransformed protocols as well as for single comparison star versus ensemble comparison star protocols. Each such recalculation of the data is referred to as a "treatment." We ask four questions about both accuracy and precision:

1. Does transforming data into the standard Johnson-Cousins magnitude system (BVR_cI_c) using differential photometric protocols improve the accuracy of magnitude estimates?

2. If so, what is the effect on accuracy if we use more than one comparison star to form a small ensemble?

3. What is the relationship between accuracy and precision?

4. What differences are there between magnitude estimates made with two 16-bit CCD sensors and those taken with one 12-bit CMOS sensor?

2. Equipment

The following systems were utilized to conduct this study:

(a) Live Oaks Observatory (LOO). Location: 30.98° N 98.94° W. Mount: AstroPhysics Ap900 (German Equatorial). OTA: Celestron on HD with focal reducer, 280 mm f/7. Detector: Moravian G21600 Mk.1 (1536 × 1024 pixels, 9-micron square pixels, bin 1). Filters: B,V,I_c. Flats: Light box. Capture software: PD Capture. Reduction software: LesvePhotometry (de Ponthière 2011) Field of View: 24 × 16 arcminutes.

(b) Tigh Speuran Observatory (TSO). Location: 42.31° N 71.42° W. Mount: Paramount ME (German Equatorial). OTA: Hyperion, 317 mm f/8. Detector: SBIG STL-6303e (3072 × 2048 pixels, 9-micron square pixels, bin 2). Filters: B,V,I_c. Flats: Sky. Capture software: Maxim DL. Reduction software: LesvePhotometry. Field of View: 37 × 25 arcminutes.

(c) BSM_NH2 Observatory (BSM-NH2). Location: 43.69° N 71.56° W. Mount: Paramount ME (German Equatorial). OTA: Takahashi Epsilon, 180 mm f/2.8. Detector: ZWO ASI-183 (5496 × 3672 pixels, 2.4-micron square pixels, bin 2, gain 0). Filters: B,V,I_c. Flats: Sky. Capture software: Maxim DL. Reduction software: LesvePhotometry. Field of View: 90 × 60 arcminutes.

3. Methods

Five Landolt fields were imaged at the LOO observatory and six Landolt fields were imaged at the TSO observatory, both using CCD imagers. Two Landolt fields were imaged at the BSM NH2 Bright Star Monitor Network observatory using a CMOS imager. Details of each field observed are shown in Table 1. Ten images were taken of each target field and calibrated using dark, flat, and bias frames. Acceptable images were uploaded to LesvePhotometry for analysis, resulting in 7 to 10 images of each standard field. In LesvePhotometry standard field star magnitudes were downloaded from the AAVSO VSD comparison star database via the AAVSO VSP chart-creation software. For each field, a surrogate target star that was not a Landolt Standard Star (LSS) was selected as the target; the resulting sequences (LSS comparison stars and target) were saved as a master sequence in an Excel® workbook. The surrogate target was not analyzed but used as a place holder required by LesvePhotometry.

LesvePhotometry (LP) uses terms differently than AAVSO. The AAVSO "comparison" star is designated in LP with "R" (reference). An ensemble of these comparison stars would all be labeled "R" in LP but labeled as a comparison star ensemble in AAVSO nomenclature. The check star is the same in both nomenclatures. However, in LP we can introduce additional

Table 1. Observatories, detectors, and image fields.

Observatory	*Detector*	*Field*	*Date*
L00	CCD	SA20-SF4	1/18/2020
L00	CCD	SA32-SF1	11/24/2019
L00	CCD	SA26-SF1	2/25/2020
L00	CCD	SA95 (SW)	1/19/2020
L00	CCD	SA98-SF1	2/24/2020
TSO	CCD	SA20-SF2	2/20/2020
TSO	CCD	SA23-SF1	2/21/2020
TSO	CCD	SA23-SF4	4/24/2021
TSO	CCD	SA26-SF1	2/23/2020
TSO	CCD	SA32-SF4	4/24/2021
TSO	CCD	SA38	6/8/2020
BSM_NH2	CMOS	SA38	7/7/2020
BSM_NH2	CMOS	SA32-SF4	4/24/2021

stars that would function as additional check stars by designating these available comparison stars with the LP designation "C." In a Landolt field this allows for several standard stars to function as "targets" for magnitude estimation.

A number of templates were produced from the master sequence with different combinations of standard stars to be treated as Landolt targets for magnitude estimation (CK and C stars in LP terms) and one or more stars to be treated as comp stars (R in LP). Each combination is herein termed a "treatment." Transformed treatments were labeled with "-T," and untransformed treatments with "-NT." We use the more familiar AAVSO terminology, so "1C-NT" refers to a treatment with one comparison star (R), one check star (CK), and a variable number of additional Landolt standard stars as "target" check stars (C). Treatments were as follows:

(a) 1C: single comparison star (R), one check (CK), and all remaining LSS as additional "target" check stars (C). Both a transformed treatment (1C-T) and untransformed treatment (1C-NT) analysis were performed. They were applied to all image sets.

(b) 2C: two-star comparison ensemble (R), one check (CK), and all remaining LSS as additional "target" check stars (C). As above, both transformed and untransformed treatments were performed (e.g., treatments 2C-T, 2C-NT). Two iterations of 2C analysis were performed, switching two reference comparison stars for two comp stars (e.g., switching two "R" comps to two "C" comps and vice versa) to increase sample size. They were applied only to the LOO image sets.

(c) allC: All but two LSS as an ensemble (R), with one check and one additional "target" check star (C). The allC analyses were iterated so that each LSS, in turn, was a "target," one was a check, and the remaining were a comparison ensemble (Rs). So, if the field comprised five LSS, there were five analyses. This analysis was only performed on transformed data for reasons given in the discussion and applied only to the LOO image sets.

(d) 3C: Ensemble of three comparison(R), one check (CK), and all remaining LSS as "target" check stars (C). Both transformed and untransformed analyses (3C-T, 3C-NT) were performed, and applied to both TSO and BSM-NH2 image sets, including CCD and CMOS images, respectively.

Differential aperture photometry was performed in LesvePhotometry. Results were sorted in Excel® spreadsheets by BVI$_c$ filter and treatment (T, NT). The magnitudes of target stars (CK and C stars) were averaged (N = 7–10, depending on image quality) and the standard deviations were calculated as a measure of precision. In addition to our observations, AAVSO Photometric All-Sky Survey (APASS; Henden *et al.* 2018) standard magnitudes are known for four of the Landolt Standard Fields (SA20-SF4, SA23-SF1, SA95, and SA98) for both the Johnson B and Johnson V bandpasses. We performed O–K analysis of the APASS magnitudes to compare to our own results.

Statistical tests, regression analysis, and boxplot visualizations of central tendencies and variation were conducted under the assumption that the measures of stars in the same and different fields for each filter could be combined into a single population of measures. Data were organized by filter and treatment. Statistically significant differences are denoted by an asterisk (*) in the tables.

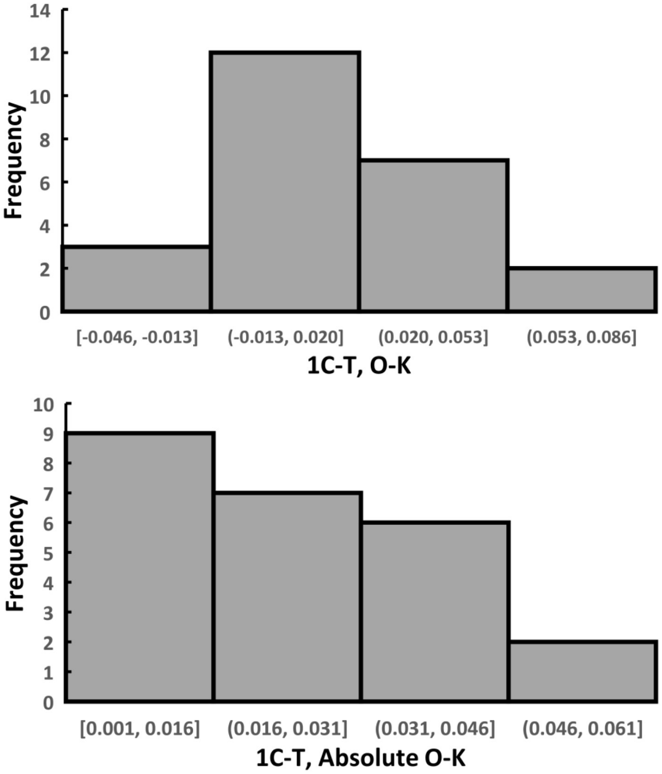

Figure 1. Frequency distributions of Johnson B filter results from Live Oak Observatory. Upper plot: frequency distribution of the O–K values of the One Comparison Star transformed analysis (1C-T). Lower plot: the same data except the O–K values have been transformed to absolute values.

The questions concerning accuracy of observed measures were addressed using observed minus known (O–K) magnitude analyses similar to the more familiar O–C (observed minus calculated) analyses. Values of O–K may be positive or negative. Untransformed ("raw") O–K values may lead to spurious estimates of accuracy since O–K = –0.1 and O–K = +0.1 average to a perfect agreement/accuracy of O–K = 0 when, in fact, both estimates are off by 0.1 magnitude. Thus, absolute values of O–K are more appropriate to assess accuracy. However, transforming O–K values to absolute O–K values sometimes resulted in data distributions that were not normally distributed (Figure 1a, b). Because of this we chose to express central tendencies as medians and adopted a non-parametric approach to evaluate the equality of median absolute O–K values for different treatments.

We used box plots prepared in Excel® to visualize medians and interquartile ranges of different treatments chosen for statistical treatment. Median and interquartile range (IQR) were conducted using a convenient on-line calculator (https://www.calculatorsoup.com).

Statistical comparisons consisted of analyzing the difference between different treatments under the null hypothesis that median values of absolute O–K were statistically identical. However, these data are frequently not normally distributed, and they are also highly correlated, that is, consisting of data of the same star under different treatments. Because of this, we evaluate the null hypothesis that the observed absolute O–K values between treatments are statistically identical using the Wilcoxon Signed Rank test, a non-parametric test designed to evaluate the effects of treatment when the samples are correlated, as is the case here. Where sample size was different between treatments (e.g., 1C data versus 2C data), restricted matrices were prepared that contain only stars common to both analyses. This meets a necessary condition of the Wilcoxon test that requires paired data. Otherwise, all stars were included for 1C-NT versus 1C-T. The null hypothesis is that the medians of the absolute O–K values and their distributions were statistically similar at the p = 0.05 significance level. The tests were conducted on a convenient on-line calculator (https://www.socscistatistics.com).

Questions about the effects of transformation are addressed with untransformed (“raw”) O–K values and regression analysis in Excel®. The B–V color index was designated as the independent variable and the O–K value was designated as the dependent variable. In each treatment the significance of the B–V color index to predict the O–K value was taken as the effect of transformation under the hypothesis that a significant lack of prediction (acceptance of the null hypothesis that there was no association between B–V and O–K, p = >0.05) indicates the positive result of a successful transformation to the Standard Magnitude System. For example, if 1C-NT rejects the null and a 1C-T accepts the null, this indicates that transformation is effective. How effective is a matter of each individual measure, but the overall effect can be judged by the slope of the least-squares fit. A perfect transformation would result in a flat (zero slope) least-squares fit along the O–K = 0 axis. Lack of independence prevents further tests.

Precision was determined by a correlation analysis of absolute O–K and the standard deviation of the mean value of 7 to 10 individual measures of each target star. Correlation analysis was conducted using regression analysis in Excel® where the “Multiple R” value is the correlation coefficient, and a significant value is returned.

4. CCD accuracy and precision—results and discussion

Absolute O–K medians and variation around the median for each treatment are reported in Table 2 and visualized in Figure 2. The general trend is for untransformed data to be less accurate (i.e., larger O–K) and have greater variation (i.e., broader IQR) than transformed data. Most obvious findings were the Johnson B results where both LOO and TSO data show significant differences between untransformed absolute O–K averages (range 0.024–0.076) compared to transformed averages (0.012–0.019). A similar, albeit less dramatic, difference was noted for Cousins I_c. TSO Johnson V also showed improvement for the TSO analyses, but LOO Johnson V showed little to no transformation effect. To informally compare our results to APASS secondary standards we also show box plots of median, quartile, and range variation of transformed Johnson B and V magnitudes of APASS stars from four of the fields that had those data (Figure 2). We note that our transformed data compare well with the APASS data.

The average precision is also reported in Table 2. Precision estimates do not show any obvious differences between transformed and untransformed accuracy estimates. The range of standard deviation among both transformed (0.006–0.019)

Table 2. Summary data for combined standard fields, CCD.

Obs.	*Filter*	*Treatment*	*Median Abs. O–K*	*IQR O–K*	*Precision*	*N*
LOO	B	1C-NT	0.062	0.092	0.013	24
LOO	B	1C-T	0.019	0.031	0.016	24
LOO	B	2C-NT	0.076	0.081	0.013	24
LOO	B	2C-T	0.014	0.023	0.019	29
LOO	B	allC	0.021	0.023	0.012	29
LOO	V	1C-NT	0.011	0.01	0.008	24
LOO	V	1C-T	0.01	0.009	0.009	24
LOO	V	2C-NT	0.001	0.017	0.006	29
LOO	V	2C-T	0.009	0.016	0.006	29
LOO	V	allC	0.001	0.016	0.01	29
LOO	I_c	1C-NT	0.024	0.031	0.01	25
LOO	I_c	1C-T	0.005	0.014	0.011	25
LOO	I_c	2C-NT	0.011	0.085	0.008	28
LOO	I_c	2C-T	0.001	0.039	0.009	29
LOO	I_c	allC	0.002	0.01	0.009	29
TSO	B	1C-NT	0.032	0.03	0.016	34
TSO	B	1C-T	0.012	0.014	0.015	34
TSO	B	3C-NT	0.024	0.0385	0.014	24
TSO	B	3C-T	0.013	0.0185	0.015	24
TSO	V	1C-NT	0.014	0.015	0.01	34
TSO	V	1C-T	0.009	0.009	0.011	34
TSO	V	3C-NT	0.013	0.023	0.008	24
TSO	V	3C-T	0.007	0.0115	0.009	24
TSO	I_c	1C-NT	0.021	0.017	0.017	34
TSO	I_c	1C-T	0.011	0.012	0.018	34
TSO	I_c	3C-NT	0.013	0.0175	0.015	24
TSO	I_c	3C-T	0.009	0.0135	0.016	24

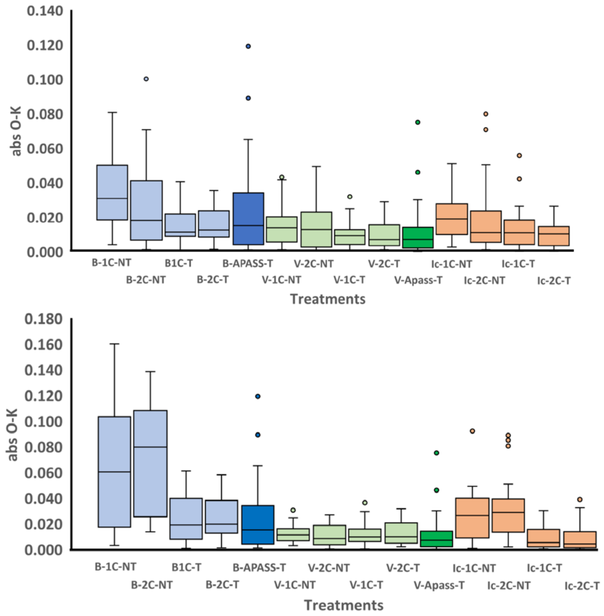

Figure 2. Boxplots of different treatments of absolute O–K values for different treatments Landolt standard stars taken with the telescopes and CCD cameras at (upper plot) the Tigh Speuran Observatory (TSO) and (lower plot) The Live Oak Observatory (LOO), with a comparison of APASS photometry on selected Landolt fields. Median values are horizonal bars within the quartile variation boxes, ranges are the vertical bars, outliers are circles.

and untransformed treatment/analyses (0.006–0.017) were almost identical.

Given the general trend that untransformed data appear less accurate (i.e., larger absolute O–K value), on the whole, than transformed data, we evaluated the null hypothesis that absolute O–K medians were statistically equal in paired treatments (Table 3). In general, tests between transformed versus untransformed absolute O–K values were significantly different (e.g., 1C-NT versus 1C-T). In contrast, tests between transformed data (1C-T versus 3C-T or 1C-NT versus 3C-NT) were not significant at the $p = 0.05$ significance level (Table 3). There were three exceptions, two Cousins I_c from TSO and one Johnson V from LOO (easily identified in Figure 2).

Given the precision values in Table 2, we evaluated the null hypothesis that there was a correlation between precision and accuracy as measured by absolute O–K values (Table 4). We found only five of 24 correlations to be significant ($p = 0.05$). We note that the stars used in this study were picked by us based on what we interpreted as stars with sufficient SNR (e.g., SNR > 20) to expect reasonable photometry. We conclude that under these conditions there is no correlation between accuracy and precision. This supports the fact that accuracy and precision measure different uncertainties (i.e., systematic error vs. random error). We would expect a correlation between SNR, magnitude, and precision (with standard deviation increasing as SNR decreases), but that was not studied here, nor could we investigate the relationship between SNR and accuracy because LesvePhotometry does not return SNR values for our target/check stars. We speculate that pushing the limits of target SNR under difficult or suboptimal seeing conditions would affect both precision and accuracy.

Given Wilcoxon analyses (Table 3) that showed a predominance of significant differences between the accuracy of transformed and untransformed analyses, we explored the effect of transformation on color correlation by performing least-squares fits to pairs of comparable treatments with the color index B–V as the independent variable and the "raw" untransformed O–K value as the dependent variable. The null hypothesis for each analysis is that the slope fit is not statistically different from a slope = 0 ($p = 0.05$). Acceptance of the null hypothesis (and its associated small coefficient of determination) is interpreted herein as a successful color transformation as there would be no statistical association between the B–V color index of a star and its estimated magnitude for a particular filter. Rejection of the null (and a higher coefficient of determination) would imply either untransformed or poorly transformed estimates.

Regression analyses results are reported in Table 4. All untransformed analyses reject the null hypotheses. That is, in all untransformed analysis there was a significant slope fitted to the data and the magnitude of that slope was significantly different from the null of slope = 0. In contrast, twenty-one transformed analyses accept the null. That is, the line fitted to the data have a slope that is statistically flat (slope = 0). A visualization of two regression analyses from TSO for the Johnson B filter using a single comparison star and the same ensemble using three comparison stars are shown in Figure 3 to illustrate these differences. The transformed fits are close

Table 3. Wilcoxon test results, CCD[1].

Observatory	*Filter*	*Treatment*	*N*	*z-Value p*
TSO	B	1C-NT/1C_T	33	<0.001*
TSO	B	3C-NT/3C-T	24	0.006*
TSO	B	1C-T/3C-T	24	0 .920
TSO	B	1C-NT/3C-NT	24	0.406
TSO	V	1C-NT/1C_T	24	0 .004*
TSO	V	3C-NT/3C-T	23	0 .031*
TSO	V	1C-T/3C-T	22	0.162
TSO	V	1C-NT/3C-NT	20	0.379
TSO	I_c	1C-NT/1C_T	22	0.072
TSO	I_c	3C-NT/3C-T	23	0.11
TSO	I_c	1C-T/3C-T	24	0.575
TSO	I_c	1C-NT/3C-NT	21	0.453
LOO	B	1C-NT/1C-T	24	0.001*
LOO	B	2C-NT /2C-T	24	0.001*
LOO	B	1C-T/2C-T	22	0.952
LOO	B	1C-T/allC-T	23	0.412
LOO	B	1C-NT/2C-NT	24	0.646
LOO	I_c	1C-NT/1C-T	23	0.001*
LOO	I_c	2C-NT/2C-T	17	0.01*
LOO	I_c	1C-T/2C-T	22	0.952
LOO	I_c	1C-T/allC-T	19	0.184
LOO	I_c	1C-NT/2C-NT	24	0.124
LOO	V	1C-NT/1C-T	19	0.276
LOO	V	2C-NT /2C-T	18	0.003*
LOO	V	1C-T/2C-T	24	0.944
LOO	V	1C-T/allC-T	24	0.834
LOO	V	1C-NT/2C-NT	24	0.124

[1] *N, number of observations varies due to ties.*

Table 4. Correlation and regression analyses of CCD Observations[1].

Obs.	*Filter/ Treatment*	*Corr. Pearson r*	*Regress p-value*	*R-sqr.*	*p-value*	*N*
LOO	B/1C-NT	0.1064	0.61	0.8	< 0.001*	25
LOO	B/1C-T	0.197	0.36	0.153	0.059	24
LOO	B/2C-NT	0.3726	0.04*	0.65	< 0.0004*	31
LOO	B/2C-T	0.1303	0.48	0.022	0.423	31
LOO	V/1C_NT	0.042	0.85	0.216	0.022*	23
LOO	V/1C-T	0.0899	0.68	0.338	0.003*	24
LOO	V/2C-NT	0.0407	0.83	0.065	0.167	30
LOO	V/2C-T	0.0793	0.68	0.259	0.004*	30
LOO	I_c/1C-NT	0.2099	0.32	0.671	< 0.00001*	24
LOO	I_c/1C-T	0.4171	0.04*	0.025	0.769	24
LOO	I_c/2C-NT	0.0605	0.75	0.15	0.034*	30
LOO	I_c/2C-T	0.3349	0.08	0.011	0.589	24
TSO	B/1C-NT	0.2489	0.16	0.513	< 0.001*	33
TSO	B/1C-T	0.2874	0.1	0.033	0.315	32
TSO	B/3C-NT	0.4021	0.046*	0.697	< 0.001*	33
TSO	B/3C-T	0.4181	0.053	0.006	0.723	25
TSO	V/1C_NT	0.0038	0.98	0.448	< 0.001*	32
TSO	V/1C-T	0.1843	0.3	0.126	0.042*	33
TSO	V/3C-NT	0.0108	0.96	0.409	0.001*	24
TSO	V/3C-T	0.2041	0.35	0.086	0.173	22
TSO	I_c/1C-NT	0.2655	0.13	0.413	< 0.001*	33
TSO	I_c/1C-T	0.794	<0.001*	0.004	0.741	33
TSO	I_c/3C-NT	0.3059	0.15	0.277	0.007*	33
TSO	I_c/3C-T	0.737	<0.001*	0.054	0.286	23

[1] *Filter/Treatment is filter and treatment; Corr. Pearson r is Pearson r of the correlation between the absolute O–K and the standard deviation of N stars; p(r) probability of rejecting the null hypothesis that absolute O–K values are correlated with standard deviation (a measure of precision). R-sqr. is the coefficient of determination of (B–V|untransformed O–K) of N stars; p(R-sq) tests the null hypothesis is that the slope of the least squares fit is zero (0). N is the number of Landolt standard stars used in each analysis.*

Table 5. Summary data, combined standard fields, CMOS.

Observatory	*Filter*	*Treatment*	*Median abs. O–K*	*IQR O–K*	*Precision*	*N*
BSM-NH2	B	1C-NT	0.006	0.039	0.004	18
BSM-NH2	B	1C-T	0.016	0.016	0.004	18
BSM-NH2	B	3C-NT	0.016	0.016	0.01	14
BSM-NH2	B	3C-T	0.011	0.012	0.01	14
BSM-NH2	V	1C-NT	0.016	0.022	0.004	18
BSM-NH2	V	1C-T	0.022	0.027	0.003	18
BSM-NH2	V	3C-NT	0.009	0.017	0.01	14
BSM-NH2	V	3C-T	0.012	0.016	0.01	14
BSM-NH2	I_c	1C-NT	0.019	0.032	0.008	18
BSM-NH2	I_c	1C-T	0.015	0.023	0.009	18
BSM-NH2	I_c	3C-NT	0.014	0.025	0.014	14
BSM-NH2	I_c	3C-T	0.014	0.011	0.015	14

Table 6. Wilcoxon test results, CMOS and CMOS/CCD[1].

Observatory	*Filter*	*Treatment*	*N*	*z-Value p*	*w-Value p*
BSM-NH2	B	1C-NT/1C-T	18	0. 347	>0.05
BSM-NH2	B	3C-NT/3C-T	14	†0.022*	<0.5
BSM-NH2	V	1C-NT/1C-T	18	0.928	>0.05
BSM-NH2	V	3C-NT/3C-T	14	0.726	>0.05
BSM-NH2	I_c	1C-NT/1C-T	18	0.267	>0.05
BSM-NH2	I_c	3C-NT/3C-T	14	0.952	>0.05
CMOS/CCD	B*	1C-NT	18	0.040*	<0.05
CMOS/CCD	B*	1C-T	18	0.031*	<0.05
CMOS/CCD	B	3C-NT	14	0.529	>0.05
CMOS/CCD	B	3C-T	14	0.298	>0.05
CMOS/CCD	V	1C-NT	15	0.177	>0.05
CMOS/CCD	V**	1C-T	18	0.025*	<0.05
CMOS/CCD	V	3C-NT	11	0.424	>0.05
CMOS/CCD	V	3C-T	11	0.424	>0.05
CMOS/CCD	I_c	1C-NT	18	0.447	>0.05
CMOS/CCD	I_c	1C-T	18	0.171	>0.05
CMOS/CCD	I_c	3C-NT	14	0.826	>0.05
CMOS/CCD	I_c	3C-T	13	0.384	>0.05

[1] BSM-NH2 are COMS-to-COMS tests, CMOS/CCD tests medians obtained for the same sample with different sensors. An asterisk in the z-value column marks rejection of the null hypothesis that the medians are equal. A single asterisk (*) in the Filter column denotes that CMOS absolute O–K estimates were significantly more accurate than CCD estimates; a double asterisk (**) denotes CCD estimate are more accurate.

Table 7.Correlation and regression analyses of CMOS observations[1].

Obs.	*Fltr/Treat*	*r*	*p(r)*	*R-sqr.*	*p(R-sqr.)*	*N*
		Abs. O–K | StDev		*B–V | O–K*		
BSM-NH2	B/1C-NT	0.139	0.584	0.408	0.004*	18
BSM-NH2	B/1C-T	0.571	0.013*	0.008	0.724	18
BSM-NH2	V/1C NT	0.339	0.169	0.291	0.021*	18
BSM-NH2	V/1C-T	0.231	0.356	0.025	0.531	18
BSM-NH2	I_c/1C-NT	0.432	0.073	0.089	0.28	18
BSM-NH2	I_c/1C-T	0.66	0.003*	0.014	0.646	18
BSM-NH2	B/3C-NT	0.154	0.598	0.517	0.004*	14
BSM-NH2	B/3C-T	0.703	0.005*	0.0004	0.996	14
BSM-NH2	V/3C NT	0.433	0.122	0.339	0.029*	14
BSM-NH2	V/3C-T	0.307	0.307	0.138	0.221	14
BSM-NH2	I_c/3C-NT	0.544	0.044*	0.055	0.418	14
BSM-NH2	I_c/3C-T	0.74	0.002*	0.073	0.352	14

[1] Fltr/Treat is filter and treatment; r is Pearson r of the correlation between the absolute O–K and the standard deviation of N stars; p(r) probability of rejecting the null hypothesis that absolute O–K values are correlated with standard deviation (a measure of precision). R-sqr. is the coefficient of determination of (B–V | "raw" O–K) of N stars; p(R-sq) tests the null hypothesis that the slope of the least squares fit is zero (0). N is the number of Landolt standard stars used in each analysis.

to zero slope and the scatter of actual magnitude estimates are less than the untransformed fits. This demonstrates visually that there is no relationship between the color of the star (B–V) and the magnitude, thus the transformed data are successfully color-transformed. In contrast the "raw" untransformed O–K estimates show a significant slope, as expected given that they are not transformed.

5. CMOS precision and accuracy—results and discussion

CMOS analyses are similar to CCD analyses except that only two Landolt Fields were used. Table 5 documents median values and variation for absolute O–K values as well as average precision as estimated from standard deviations of ten individual measures. Figure 4 visualizes these data. Note that the overall variation is less than the CCD data and the effects of transformation are less. Transformation yields consistently better results in accuracy in only three of the six pairs of treatments and a tie in one treatment pair (3C-NT versus 3C-T). The Johnson V-filter median results with untransformed data are more accurate than the median transformed results. However, when we look at the variation as measured by the IQR scores we observe that five of six pairs show less variation in the transformed results, suggesting that on the whole more accurate star magnitudes are achieved by transforming the data.

The Wilcoxon signed values pair-wise test results for the CMOS data are quite different from the CCD results (Table 6), reflecting the slight differences in medians shown in Table 5. We found only a single test result (i.e., 3C-NT versus 3C-T) to be significant.

Least-squares analyses are reported in Table 7. In spite of the failure of the Wilcoxon tests to favor one treatment over another (with one exception), the least squares fits do demonstrate why we have pointed earlier to variation around the median values shown in Table 5. The null hypothesis (slope = 0) is rejected in all untransformed regression analyses but only in two of the regression analyses of transformed data. We interpret this to mean that more of the stars measured had improved color transformed magnitude estimates compared to their estimates in untransformed treatments, in spite of the fact that the medians are similar. That is, transformation decreased the scatter and shifted the scatter towards the y = 0 axis. We conclude that transformation is, in fact, effective in increasing accuracy in these data.

We also examined precision. We found precision uncorrelated with accuracy for this sample of stars (Table 7), a result similar to the CCD analyses.

Wilcoxon signed-value pair-wise tests were used to evaluate the null hypothesis that accuracy, as measured by absolute O–K values, of similar CCD and CMOS magnitude estimates were statistically similar between treatments ($p = 0.05$). The results, using two fields imaged at TSO and BSM-NH2 (Table 6, lower), show that nine of the twelve pair-wise tests were insignificant.

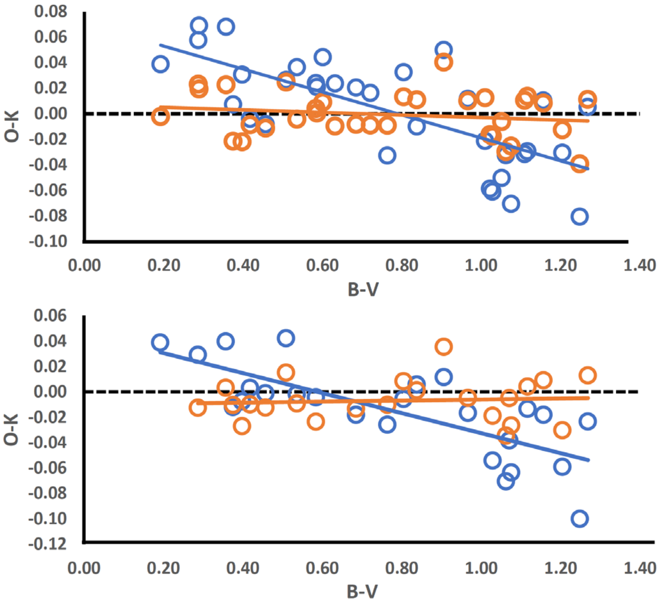

Figure 3. Regression analyses of color (B–V) and raw OK values (O–K) of transformed and untransformed analysis of Landolt standard stars for the Johnson B filter taken at the Tigh Speuran Observatory (TSO). In each case blue circles are data points and blue lines are least squares fit to data of non-transformed data while orange circles are data points, and the orange line is the least squares fit of transformed data. (Upper plot): Analyses using one comparison star (1C-NT blue, 1C-T orange). (Lower plot): Analyses using three comparison stars (3C-NT blue, 3C-T orange).

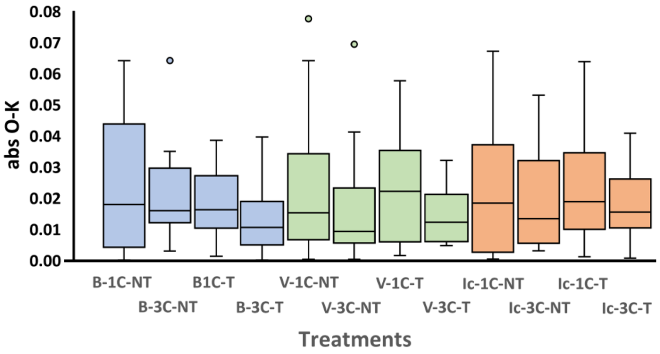

Figure 4. Boxplots of different treatments of absolute O–K values for different treatments of Landolt standard stars taken with the BSM-NH2 telescope and CMOS camera. Median values are horizonal bars with the quartile variation boxes, ranges are the vertical bars, outliers are circles.

Two of the tests (Johnson B, 1C-NT, and 1C-T) were significant with CMOS data being more accurate than CCD data. One test (Johnson V, 1C-T) was significant with CCD data being more accurate.

6. Conclusions and recommendations

Our study suggests a procedure for amateur photometrists to measure and assess the accuracy of their photometry and improve amateur photometry. Specifically, we propose that one should image Landolt Standard Fields repeatedly (N = 10) and assess Observed–Known (O–K) magnitudes for many standard stars. This procedure confirms that transformation significantly improves the accuracy of measured target magnitudes. Our results suggest that an average accuracy between ±0.02 magnitude is achievable without extraordinary efforts to pick comparisons stars of the same magnitude and color but with adequate SNR and good calibration. No doubt close attention to issues such as transformation coefficients, calibration, and comparison star choice leads to further improvement after an initial assessment.

We identified seven conclusions from our efforts:

1. Transformation improves accuracy, especially in cases where one is forced to pick a comparison star that is different in color than the target. We did not evaluate accuracy without transformation in situations where a comparison star and target are of similar color due to the nature of the study, but it can be improved by picking a comp star as close in color as possible to the target star.

2. There are no statistical differences between single-comp and ensemble comp methods shown in this study. However, we prefer ensemble methods because they can result in statistically meaningful measurement uncertainties given three or more comps using the standard deviation of all the comparison stars. We did not evaluate whether more stars in an ensemble than used in this study would result in greater accuracy than sole use of a single comparison star.

3. CCD and CMOS cameras were equally accurate in estimating magnitude.

4. Simple tests such as the Wilcoxon tests for similarities to median values may not provide a definitive answer to the effect of transformation. Least-squares fits provide a view of the entire data set and are more definitive.

5. Accuracy and precision are uncorrelated given adequate signal to noise ratios of targets and comparison stars. Precision (random error) uncertainty is not a measure of accuracy (systematic error). That said, there are many research programs for which precision is of upmost importance and accuracy is of secondary importance.

6. For variables with long periods compared to the imaging cadence, the most direct way to measure precision is to compute the mean and standard deviation of the magnitudes of a short time series of 4-10 images and report the mean as the calculated magnitude and standard deviation as the uncertainty (precision).

7. Directly measuring the accuracy of a variable is not possible. One can, of course, measure the fit of the observation to a model (O–C analysis), but this is different from accuracy as used in this study. Rather, one can do O–K analysis on the check star(s) that stand as secondary standards in the analysis or rely on the standard deviation of the ensemble variation.

7. Acknowledgements

This study would not have been possible without the resources of the American Association of Variable Star Observers, including catalogs of Standard Star photometry and charts, the AAVSO Bright Star Monitor Network, and the APASS catalog (Henden *et al.* 2018). Our thanks to Pierre de Ponthière for his help with LesvePhotometry. We thank the reviewer and editor for insightful comments and the editorial staff for their hard work.

References

de Ponthière, P. 2011, LesvePhotometry, automatic photometry software (http://www.dppobservatory.net).

Henden, A. A., Templeton, M., Terrell, D., Smith, T. C., Levine, S., and Welch, D. 2018, AAVSO Photometric All-Sky Survey, data release 10 (https://www.aavso.org/apass).

Koppelmann, M. 2005. in *Proceedings for the 24th Annual Conference of the Society for Astronomical Sciences*, eds. B. D. Warner, D. Mais, D. A. Kenyon, J. Foote, Society for Astronomical Sciences, Rancho Cucamonga, CA, 107.

Landolt, A. U. 1983, *Astron. J.*, **88**, 439.

Landolt, A. U. 2013, *Astron. J.*, **146**, 131 (DOI:10.1088/0004-6256/146/5/131).

Mandel, J. 1964, *The Statistical Analysis of Experimental Data*, Dover Publ., Inc. New York.

Newberry, M. V. 1999, in *Precision CCD Photometry*, ASP Conf. Ser. 189, eds. E. R. Crain, D. L. Crawford, R. A. Tucker, Astronomical Society of the Pacific, San Francisco, CA, 74.

Sonnett, S., Meech, K., Jedicke, R., Bus, S., Tonry, J., and Hainaut, O. 2013, *Publ. Astron. Soc. Pacific*, **125**, 456.

Stubbs, C. W., and Tonry, J. L. 2006, *Astrophys. J.*, **646**, 1436.

Light Curve Modeling and Secular Analyses of the Totally Eclipsing Overcontact Binary System, V625 Hydrae

Kevin B. Alton

UnderOak Observatory, 70 Summit Avenue, Cedar Knolls, NJ 07927; kbalton@optonline.net

Received January 1, 2021; revised February 5, 2021; accepted February 8, 2021

Abstract Precise time-series CCD-derived photometric data (BVI_c) were acquired from V625 Hya at Desert Blooms Observatory in 2020. An updated linear ephemeris was calculated from sixteen new times of minimum (ToM) produced from these measurements along with thirteen other values from four ground-based surveys and the literature. Secular analyses (observed minus predicted ToM vs. epoch) revealed changes in the orbital period of V625 Hya over the past two decades, suggesting an apparent increase in the orbital period based on a parabolic fit of the residuals. In addition, simultaneous modeling of these multi-bandpass light curve data was accomplished using the Wilson-Devinney code. Since a total eclipse is observed, a photometrically derived value for the mass ratio (q_{ptm}) with acceptable uncertainty could be determined which consequently provided estimates for some physical and geometric elements of V625 Hya.

1. Introduction

Sparsely sampled monochromatic photometric data from V625 Hya (= NSVS 12914400) were first captured during the ROTSE-I survey between 1999 and 2000 (Akerlof *et al.* 2000; Woźniak *et al.* 2004). Gettel *et al.* (2006) included V625 Hya in their catalog of bright contact binary stars from the ROTSE-I survey while Hoffman *et al.* (2009) classified this system as a W UMa-type variable. Other sources of photometric data from this eclipsing binary included the All-Sky Automated Survey (ASAS: Pojmański *et al.* 2005), the All-Sky Automated Survey for SuperNovae (ASAS-SN: Shappee *et al.* 2014; Jayasinghe *et al.* 2018), the Catalina Sky Survey (CSS: Drake *et al.* 2014) and a multi-bandpass photometric study of W Ursae Majoris binaries by Terrell *et al.* (2012). Herein, the first multi-bandpass (BVI_c) light curves (LCs) from V625 Hya modeled with the Wilson-Devinney code (WD; Wilson and Devinney 1971; Wilson 1979, 1990) are reported. This investigation also includes secular analyses of the observed-minus-predicted eclipse timing differences (ETD) over the past 21 years.

2. Observations and data reduction

Precise time-series photometric observations were acquired in 2020 at Desert Blooms Observatory (DBO, USA: 31.941 N, 110.257 W) using a QSI 683 wsg-8 CCD camera mounted at the Cassegrain focus of a 0.4-m Schmidt-Cassegrain telescope. This focal-reduced (f/7.2) instrument produces an image scale of 0.76 arcsec/pixel (bin = 2 × 2) and a field-of-view (FOV) of 15.9 × 21.1 arcmin. The CCD camera was equipped with photometric B, V, and I_c filters manufactured to match the Johnson-Cousins Bessell specification. Image (science, darks, and flats) acquisition software (TheSkyX Pro Edition 10.5.0; Software Bisque 2019) controlled the main and integrated guide cameras. Computer time was updated immediately prior to each session. Dark subtraction, flat correction, and registration of all images collected at DBO were performed with AIP4Win v2.4.0 (Berry and Burnell 2005). Instrumental readings from V625 Hya were reduced to catalog-based magnitudes using APASS DR9 values (Henden *et al.* 2009, 2010, 2011; Smith *et al.* 2011) built into MPO Canopus v 10.7.1.3 (Minor Planet Obs. 2011).

Magnitude values for V625 Hya were produced from an ensemble of four comparison stars, the average of which remained constant (± 0.015 mag) throughout every imaging session. The identity, J2000 coordinates, and color indices (B–V) for these stars are provided in Table 1. A CCD image annotated with the location of the target (T) and comparison stars (1–4) is shown in Figure 1. Only data acquired above 30° altitude (airmass < 2.0) were evaluated; considering the close proximity of all program stars, differential atmospheric extinction was ignored. All photometric data acquired from V625 Hya at DBO can be retrieved from the AAVSO International Database (Kafka 2021).

3. Results and discussion

Results and detailed discussion about the determination of linear and quadratic ephemerides are provided in this Section. Thereafter, the multi-source approach for estimating the effective temperature of V625 Hya and Roche-lobe modeling results with the WD code are examined. Finally, preliminary estimates for mass ($M_\odot$) and radius ($R_\odot$), along with corresponding calculations for luminosity ($L_\odot$), surface gravity (log (g)), semi-major axis ($R_\odot$), and bolometric magnitude (M_{bol}), are derived.

Table 1. Astrometric coordinates (J2000), V-magnitudes, and color indices (B–V) for V625 Hya (Figure 1), and the corresponding comparison stars used in this photometric study.

Star Identification	*R.A. (J2000)*[a] *h m s*	*Dec. (J2000)*[a] *° ′ ″*	*V-mag.*[b]	*(B–V)*[b]
(1) GSC 4867–1095	08 43 01.4248	–03 38 20.446	12.721	0.684
(2) GSC 4867–0905	08 43 18.2833	–03 44 54.223	12.275	0.562
(3) GSC 4867–1061	08 43 44.5488	–03 40 26.159	12.578	0.327
(4) GSC 4867–0766	08 44 07.4620	–03 39 27.861	11.868	0.452
(T) V625 Hya	08 43 03.9741	–03 42 52.541	11.702	0.751

a. R.A. and Dec. from Gaia DR2 (Gaia Collab. et al. *2016, 2018).*

b. V-mag and (B–V) for comparison stars derived from APASS DR9 database described by Henden et al. *2009, 2010, 2011 and Smith* et al. *2011.*

3.1. Photometry and ephemerides

A total of 245 photometric values in B-, 253 in V-, and 247 in I_c-passbands were acquired from V625 Hya at DBO between 03 December and 21 December 2020. Photometric uncertainty, which typically remained within ± 0.004, was calculated according to the so-called "CCD Equation" (Mortara and Fowler 1981; Howell 2006). ToM values and associated errors from data acquired at DBO were calculated according to Andrych and Andronov (2019) and Andrych *et al.* (2020) using the program MAVKA (https://uavso.org.ua/mavka/). Around Min II, simulation of extrema was automatically optimized by finding the most precise degree (α) and best fit algebraic polynomial expression (Figure 2, top panel). During Min I, a "wall-supported line" (WSL) algorithm (Andrych *et al.* 2017) provided the best fit as the eclipse passes through totality, resulting in a flattened bottom (Figure 2, bottom panel). ToM differences (ETD) vs. epoch were fit using scaled Levenberg-Marquardt algorithms (QtiPlot 0.9.9-rc9; IONDEV SRL 2021).

Sixteen new ToM values were derived from photometric data acquired at DBO. An additional eleven ToM values were extrapolated from the NSVS, CSS, ASAS, and ASAS-SN surveys, along with two other observations gathered from the literature (Table 2). A new linear ephemeris based on near-term (2014–2021) results was determined as follows:

$$\mathrm{Min\,I\,(HJD)} = 2459204.72825\,(9) + 0.3485618\,(1)\,\mathrm{E}\,. \quad (1)$$

The difference (ETD) between observed eclipse times (Figure 3) and those predicted by the linear ephemeris against epoch (cycle number) reveals what appears to be a quadratic relationship where:

$$\mathrm{ETD} = -6.698 \pm 49.457 \cdot 10^{-5} + 4.0261 \pm 1.7500 \cdot 10^{-7}\,\mathrm{E} \\ 7.600 \pm 0.8634 \cdot 10^{-11}\,\mathrm{E}^2\,. \quad (2)$$

Given that the coefficient of the quadratic term (Q) is positive, this result would suggest that the orbital period has been increasing at the rate ($dP/dt = 2Q/P$) of 0.0138 ± 0.0016 $\mathrm{s \cdot y^{-1}}$. This rate is similar to many other overcontact systems reported in the literature (Latković *et al.* 2021). Period change over time that can be described by a parabolic expression is often attributed to mass transfer or by angular momentum loss (AML) due to magnetic stellar wind (Qian 2001, 2003; Li *et al.* 2019). Ideally when AML dominates, the net effect is a decreasing orbital period. If conservative mass transfer from the more massive to its less massive secondary star prevails, then the orbital period can also decrease. Separation increases when conservative mass transfer from the less massive to its more massive binary cohort takes place or spherically symmetric mass loss from either body (e.g. a wind but not magnetized) occurs. In mixed situations (e.g. mass transfer from less massive star, together with AML) the orbit evolution depends on which process dominates.

Table 2. V625 Hya times of minimum (20 April 1999–21 December 2020), cycle number, and residuals (ETD) between observed and predicted times derived from the updated linear ephemeris (Equation 1).

HJD 2400000+	*HJD Error*	*Cycle No.*	*ETD*[a]	*Reference*
51288.7463	0.0010	–22710.5	0.0311	1
51513.9111	0.0010	–22064.5	0.0250	1
51536.7427	0.0010	–21999	0.0258	1
52635.7510	0.0010	–18846	0.0187	2
52790.5167	0.0010	–18402	0.0229	3
53357.7951	0.0010	–16774.5	0.0170	2
53772.7511	0.0010	–15584	0.0102	2
53852.5766	0.0010	–15355	0.0150	2
55571.8447	0.0002	–10422.5	0.0020	4
55929.8215	0.0010	–9395.5	0.0057	3
55931.9044	0.0003	–9389.5	–0.0027	5
56751.7245	0.0010	–7037.5	0.0000	6
57753.6654	0.0010	–4163	0.0000	6
59190.9605	0.0002	–39.5	0.0005	7
59190.9606	0.0002	–39.5	0.0005	7
59192.8765	0.0004	–34	–0.0006	7
59192.8773	0.0004	–34	0.0001	7
59198.9771	0.0002	–16.5	0.0001	7
59198.9771	0.0004	–16.5	0.0001	7
59198.9778	0.0002	–16.5	0.0008	7
59200.8939	0.0001	–11	–0.0002	7
59200.8939	0.0001	–11	–0.0001	7
59200.8940	0.0001	–11	–0.0001	7
59202.9852	0.0004	–5	–0.0003	7
59202.9852	0.0001	–5	–0.0002	7
59202.9853	0.0001	–5	–0.0001	7
59204.9020	0.0003	0.5	–0.0005	7
59204.9026	0.0004	0.5	0.0001	7
59204.9026	0.0002	0.5	0.0001	7

a. ETD = Observed – Predicted Eclipse Time Difference.

References: 1. NSVS (Akerlof et al. *2000); 2. ASAS (Pojmański* et al. *2005); 3. CSS (Drake* et al. *2014); 4. Diethelm 2011; 5. Diethelm 2012; 6. ASAS-SN (Jayasinghe* et al. *2018); 7. This study.*

3.2. Effective temperature estimation

The effective temperature (T_{eff1}) of the more massive, and therefore more luminous component (herein defined as the primary star), was derived from a composite (USNO-A2, 2MASS, APASS, Terrell *et al.* 2012) of photometric determinations that were as necessary transformed to (B–V).[1, 2] Interstellar extinction (A_V) and reddening ($E(B-V) = A_V/3.1$) was estimated according to a galactic dust map model derived by Schlafly and Finkbeiner (2011). Additional sources used to establish a mean value for each T_{eff1} included the Gaia DR2 release of stellar parameters (Andrae *et al.* 2018), the LAMOST DR6 survey (Zhao *et al.* 2012; Wang *et al.* 2019), and an empirical relationship (Houdashelt *et al.* 2000) based on intrinsic color, $(B-V)_0$. The mean result ($T_{\mathrm{eff1}} = 5450 \pm 108$ K) was adopted for WD modeling of LCs from V625 Hya (Table 3).

3.3. LC Modeling with the Wilson-Devinney code

Modeling of LC data (Figure 4) was initially performed with PHOEBE 0.31a (Prša and Zwitter 2005) and then refined using WDwint56a (Nelson 2009). Both programs feature a graphical interface to the Wilson-Devinney WD2003 code (Wilson and Devinney 1971; Wilson 1979, 1990). WDwint56a incorporates Kurucz's atmosphere models (Kurucz 2002) that

---

[1] http://www.aerith.net/astro/color_conversion.html

[2] http://brucegary.net/dummies/method0.html

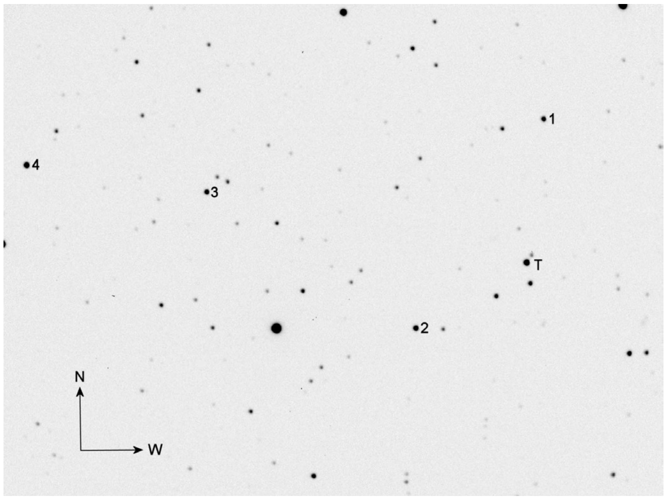

Figure 1. CCD image (V-mag; 90-s) of V625 Hya (T) acquired at DBO (FOV = 15.9 × 21.1 arcmin) showing the location of comparison stars (1–4) used to generate APASS DR9-derived magnitude estimates.

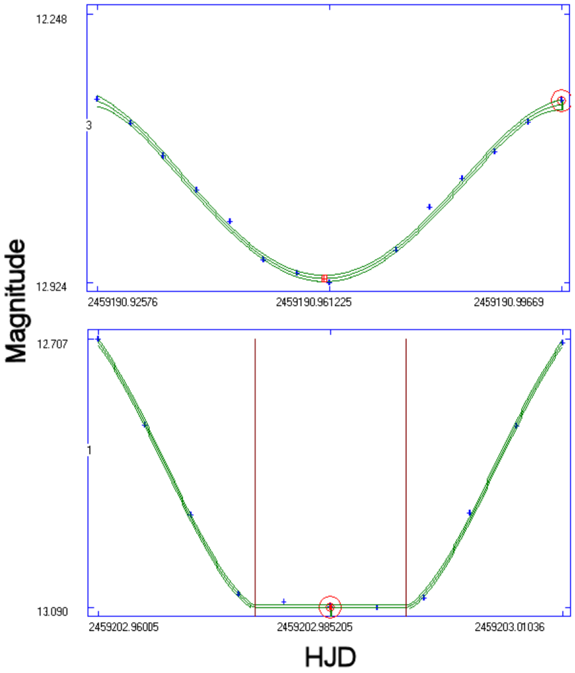

Figure 2. The top panel depicts a representative ToM estimate during Min II using polynomial approximation (α = 4), while the bottom panel shows the fit achieved with the wall-supported line (WSL) algorithm during Min I. In both cases, a red dot signifies the moment of extremum. The boundary lines which indicate the duration of the Min I total eclipse (0.014366 d) are conveniently calculated by MAVKA.

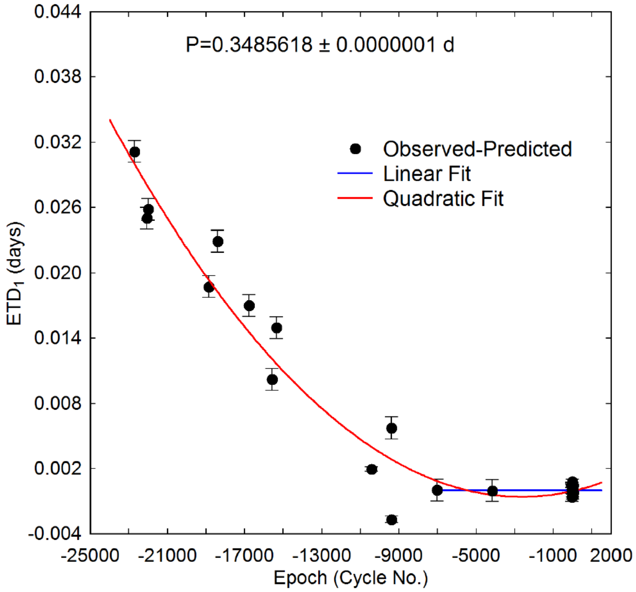

Figure 3. Linear and quadratic fits of ToM differences (ETD_1) vs. epoch for V625 Hya calculated using the new linear ephemeris (Equation 1). Measurement uncertainty is denoted by the error bars.

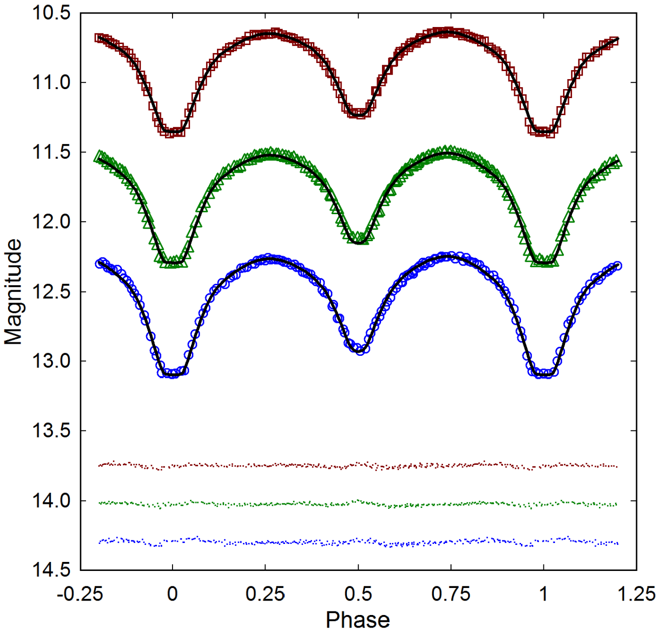

Figure 4. Period-folded (0.3485618 ± 0.0000001 d) CCD-derived LCs for V625 Hya produced from photometric data collected at DBO between 03 December 2020 and 21 December 2020. The top (I_c), middle (V), and bottom curves (B) were transformed to magnitudes based on APASS DR9-derived catalog values from comparison stars. In this case, the model assumed a W-subtype overcontact binary with two cool spots on the primary star; residuals from the model fits are offset at the bottom of the plot to compress the y-axis.

Table 3. Estimation of the primary star effective temperature (T_{eff1}) for V625 Hya.

Parameter	*Value*
DBO $(B–V)_0$[a]	0.727 ± 0.022
Mean combined $(B–V)_0$[a]	0.733 ± 0.018
Galactic reddening E(B–V)[b]	0.0149 ± 0.0004
Survey T_{eff1}[c] (K)	5496 ± 45
Gaia T_{eff1}[d] (K)	5355^{+326}_{-105}
Houdashelt T_{eff1}[e] (K)	5481 ± 282
LAMOST DR5 T_{eff1}[f] (K)	5448 ± 26
Mean T_{eff1} (K)	5450 ± 108
Spectral Class[g]	G7V-G8V

a. Surveys and DBO intrinsic $(B–V)_0$ determined using reddening values (E(B–V)).

b. https://irsa.ipac.caltech.edu/applications/DUST/

c. T_{eff1} interpolated from mean combined $(B–V)_0$ using Table 4 in Pecaut and Mamajek (2013).

d. Values from Gaia DR2 (Gaia Collab. 2016, 2018): http://vizier.u-strasbg.fr/viz-bin/VizieR?-source=I/345/gaia2

e. Values calculated with Houdashelt et al. *(2000) empirical relationship.*

f. Spectral class estimated from LAMOST DR 6 low resolution spectrum = G7V.

g. Spectral class estimated from Pecaut and Mamajek (2013).

Table 4. LC parameters evaluated by WD modeling and the geometric elements derived for V625 Hya (2020) assuming it is a W-type W UMa variable

Parameter[a]	*No Spot*	*Spotted*
T_{eff1} (K)[b]	5450 (108)	5450 (108)
T_{eff2} (K)	5966 (118)	5593 (111)
q (m_2 / m_1)	0.394 (1)	0.431 (1)
A[b]	0.50	0.50
g[b]	0.32	0.32
$\Omega_1 = \Omega_2$	2.624 (2)	2.726 (3)
i°	89.4 (2)	86.1 (3)
$A_P = T_S / T_\star$[c]	—	0.85 (1)
θ_P(spot co-latitude)[c]	—	98.9 (3.2)
φ_P (spot longitude)[c]	—	95.2 (2.8)
r_P (angular radius)[c]	—	10.4 (2)
$A_P = T_S / T_\star$[c]	—	0.77 (1)
θ_P(spot co-latitude)[c]	—	90 (1)
φ_P (spot longitude)[c]	—	180 (1)
r_P (angular radius)[c]	—	18.5 (1)
$L_1 / (L_1 + L_2)_B$[d]	0.5708 (4)	0.6470 (3)
$L_1 / (L_1 + L_2)_V$	0.6054 (3)	0.6565 (2)
$L_1 / (L_1 + L_2)_{I_c}$	0.6322 (3)	0.6641 (2)
r_1 (pole)	0.4421 (4)	0.4292 (4)
r_1 (side)	0.4740 (5)	0.4578 (5)
r_1 (back)	0.5040 (6)	0.4860 (6)
r_2 (pole)	0.2906 (4)	0.2909 (12)
r_2 (side)	0.3042 (5)	0.3037 (14)
r_2 (back)	0.3436 (8)	0.3381 (24)
Fill-out factor (%)	17.6	5.5
RMS (B)[e]	0.01227	0.00944
RMS (V)	0.01035	0.00715
RMS (I_c)	0.01073	0.00763

a. All DBO uncertainty estimates for T_{eff2}, q, $\Omega_{1,2}$, i, $r_{1,2}$, and L_1 from WDWINT56A (Nelson 2009).

b. Fixed with no error during DC.

c. Spot parameters in degrees (θ_P, φ_P and r_P); A_P equals the spot temperature (T_S) divided by star temperature, $T_\star$.

d. L_1 and L_2 refer to scaled luminosities of the primary and secondary stars, respectively.

e. Monochromatic residual mean square error from observed values.

are integrated over BVI_c passbands. The ultimate model selected was Mode 3 for an overcontact binary; other modes (detached and semi-detached) never improved LC simulation as defined by the model residual mean square errors. Since the effective temperature was estimated to be 5450 K, internal energy transfer to the stellar surface is driven by convective (7200 K) rather than by radiative processes (Bradstreet and Steelman 2004). Therefore, bolometric albedo was assigned ($A_{1,2} = 0.5$) according to Ruciński (1969) while the gravity darkening coefficient was adopted ($g_{1,2} = 0.32$) from Lucy (1967). Logarithmic limb darkening coefficients (x_1, x_2, y_1, y_2) were interpolated (van Hamme 1993) following any change in the effective temperature during model fit optimization by differential corrections (DC). All but the temperature of the more massive star (T_{eff1}), $A_{1,2}$, and $g_{1,2}$ were allowed to vary during DC iterations. In general, the best fits for T_{eff2}, i, q, and Roche potentials ($\Omega_1 = \Omega_2$) were collectively refined (method of multiple subsets) by DC using the multi-bandpass LC data until a simultaneous solution was found. Most obvious in the B-bandpass, a LC asymmetry (Max I < Max II), the so-called "O'Connell effect" (O'Connell 1951), requires some sort of surface inhomogeneity. Surface inhomogeneity, often associated with star spots, was simulated by the addition of two cool spots on the primary star to obtain the best fit LC models. V625 Hya did not require third light correction ($l_3 = 0$) to improve WD model fits.

3.4. Wilson-Devinney modeling results

It is generally not possible to unambiguously determine the mass ratio or total mass of an eclipsing binary system without spectroscopic radial velocity (RV) data. In this case the flattened bottom at Min I indicative of a total eclipse suggests that V625 Hya is a W-subtype overcontact binary system (Binnendijk 1970). This finding provided strong motivation to seek a photometric solution for the mass ratio (q_{ptm}) using the WD code. With totality, degeneracy between the radii and inclination is broken (Terrell and Wilson 2005) such that a mass ratio can be determined with very small (< 1%) relative error (Liu 2021).

Standard errors reported in Table 4 are computed from the DC covariance matrix and only reflect the model fit to the observations which assume exact values for any fixed parameter. These formal errors are generally regarded as unrealistically small considering the estimated uncertainties associated with the mean adopted T_{eff1} values along with basic assumptions about $A_{1,2}$, $g_{1,2}$, and the influence of spots added to the WD model. Normally, the value for T_{eff1} is fixed with no error during modeling with the WD code. When T_{eff1} is varied by as much as ± 10%, investigations with other OCBs, including A- (Alton 2019; Alton *et al.* 2020) and W-subtypes (Alton and Nelson 2018), have shown that uncertainty estimates for i, q, or $\Omega_{1,2}$ were not appreciably (< 2.5%) affected. Assuming that the actual T_{eff1} value falls within ± 10% of the adopted values used for WD modeling (a reasonable expectation based on T_{eff1} data provided in Table 4), then uncertainty estimates for i, q, or $\Omega_{1,2}$, along with spot size, temperature, and location, would likely not exceed this amount.

The fill-out parameter (f) which corresponds to the outer surface shared by each star was calculated according to Kallrath and Malone (2009) and Bradstreet (2005) where:

$$f = (\Omega_{inner} - \Omega_{1,2}) / (\Omega_{inner} - \Omega_{outer}) , \qquad (3)$$

wherein Ω_{outer} is the outer critical Roche equipotential, Ω_{inner} is the value for the inner critical Roche equipotential, and $\Omega = \Omega_{1,2}$ denotes the common envelope surface potential for the binary system. In this case V625 Hya is considered overcontact since $0 < f < 1$.

There is significant disparity in the mass ratio (0.431 vs. 0.394) and fill-out factor when the LCs are modeled with (5.5%) and without (17.6%) spots. The effects of adding spots to best fit a WD-derived LC model are well documented (Maceroni and van't Veer 1993; Berdyugina 2005; Terrell 2022). A multi-year (1969–2018) study on AU Ser (Alton *et al.* 2018), another OCB, revealed that fill-out factors (4% to 27.3%) were heavily influenced by variously sized spots which were consistently observed in the neck region. Furthermore, during modeling, each spot contributes four additional degrees-of-freedom (size, latitude, longitude, and temperature), challenging attempts to find a global non-degenerate solution. Despite the much smaller residual mean square error from the 2-spot simulation provided herein, the addition of RV data to constrain q and Doppler imaging to map the putative location of spot(s) would be critical to deriving a more robust LC solution for V625 Hya.

Spatial renderings (Figure 5) were produced with BINARY MAKER 3 (BM3: Bradstreet and Steelman 2004) using the final WDWINT56A modeling results from 2020. The smaller secondary is shown to fully transit across the primary face during Min II ($\varphi = 0.5$), thereby confirming that the secondary star is totally eclipsed at Min I.

3.5. Preliminary stellar parameters

Mean physical characteristics were estimated for V625 Hya (Table 5) using results from the best fit (spotted) LC simulations from 2020. Without the benefit of RV data which define the orbital motion, mass ratio, and total mass of the binary pair, these results should be considered "relative" rather than "absolute" parameters and regarded as preliminary. Nonetheless, since the photometric mass ratio (q_{ptm}) is derived from a totally eclipsing OCB, there is a reasonable expectation that DC optimization with the WD2003 code would have arrived at a solution with acceptable uncertainty for q (Terrell and Wilson 2005; Liu 2021).

Calculations are described below for estimating the solar mass and size, semi-major axis, solar luminosity, bolometric V-mag, and surface gravity of each component. Four empirically derived mass-period relationships (M-PR) for W UMa-binaries were used to estimate the primary star mass. The first M-PR was reported by Qian (2003), others followed from Gazeas and Stępień (2008), Gazeas (2009), and more recently Latković *et al.* (2021). According to Qian (2003), when the primary star is less than $1.35\,M_\odot$ or the system is W-type its mass can be determined from:

$$M_1 = 0.391\,(59) + 1.96\,(17) \cdot P, \qquad (4)$$

where P is the orbital period in days. This leads to $M_1 = 1.074 \pm 0.084\,M_\odot$ for the primary.

Table 5. Fundamental stellar parameters for V625 Hya using the photometric mass ratio ($q_{ptm} = m_2 / m_1$) from the spotted WD model fits of LC data (2020) and the estimated primary star mass based on four empirically derived M-PRs for overcontact binary systems.

Parameter	*Primary*	*Secondary*
Mass ($M_\odot$)	1.146 ± 0.044	0.494 ± 0.019
Radius ($R_\odot$)	1.114 ± 0.011	0.759 ± 0.007
a ($R_\odot$)	2.458 ± 0.024	2.458 ± 0.024
Luminosity ($L_\odot$)	0.987 ± 0.080	0.508 ± 0.041
Mbol	4.765 ± 0.021	5.485 ± 0.088
Log (g)	4.404 ± 0.019	4.371 ± 0.019

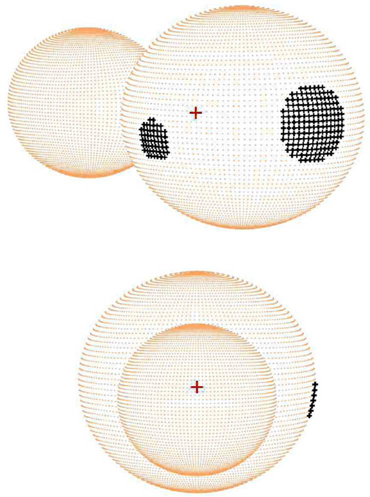

Figure 5. A spatial model of V625 Hya observed during 2020 illustrating (top) the location of two cool (black) spots on the primary star, and (bottom) the secondary star transit across the primary star face at Min II ($\varphi = 0.5$).

The M-PR derived by Gazeas and Stępień (2008):

$$\log(M_1) = 0.755\,(59) \cdot \log(P) + 0.416\,(24), \qquad (5)$$

corresponds to an OCB system where $M_1 = 1.176 \pm 0.098\,M_\odot$.

Gazeas (2009) reported another empirical relationship for the more massive (M_1) star of a contact binary such that:

$$\log(M_1) = 0.725\,(59) \cdot \log(P) - 0.076\,(32) \cdot \log(q) + 0.365\,(32), \qquad (6)$$

from which $M_1 = 1.151 \pm 0.050\,M_\odot$.

Finally, Latković *et al.* (2021) conducted an exhaustive analysis from nearly 700 W UMa stars in which they established mass-period, radius-period, and luminosity-period relationships for the primary and secondary stars. Accordingly, the M-PR:

$$M_1 = (2.94 \pm 0.21 \cdot P) + (0.16 \pm 0.08), \qquad (7)$$

leads to a primary star mass of $1.185 \pm 0.108\,M_\odot$.

The mean from these four values ($M_1 = 1.146 \pm 0.044\,M_\odot$) was used for subsequent determinations of M_2, semi-major axis a, volume-radii r_L, and bolometric magnitudes (M_{bol}) using the formal errors calculated by WDWINT56A (Nelson 2009).

The secondary mass ($0.494 \pm 0.019\,M_\odot$) and total mass ($1.640 \pm 0.048\,M_\odot$) were determined using the photometric mass ratio ($q_{ptm} = 0.431 \pm 0.001$) derived from the best fit (spotted) model.

The semi-major axis, $a(R_\odot) = 2.458 \pm 0.024$, was calculated from Newton's version of Kepler's third law where:

$$a^3 = G \cdot P^2 (M_1 + M_2) / 4\pi^2. \qquad (8)$$

The effective radius of each Roche lobe (r_L) can be calculated over the entire range of mass ratios ($0 < q < \infty$) according to an expression derived by Eggleton (1983):

$$r_L = 0.49q^{(2/3)} / (0.6q^{(2/3)} + \ln(1 + q^{(1/3)})), \qquad (9)$$

from which values for r_1 (0.4533 ± 0.0003) and r_2 (0.3089 ± 0.0002) were determined for the primary and secondary stars, respectively. The radii in solar units for both binary components can be calculated such that $R_1 = a \cdot r_1 = 1.114 \pm 0.011\ R_\odot$ and $R_2 = a \cdot r_2 = 0.759 \pm 0.007\ R_\odot$.

Luminosity in solar units ($L_\odot$) for the primary (L_1) and secondary stars (L_2) was calculated from the well-known relationship derived from the Stefan-Boltzmann law where:

$$L_{1,2} = (R_{1,2} / R_\odot)^2 (T_{1,2} / T_\odot)^4. \qquad (10)$$

Assuming that $T_{eff1} = 5450\,K$, $T_{eff2} = 5593\,K$, and $T_\odot = 5772\,K$, then the solar luminosities ($L_\odot$) for the primary and secondary are $L_1 = 0.987 \pm 0.080$ and $L_2 = 0.508 \pm 0.041$, respectively.

4. Conclusions

The results from this first detailed investigation of V625 Hya have supplemented an increasingly expanding list of W UMa-type variables that have been physically and geometrically characterized using a reliable mass ratio. Similar to other W-type OCBs, V625 Hya is comprised of relatively cool (late spectral class G) stars orbiting their common gravitational center in less than 0.4~d. In addition, all LCs exhibited a flattened bottom during Min I, a characteristic feature typically observed with totally eclipsing W-subtype systems. Sixteen new ToM values were determined from LCs acquired at DBO in 2020. These, along with eleven other values extrapolated from four surveys (1999–2016) employing sparse-sampling strategies and two from the literature, led to updated linear and quadratic ephemerides. Secular analyses suggested that the orbital period of V625 Hya is changing at a rate ($+0.0137\ s \cdot y^{-1}$) consistent with other similarly classified OCBs. The photometric mass ratio ($q_{ptm} = 0.417 \pm 0.003$) determined by WD modeling is expected to compare favorably with a mass ratio (q_{sp}) derived from RV data. Regardless, spectroscopic studies (RV and high resolution classification spectra) are necessary to unequivocally determine a total mass and spectral class for this binary system. Consequently, all parameter values and corresponding uncertainties reported herein should be considered preliminary.

5. Acknowledgements

This research has made use of the SIMBAD database operated at Centre de Données astronomiques de Strasbourg, France. In addition, the Northern Sky Variability Survey hosted by the Los Alamos National Laboratory (https://skydot.lanl.gov/nsvs/nsvs.php), the All-Sky Automated Survey (http://www.astrouw.edu.pl/asas/? page=acvs), the All-Sky Automated Survey for Supernovae (https://asas-sn.osu.edu/variables), the Catalina Sky Survey (http://nesssi.cacr.caltech.edu/DataRelease/), and the International Variable Star Index (AAVSO) were mined for essential information. This work also presents results from the European Space Agency (ESA) space mission Gaia. Gaia data are being processed by the Gaia Data Processing and Analysis Consortium (DPAC). Funding for the DPAC is provided by national institutions, in particular the institutions participating in the Gaia MultiLateral Agreement (MLA). The Gaia mission website is https://www.cosmos.esa.int/gaia. The Gaia archive website is https://archives.esac.esa.int/gaia. This paper makes use of data from the first public release of the WASP data as provided by the WASP consortium and services at the NASA Exoplanet Archive, which is operated by the California Institute of Technology, under contract with the National Aeronautics and Space Administration under the Exoplanet Exploration Program. The use of public data from LAMOST (http://dr6.lamost.org/) is also acknowledged. Guoshoujing Telescope (the Large Sky Area Multi-Object Fiber Spectroscopic Telescope LAMOST) is a National Major Scientific Project built by the Chinese Academy of Sciences. Funding for the project has been provided by the National Development and Reform Commission. LAMOST is operated and managed by the National Astronomical Observatories, Chinese Academy of Sciences. Many thanks to the anonymous referee and Editor Morrison, both of whom provided valuable commentary along with corrections.

References

Akerlof, C., *et al.* 2000, *Astron. J.*, **119**, 1901.

Alton, K. B. 2019, *J. Amer. Assoc. Var. Star Obs.*, **47**, 7.

Alton, K. B., and Nelson, R. H. 2018, *Mon. Not. Roy. Astron. Soc.*, **479**, 3197.

Alton, K. B., Nelson, R. H. and Stępień, K. 2020, *J. Astrophys. Astron.*, **41**, 26.

Alton, K. B., Nelson, R. H., and Terrell, D. 2018, *Info. Bull. Var. Stars*, No. 6256, 1.

Andrae, R., *et al.* 2018, *Astron. Astrophys.*, **616A**, 8.

Andrych, K. D. and Andronov, I. L. 2019, *Open Eur. J. Var. Stars*, **197**, 65.

Andrych, K. D., Andronov, I. L., and Chinarova, L. L. 2017, *Odessa Astron. Publ.*, **30**, 57.

Andrych, K. D., Andronov, I. L., and Chinarova, L. L. 2020, *J. Phys. Stud.*, **24**, 1902.

Berdyugina, S. V. 2005, *Living Rev. Solar Phys.*, **2**, 8.

Berry, R., and Burnell, J. 2005, *The Handbook of Astronomical Image Processing*, 2nd ed., Willmann-Bell, Richmond, VA.

Binnendijk, L. 1970, *Vistas Astron.*, **12**, 217.

Bradstreet, D. H. 2005, in *The Society for Astronomical Sciences 24th Annual Symposium on Telescope Science*, Society for Astronomical Sciences, Rancho Cucamonga, CA, 23.

Bradstreet, D. H., and Steelman, D. P. 2004, BINARY MAKER 3, Contact Software (http://www.binarymaker.com).

Diethelm, R. 2011, *Info. Bull. Var. Stars*, No. 5992, 1.

Diethelm, R. 2012, *Info. Bull. Var. Stars*, No. 6011, 1.

Drake, A. J., *et al.* 2014, *Astrophys. J., Suppl. Ser.*, **213**, 9.

Eggleton, P. P. 1983, *Astrophys. J.*, **268**, 368.

Gaia Collaboration, *et al.* 2016, *Astron. Astrophys.*, **595A**, 1.

Gaia Collaboration, *et al.* 2018, *Astron. Astrophys.*, **616A**, 1.

Gazeas, K. D. 2009, *Commun. Asteroseismology*, **159**, 129.

Gazeas, K., and Stępień, K. 2008, *Mon. Not. Roy. Astron. Soc.*, **390**, 1577.

Gettel, S. J., Geske, M. T., and McKay, T. A. 2006, *Astron. J.*, **131**, 621.

Henden, A. A., Levine, S. E., Terrell, D., Smith, T. C., and Welch, D. L. 2011, *Bull. Amer. Astron. Soc.*, **43**, 2011.

Henden, A. A., Terrell, D., Welch, D., and Smith, T. C. 2010, *Bull. Amer. Astron. Soc.*, **42**, 515

Henden, A. A., Welch, D. L., Terrell, D., and Levine, S. E. 2009, *Bull. Amer. Astron. Soc.*, **41**, 669.

Hoffman, D. I., Harrison, T. E., and McNamara, B. J. 2009, *Astron. J.*, **138**, 466.

Houdashelt, M. L., Bell, R. A., and Sweigart, A. V. 2000, *Astron. J.*, **119**, 1448.

Howell, S. B. 2006, *Handbook of CCD Astronomy*, 2nd ed., Cambridge Univ. Press., Cambridge.

IONDEV SRL. 2021, QtiPlot—Data Analysis and Scientific Visualisation (https://www.qtiplot.com/).

Jayasinghe, T., *et al.* 2018, *Mon. Not. Roy. Astron. Soc.*, **477**, 3145.

Kafka, S. 2021, *Observations from the AAVSO International Database* (https://www.aavso.org/data-download).

Kallrath, J., and Milone, E. F. 2009, *Eclipsing Binary Stars: Modeling and Analysis*, Springer-Verlag, New York.

Kurucz, R. L. 2002, *Baltic Astron.*, **11**, 101.

Latković, O., Čeki, A., and Lazarević, S. 2021, *Astrophys. J., Suppl. Ser.*, **254**, 10.

Li, K., *et al.* 2019, *Res. Astron. Astrophys.*, **19**, 147.

Liu, L. 2021, *Publ. Astron. Soc. Pacific*, **133**, 084202.

Lucy, L. B. 1967, *Z. Astrophys.*, **65**, 89.

Maceroni, C., and van't Veer, F. 1993, *Astron. Astrophys.*, **277**, 515.

Minor Planet Observer. 2011, MPO Canopus v 10.7.1.3 (http://www.minorplanetobserver.com).

Mortara, L., and Fowler, A. 1981, in *Solid State Imagers for Astronomy*, SPIE Conf. Proc. 290, Society for Photo-Optical Instrumentation Engineers, Bellingham, WA, 28.

Nelson, R. H. 2009, WDwint56a: Astronomy Software by Bob Nelson (https://www.variablestarssouth.org/bob-nelson).

O'Connell, D. J. K. 1951, *Publ. Riverview Coll. Obs.*, **2**, 85.

Pecaut, M. J., and Mamajek, E. E. 2013, *Astrophys. J., Suppl. Ser.*, **208**, 9.

Pojmański, G., Pilecki, B., and Szczygiel, D. 2005, *Acta Astron.*, **55**, 275.

Prša, A., and Zwitter, T. 2005, *Astrophys. J.*, **628**, 426.

Qian, S. 2001, *Mon. Not. Roy. Astron. Soc.*, **328**, 635.

Qian, S. 2003, *Mon. Not. Roy. Astron. Soc.*, **342**, 1260.

Ruciński, S. M. 1969, *Acta Astron.*, **19**, 245.

Schlafly, E. F., and Finkbeiner, D. P. 2011, *Astrophys. J.*, **737**, 103.

Shappee, B. J., *et al.* 2014, *Astrophys. J.*, **788**, 48.

Smith, T. C., Henden, A. A., and Starkey, D. R. 2011, in *The Society for Astronomical Sciences 30th Annual Symposium on Telescope Science*, Society for Astronomical Sciences, Rancho Cucamonga, CA, 121.

Software Bisque. 2019, The Sky X professional edition 10.5.0 (https://www.bisque.com).

Terrell, D. 2022, *Galaxies*, **10**, 8.

Terrell, D., and Wilson, R. E. 2005, *Astrophys. Space Sci.*, **296**, 221.

Terrell, D., Gross, J., and Cooney, W. R. 2012, *Astron. J.*, **143**, 99.

van Hamme, W. 1993, *Astron. J.*, **106**, 2096.

Wang, R., *et al.* 2019, *Publ. Astron. Soc. Pacific*, **131**, 024505.

Wilson, R. E. 1979, *Astrophys. J.*, **234**, 1054.

Wilson, R. E. 1990, *Astrophys. J.*, **356**, 613.

Wilson, R. E., and Devinney, E. J. 1971, *Astrophys. J.*, **166**, 605.

Woźniak, P. R., *et al.* 2004, *Astron. J.*, **127**, 2436.

Zhao, G., Zhao, Y.-H., Chu, Y.-Q., Jing, Y.-P., and Deng, L.-C. 2012, *Res. Astron. Astrophys.*, **12**, 723.

Long-Term Period Behavior of the Semiregular Variable V1 and the Type II Cepheids V2 and V3 in the Globular Cluster M10

Pradip Karmakar
Department of Mathematics, Madhyamgram High School (H.S.), Sodepur Road, Madhyamgram, Kolkata-700129, India; pradipkarmakar39@gmail.com

Horace A. Smith
Department of Physics and Astronomy, Michigan State University, East Lansing, MI 48824; smithhh@msu.edu

Wayne Osborn
Department of Physics, Central Michigan University, Mount Pleasant, MI 48859; wayne.osborn@cmich.edu

Peter B. Stetson
NRC-Herzberg, Dominion Astrophysical Observatory, 5071 West Saanich Road, Victoria BC V9E 2E7, Canada; Peter.Stetson@nrc.ca

Received January 7, 2022; revised March 28, 2022; accepted April 1, 2022

Abstract We present new U, B, V, R_C, and I_C-band photometry for the semiregular variable V1 and the type II Cepheids V2 and V3 in the globular cluster M10. Using old and new observations, we updated the most recent—1985—period change study of these variables. Observations made from 1912 through 2020 show that V1 has a recent average period of 48.9 days and, for the Cepheid variables, the 18.7-day pulsation period of V2 has decreased and the 7.8-day pulsation period of V3 has remained constant. The Fourier spectrum of the V-band observations of V2 yields a pattern of additional peaks at $0.5f_0$ and $1.5f_0$, where $f_0$is the frequency of the fundamental mode, similar to those that have been reported for W Virginis that indicate probable period-doubling.

1. Introduction

The period of a pulsating variable star is a basic parameter for determining its type (see Samus *et al.* 2017). Furthermore, periods of regularly pulsating stars can often be determined more accurately than any other of their measurable quantities, and observing changes in period have the potential to reveal evolution effects of a pulsating star before it shows in any other manner.

In this paper we study the light curves and period behavior of three variables in the globular cluster M10 (NGC 6254, C1654-040): V1, V2, and V3 (Table 1). A finding chart is given by Clement *et al.* (1985). One of these stars, V1, is a red semiregular variable. The other two, V2 and V3, are type II Cepheids with periods of 18.7 days and 7.8 days, respectively. Type II Cepheids of periods longer than about 5 days, such as V2 and V3, are classified as W Virginis type, while those with shorter periods are designated BL Herculis variables (Soszyński *et al.* 2011, Figure 4; Bono *et al.* 2020). Our study extends the period change analyses of these stars by Clement *et al.* (1985), and compares our results to other observed rates of period change for type II Cepheids.

Table 1. Coordinates from the *Catalogue of Variable Stars in Galactic Globular Clusters* (Clement *et al.* 2001).

Object	*R.A. (J2000)* *h m s*	*Dec. (J2000)* *° ‘ “*
V1	16 57 10.12	–04 05 36.1
V2	16 57 11.74	–04 03 59.7
V3	16 56 55.95	–04 04 16.3

2. The observational data sets

We draw upon five sets of photometric observations of M10 that date from 1983, the date of the last observations included in the Clement *et al.* (1985) investigation: (1) the archival U, B, V, R_C, and I_C CCD photometry compiled by Stetson *et al.* (2019, hereafter referred to as "Stetson"); (2) B, V, and I_C CCD photometry from the Michigan State University Observatory (MSU); (3) V and R_C CCD photometry (for V1 only) from the National Undergraduate Research Observatory (NURO); (4) V-band and g-band data from the All-Sky Automated Survey for Supernovae (ASAS-SN); and (5) B and V brightness estimates on photographic plates from the United States Naval Observatory (USNO) and the Las Campanas and Hale Observatories.

Data Set 1 The Stetson photometry was obtained from heterogeneous archival CCD images from many observatories and observing runs, reduced and calibrated in a consistent way by one of the authors (PBS). His approach to this data reduction is described in Stetson *et al.* (2019). Observations of primary and secondary photometric standard fields obtained during each run were used to derive the color-transformation and extinction corrections for each night. These were used to transform instrumental magnitudes to the Landolt photometric system. The heterogeneous nature of the Stetson photometry is illustrated in Table 2, which shows the data from three of the 32 observing runs used: Run 7 and Run 9 with the La Silla ESO 2.2-m telescope in 2000 and 2001, Run 10 with the La Palma 1-m telescope in 2002. The complete photometry is included in the AAVSO ftp site[1] in a somewhat different format.

Table 2. A sample of the Stetson CCD U, B, V, R_C, and I_C photometry of V1, V2, and V3.

Run	*HJD*	*Filter*	*V1*	*Error*	*V2*	*Error*	*V3*	*Error*
7	2451633.8891	B	13.528	0.0040	13.065	0.0037	13.676	0.0051
7	2451633.8930	B	13.471	0.0110	13.057	0.0043	13.639	0.0077
7	2451633.8969	B	13.478	0.0113	13.048	0.0071	13.645	0.0054
7	2451635.9030	V	12.008	0.0045	12.453	0.0050	12.579	0.0053
7	2451635.9068	V	12.006	0.0041	12.453	0.0076	12.562	0.0054
7	2451635.9106	V	12.002	0.0049	12.455	0.0049	12.562	0.0071
7	2451635.8934	I_C	10.383	0.0080	11.108	0.0051	11.619	0.0050
7	2451635.8971	I_C	10.381	0.0141	11.120	0.0068	11.604	0.0046
7	2451635.9016	I_C	10.397	0.0159	11.111	0.0041	11.601	0.0052
9	2451998.8970	U	—	—	12.415	0.0043	13.922	0.0040
9	2451998.9030	U	14.465	0.0046	12.421	0.0043	13.922	0.0036
9	2451998.8730	B	—	—	12.104	0.0037	13.528	0.0041
9	2451998.8742	B	13.237	0.0054	12.087	0.0044	13.529	0.0046
9	2451998.8573	V	—	—	11.448	0.0038	12.700	0.0029
9	2451998.8586	V	11.772	0.0036	11.443	0.0027	12.705	0.0037
9	2451998.8637	V	—	—	11.476	0.0032	12.684	0.0017
9	2451998.8706	V	11.768	0.0051	11.464	0.0034	12.680	0.0026
9	2451998.8853	V	—	—	11.459	0.0038	12.684	0.0032
9	2451998.8899	V	11.773	0.0046	11.459	0.0039	12.687	0.0021
10	2452404.5846	B	13.684	0.0093	13.532	0.0055	—	—
10	2452404.5821	V	12.150	0.0198	12.584	0.0156	—	—
10	2452404.5791	R_C	11.356	0.0222	11.946	0.0118	—	—

The complete photometry is included in the AAVSO ftp site in a somewhat different format (ftp://ftp.aavso.org/public/datasets/501-Karmakar-StetsonPhotometry.txt). *A summary table of the Stetson photometry observing runs is also available there* (ftp://ftp.aavso.org/public/datasets/501-Karmakar-StetsonSummary.txt).

Data Set 2 We obtained B, V, and I_C-band images of M10 in 2006 using the 0.6-m telescope of the Michigan State University (MSU) campus observatory with an Apogee Alta U47 CCD camera (0.6 arc-second pixels, 10 × 10 arcmin field of view). Bias and dark images were subtracted in the conventional way and twilight images were used as flat field images. Exposures were about 1-minute long, varying somewhat with sky conditions. Instrumental photometry was obtained using the DAOPHOT and ALLSTAR routines (Stetson 1987, 1994), as in Rabidoux *et al.* (2010). Standard stars for calibration of instrumental photometry to the standard B, V, and I_C systems were selected from the photometry in Stetson's web-based catalogue[2] (Stetson *et al.* 2019, Table 4). Six to ten relatively unblended stars were used to set the zero-point for each filter. Color terms were applied as in Rabidoux *et al.* (2010). The MSU photometry obtained in this way produces light curves that closely match those from the Stetson photometry. The MSU observations are listed in Table 3.

Data Set 3 We located archival V and R_C CCD images of M10 obtained over four consecutive nights in 2004 from the 0.8-m telescope of the National Undergraduate Research Observatory (NURO). The small 4 × 4 arcmin field of view meant that only V1 was visible on these images. They were reduced in a similar manner as for the MSU observations. The resulting magnitudes are given in Table 4.

Data Set 4 We downloaded observations of V1, V2, and V3 from the All-Sky Automated Survey for Supernovae (ASAS-SN; Shappee *et al.* 2014; Kochanek *et al.* 2017) from the Sky Patrol option on the ASAS-SN webpage, using the positions for the variables given in Table 1. Only V-band observations are available for most of the 2012–2020 time period we utilized, although g-band data are more recently available, including for 2020. The different cameras used to collect the ASAS-SN data sometimes have slightly different zero-points, resulting in increased light curve scatter. In the cases of the M10 observations, these shifts, if present, appear to be smaller than a few hundredths of a magnitude and we have not applied corrections for them. The relatively large ASAS-SN pixels mean, however, that these observations show the effects of blending more seriously than is the case for the MSU and Stetson CCD photometry. This is somewhat mitigated for V2 and V3 because they are not close to the center of the cluster.

Data Set 5 Finally, we made use of archival photographic plates. We possessed 20 plates (ten B and ten V plates) of M10 taken with the USNO-Flagstaff, Arizona, 1.5-m reflector over a 24-day span in 1983. To these we added six Las Campanas plates taken 1992–1993 and one Hale (Mt. Wilson) plate from 1932 found in the Yerkes Observatory plate vault. All but the Hale plate were exposed with filter and emulsion combinations that gave images approximating either B or V magnitudes. Magnitudes for the variable stars were derived by eye estimates of the variable's brightness relative to several non-variable stars having Stetson *et al.* (2019) photometry. Because V1, V2, and V3 are among the very brightest stars in the cluster, there are only a few suitable comparison stars and at times magnitude estimates had to be made by extrapolating from the comparison sequence, leading to significant uncertainties.

Five to ten independent brightness estimates were made for each plate using a loupe. The average of the different estimates for a star yielded its adopted magnitude while their dispersion

---

[1] ftp://ftp.aavso.org/public/datasets/501-Karmakar-StetsonPhotometry.txt

[1] https://www.canfar.net/storage/vault/list/STETSON/homogeneous/Latest_photometry_for_targets_with_at_least_BVI/NGC6254_(UBVRI)

Table 3. The MSU CCD photometry of V1, V2, and V3.

HJD	*Filter*	*V1*	*Error*	*V2*	*Error*	*V3*	*Error*
2453892.6279	B	13.11	0.02	12.25	0.02	13.32	0.02
2453895.6290	B	13.18	0.02	12.58	0.02	13.75	0.02
2453899.6211	B	13.18	0.03	13.46	0.02	13.37	0.02
2453901.6280	B	13.20	0.03	13.40	0.02	13.44	0.02
2453903.6192	B	13.31	0.03	13.08	0.02	13.75	0.02
2453906.6196	B	13.22	0.02	11.97	0.02	13.50	0.02
2453907.6175	B	13.27	0.03	12.09	0.02	13.26	0.02
2453907.6200	B	13.30	0.03	12.11	0.02	13.26	0.02
2453935.6317	B	13.33	0.03	13.21	0.02	13.67	0.02
2453936.6353	B	13.35	0.03	13.35	0.02	13.59	0.02
2453937.6154	B	13.29	0.03	13.49	0.02	13.43	0.02
2453943.6025	B	13.19	0.03	12.01	0.02	13.77	0.02
2453892.6230	V	11.88	0.03	11.45	0.02	12.60	0.02
2453895.6252	V	12.00	0.03	11.69	0.02	12.92	0.02
2453899.6179	V	11.99	0.03	12.43	0.02	12.52	0.02
2453901.6259	V	12.13	0.03	12.46	0.02	12.58	0.02
2453903.6175	V	12.17	0.03	12.39	0.02	12.90	0.02
2453906.6172	V	12.06	0.03	11.53	0.02	12.69	0.02
2453907.6159	V	12.10	0.03	11.48	0.02	12.54	0.02
2453910.6284	V	—	—	11.47	0.02	12.75	0.02
2453910.6314	V	12.10	0.04	11.49	0.02	12.78	0.02
2453935.6341	V	12.13	0.03	12.52	0.02	13.02	0.02
2453936.6375	V	12.16	0.02	12.38	0.02	12.86	0.02
2453937.6205	V	12.18	0.03	12.40	0.02	12.64	0.02
2453943.6050	V	12.01	0.03	11.45	0.02	12.98	0.02
2453892.6303	I_C	10.32	0.02	10.52	0.02	11.60	0.02
2453892.6317	I_C	10.36	0.02	10.55	0.02	11.62	0.02
2453895.6326	I_C	10.40	0.03	10.60	0.02	11.91	0.02
2453899.6254	I_C	10.37	0.03	11.37	0.02	11.63	0.02
2453901.6301	I_C	10.40	0.03	11.34	0.02	11.58	0.02
2453903.6242	I_C	10.43	0.03	11.29	0.02	11.88	0.02
2453935.6279	I_C	10.34	0.03	11.19	0.02	11.97	0.02
2453906.6220	I_C	10.38	0.03	10.65	0.02	11.70	0.02
2453907.6218	I_C	10.39	0.03	10.57	0.02	11.56	0.02
2453910.6207	I_C	10.42	0.03	10.51	0.02	11.72	0.02
2453936.6333	I_C	10.46	0.02	11.24	0.02	11.72	0.02
2453936.6344	I_C	10.41	0.03	11.28	0.02	11.80	0.02
2453937.6180	I_C	10.30	0.03	11.31	0.02	11.66	0.02
2453937.6195	I_C	10.35	0.03	11.35	0.02	11.67	0.02
2453943.6001	I_C	10.32	0.03	10.70	0.02	11.90	0.02

Table 4. The NURO CCD V and R_C photometry of V1.

HJD	*Filter*	*Mag.*	*Error*
2453140.7692	V	12.007	0.038
2453140.7697	V	12.016	0.023
2453140.7704	V	11.979	0.016
2453141.9262	V	11.944	0.015
2453141.9270	V	11.929	0.020
2453142.8997	V	11.923	0.018
2453142.9006	V	11.908	0.031
2453143.8416	V	11.899	0.009
2453143.8424	V	11.895	0.020
2453140.7669	R_C	11.115	0.028
2453140.7674	R_C	11.124	0.013
2453140.7681	R_C	11.134	0.017
2453141.9283	R_C	11.078	0.016
2453141.9289	R_C	11.090	0.013
2453142.9016	R_C	11.083	0.008
2453142.9023	R_C	11.097	0.015
2453143.8434	R_C	11.061	0.026
2453143.8442	R_C	11.061	0.024

indicated the error. Including possible magnitude zero-point errors, we adopt as the uncertainties in our photographic magnitudes: 0.20 mag for V1, 0.15 mag for V2, and 0.10 mag for V3 from the USNO B and V plates, 0.12 mag from the Las Campanas B and V plates, and 0.10 mag from the Hale B plate. The photographic data are given in Table 5.

3. Periods and light curves

We used two period-finding routines to search for periodicities in the V1, V2, and V3 data: Period04 (Lenz and Breger 2005) and a date-compensated discrete Fourier transform, as implemented in Peranso 2.0 (Vanmunster 2006; Paunzen and Vanmunster 2016). Independent searches were carried out on the combined MSU and Stetson B, V, and I_C photometry and on the ASAS-SN photometry. No single period was found that produced a good phased light curve for V1 for all the MSU-Stetson data. This is probably a consequence of the semiregular nature of the variations and the relatively large number of years (1996–2018) spanned by those observations.

Table 5. B and V magnitudes from USNO, Las Campanas (LC) and Hale photographic plates for V1, V2, and V3.

Plate Number	*Filter*	*HJD*	*V1*	*V2*	*V3*
USNO 48325	B	2445496.7880	13.09	13.57	13.44
USNO 48327	B	2445496.7949	13.07	13.62	13.45
USNO 48486	B	2445514.7727	13.42	13.51	13.57
USNO 48488	B	2445514.7803	13.46	13.57	13.54
USNO 48516	B	2445516.7472	13.44	13.73	13.94
USNO 48518	B	2445516.7542	13.45	13.72	13.79
USNO 48556	B	2445519.7549	13.42	13.65	13.50
USNO 48558	B	2445519.7628	13.39	13.72	13.55
USNO 48579	B	2445520.7827	14.36	13.60	13.54
USNO 48581	B	2445520.7897	13.43	13.62	13.49
LC CD-2964	B	2448800.674	—	12.40	13.38
LC CD-2965	B	2448800.684	—	12.57	13.40
LC CD-2966	B	2448800.695	—	12.36	13.41
LC CD-2967	B	2448800.707	—	12.48	13.41
Hale B61	B	2426799.978	—	12.57	13.95
USNO 48324	V	2445496.7852	11.90	12.14	12.75
USNO 48326	V	2445496.7915	11.89	12.18	12.80
USNO 48485	V	2445514.7688	12.04	12.03	12.75
USNO 48487	V	2445514.7765	11.97	11.93	12.83
USNO 48517	V	2445516.7511	12.10	12.60	13.05
USNO 48519	V	2445516.7574	12.08	12.53	13.03
USNO 48557	V	2445519.7588	12.08	12.58	12.85
USNO 48559	V	2445519.7668	12.07	12.57	12.80
USNO 48578	V	2445520.7791	12.09	12.54	12.78
USNO 48580	V	2445520.7862	12.03	12.51	12.83
LC CD-3043	V	2449158.641	—	11.50	12.98
LC CD-3044	V	2449158.651	—	11.65	12.94

Table 6. Period search results for V1, V2, and V3 data with Period04 and the Peranso 2.0 DCDFT routine.

Data Set	*Period04 Result (d)*	*Peranso 2.0 Result (d)*
V1-ASAS-SN g-data	48.94 ± 0.10	48.95 ± 0.25
V1-ASAS-SN V-data	48.89 ± 0.02	48.90 ± 0.10
V2-ASAS-SN g-data	18.70 ± 0.02	18.70 ± 0.06
V2-Stetson & MSU B-data	18.703 ± 0.005	18.702 ± 0.010
V2-ASAS-SN V-data	18.702 ± 0.005	18.701 ± 0.008
V2-Stetson & MSU V-data	18.704 ± 0.005	18.707 ± 0.010
V2-Stetson & MSU I_C-data	18.70 ± 0.02	18.71 ± 0.01
V3-ASAS-SN g-data	7.833 ± 0.002	7.833 ± 0.003
V3-Stetson & MSU B-data	7.8330 ± 0.0004	7.8331 ± 0.0008
V3-ASAS-SN V-data	7.8343 ± 0.0005	7.8351 ± 0.0008
V3-Stetson & MSU V-data	7.8329 ± 0.0006	7.8330 ± 0.0009
V3-Stetson & MSU I_C-data	7.834 ± 0.001	7.833 ± 0.002

Table 7. Frequency and Amplitude results of V2 in V band.

Frequence (c/d)	*Amplitude V*	*ID*
0.0534849(11)	0.439(2)	f_0
0.1069698	0.099(2)	$2f_0$
0.1604547	0.059(2)	$3f_0$
0.213940	0.045(2)	$4f_0$
0.267424	0.022(2)	$5f_0$
0.320909	0.009(2)	$6f_0$
0.026676(12)	0.042(2)	$f_{(low)}$
0.080222(13)	0.038(2)	f_1

On the other hand, consistent periods were found in more numerous ASAS-SN V and g-band observations of 2012–2020. We found unique periods for V2 and V3 that fit the Stetson-MSU and ASAS-SN data. The period search results are given in Table 6, which shows that the Period04 and Peranso results agree well. For Period04, the listed uncertainties derive from the least squares fitting routine, while for the Peranso 2.0 results, uncertainties depend upon the noise in the amplitude spectrum, which we estimated independently of the default values in the Peranso routine.

Variable 1 Figure 1 shows the U, B, V, R_C, and I_C-band light curves for V1 from our CCD data, i.e. from the Stetson, MSU, and NURO sources. Brightness changes over 0.5 mag are seen. Figure 2 shows the light curve for just one observing season, 2018, using the ASAS-SN data. Cycle-to-cycle variations are clearly seen, as is often the case for red giant variables. Other observing seasons show similar effects. Finally, Figure 3 shows that the ASAS-SN data yield a reasonable phased light curve assuming an average period of 48.9 days since 2012. This agrees with the "a little less than 50 days" period found by Clement *et al.* (1985), but is significantly shorter than the period of 70.88 published by Rozyczka *et al.* (2018).

Variable 2 The phased U, B, V, R_C, and I_C light curves of V2 using a period of 18.703 days from the Stetson (dots) and MSU (Xs) CCD photometry are shown in Figure 4. Figure 5 and Figure 6 present the light curves using the same reference epoch and period for the ASAS-SN V observations and the photographic data, respectively. The phase shifts of the photographic light curves compared to the CCD ones in Figures 4 and 5 likely reflect the changing period as discussed in the following section.

The Figure 4 light curves show broad maxima and that the times (i.e., phase) of maximum and of minimum light increase somewhat with longer wavelength; these effects were noted by Arp (1955). The detailed nature of the broad maximum—called double-peaked by Arp—is obvious in the ASAS-SN data of Figure 5, but those observations average about 0.3 mag brighter than ours. We note that our period supports the 18.7226-day period for V2 found by Clement *et al.* (1985) but disagrees with the 19.470995-day period found by Rozyczka *et al.* (2018). We suspect this is due to an incorrect cycle count being used in linking their 1998 and 2002 observation sets.

Arp (1955) suggested that the amplitude of the light curve of V2 might differ in alternate cycles of the 18.7-day period. This effect (commonly called period doubling), was discovered in RV Tauri variables—Cepheid-like pulsating stars with periods longer than 20 days—but now has been seen in the two type II Cepheid subtypes, the BL Her and W Vir stars (for more details see Smolec and Moskalik 2012, Plachy *et al.* 2017, Smolec *et al.* 2018 and references therein). Period doubling in V2 is seen in our observations, most clearly in the numerous ASAS-SN V data. Figure 7 presents the ASAS-SN light curve of V2 phased with a 37.406-day period, twice our adopted P = 18.703 days. Although one could regard V2 as having a true period of 37.4 days, we retain the 18.7-day period in studying its long term period changes. As noted by Clement *et al.* (1985), the early photographic observations are not adequate for using the doubled period.

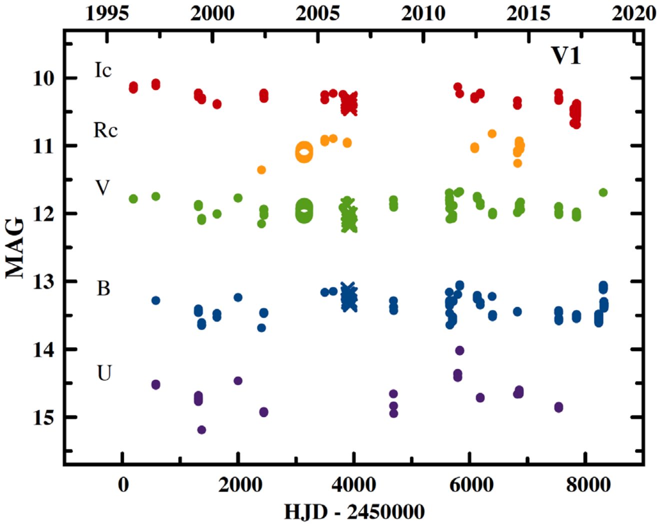

Figure 1. The U, B, V, R_C, and I_C-band light curves of V1 from 1996 to 2018 from our CCD data (Data sets 1–3). Observations from Stetson are shown as dots, those from MSU as Xs, and those from NURO as open circles.

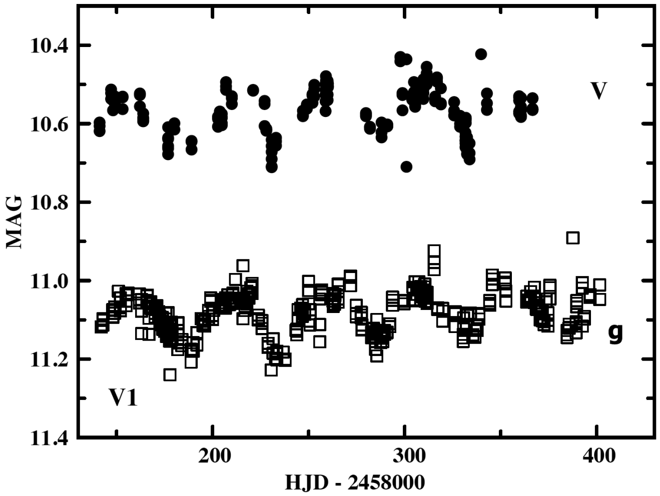

Figure 2. Light curves of V1 from the ASAS-SN V-band and g-band observations for the 2018 observing season. V data are represented by closed circles and g-data by open squares. The semiregular nature of the variations on a time scale of about 50 days is seen in the figure.

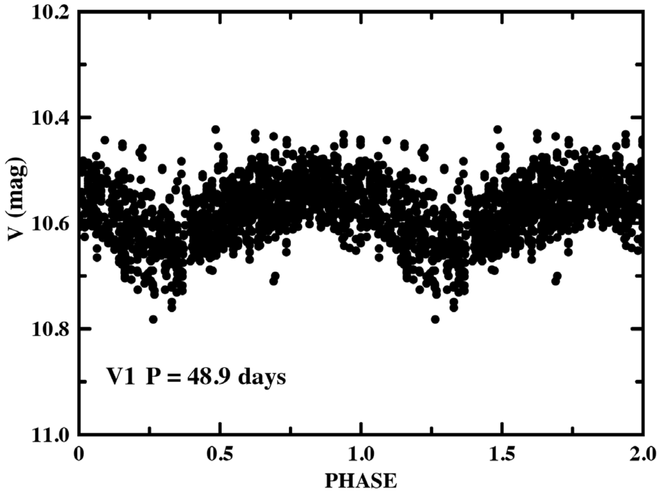

Figure 3. The phased light curve of V1 from all ASAS-SN V-band observations using a period of 48.9 days.

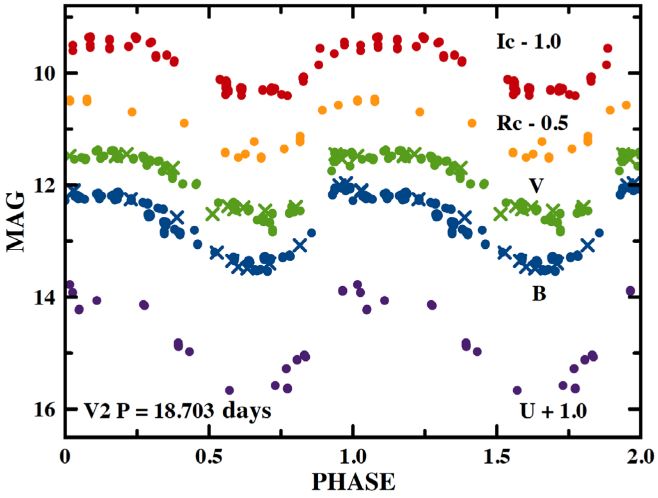

Figure 4. The U, B, V, R_C, and I_C-band phased light curves of V2 from the Stetson (dots) and MSU (Xs) CCD observations. Phases were computed using a period of 18.703 days. The indicated zero-point shifts have been added to the U, R_C, and I_C curves to make the different light curves easier to see.

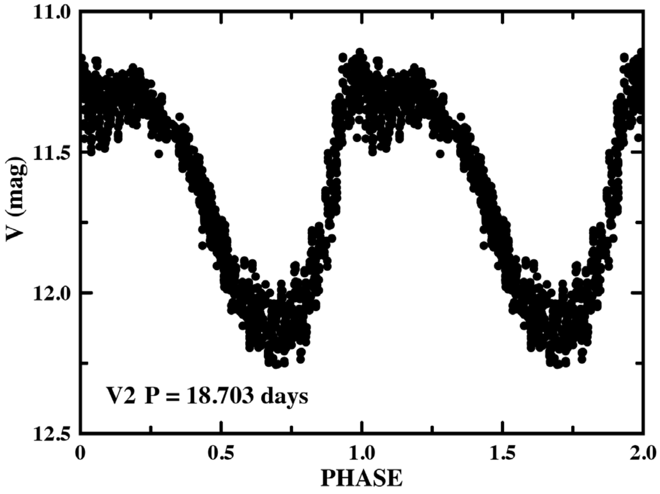

Figure 5. The light curve of all ASAS-SN V-band observations of V2, phased with a period of 18.703 days.

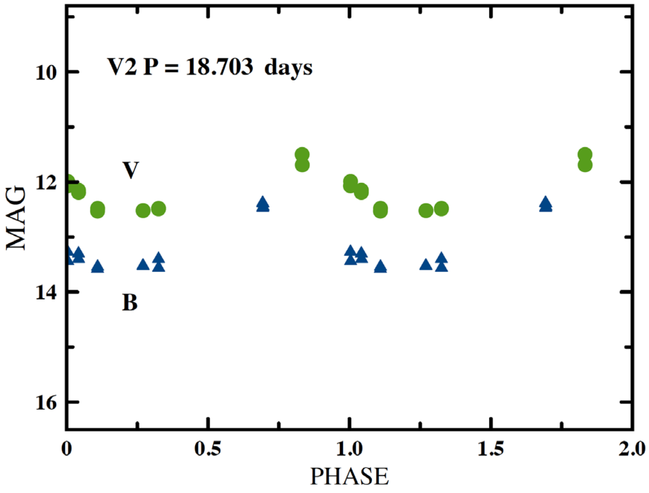

Figure 6. The B and V phased light curves of V2 from the photographic data. Phases were computed using a period of 18.703 days.

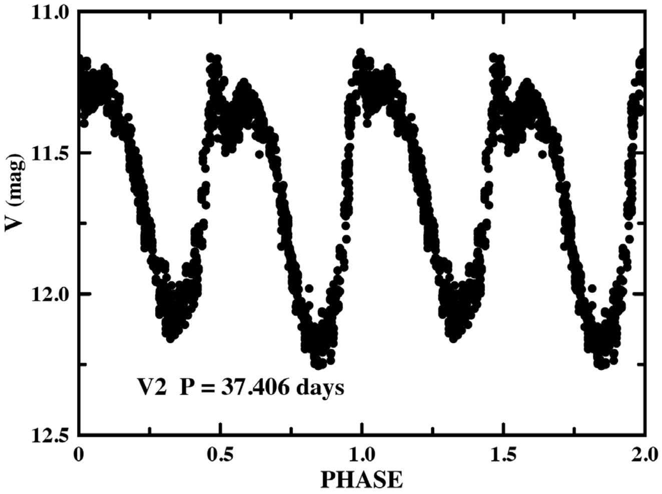

Figure 7. The light curve of all ASAS-SN V-band observations of V2, phased with a period of 37.406 days. Cycle differences, particularly the magnitude of minimum, are seen.

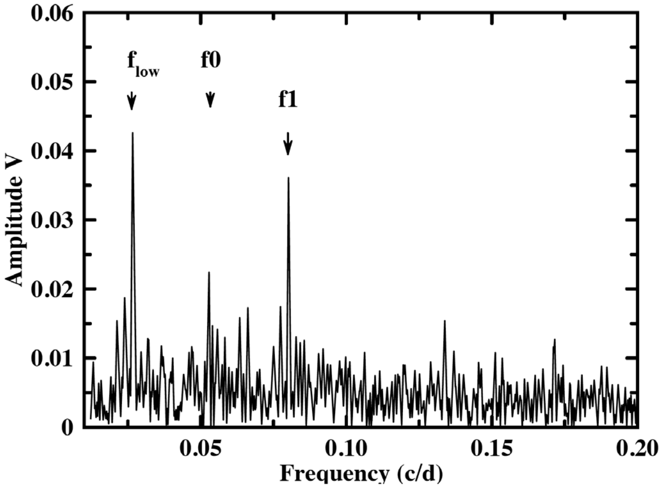

Figure 8. Fourier spectrum of the ASAS-SN V observations of V2 after removal of f_0 and its first five harmonics. Frequencies $f_{(low)}$ and f_1 are now dominant.

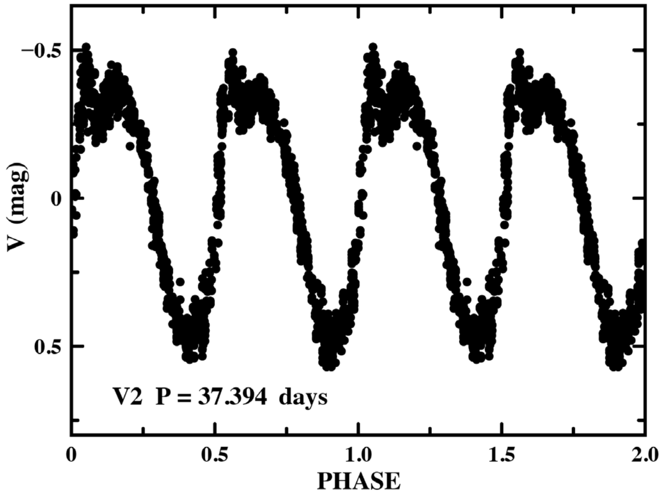

Figure 9. Subtracting frequencies $f_{(low)}$ and f_1 from the ASAS-SN data leaves a light curve with most of the alternate cycle variations seen in Figure 7 eliminated.

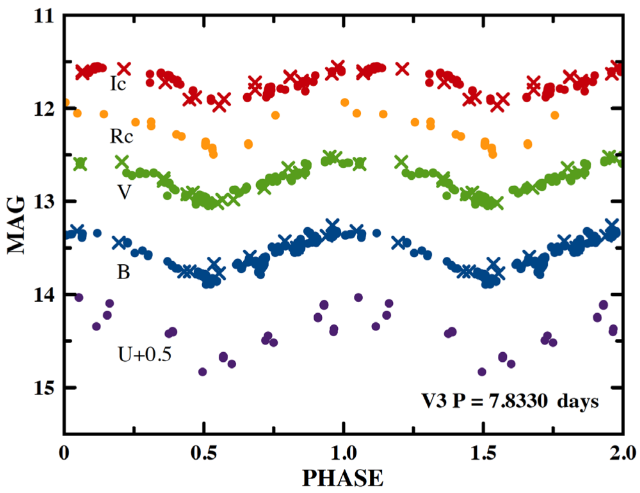

Figure 10. The U, B, V, R_C, and I_C-band phased light curves of V3 from the Stetson (dots) and MSU (Xs) observations. Phases were computed using a period of 7.8330 days. The indicated zero-point shift has been added to the U observations.

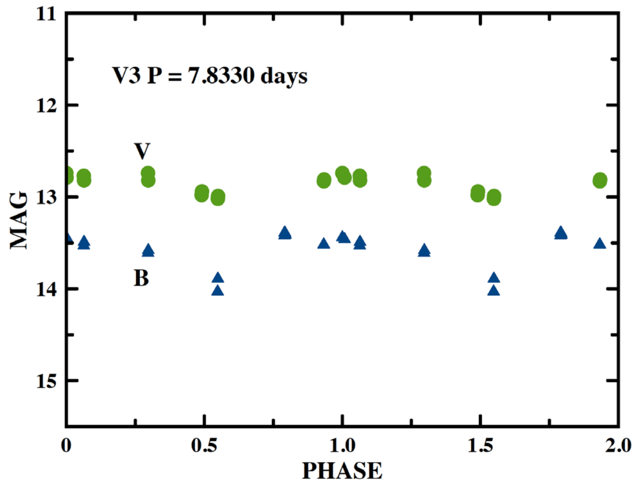

Figure 11. The B and V phased light curves of V3 from the photographic data. Phases were computed using a period of 7.8330 days.

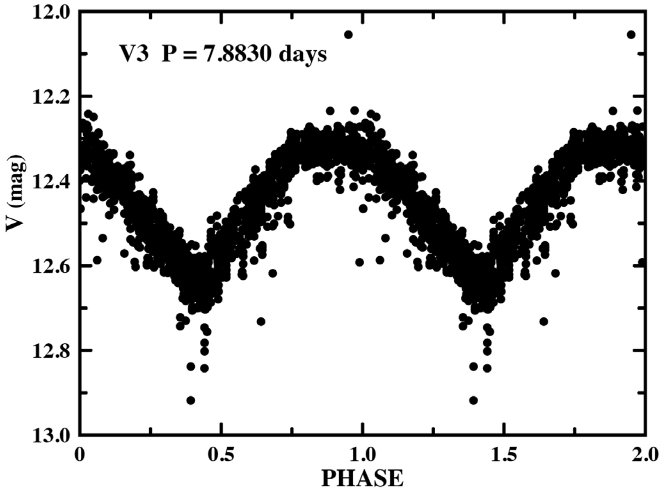

Figure 12. The light curve of all ASAS-SN V-band observations of V3, phased with a period of 7.8330 days.

Table 8. The magnitude-weighted mean magnitudes for V1, V2, and V3 using the Stetson and MSU photometry (and NURO for V1) and some results from the literature.

Star	*<U>*	*<B>*	*<V>*	*<R>*	*<I>*	*<B>–<V>*	*<V>–<I>*	*Source*
V1	14.59	13.40	11.94	11.00	10.32	1.46	1.62	Our results
V2	13.29	12.89	12.08	11.48	10.90	0.81	1.15	Our results
V3	13.88	13.57	12.78	12.29	11.73	0.79	1.05	Our results
V1	—	—	11.809	—	10.226	—	1.58	Arellano Ferro *et al.* (2020)
V2	—	—	12.127	—	10.934	—	1.19	Arellano Ferro *et al.* (2020)
V3	—	—	12.761	—	11.721	—	1.04	Arellano Ferro *et al.* (2020)
V1	—	—	11.83	—	—	1.52	—	Rozyczka *et al.* (2018), Table 1
V2	—	—	12.05	—	—	0.96	—	Rozyczka *et al.* (2018), Table 1
V3	—	—	12.75	—	—	0.87	—	Rozyczka *et al.* (2018), Table 1

Given the occurrence of period doubling, we used PERIOD04 to perform a Fourier analysis for the extensive ASAS-SN V observations of V2. The results showed only one high-power frequency (denoted f_0), which corresponds to P = 18.697 d. We then performed a new search with f_0 and its harmonics ($2f_0$, $3f_0$, $4f_0$, $5f_0$, and $6f_0$) removed from the data. As shown in Figure 8, the new Fourier spectrum revealed two additional frequencies of significant power, which we name $f_{(low)}$ and f_1, following Templeton and Henden's (2007) similar analysis for W Vir. We then performed a simultaneous frequency search for f_0, f_1, and $f_{(low)}$, using the "improve all" option in PERIOD04, while holding the harmonic terms fixed to f_0. Table 7 lists our final frequency and amplitude results. Values in parentheses indicate uncertainties returned by PERIOD04. Amplitudes will, of course, be influenced by any blending effects from the large ASAS-SN pixels. The frequency f_0 found in this fashion corresponds to a period of 18.697 days, close to the V2 periods we found (see Table 6), and can be identified as the fundamental mode frequency (Bono *et al.* 2020).

The frequency pattern in Table 7 broadly matches that in Templeton and Henden's (2007) Table 2 for W Vir. They noted that, in the case of W Vir (main period 17.3 days), $f_{(low)}$ was similar but not identical, to both 0.5 f_0 and f_1–f_0. That is also the case for V2. Period doubling, that is alternating cycles having differences in light curve shape and amplitude, has now been identified for a number of W Vir stars, but especially those with periods longer than 15 days (Smolec *et al.* 2018; Jurkovic 2021). The presence of frequencies very near 0.5 f_0 and 1.5 f_0 in the Fourier spectrum of V2 is consistent with period doubling.

Given the 0.5 f_0 symmetry of $f_{(low)}$ and f_1 relative to f_0, it is tempting to say that W Vir alternate cycle effects result from a secondary period and its harmonics interacting with the fundamental mode of pulsation. In our case, that is supported by the fact that subtracting frequencies $f_{(low)}$ and f_1 from the ASAS-SN data leaves a light curve with most of the period doubling effects eliminated as shown in Figure 9, which can be compared to Figure 7.

Variable 3 Figure 10 shows the U, B, V, R_C, and I_C phased light curves of V3 from the Stetson and MSU CCD photometry using a period of 7.8330 days. Any variation of the time of maximum with wavelength is small. Figures 11 and 12 show, respectively, the light curves of V3 from the photographic observations and the ASAS-SN V data computed using the same period and epoch. The photographic curves agree with the CCD ones taking into account their larger errors. The ASAS-SN curve has similar phase but averages about 0.4 mag brighter than our V light curves, reflecting the blending effects seen in those observations.

Rozyczka *et al.* (2018) give a period of 7.872181 days for V3, somewhat higher than our value and the Clement *et al.* (1985) period of 7.831 days. The Arellano Ferro *et al.* (2020) period for V3, 7.835134 days, is closer to our own, although still a little higher.

4. Mean magnitudes

We have determined mean magnitudes for V1, V2, and V3 from our observations. These are given in Table 8 with some results from previous studies for comparison. Our means are magnitude averages over phase for V2 and V3. That, however, was not possible for the red semiregular variable V1, so those values are averages over time from the Stetson and MSU observations. Mean magnitudes from the ASAS-SN photometry are not listed in Table 8 because that camera's large pixels make images subject to blending. No corrections for interstellar extinction have been applied to the mean magnitudes, although we note that Arellano Ferro *et al.* (2020) adopted E(B–V) = 0.25 for the cluster.

5. Long term period changes

Clement *et al.* (1985) investigated the long-term period changes of V2 and V3 using the photographic observations then available. Their Table II and Figure 4 show the relative phase shifts of the light curves of V2 and V3 at different epochs, determined using their adopted periods of 18.7226 days and 7.831 days for V2 and V3. We double-checked the Clement *et al.* (1985) phase shift values to verify that we find the same shifts to within the expected uncertainties. One exception was the phase shift for the 1932 observations of V3, for which we find a shift of 0.01 preferable to the Clement *et al.* value of 0.11. Our estimated error for that point is, however, large, about 0.1.

We used our more recent data to extend the time coverage of the period change investigations. The B and V light curves from photometry in our datasets (1) through (5) were used to determine relative phase shifts for recent epochs on the Clement *et al.* (1985) system. We did not use our U, R_C, and I_C-band

Table 9. Phase shifts of maximum light of V2 (in fractions of a period).

Year	*Shift*	*Error*	*Source*
1912–1919	0.05	0.12	Clement *et al.* (1985), Table II
1931–1934	–0.17	0.04	Clement *et al.* (1985), Table II
1935–1936	–0.16	0.07	Clement *et al.* (1985), Table II
1937–1939	–0.13	0.06	Clement *et al.* (1985), Table II
1940–1949	–0.04	0.08	Clement *et al.* (1985), Table II
1948–1949	0.02	0.06	Clement *et al.* (1985), Table II
1950–1957	–0.02	0.06	Clement *et al.* (1985), Table II
1951–1952	0.02	0.10	Clement *et al.* (1985), Table II
1952	0.00	0.02	Clement *et al.* (1985), Table II
1954	0.01	0.04	Clement *et al.* (1985), Table II
1954–1956	0.01	0.08	Clement *et al.* (1985), Table II
1957	0.02	0.07	Clement *et al.* (1985), Table II
1959–1968	0.01	0.05	Clement *et al.* (1985), Table II
1968–1971	0.05	0.09	Clement *et al.* (1985), Table II
1972	0.04	0.07	Clement *et al.* (1985), Table II
1972–1973	0.04	0.05	Clement *et al.* (1985), Table II
1973–1974	0.02	0.05	Clement *et al.* (1985), Table II
1975	0.04	0.10	Clement *et al.* (1985), Table II
1979	0.01	0.05	Clement *et al.* (1985), Table II
1980–1983	0.10	0.10	Clement *et al.* (1985), Table II
1983	–0.12	0.12	USNO plates
1996–2000	–0.26	0.12	Stetson
2001–2011	–0.29	0.08	Stetson, MSU
2012	–0.55	0.12	ASAS-SN
2013	–0.60	0.05	ASAS-SN
2012–2018	–0.42	0.12	Stetson
2014	–0.62	0.03	ASAS-SN
2015	–0.66	0.03	ASAS-SN
2016	–0.66	0.03	ASAS-SN
2017	–0.68	0.03	ASAS-SN
2018	–0.68	0.03	ASAS-SN
2019	–0.69	0.03	ASAS-SN
2020	–0.72	0.03	ASAS-SN

Table 10. Phase shifts of maximum light of V3 (in fractions of a period).

Year	*Shift*	*Error*	*Source*
1932	0.01	0.10	Clement *et al.* (1985) (modified)
1933	–0.22	0.08	Clement *et al.* (1985), Table II
1935–1936	–0.22	0.15	Clement *et al.* (1985), Table II
1937	–0.25	0.06	Clement *et al.* (1985), Table II
1938–1940	–0.09	0.10	Clement *et al.* (1985), Table II
1941–1949	–0.17	0.15	Clement *et al.* (1985), Table II
1948–1952	–0.02	0.07	Clement *et al.* (1985), Table II
1952	0.00	0.01	Clement *et al.* (1985), Table II
1954	–0.10	0.05	Clement *et al.* (1985), Table II
1954	0.14	0.06	Clement *et al.* (1985), Table II
1955	0.05	0.08	Clement *et al.* (1985), Table II
1957	0.11	0.10	Clement *et al.* (1985), Table II
1956–1960	0.03	0.22	Clement *et al.* (1985), Table II
1961–1968	0.08	0.10	Clement *et al.* (1985), Table II
1968–1972	–0.05	0.08	Clement *et al.* (1985), Table II
1972–1973	–0.02	0.08	Clement *et al.* (1985), Table II
1973–1975	0.01	0.06	Clement *et al.* (1985), Table II
1979	–0.02	0.07	Clement *et al.* (1985), Table II
1980	0.03	0.07	Clement *et al.* (1985), Table II
1983	0.04	0.08	USNO plates
1992	–0.04	0.15	Las Campanas plates
1996–2000	0.07	0.08	Stetson
2006	0.18	0.09	MSU
2001–2011	0.11	0.05	Stetson
2012	0.20	0.12	ASAS-SN
2013	0.24	0.04	ASAS-SN
2012–2018	0.23	0.05	Stetson
2014	0.25	0.03	ASAS-SN
2015	0.26	0.03	ASAS-SN
2016	0.27	0.03	ASAS-SN
2017	0.28	0.03	ASAS-SN
2018	0.29	0.03	ASAS-SN
2019	0.30	0.03	ASAS-SN
2020	0.31	0.03	ASAS-SN

light curves for phase shift determinations as they differ too greatly in shape compared to the V and B band light curves. Allowance was made for a small difference between the B and V light curves of V2 in that its V light curve is shifted to longer phases by 0.03 ± 0.02 relative to B. For the ASAS-SN observations, light curves were determined for each year for which a sufficient number of observations was available. Because of the long time coverage of the Stetson CCD data, those observations were divided into three separately-treated sets: 1996–2000, 2001–2011, and 2012–2018.

Following Clement *et al.* (1985), we adopted the Arp (1955) observations from 1952 as having a phase shift of 0.00 and used the Clement *et al.* periods of 18.7226 days for V2 and 7.831 days for V3 for computing our light curves. Our curves were then compared to light curves from several datasets in Table II of Clement *et al.* (1985) and the relative phase shifts determined for each case. When both B and V light curves were available for an epoch, the shift results were averaged to obtain the adopted value. We emphasize that for many of the datasets in Table II of Clement *et al.* (1985), as well as for our more sparse new datasets, using the entire light curve to determine a phase shift is preferable to determining an O–C value using just the data near maximum or near minimum light.

Our adopted phase shifts for V2 and V3 are listed in Tables 9 and 10, respectively. The listed errors are those given by Clement *et al.* (1985) for their data, while for ours they are eye estimates of how uncertain the phase shift determination was when comparing our light curve to the Clement *et al.* reference ones. The time of maximum of V3 from Table 3 in Arellano Ferro *et al.* (2020) has been neglected because it was calculated using a period different from ours and the ASAS-SN observations already provide good recent time coverage around their epoch.

The phase shifts are shown as a function of time in Figures 13 and 14. The cycle count for the point representing the 1912–1919 observations of V2 is uncertain. The point could be plotted at a phase shift of 0.05 or –0.95. Inspection of Figure 13 reveals a decreasing period for V2. Figure 14 shows a nearly constant period for V3, although some fluctuation in period is possible. The slope of the phase shift–date correlation reflects a slight difference between the period adopted by Clement *et al.* (1985) and the average period over the 90 years covered by our data.

Period change rates for RR Lyrae stars and Cepheids are often described as the rate of period change in days per million years, denoted by β (see, for example, Le Borgne *et al.* 2007, Equation 3, and Osborn *et al.* 2019, Equation 5). In calculating β for V2, we excluded the 1912–1919 point because of its cycle count ambiguity. A parabolic least squares fit to the other phase shift points in that table, weighted by $1/\text{error}^2$, yielded $\beta = -452 \pm 23$ d/Myr, thus confirming a significantly decreasing period.

The –0.95 phase shift option for the 1912–1919 observations for V2 is most consistent with our decreasing period result.

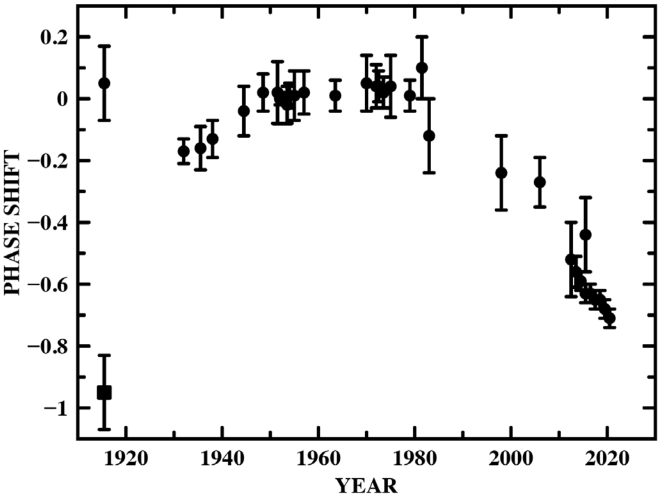

Figure 13. The phase shift diagram for V2. Two alternative shifts are possible for the first data point because of a cycle count ambiguity. The data indicate a significant period decrease.

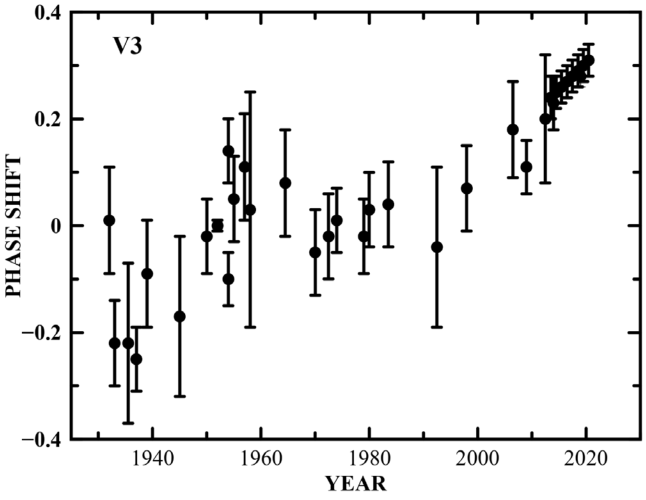

Figure 14. The phase shift diagram for V3. No obvious evidence of a period change is seen.

For V3, we calculated β = +7.9 ± 7.8 d / Myr, indicating any long-term period increase is doubtful. The overall slope of the points is consistent with an average period of 7.832 days.

6. Conclusions

Our observations confirm that V1 is a red semiregular variable. We find a B–V of 1.46 and that the light variations cycle on a time scale of about 49 days, at least over the past few decades.

V2 and V3 are type II Cepheids. These are commonly divided into two subtypes, the BL Her stars, with P ≤ 5 d, and the longer period W Vir ones, having 5 d < P ≤ 20 d, while the related stars with periods longer than 20 d are called RV Tau variables (Soszyński *et al.* 2011; Bono *et al.* 2020). Thus, both stars are W Vir subtype.

The period of V2, P = 18.70 d, falls near the upper end of the range of W Vir periods, close to the period range for RV Tau stars. Period doubling, such as seen in V2, is often exhibited by RV Tau variables. On the other hand, the period of V3, P = 7.8330 d, is near the lower end of the W Vir period range.

W Virginis variables have been observed to have increasing periods, decreasing periods, or even erratic period changes (Neilson *et al.* 2016; Karmakar *et al.* 2019). The decreasing period of V2 is thus not extraordinary. As noted in Neilson *et al.* (2016), however, interpreting the observed period changes of W Vir stars is made difficult by uncertainties concerning the mechanism by which such stars enter the instability strip. Bono *et al.* (2020) predicted that W Vir variables should show both period increases and decreases, but that increases should be more commonly observed. Negative period changes should mainly affect the long-period tail of the W Vir stars in their model, which would apply to V2. However, Bono *et al.* (2020) also noted that those conclusions might need to be altered if gravo-nuclear loops occur inside the instability strip, something not included in their model.

Relatively few type II Cepheids are found with periods of 5 to 8 days in galactic globular clusters, although that period range is more populated in some other systems (see Figure 4 in Soszyński *et al.* 2011 and Figure 2 in Bono *et al.* 2020). While the period of V3 makes it by definition too long for inclusion in the BL Her class, it might be considered as in the transition range between W Vir and BL Her subtypes. Metal-poor BL Her variables with measured rates of period change have increasing or constant periods (see Wehlau and Bohlender 1982 and Osborn *et al.* 2019, Table 9). The nearly constant period of V3 is consistent with the behavior of BL Her variables. Further, some BL Her stars have been observed to exhibit short term period fluctuations (Osborn *et al.* 2019), as our O–C results suggest may be the case for V3.

7. Acknowledgements

We thank Christine Clement for her help and advice and Yerkes Observatory for allowing access to its photographic plate archive. This research made use of the Peranso light curve and period analysis software. We thank the ASAS-SN project for providing public access to its observations. We thank those who created and who maintain the Period04 program. We thank the anonymous referee for the detailed comments that allowed us to significantly improve the paper.

References

Arellano Ferro, A., Yepez, M. A., Muneer, S., Bustos Fierro, I. H., Schröder, K. P., Giridhar, S., and Calderón, J. H. 2020, *Mon. Not. Roy. Astron. Soc.*, **499**, 4026.
Arp, H. C. 1955, *Astron. J.*, **60**, 1.
Bono, G., *et al.* 2020, *Astron. Astrophys.*, **644**, A96.
Clement, C. M., Hogg, H. S., and Wells, T. R. 1985, *Astron. J.*, **90**, 1238.
Clement, C. M., *et al.* 2001. *Astron. J.*, **122**, 2587.
Jurkovic, M. I. 2021, in *RR Lyrae/Cepheid 2019: Frontiers of Classical Pulsators*, ASP Conf. Ser. 529, eds. K. Kinemuchi, C. Lovekin, H. Neilson, K. Vivas, Astronomical Society of the Pacific, San Francisco, 305.

Karmakar, P., Smith, H. A., and De Lee, N. 2019, *J. Amer. Assoc. Var. Star Obs.*, **47**, 167.

Kochanek, C. S., *et al.* 2017, *Publ. Astron. Soc. Pacific*, **129**, 104502 (https://asas-sn.osu.edu).

Le Borgne, J. F., *et al.* 2007, *Astron. Astrophys.*, **476**, 307.

Lenz P., and Breger M. 2005, *Commun. Asteroseismology*, **146**, 53.

Neilson, H. R., Percy, J. R., and Smith, H. A. 2016, *J. Amer. Assoc. Var. Star Obs.*, **44**, 179.

Osborn, W., Kopacki, G., Smith, H. A., Layden, A., Pritzl, B., Kuehn, C., and Anderson, M. 2019, *Acta Astron.*, **69**, 101.

Paunzen, E., and Vanmunster, T. 2016, *Astron. Nachr.*, **337**, 239.

Plachy, E., Molnár, L., Jurkovic, M. I., Smolec, R., Moskalik, P. A., Pál, A., Szabados, L., and Szabó, R. 2017, *Mon. Not. Roy. Astron. Soc.*, **465**, 173.

Rabidoux, K., *et al.* 2010, *Astron. J.*, **139**, 2300.

Rozyczka, M., Narloch, W., Schwarzenberg-Czerny, A., Thompson, I. B., Poleski, R., and Pych, W. 2018, *Acta Astron.*, **68**, 237.

Samus, N. N., Kazarovets, E. V., Durlevich, O. V., Kireeva, N. N., and Pastukhova, E. N. 2017, *Astron. Rep.*, **61**, 80, *General Catalogue of Variable Stars: Version GCVS 5.1* (http://www.sai.msu.su/gcvs/gcvs/index.htm).

Shappee, B. J., *et al.* 2014, *Astrophys. J.*, **788**, 48 (https://asas-sn.osu.edu).

Smolec, R., and Moskalik, P. 2012, *Mon. Not. Roy. Astron. Soc.*, **426**, 108.

Smolec, R., Moskalik, P., Plachy, E., Soszyński, I., and Udalski, A. 2018, *Mon. Not. Roy. Astron. Soc.*, **481**, 3724.

Soszyński, I., *et al.* 2011, *Acta Astron.*, **61**, 285.

Stetson, P. B. 1987, *Publ. Astron. Soc. Pacific*, **99**, 191.

Stetson, P. B. 1994, in *Astronomy with the CFHT Adaptive Optics Bonnette*, ed. R. Arsenault, Canada-France-Hawaii Telescope Corp., Kamuela, HI, 72.

Stetson, P. B., Pancino, E., Zocchi, A., Sanna, N., and Monelli, M. 2019, *Mon. Not. Roy. Astron. Soc.*, **485**, 3042.

Templeton, M. R., and Henden, A. A. 2007, *Astron. J.*, **134**, 1999.

Vanmunster, T. 2006, PERANSO 2.0 Manual, CBA Belgium (https://www.cbabelgium.com/peranso).

Wehlau, A., and Bohlender, D. 1982, *Astron. J.*, **87**, 780.

What Are the SRd Variables?

John R. Percy

Department of Astronomy and Astrophysics, and Dunlap Institute for Astronomy and Astrophysics, University of Toronto, 50 St. George Street, Toronto, ON M5S 3H4, Canada; john.percy@utoronto.ca

Received January 13, 2022; revised February 25, 2022; accepted March 7, 2022

Abstract SRd variables are semiregular pulsating variable giants or supergiants of spectral type F, G, or K. But why are they not regular? This paper presents a detailed study, using light curve analysis, and Fourier and wavelet analysis, of data from the All-Sky Automated Survey for Supernovae (ASAS-SN), on 37 arbitrarily-selected SRd variables to examine the possible causes of their non-regularity. Of the 37 variables, 30 showed significant variations in pulsation amplitude, 11 showed significant "wandering" of the period, 6 showed abrupt period shifts, 7 showed a possible long secondary period (LSP), 8 showed possible bimodal pulsation, and 4 showed otherwise complicated behavior. Variable pulsation amplitude is therefore the most common of several phenomena which lead to their non-regularity. It also occurs in RV Tauri variables and pulsating red giants, but its physical cause is not known, nor is the cause of period wandering. Because there was some previous evidence that LSPs were rare among SRd variables, 13 SRd stars with the longest ASAS-SN periods were similarly analyzed. That analysis, and examination of the light curves of several dozen other SRd variables with long ASAS-SN periods showed clearly that LSPs are common in SRd variables. In longer-period SRd variables in the ASAS-SN variable star catalog, the catalog period is usually the LSP, rather than the pulsation period. LSPs in RV Tauri variables and in red giants have been ascribed to binarity; that may be the case in SRd variables also. A dozen W Virginis variables and 30 RV Tauri variables were also analyzed to study the overlap and possible relationship between CW, RV, and SRd stars. There is considerable overlap between these types.

1. Introduction

Yellow giants and supergiants lie in the upper middle of the Hertzsprung-Russell (H-R) diagram, which plots the luminosity of the stars against their surface temperatures. They are unstable against pulsation, and are classified according to the character of their variability: W Virginis (CWA) stars or Population II Cepheids have periods of 8 to 35 days, and generally regular light curves. RV Tauri (RV) stars have periods of 30 to 150 days and are defined by their alternating deep and shallow minima. According to the *General Catalogue of Variable Stars* (Samus *et al.* 2017), SRd stars are *semiregular* giants and supergiants of spectral type F, G, or K, with amplitudes in the range 0.1 to 4 mag, and periods in the range 30 to 1,100 days. Miller Bertolami (2016) and Bono *et al.* (2020) have carried out important studies of the evolution of variable stars in this part of the H-R diagram, and Bódi and Kiss (2019) have determined the physical properties of galactic RV Tauri stars from *Gaia* data, but there has been very little study of the SRd variables specifically. RV and SRd variables appear to be post-AGB stars. They are relatively rare.

Most Population I and II Cepheids are regular; their phase curves show little or no scatter. Why are SRd stars non-regular? Because their pulsation amplitude varies with time? Because their period "wanders" sufficiently to produce scatter in the phase curve? Because they have two or more pulsation periods? Because they have long secondary periods (LSPs), as many RV stars do? Or some combination of these? Or something else?

The purpose of this paper is to investigate these questions by carrying out a careful analysis of two samples of SRd stars in the All-Sky Automated Survey for Supernovae (ASAS-SN) variable star catalogue (Shappee *et al.* 2014; Jayasinghe *et al.* 2018, 2019). Some RV stars and long-period CW stars were also analyzed to put the SRd variables in context, in the hope of clarifying the relationship between these different types. This paper builds upon the results of an earlier limited study using AAVSO visual data (Percy and Kim 2014).

2. Data and analysis

From the ASAS-SN variable star website and catalog (Shappee *et al.* 2014, Jayasinghe *et al.* 2018, 2019), data on the following star samples were downloaded and analyzed with light curve analysis and time-series analysis: 37 arbitrarily-chosen SRd stars, 13 SRd stars with the longest ASAS-SN periods (348–477 days), and 4 CWA stars with the longest ASAS-SN periods. In addition, the light curves and phase curves of the following star samples were inspected on the ASAS-SN variable star website: several dozen more SRd stars with the longest periods, a dozen CW stars with periods of 40–80 days, and 30 RV variables from Bódi and Kiss (2019). The ASAS-SN data and light curves are freely available on-line (asas-sn.osu.edu/variables). The error bars on the ASAS-SN observations are typically 0.02 mag, and this is consistent with the noise level in the Fourier analyses.

Because of the complexity of the variability in many of the stars, and the different time scales involved, careful visual light curve analysis proved to be especially useful.

Fourier and wavelet analysis was then done using the AAVSO time-series analysis package VStar (Benn 2012). Note that the amplitudes which are given in this paper are actually semi-amplitudes—the coefficient of the sine curve with the given period—rather than the full amplitude or range.

Two caveats: First, the star samples analyzed and inspected here are based on the classifications in the ASAS-SN catalog, with all their limitations and possible biases. Second: the datasets are only a few years long. The ASAS-SN classifications are based on a variety of measured properties of the stars. Other classifications of the stars in our sample—most based on limited data—range from SRd to SR, SRa, SRb, to L, I, and even Cep:.

3. Results

3.1. The cause of non-periodicity.

Table 1 summarizes the analysis of 37 randomly-chosen SRd variables from the ASAS-SN catalog with mean V magnitudes between 11 and 13. The columns give: the variable star name, the ASAS-SN period in days, the ASAS-SN mean V magnitude, the *fractional* variation or wander ($\Delta P/P$) in the period during the interval of observation, the range (variation) in pulsation amplitude ΔA as determined by wavelet analysis, and various notes. These include apparent presence of LSPs, and additional periods which may or may not be due to a second pulsation mode. MP indicates that there were more than two peaks of appreciable strength in the Fourier spectrum, i.e. the spectrum was complex, and VM indicates that, in the phase curve, the minimum showed noticeably more scatter than the maximum—a common occurrence. An asterisk (*) indicates that there is a note about the star in section 3.1.

Of the 37 stars, 30 showed variations of more than 10 percent in the pulsation amplitude, 11 showed a fractional period "wander" of more than 0.03, 6 showed an apparent abrupt period shift, 7 showed a probable or possible LSP, 8 showed two peaks, possibly due to bimodal pulsation, 4 showed multiple peaks (usually more than 3, and not necessarily statistically significant), and 5 showed the variable minimum phenomenon. These can all contribute to producing a phase curve with much scatter, and thereby lead to a classification of SRd. Keep in mind, however, that these conclusions are based on only a few seasons of ASAS-SN data, with seasonal gaps.

Clearly the most common phenomenon which leads to semiregularity is variable pulsation amplitude. Figure 1 shows a specific example—BP Her—whose amplitude varies by a factor of two over the interval of the dataset. The cause of the amplitude variation is not known. There is no obvious correlation between the period and the mean amplitude, or between the period and the fractional variation in amplitude in the stars in Table 1. The following are notes on some specific stars.

HL And The period switches between 104 and 92 days.

V578 CrA The period switches between 62 and 78 days. In the light curve, the cycle lengths range from 50 to 70 days.

V537 Dra The period switches between 30 and 49 days. The ASAS-SN period of 221 days is presumably an LSP.

FQ Her The period "wander" is unusually large.

KQ Lyr Some very faint, presumably-spurious observations were omitted.

LV Lyr There are many peaks with amplitudes less than 0.05 mag. There is also a possible LSP of 352 days, with an amplitude of 0.08 mag. The data on this star in the AAVSO International Database give a possible period of 57.44 days, but the 352-day period does not appear in the AAVSO data.

V1183 Sgr According to the wavelet analysis, the period switches between about 50 and 65 days, each having a variable amplitude (Figure 2).

V1991 Sgr In the light curve, there are cycles of many lengths between 50 and 120 days but, in the Fourier spectrum, no peak is dominant. The highest is the 74.46-day period in Table 1.

V2221 Sgr The period switches between 62 and 75 days.

V3070 Sgr There is no significant period or amplitude variation, or LSP; the phase curve therefore has relatively little scatter. The light curve, however, shows some evidence of a second, shorter period— possibly due to an additional pulsation mode.

AO Sco The light curve is very complicated. The highest of many peaks in the Fourier spectrum is 99.33 days, with an amplitude varying between 0.12 and 0.25 mag. There is some suggestion, in the wavelet plot, that the period switches from 98 to 111 days for some time.

V830 Sco The period seems to switch between 50.6 and 57.7 days, each with an amplitude of 0.08. The phase curve is rather scattered.

3.2. Long secondary periods in SRd stars

Many RV variables have LSPs, 5 to 10 times longer than thepulsation period, and are subclassified as RVb. However, there seem to be few if any SRd variables with LSPs (Percy and Ursprung (2006); Percy (2015); Percy and Haroon (2021)). RU Cep and WW Tau are possible cases. Fourier analysis of AAVSO visual data on RU Cep shows a possible LSP of 520.17 days, with an amplitude of 0.06 mag, but no LSP is apparent in the AAVSO visual data on WW Tau.

The sample of SRd stars in Table 1 includes several with LSPs. Figure 3 shows a specific example—V3724 Sgr. The pulsational variability dominates, but a fourth-order polynomial, fitted to the data, shows the LSP clearly. But the period is long, and only one cycle is covered by the data, so one should technically not call it a period.

The ASAS-SN catalog includes 229 SRd variables, with periods ranging up to 476.74 days. The 12 with longest period were chosen for analysis and are listed in Table 2, along with ASAS-SN J192917.35+525332.8, whose period is almost as long, and whose light curve is shown in Figure 4. It was chosen because it was particularly illustrative. The columns in Table 2 give the star name, the ASAS-SN period in days, mean V magnitude, amplitude, and estimates of the pulsation period from the light curve (LC) and Fourier analysis (FA). A colon denotes uncertainty. Ten of the 12 longest-period stars in Table 2, with ASAS-SN periods of 348.13 to 476.74 days, also show shorter-period (typically 30–60 days) variability superimposed on the light curve, as shown in Figure 4. The shorter-period variability is presumably due to pulsation, as in the case of RVb stars and red giants with LSPs. The pulsation period in ASAS-SN J192917.+525332.8 is about 43 days from the light curve and 41 ± 1 days from Fourier analysis. The ASAS-SN catalog period is an LSP. The pulsation amplitude varies from 0.03 to 0.08 on a time scale of about 20 pulsation periods, as in other RV, SRd, and red SR variables.

3.3. Relation to CWA variables

There are 559 CWA variables in the ASAS-SN catalog. Most of these have short (10–20 day) periods, with saw-tooth

Table 1. Period Analysis of ASAS-SN Observations of some SRd Variables.

Name	*PA(d)*	*mean V*	*ΔP/P*	*ΔA*	*Notes*
HL And	101	11.01	—	0.07–0.19	LSP = 417d, *
V389 Aps	108	11.15	0.024	0.50–0.55	
V555 Cen	73	12.53	0.011	0.24–0.26	MP, LSP?
V652 Cen	86	11.80	0.023	0.16–0.22	also P = 48.71d
V1387 Cen	98	11.28	0.030	0.20–0.33	Cepheid-like LC
V578 CrA	—	11.95	—	—	LSP = 443d?, *
V651 CrA	81	12.40	0.019	0.22–0.44	VM
V654 CrA-	85	12.74	0.035	0.15–0.19	LSP = 760d
V340 Dra	99	11.03	0.105	0.10–0.13	
V537 Dra	30:	11.78	—	0.03–0.10	also P = 50d and 221d, *
AR For	126	11.16	0.030	0.35–0.39	also P = 75.9d
BP Her	82	11.98	0.025	0.19–0.41	
FQ Her	128	11.21	0.066	0.22–0.37	also P = 89.4d, *
V361 Her	95	11.18	0.041	0.18–0.29	VM
KQ Hya	96	11.54	0.013	0.22–0.28	sawtooth LC
DP Lyr	88	11.79	0.029	0.18–0.28	
KQ Lyr	84	12.90	0.013	0.36–0.52	*
LV Lyr	—	12.31	—	0.06–0.12	P = 40d, 60d, 352d?, *
V2844 Oph	103	12.11	0.025	0.19–0.30	also harmonic?
V1183 Sgr	—	12.92	—	—	complex; P = 50d and 65d, *
V1991 Sgr	74	12.45	0.075	0.10–0.28	MP, *
V2221 Sgr	73	12.21	—	0.05–0.20	MP, *
V2336 Sgr	92	12.56	0.008	0.16–0.21	also harmonic
V3070 Sgr	101	12.08	0.001	0.22–0.22	MP, ampl. constant, *
V3101 Sgr	81	12.45	0.042	0.24–0.26	also P = 56.24d
V3724 Sgr	82	12.48	0.011	0.43–0.62	LSP = 900d
V4061 Sgr	91	11.42	0.014	0.12–0.15	also P = 185.2d?
AO Sco	99	12.37	—	0.12–0.25	plus harmonic; *
V830 Sco	51	12.04	—	0.08–0.11	also P = 57.70d, *
V1039 Sco	83	11.15	0.017	0.26–0.33	VM
V1633 Sco	79	11.92	0.032	0.21–0.30	sparse
CD TrA	85	11.87	0.034	0.14–0.16	
GN Vir	48	11.91	0.015	0.13–0.17	also harmonic
OO Vir	111	12.69	0.016	0.55–0.64	VM
NSV 10702	106	12.04	0.009	0.23–0.29	VM, also P = 66.2d
NSV 11150	96	12.38	0.001	0.33–0.34	VM
NSVS 16356719	83	12.73	0.030	0.20–0.23	long-term variation

** An asterisk indicates a note in section 3.1.*

Table 2. Period Analysis of ASAS-SN Observations of some Long-period SRd Variables.

Name: ASAS-SN-V	*P(ASAS)*	*mean V*	*A(ASAS)*	*Pulsation period*
J202338.34-431055.9	476.74	12.37	0.20	LC: 40d; FS: 42:d
J010054.02-725136.8	458.29	11.91	0.53	unusual LC
J171232.57+580052.9	456.11	12.22	0.18	LC: 40d; FS: 39.9d
J075241.54+031701.9	442.94	12.49	0.24	LC: 55d; FS: 50.9d
J120428.99+583354.0	416.52	11.09	0.20	LC: 40d; FS: 62.3d
J010601.38-725243.3	406.50	12.77	0.31	no evidence of pulsation
J205705.36-452412.0	396.72	11.82	0.18	LC: 75–80; FS: 38.5d
J170819.10+024921.3	374.53	13.41	0.22	LC: 40d; FS: 42.8d
J174744.53+453435.9	359.26	13.37	0.21	LC: 40d; FS: 40d:
J195314.29-391128.9	353.41	12.40	0.25	LC: 50d; FS: 42.4d
J051419.34-400423.9	349.65	13.69	0.41	LC: 40d; FS: 42±1
J021014.93-752861.7	348.13	13.39	0.39	LC: 60d; FS: 57.1d
J192917.35+525332.8	322.39	12.13	0.37	LC: 43d; FS: 41±1d

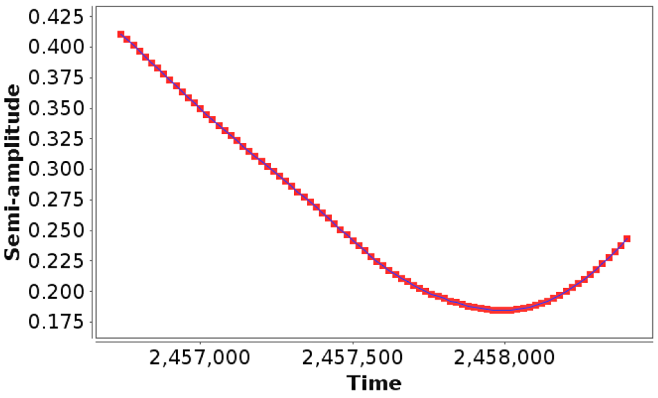

Figure 1. The pulsation amplitude variability of BP Her, determined from ASAS-SN data by wavelet analysis. The pulsation period is 81.64 days. The amplitude varies by a factor of two, on a time scale of about 20 pulsation periods. This behavior is similar to that of other SRd, RV, and red SR variables.

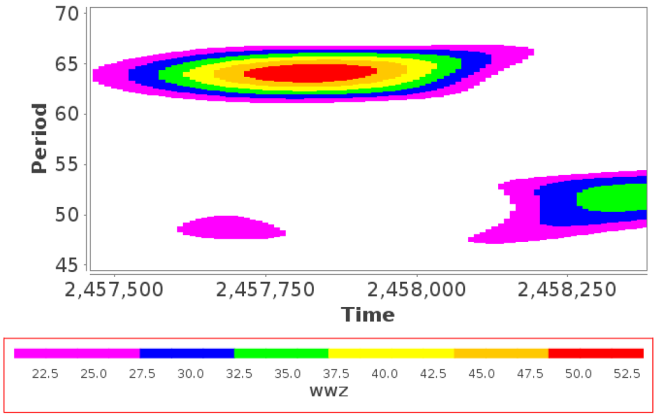

Figure 2. The wavelet contour diagram of V1183 Sgr, determined from ASAS-SN data, showing the presence of two pulsation periods of about 50 and 65 days, with variable pulsation amplitudes, resulting in apparent mode-switching.

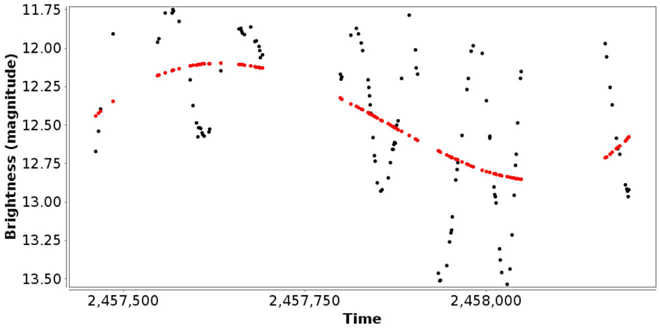

Figure 3. The V light curve of V3724 Sgr, from ASAS-SN data, showing a pulsation period of 81.77 days, with variable amplitude, and an LSP of about 900 days. The model (red line) is a fourth-order polynomial fit.

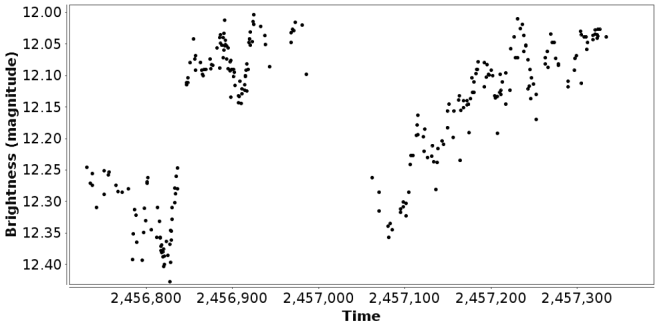

Figure 4. Part of the V light curve of ASAS-SN J192917.35+525332.8, showing the presence of both an LSP of 322 days (the ASAS-SN period), and a pulsation period of 41 days. This star was chosen because the pulsation period and the LSP are both clearly visible.

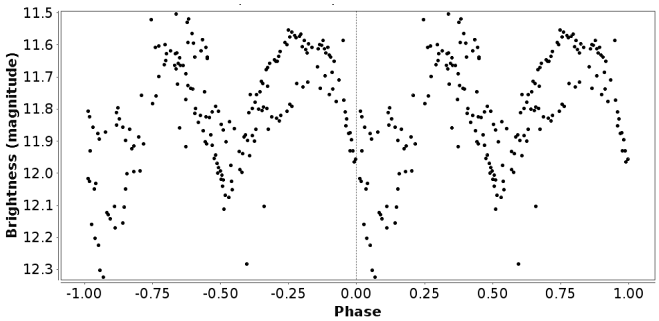

Figure 5. The phase curve of the SRd star V652 Cen, using a period of twice the value in Table 1, showing the mild tendency of alternating deep and shallow minima.

phase curves with minimal scatter. There are, however, 43 with periods greater than 50 days, and 8 with periods greater than 75 days. Of the latter, 4 stars were either too bright or too faint for analysis. ASAS-SN J054347.27-663509.1 has the same kind of low-scatter, saw-tooth phase curve as shorter-period CWA variables, but ASAS-SN J074929.27+530753.2, J130634.33+185820.7, and J093857.44-092132.8 have more scattered phase curves, mostly due to variability in the pulsation amplitude. Indeed, the same seems to be true of most of the other CWA stars with periods greater than 50 days. It is therefore not clear why ASAS-SN did not classify them as SRd stars. There is clearly some overlap.

3.4. Relation to RV variables

Five stars in Table 1 had two periods in a ratio close to 2: V555 Cen, V652 Cen, V2844 Oph, V2221 Sgr, and V2336 Sgr. Of these, V652 Cen (Figure 5) and V2844 Oph had phase curves which were marginally RV-like; alternating minima were of slightly different depths.

Out of curiosity, I looked up the ASAS-SN data on the 11 high-confidence Galactic RV stars in Table 1 of Bódi and Kiss (2019). Four were not in the ASAS-SN catalog, 4 were misclassified as CWA stars, and 4 were correctly classified as RVa stars. For the 20 other Galactic RV stars listed in Table 2 of Bódi and Kiss (2019), only 7 were correctly classified by ASAS-SN as RVa stars. The ASAS-SN analysis and classification system is relatively limited and simple, and understandably has problems with complex variables like RV and SRd variables.

This should be kept in mind when using the classifications and analyses in that catalog.

Both these observations show that the boundary between SRd and RV stars is a rather fuzzy one.

4. Discussion

The most common phenomenon which leads to SRd non-regularity is variable pulsation amplitude. It is not clear why the RV and SRd stars show this behavior and the Cepheids do not. Some process which depends on the gravity or luminosity of the star must come into operation. Variable pulsation amplitudes are found in most pulsating red giants (Percy and Abachi 2013).

The period wander in SRd stars may be due to the same process which causes a similar phenomenon in pulsating red giants (Eddington and Plakidis (1929); Percy and Colivas (1999)). It can be modelled as random cycle-to-cycle period fluctuations, and may be due to the effect of the very large convective cells in the outer layers of these stars.

The defining characteristic of RV stars is the alternating deep and shallow minima, but this behavior is often irregular. Percy *et al.* (2003) analyzed a sample of 33 RV and SRd stars in the LMC using MACHO data, using self-correlation analysis. Using the results, and also simulations of RV light curves, they were able to emphasize that there is a range of behavior in RV stars—including the alternating minima phenomenon—which would make them overlap with SRd stars. One might imagine that there was a continuous sequence from the regular CW stars, to the RV and semiregular stars, to irregular stars—though Lebzelter and Obbrugger (2009) have shown that, when datasets are equivalent, there is no difference in regularity between the SRd variables and the supposedly-irregular Lb variables.

For the SRd stars with two distinct, non-LSP periods, most—but not all—have period ratios in the range 0.55 to 0.65, which could indicate that the periods are the fundamental and first overtone. Given the uncertainties in the models of these low-gravity stars, and the limitations of the observational datasets, we will not attempt to compare observed period ratios with theoretical values. However, the higher period ratios, found in a few stars, are interesting, and should be followed up. That would best be done with denser, longer datasets, such as AAVSO visual data.

The LSPs in RV stars are believed to be due to some aspect of binarity. This was proposed by Percy (1993), primarily on the basis of the long-term light curve of stars like U Mon. The LSP minima were periodic, but the depth and form of the minima were variable, suggesting a role for dust of varying opacity. The hypothesis was much strengthened by long-term systematic photometric and spectroscopic observations of RVb stars by Pollard *et al.* (1996), who also provided a clear discussion of RV stars in general. Fokin (1994) carried out a study of non-linear pulsations in models of RV stars, and provided an analytical critique of the binary and possible pulsation mechanism for the LSP, including an important discussion of the ratio of the pulsational periods to the LSPs. Van Winckel *et al.* (1999) concentrated specifically on the matter of binarity, the general observational characteristics of RV stars, how they support the binarity hypothesis, and how binarity actually produces the RVb phenomenon. Kiss and Bódi (2017) provided additional evidence based on how the apparent pulsation amplitude changed through the LSP cycle. Most recently, Vega *et al.* (2021) have carried out a detailed multiwavelength study of the RVb star U Mon, and explained the LSP phenomena in terms of binary interactions within a circumbinary disc.

The LSPs in SRd stars presumably have the same cause, since RV and SRd variables are similar in so many ways. There is also strong evidence (Soszyński *et al.* 2021) that the LSPs in red giants are due to binarity. According to this model, the red giant's low-mass companion is a former planet that accreted a significant amount of mass from the red giant wind, and grew into a brown dwarf or very low-mass star, enveloped in a dust cloud.

Red supergiants also have LSPs (Kiss *et al.* (2006), Percy and Sato (2009)), and some are spectroscopic binaries. In both Antares (Pugh and Gray (2013)) and Betelgeuse (Goldberg (1984)), the length of the LSP is not statistically different from the radial velocity period. For Antares, the spectroscopic period and LSP are 2170 and 1650 ± 640 days, respectively; for Betelgeuse, they are 2100 and 2050 ± 460 days, respectively. The radial-velocity curve of Antares is similar in amplitude and shape to those found for LSPs in red SR stars. Furthermore, during the "great dimming" of Betelgeuse in 2020, there was a dust cloud obscuring the disc of the star (Montargès *et al.* (2021). The "great dimming" may therefore not be a one-off event, but may occur periodically when the pulsation period and LSP are both at minimum, and at their largest amplitudes, as was the case in 2020 (Percy 2020).

Information about variable stars in catalogs such as ASAS-SN and the *General Catalogue of Variable Stars* (Samus *et al.* 2017) tends to be restricted to a (mean) period and (mean) amplitude, leading to a classification such as SRd. Detailed studies of individual stars, such as that done here, provide a much more complete picture. This same point was made by Pollard *et al.* (1996) many years ago. Surveys which determine mean periods and amplitudes for large numbers of variables are important, but it is also important to extract information about more complex stars (like SRd stars), if possible, especially if the nature and cause of the complications are poorly-understood. This is work that would be appropriate for students and amateur astronomers, as well as professionals.

5. Conclusions

For SRd variables, the period wanders by a few percent. The pulsation amplitude varies significantly on a time scale of 20 to 30 periods. An additional pulsation period may be present, or an LSP—all with variable amplitudes. All of these contribute to non-regularity when a phase diagram for the average period is plotted. Bimodal pulsation occurs in other types of stars, but not necessarily with variable amplitude. LSPs occur in RVb and red SR variables, as well as SRd variables.

An interesting and important question is what causes these phenomena which contribute to non-regularity. By analogy with the RV stars, the LSP in SRd stars is probably due to binarity. The causes of the period wander and amplitude variability remains unknown, but seem to be associated with the low gravity and high luminosity of the stars in which they occur, and with possible strong non-linear effects, and also with the presence of large convective cells in the outer layers of the stars.

6. Acknowledgements

This paper made use of ASAS-SN photometric data. We thank the ASAS-SN project team for their remarkable contribution to stellar astronomy, and for making the data freely available on-line. I also thank the AAVSO for creating and making available the VStar time-series analysis package and the AAVSO International Database of observations, and the referee for their very helpful comments. The Dunlap Institute is funded through an endowment established by the David Dunlap Family and the University of Toronto.

References

Benn, D. 2012, *J. Amer. Assoc. Var. Star Obs.*, **40**, 852.

Bódi, A., and Kiss, L. L. 2019, *Astrophys. J.*, **872**, 60.

Bono, G. *et al.* 2020, *Astron. Astrophys.*, **644A**, 96.

Eddington, A. S., and Plakidis, S. 1929, *Mon. Not. Roy. Astron. Soc.*, **90**, 65.

Fokin, A. B. 1994, *Astron. Astrophys.*, **292**, 133.

Goldberg, L. 1984, *Publ. Astron. Soc. Pacific*, **96**, 366.

Jayasinghe, T., *et al.* 2018, *Mon. Not. Roy. Astron. Soc.*, **477**, 3145.

Jayasinghe, T., *et al.* 2019, *Mon. Not. Roy. Astron. Soc.*, **486**, 1907.

Kiss, L. L., and Bódi, A. A. 2017, *Astron. Astrophys.*, **608A**, 99.

Kiss, L. L., Szabó, G., and Bedding, T. R. 2006, *Mon. Not. Roy. Astron. Soc.*, **372**, 1721.

Lebzelter, T., and Obbrugger, M. 2009, *Astron. Nachr.*, **330**, 390.

Miller Bertolami, M. M. 2016, *Astron. Astrophys.*, **588A**, 25.

Montargès, M., *et al.* 2021, *Nature*, **594**, 365.

Percy, J. R. 1993, in *Luminous High-Latitude Stars*, ed. D. D. Sasselov, ASP Conf. Ser. 45, Astronomical Society of the Pacific, San Francisco, 295.

Percy, J. R. 2015, *J. Amer. Assoc. Var. Star Obs.*, **43**, 176.

Percy, J. R. 2020, *J. Roy. Astron. Soc. Canada*, **114**, 134.

Percy, J. R., and Abachi, R. 2013, *J. Amer. Assoc. Var. Star Obs.*, **41**, 193.

Percy, J. R., and Colivas, T. 1999, *Publ. Astron. Soc. Pacific*, **111**, 94.

Percy, J. R., and Haroon, S. 2021, paper presented at the 2021 Fall Meeting of the AAVSO.

Percy, J. R., Hosick, J., and Leigh, N. W. C. 2003, *Publ. Astron. Soc. Pacific*, **115**, 59.

Percy, J. R., and Kim, R. Y. H. 2014, *J. Amer. Assoc. Var. Star Obs.*, **42**, 267.

Percy, J. R., and Sato, H. 2009, *J. Roy. Astron. Soc. Canada*, **103**, 11.

Percy, J. R., and Ursprung, C. 2006, *J. Amer. Assoc. Var. Star Obs.*, **34**, 125.

Pollard, K. R., Cottrell, P. L., Kilmartin, P. M., and Gilmore, A. C. 1996, *Mon. Not. Roy. Astron. Soc.*, **279**, 949.

Pugh, T., and Gray, D. F. 2013, *Astron. J.*, **145**, 38.

Samus, N. N., Kazarovets, E. V., Durlevich, O. V., Kireeva, N. N., and Pastukhova, E. N. 2017, *Astron. Rep.*, **61**, 80.

Shappee, B. J. *et al.* 2014, *Astrophys. J.*, **788**, 48 (asas-sn.osu.edu/variables).

Soszyński, I., *et al.* 2021, *Astrophys. J., Lett.*, **911**, L22.

Van Winckel, H., Waelkens, C., Fernie, J. D., and Waters, L. B. F. M. 1999, *Astron. Astrophys.*, **343**, 202.

Vega, L. D., *et al.* 2021, *Astrophys. J.*, **909**, 138.

Observation and Analysis of Qatar-1b Transit Timing Variations: No Evidence for Additional Bodies in Qatar-1

Paloma Lenz
Lindsay Koo
Vincent Tran
Iván Álvarez
Exoplanet Research Workshop; palomaisabellenz@gmail.com; lindsay.koo21@gmail.com; tran_vincent@protonmail.ch; ivan.alvsancho@gmail.com

Received January 17, 2022; revised January 20, March 7, 2022; accepted March 14, 2022

Abstract Existing literature confirms that the Qatar-1 stellar system has a transiting exoplanet, Qatar-1b, which past research suggests is the sole planetary member of this system. Using archival images from the Harvard-Smithsonian MicroObservatory and NASA's EXOplanet Transit Interpretation Code (EXOTIC), 28 transits of Qatar-1b were reduced to further analyze the nature of the Qatar-1 system. Corrupted image series were edited to ensure the reliability of the light curves outputted by EXOTIC; the resulting Observed – Calculated plot, which was produced after these reduced transits were compiled, indicates that no transit timing variations were found for Qatar-1b, meaning that there are likely no other proximal bodies impacting the exoplanet's orbit. χ^2 and Lomb-Scargle analysis were also conducted, revealing no significant periodicity in Qatar-1b's orbit and further confirming the absence of additional bodies impacting the exoplanet's orbit.

1. Introduction

Small telescopes have become of increasing significance to the exoplanet community, serving as effective vehicles for follow-up observation of transiting exoplanets. Minimizing observing overheads is necessary for large telescopes such as NASA's James Webb Space Telescope and ESA'S ARIEL; as mid-transit times can become uncertain over time, these observatories run the risk of requiring greater overheads to fully detect a transit (Zellem *et al.* 2020). Amassing data collected worldwide by smaller observatories can assist in pinpointing exoplanets' expected mid-transit times. This optimizes future large telescope time allocation and space telescope missions. Among these efforts, NASA's Universe of Learning Exoplanet Watch relies on citizen scientist-powered research to observe transiting exoplanets and reduce and analyze their own data. Professional astronomers can access the data collected by citizen scientists when uploaded to the American Association of Variable Star Observers (AAVSO) Exoplanet Database.

Among star systems of interest is the Qatar-1 system. Using previously identified planetary parameters of Qatar-1b, this study involves the reduction of photometric data collected by MicroObservatory network telescopes on exoplanet Qatar-1b. Discovered in 2010 (Alsubai *et al.* 2011), Qatar-1b is part of a group of exoplanets known as Hot Jupiters, which are gas giants with an orbital period of less than 10 days and a mass greater than or equal to 0.25 of Jupiter's (Dawson and Johnson 2018). The relative proximity of Hot Jupiters to their host stars (generally far less than 1 AU) means that they can readily be discovered and observed via the transit method of exoplanet detection (Dawson and Johnson 2018). Qatar-1b orbits a K-type star with an orbital radius of 0.023 AU and orbital period of 1.42002 ± 7.1^{-07} days, as identified by NASA's Exoplanet-Catalog (NASA 2021). The Qatar-1 system (Figure 1) is located in the Draco constellation (R.A. $20^{h} 13^{m} 31^{s}$, Dec. $+65° 09' 44''$). Qatar-1b's mid-transit time was defined as $2456234.103218 \pm 6 \cdot 10^{-5}$ in BJD-UTC (Collins *et al.* 2017). The ratio of the Qatar-1b radius to its host star's radius is 0.146 ± 0.00065 (R_p / R_s). EXOTIC also gave parameters for the ratio of distance to stellar radius as 6.6 ± 0.04 (a / R_s), orbital inclination of 84.5 ± 0.1 (deg), and orbital eccentricity as 0.012.

Recent research has investigated the possible presence of additional planets in the Qatar-1b system (von Essen *et al.* 2013), yet no evidence of sinusoidal transit timing variations (TTVs) indicative of additional bodies has been found (Collins *et al.* 2017), even when dynamical simulations modeled fictitious planets (Maciejewski *et al.* 2015). This information strengthens certainty in the precision and accuracy of the light curves generated in this investigation. It also reinforces previously observed trends noting how Hot Jupiters are singular orbiting bodies in planetary systems (Maciejewski *et al.* 2015).

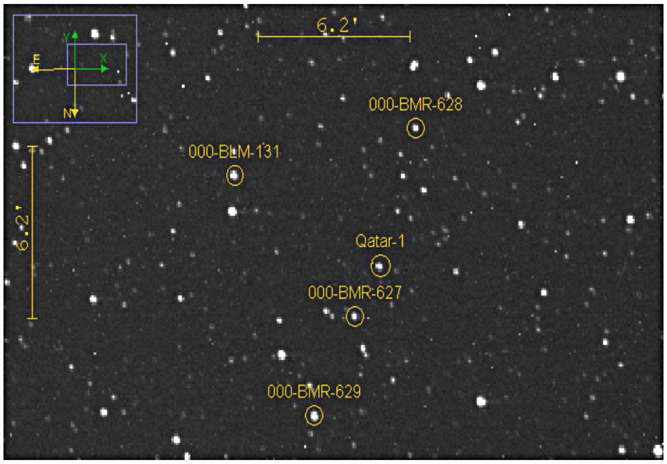

Figure 1. Labeled Qatar-1b starfield. As recommended by the AAVSO Variable Star Plotter, comparison star 000-BMR-627 was most frequently consulted. Comparison stars are labeled according to the AAVSO Variable Star Plotter.

This study aims to determine if there is periodic variation in the residuals of Qatar-1b's observed transits. Data collected as part of this investigation are contributions to a larger group research project under the Exoplanet Research Workshop. Project teams were each assigned Qatar-1b transit observations spanning from 2011 to 2019 for interpretation by EXOTIC. Teams individually uploaded light curves outputted by the program to the AAVSO Exoplanet Database.

The software utilized for this project, along with the preparation of image series for input into EXOTIC and the light curves and planetary parameters outputted by the program, is discussed in greater detail below.

2. Instruments used

The images were taken by 6-inch robotic telescopes in the MicroObservatory network, a group of automated imaging telescopes designed for remote student and public use and operated by the Harvard-Smithsonian Center for Astrophysics (Sadler *et al.* 2001). The network comprises five compact telescopes situated in Amado, Arizona; Cambridge, Massachusetts; Mauna Kea, Hawaii; and Canberra, Australia (Sadler *et al.* 2001). The telescopes have been in service since 1995 (Sadler *et al.* 2001), and the images obtained for this study were taken from 2014 to 2018.

Specifically, the images for Qatar-1b were taken by a MicroObservatory telescope located in Fred Lawrence Whipple Observatory's visitor center on Mount Hopkins, Arizona (Lat. +31.675°, *Long.* –110.952°); the visitor center has an altitude of 1,268 meters. The telescope has an aperture of 138 mm and a focal length of 560 mm, and utilizes a CCD detector and a Kodak KAF-1403-ME camera with 1400 × 1000 (w × h) resolution where pixels are 6.9 micrometers on each side (Sadler *et al.* 2001). It also has a pixel scale of 5.2" per pixel. The CCD detector utilizes 2 × 2 binning to help reduce image noise, and images are taken with a clear (CV) filter (Sadler *et al.* 2001).

3. Light curves

Following the reduction of images, EXOTIC outputs a light curve, a graph representing the decrease in stellar flux from Qatar-1 during the transits of Qatar-1b. These transits have continuously shown Qatar-1b blocking ~2.5% of the relative flux, as seen on the y-axis of the plot, during the peak of the transits. In Figure 2, a clear dip in light levels can be seen due to the exoplanet blocking its host star. Observed dips in stellar flux align with transit parameters outputted by EXOTIC, as a dip of ~2% is expected from the exoplanet's stellar radius ($0.146 \pm 0.00065\, R_p / R_s$).

To generate accurate light curves, optimal comparison stars were consistently of similar magnitude to the target, Qatar-1. To provide accurate reference points, all comparison stars used were also relatively close to the target in the night sky and isolated from other stars in the MicroObservatory images. Additionally, oversaturated comparison stars were not entered for EXOTIC to analyze.

4. Data reduction

Data collected during specific transit observation dates were reduced using the EXOplanet Transit Interpretation Code (EXOTIC), a PYTHON program that analyzes astronomical images to produce light curves. The program reduces a series of FITS file images, plate-solves most images, and determines the best comparison star and alignment to fit a light curve to the transit data. EXOTIC also outputs several planetary parameters after the target's and comparison stars' x and y pixel locations are manually inputted. EXOTIC also performs other calculations, including determining the transit depth and mid-transit time. As a basis for selecting comparison stars to produce the clearest light curves, nearby stars with a similar luminosity to Qatar-1b and preferably in an isolated region of the night sky were used. EXOTIC would then locate and align those stars on a plate-solved version of the images to create a light curve reflective of variations in the images' stellar flux, thus allowing the visualization of the planet's movement across its host star.

5. Results

Out of 28 transits, EXOTIC fitted light curves to 25, and of those, 16 were clean (Table 1). Clean light curves were distinguished by their transit's residual scatter and midpoint uncertainty: transits with a residual scatter of 0.01 ± 0.04 and a midpoint uncertainty value of 0.001 ± 0.004 displayed prominent dips in light, and were therefore considered clean.

Of the nine poor results, five contained images that were saturated or contained passing clouds, yielding low signal-to-noise ratios; two failed to plate solve; and two others encountered technical errors where the estimated mid-transit time was not within an observable range. Consequently, EXOTIC fit poor light curves to them (Table 2).

Zellem's equation (Equation 1) was used to calculate O–C uncertainty, as seen in Figure 3, where T_{obs} is defined as uncertainty in the observed transit time based on EXOTIC's output. To determine a planet's expected transit midpoint time in Keplerian motion, the product of the period P is added to an integer number of epochs and to a published midpoint time T_0 (Zellem *et al.* 2020).

$$\sqrt{(\Delta T_{obs} + E^2 \cdot \Delta P^2 + 2 \cdot E \cdot \Delta P \cdot \Delta T_0 + \Delta T_0^{\,2})} \qquad (1)$$

A transit's epoch is calculated in days and is determined by the subtraction of the published midpoint transit time (2456234.1 days) from a transit's expected transit midpoint, divided by the orbital period (1.42 days).

Performing a χ^2 test assuming 22 degrees of freedom resulted in the deviation being statistically insignificant using a p-value of 0.025, with a reduced χ^2 test indicating that the observed and expected transit midpoints are very close (χ^2 value $< 10^{-5}$) Lomb-Scargle analysis, produced by Astropy, a common core PYTHON astronomy package, is useful for unevenly-sampled time-series data as it can check for a periodic trend among residuals of the O–C plot (Astropy Collaboration *et al.* 2013). Since there are multiple varied peaks present rather than a single clear peak, the

Table 1. EXOTIC's outputted parameters; transits which yielded good light curves.

Date (yyyy-mm-dd)	*Residual Scatter*	*Observed Transit Midpoint (BJD)*	*Transit Midpoint Uncertainty*	*Expected Transit Midpoint (BJD)*	*Epoch*	*O–C (min)*	*O–C Uncertainty (min)*
2014-06-16	0.0214	2456824.833	0.0027	2456824.833	416	–1.13	3.90
2014-07-20	0.0128	2456858.914	0.00073	2456858.914	440	–0.25	1.06
2014-08-19	0.0352	2456888.735	0.0011	2456888.734	461	1.19	1.60
2014-09-12	0.0138	2456912.874	0.0013	2456912.875	478	–0.70	1.88
2017-09-21	0.0064	2458017.654	0.0012	2458017.654	1256	–0.16	1.77
2017-10-08	0.0096	2458034.696	0.0019	2458034.694	1268	2.73	2.77
2017-10-15	0.0117	2458041.79	0.0023	2458041.794	1273	–5.22	3.34
2017-10-18	0.0299	2458044.616	0.0051	2458044.634	1275	–26.31	7.36
2017-10-25	0.0083	2458051.735	0.0013	2458051.734	1280	0.73	1.92
2018-03-13	0.0146	2458190.895	0.0027	2458190.897	1378	–1.68	3.91
2018-04-09	0.0127	2458217.875	0.0045	2458217.877	1397	–2.77	6.50
2018-05-06	0.0117	2458244.854	0.0021	2458244.857	1416	–4.44	3.06
2018-05-16	0.0092	2458254.802	0.002	2458254.798	1423	6.55	2.92
2018-05-23	0.0087	2458261.899	0.0019	2458261.898	1428	1.33	2.77
2018-06-02	0.0097	2458271.84	0.0019	2458271.838	1435	3.10	2.77
2018-06-05	0.0168	2458274.675	0.0027	2458274.678	1437	–4.31	3.91

Note: 16 out of 28 transits yielded clean light curves. All clean light curves (above table) were used to determine the existence of transit timing variations for Qatar-1b.

Table 2. EXOTIC's outputted parameters; transits which yielded poor light curves (not used in analysis).

Date (yyyy–mm–dd)	*Residual Scatter*	*Observed Transit Midpoint (BJD)*	*Transit Midpoint Uncertainty*	*Expected Transit Midpoint (BJD)*	*Epoch*	*O–C (min)*	*O–C Uncertainty (min)*
2014-07-06	0.5431	2456844.713	0.00061	2456844.714	430	–0.80	0.89
2014-07-23	0.4412	2456861.753	0.00078	2456861.754	442	–0.78	1.13
2014-08-02	0.0699	2456871.694	0.00085	2456871.694	449	–0.77	1.23
2014-08-09	0.0202	2456878.794	0.00092	2456878.794	454	–0.78	1.33
2017-09-23	1.0577	2458019.074	0.012	2458019.074	1257	0.52	17.28
2017-10-06	0.0119	2458031.855	0.012	2458031.854	1266	1.65	17.28
2017-11-04	0.2727	2458061.674	0.0013	2458061.674	1287	–0.52	1.92
2017-11-11	0.2554	2458068.797	0.0095	2458068.774	1292	32.71	13.69
2017-11-14	0.0165	2458071.615	0.012	2458071.615	1294	0.67	17.28

Note: 12 out of 28 transits yielded poor light curves. These were not used in analysis, but are displayed above for completeness.

data do not follow a periodic trend (VanderPlas 2018). Lack of a periodic trend in Figure 4 indicates that there are few variations in the timing of Qatar-1b's orbit, further suggesting that there are no additional bodies impacting the exoplanet's orbit.

6. Conclusion

While the results do not reveal any significant transit timing variations, the data collected in this study can still update Qatar-1b's ephemeris. Figure 5 displays all light curves that were used for this study. These light curves were contributed to the American Association for Variable Star Observers (AAVSO) Exoplanet Database for use by the larger exoplanet research community and can be found under observer codes LIVA, KLIC, LPIC, and TVIC. This will further assist with time allocation for future large-scale space telescope missions.

Future replication of this study with different MicroObservatory archival data will further confirm that no additional bodies surround Qatar-1b. This study analyzed light curves from 2014, 2017, and 2018, but comparing results with other dates, including more recent measurements, will continue to help update the accuracy of Qatar-1b's ephemeris. Additionally, as EXOTIC is updated, further research can be conducted on Qatar-1b and other exoplanets. This study is a testament to the promising nature of small telescopes and the accessibility of transit data reduction programs for the larger exoplanet community.

7. Acknowledgements

This study made use of the EXOTIC data reduction package from Exoplanet Watch, a citizen science project managed by NASA's Jet Propulsion Laboratory on behalf of NASA's Universe of Learning. This work is supported by NASA under award number NNX16AC65A to the Space Telescope Science Institute.

All images used in this study were collected and made available to the public by the Harvard-Smithsonian Institute for Astrophysics MicroObservatory, a network maintained and operated as an educational service and a project of NASA's Universe of Learning, supported by NASA Award Number NNX16AC65A. Additional MicroObservatory sponsors include the National Science Foundation, NASA, the Arthur Vining Davis Foundations, Harvard University, and the Smithsonian Institution.

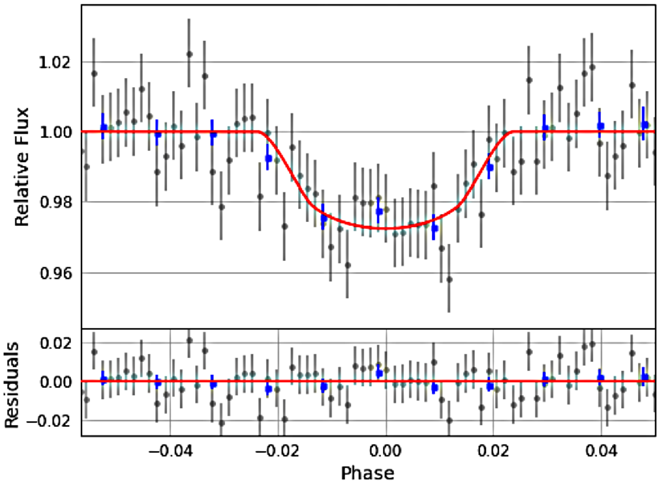

Figure 2. Final light curve produced by EXOTIC from a transit observed 2018-05-16 using 74 MicroObservatory images.

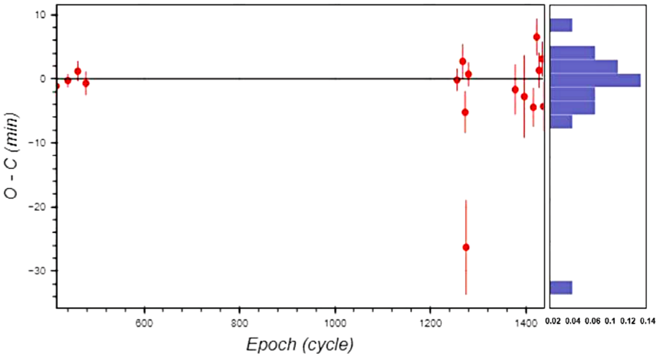

Figure 3. Observed – Calculated plot for Qatar-1b.

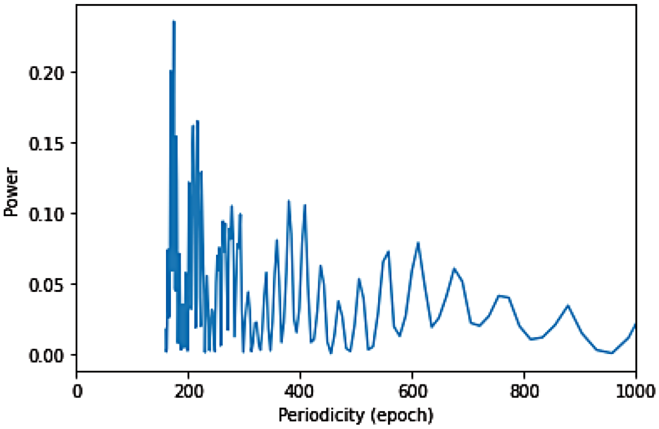

Figure 4. Lomb-Scargle periodogram for Qatar-1b TTVs.

Poor FITS image files were edited using SAOImageDS9, an astronomical image display and visualization tool currently funded by the NASA High Energy Astrophysics Science Archive Center and the Chandra X-ray Science Center. This study benefits from the American Association of Variable Star Observers for its support of the exoplanet community with free access to its Exoplanet and Variable Star Databases.

Finally, we want to thank Paige Yeung, Quinn Perian, and Kalée Tock from the Exoplanet Research Workshop, a group-run astronomy research seminar, for equipping us with the tools to elaborate this paper.

References

Alsubai, K. A., *et al.* 2011, *Mon. Not. Roy. Astron. Soc.*, **417**, 709 (DOI: 10.1111/j.1365-2966.2011.19316.x).

Astropy Collaboration, *et al.* 2013, *Astron. Astrophys.*, **558A**, 33 (DOI: 10.1051/0004-6361/201322068).

Collins, K. A., Kielkopf, J. F., and Stassun, K. G. 2017, *Astron. J.*, **153**, 78 (DOI: 10.3847/1538-3881/153/2/78).

Dawson, R. I., and Johnson, J. A. 2018, *Annu. Rev. Astron. Astrophys.*, **56**, 175 (DOI:10.1146/annurev-astro-081817-051853).

Maciejewski, G., *et al.* 2015, *Astron. Astrophys.*, **577A**, 109 (DOI: 10.1051/0004-6361/201526031).

NASA. 2021, Exoplanet Exploration: Planets Beyond Our Solar System, Exoplanet-Catalog (https://exoplanets.nasa.gov/exoplanet-catalog/5049/qatar-1-b).

Sadler, P. M., Gould, R. R., Leiker, P. S., and Antonucci, P. R. A. 2001, *J. Sci. Education Technol.*, **10**, 39 (DOI: 10.1023/A:1016668526933).

VanderPlas, J. T. 2018, *Astrophys. J., Suppl. Ser.*, **236**, 16 (DOI: 10.3847/1538-4365/aab766).

von Essen, C., Schröter, S., Agol, E., and Schmitt, J. H. M. M. 2013, *Astron. Astrophys.*, **555A**, 92 (DOI: 10.1051/0004-6361/201321407).

Zellem, R. T., *et al.* 2020, *Publ. Astron. Soc. Pacific*, **132**, 054401 (DOI: 10.1088/1538-3873/ab7ee7).

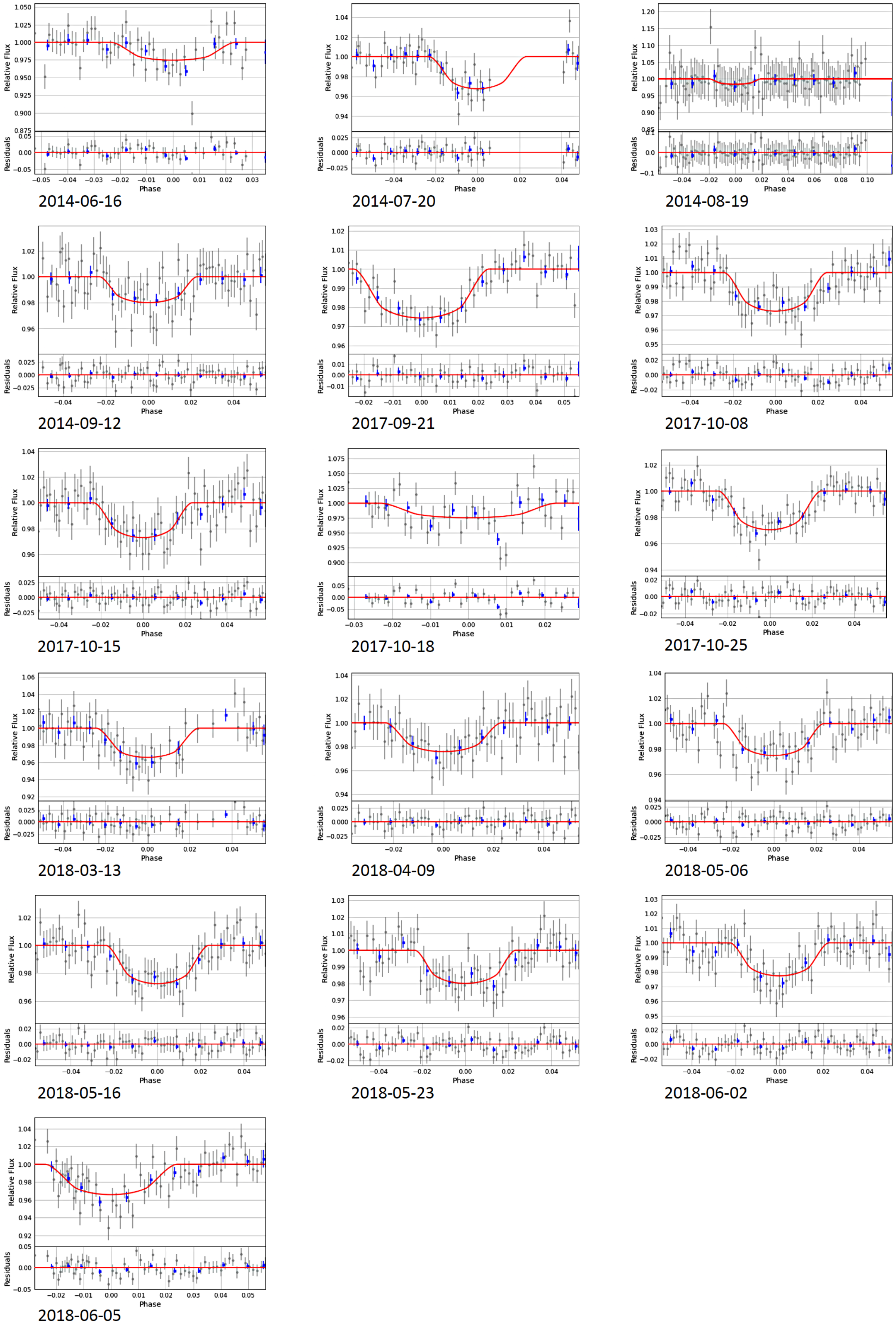

2014-06-16 2014-07-20 2014-08-19

2014-09-12 2017-09-21 2017-10-08

2017-10-15 2017-10-18 2017-10-25

2018-03-13 2018-04-09 2018-05-06

2018-05-16 2018-05-23 2018-06-02

2018-06-05

Figure 5. All clean light curves used in this study.

Issues in Frequency Analysis of δ Scuti Stars II—EE Cha (HD 104036)

Bill Rea
Richmond, New Zealand; rea.william@gmail.com

Received January 22, 2022; revised April 18, 2022; accepted May 12, 2022

Abstract Pre-whitening is a commonly used procedure in the frequency analysis of variable star light curves when multiple pulsation frequencies are active. However, each pre-whitening cycle introduces a new frequency into the data, often resulting in statistically significant frequencies appearing in the analysis which do not correspond to a pulsation within the star. In this paper we examine the effectiveness of a simple modification, permitted by some frequency analysis software packages, which we call restricted range analysis. We show that while restricted range analysis may considerably reduce the number of spurious frequencies generated it does not eliminate them. Thus each reported significant frequency must still be checked against the periodogram to confirm it matches a clear feature within it. Further, restricted range analysis appears to not detect some frequencies and these must be searched for in the periodogram. We conclude that while restricted range analysis is useful, it does not overcome all the problems associated with pre-whitening in frequency analysis.

1. Introduction

In the previous paper (Rea 2022), which we will refer to as Paper I, we set out for the amateur variable star observing community some issues which commonly arise in the analysis of stars with multiple pulsation modes excited, particularly focusing on δ Scutis. While some solutions have been proposed in the professional literature (see, for example, Lares-Maritz *et al.* (2020)), often there are no freely available software packages which implement these new methods.

In Paper I we proposed a simple modification to the standard methods of frequency analysis which can be implemented in some existing software packages and which we termed "restricted range analysis." The modification was aimed at reducing the often very large number of spurious frequencies arising from the use of pre-whitening. EE Cha appears to be an interesting case to study both because of its young age and its periodogram appears to be quite simple in structure (see below). This simple periodogram structure should make the analysis of its pulsation frequencies easier than for a star with a more complicated pulsation structure. In this paper we seek to evaluate in some detail the strengths and weaknesses of restricted range analysis using EE Cha as a test case.

1.1. EE Cha and asteroseismology

EE Cha (HD 104036) is a deeply southern δ Scuti variable which, like many other southern δ Scutis, has been little studied. It is part of the ε Cha association of very young (4–10 Myr) stars in the solar neighborhood, some of which still exhibit protoplanetary disks (Murphy *et al.* 2013), although EE Cha itself has not been reported to have such a disk. It was discovered by Kurtz and Müller (1999) who reported two periods in their data of 33.88 cycles d^{-1} and 29.31 cycles d^{-1}. Table 1 presents some parameter estimates for the star. The data were drawn from the TASOC web site (https://tasoc.dk/), SIMBAD (http://simbad.u-strasbg.fr/simbad/) Wenger et al. (2000), and the Variable Star Index (VSX, https://www.aavso.org/vsx/). The distance is from the Gaia 2020 catalog (Gaia Collab. 2020). The TIC is the TESS Input Catalog number.

Table 1. Basic stellar data for EE Cha/HD 104036.

Property	*Value*
Spectral Type (VSX)	A7V
Period	0.029516 days / 42.503 min
Distance	104.8 ± 0.29 pc
Mean Mag (V)	6.73
Amplitude (B)	0.11
TIC	454961439

Because the evolution of main sequence stars is slow, observational tests of theories of stellar evolution must be made by observing a range of similar stars with different ages. EE Cha is of particular interest because it has only recently reached the main sequence. Consequently it is a good candidate to study to understand the earliest phases of a δ Scuti's evolution. Grigahcène *et al.* (2010) report that δ Scutis have a shallower convective envelope than solar-like stars but this slowly deepens as the star ages. It is in this shallow convective zone that the p-mode pulsations originate and propagate. Aerts and Kurtz (2010, p. 52) indicate that for δ Scutis with $M_\star > 2M_\odot$ the outer zone is radiative rather than convective. A shallow convective zone could account for short periods of the p-mode pulsations seen in some δ Scutis. A second consequence of a shallow convective zone is that g-mode pulsations, which form and propagate in the radiative interior, have less material to propagate through to the surface where they can be observed, and hence are less likely to be attenuated to insignificance, such as appears to be the case with solar-like stars.

As reported in Paper I, while δ Scutis are of particular interest for asteroseismology because they often exhibit both p- and g-mode pulsations, a significant obstacle has been identifying the often many active pulsation modes in any given star. Balona (2014) showed that the commonly used technique of pre-whitening time series data during frequency analysis introduces a new frequency into the data with each pre-whitening cycle. This was sufficiently problematic that in numerical experiments numerous spurious frequencies were identified as statistically significant, while some real frequencies in his simulated data were not identified. The simulated data used by Balona (2014) met the three assumptions which are made when pre-whitening is used, that is: (1) the frequencies were generated by sinusoids; (2) they were stationary in both amplitude and frequency; and (3) they were combined into the final light curve in an additive manner. Paper I extended the work of Balona (2014) and investigated the effect of violations of these three assumptions on frequency analysis using pre-whitening, and concluded that the number of statistically significant but entirely spurious frequencies is likely to be much higher than in the ideal case.

Given that in the literature on δ Scutis sometimes hundreds of significant frequencies are reported (Poretti *et al.* 2009; Uytterhoeven *et al.* 2011) requiring hundreds of pre-whitening cycles in the frequency analysis, it is likely that many reported frequencies are an artifact of the method of analysis and do not correspond to any physically meaningful pulsation.

The remainder of the paper is structured as follows: section 2 discusses the numerical experiments and their results; section 3 discusses the data for EE Cha and the analysis methods; section 4 presents the results; section 5 contains the discussion; and section 6 gives our conclusions.

2. Numerical experiments

While the generation of a number of simulated data sets was discussed in Paper I, none of those were particularly suited to testing restricted range analysis. Consequently, a new data set was generated consisting of 18 frequencies in six groups of three frequencies; details are given in Table 2.

While the units of the simulated data were in arbitrary units, they were chosen to mimic the data from NASA's Transiting Exoplanet Survey Satellite (TESS) (Ricker *et al.* 2014) in its 120-second cadence observing mode. There were six groups of triplets with a central frequency and two side frequencies at a spacing of 0.5 cycle d^{-1}. Three sets, or nine frequencies, were sinusoids, namely "δ Scuti low 1," "δ Scuti high 1," and "δ Scuti high 3." In the first group, the "γ Dor" frequencies, the amplitudes of the sinusoids were modulated by a second sinusoid through four cycles over the length of the time series. In the third group, the "δ Scuti low 2" group, the amplitude was constant over the first quarter of the data, then reduced by a factor of one-half over the next quarter, and then remained constant to the end of the series. In the fifth group, the "δ Scuti high 2" group, the amplitude was modulated with a slow rise followed by a rapid decrease in a ratio of 3:1. There were eight complete cycles over the course of the data. Finally the data were summed, standardized to an amplitude 1 (again in arbitrary units), and noise added of 0.001 of the amplitude of the final series. There were 131,072 data points in the final series. The periodogram of the data is presented in Figure 1 in black.

The data were then subjected to both an unrestricted range analysis and an eight-stage restricted range analysis. The results from these two analyses are presented in Table 3, The second column of which reports the actual number of frequencies present in the data for that frequency range. The periodogram of the residuals from the eight stage restricted range analysis is in red in Figure 1.

Table 2. The frequencies and their properties which were used to construct the simulated light curve.

Frequency Group	*Frequency*	*Amplitude Range*
γ Dor	1.5	0.125–0.375
Amplitude	2.0	0.250–0.750
Modulation	2.5	0.125–0.375
δ Scuti low 1	8.5	0.500
Sinusoids	9.0	1.000
	9.5	0.500
δ Scuti low 2	11.5	0.250–0.500
Amplitude	12.0	0.500–1.000
Reduction	12.5	0.250–0.500
δ Scuti high 1	17.5	0.500
Sinusoids	18.0	1.000
	18.5	0.500
δ Scuti high 2	21.5	0.250–0.750
Slow rise	22.0	0.500–1.500
Rapid fall	22.5	0.250–0.750
δ Scuti high 3	31.5	0.500
Sinusoids	32.0	1.000
	32.5	0.500

Table 3. The number of statistically significant frequencies reported by SigSpec (Reegen 2011) in both the eight stage restricted range analysis and the unrestricted analysis.

Frequency Range Cycles d^{-1}	*Real Frequencies*	*No. Significant Restricted*	*Frequencies Unrestricted*
0.0–3.0	3	9	9
3.0–8.0	0	0	0
8.0–13.0	6	13	16
13.0–17.0	0	0	0
17.0–23.0	6	20	26
23.0–31.0	0	0	0
31.0–33.0	3	3	3
33.0–50.0	0	0	0
Total	18	45	54

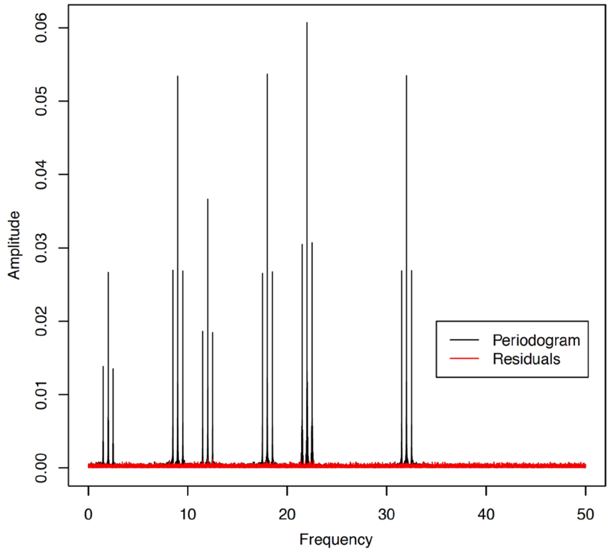

Figure 1. The periodogram of the simulated data set is in black, while the periodogram of the residuals from the eight stage restricted range analysis is in red.

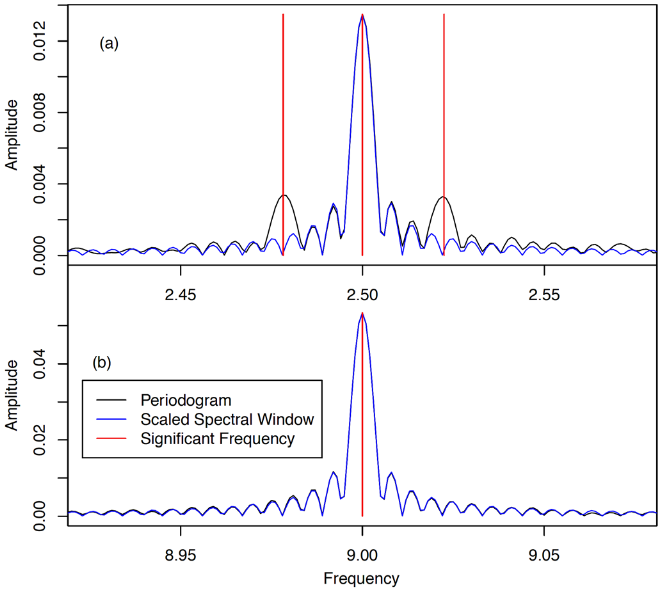

Figure 2. The periodogram simulated data set near the frequencies 2.5 (panel a) and 9.0 (panel b) cycles d^{-1}. The locations of the statistically significant frequencies are marked in red. The two frequencies on either side of the peak at 2.5 cycles d^{-1} were not present in the data and so are examples of spurious frequencies.

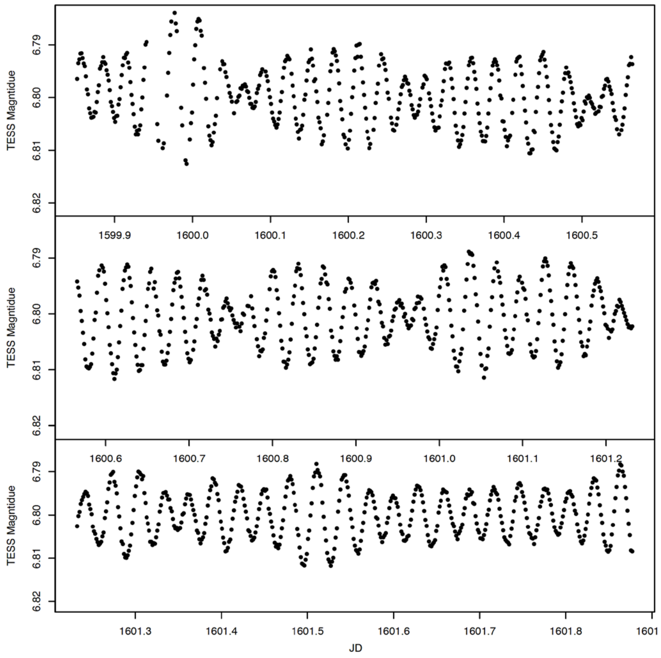

Figure 3. Approximately two days of TESS data for EE Cha (HD 104036). The units of the horizontal axis are barycentric Julian days –2457000.

Two examples of small portions of the periodogram are presented in Figure 2, in which spurious frequencies were (panel a) and were not (panel b) reported.

3. Data and analysis methods

At the initiation of this study EE Cha had no observations available in the AAVSO's International Database. However, EE Cha was observed by NASA's TESS in Sectors 11 and 12 of its mission in its two-minute cadence mode. The raw data for this paper were downloaded from the TESS Asteroseismic Science Operations Center (TASOC) web site on 09 January 2021. They covered a period of approximately 53 days. The reported corrected flux was converted to magnitudes using the value for EE Cha's magnitude in the V band as reported on the TASOC web site as the mean value for each observation run. Observations were discarded if the value in the Pixel Quality Field (PQF) was non-zero or either the date or the corrected flux was recorded as not-a-number (nan). This resulted in 34,070 usable data points. Figure 3 presents an approximately two-day continuous segment of the light curve in which beating between two or more frequencies can clearly be seen. The approximately one-day data gaps caused by the data download from the satellite to the ground do not appear in this Figure.

SigSpec (Reegen 2011), FAMIAS (Zima 2008), and user-written R code (R Core Team 2019) were used to carry out the frequency analysis. FAMIAS was limited to 100 statistically significant frequencies, whereas SigSpec has, for all practical purposes, no upper bound on the number of frequencies which may be reported.

An unrestricted frequency analysis was run using both SigSpec and FAMIAS. The significance cut-off level for SigSpec was set to 4, arguably a low value. The signal-to-noise ratio cut-off level for FAMIAS was also 4. The total numbers of significant frequencies and their types from these two analyses are given in Table 6 below.

A restricted range analysis was also carried out using SigSpec, again setting the cut-off significance level to 4. SigSpec has two keyword directives, lfreq and ufreq, which allow the user to set the lowest and highest frequencies to be included in frequency analysis with frequencies outside this range being excluded. Based on an inspection of the periodogram, the 0 to 75 cycles d^{-1} frequency range was split into nine sub-ranges, the details of these ranges are given in Table 4. As can be seen in the Table there are some small overlaps in some of these ranges. The guiding principle was to try to restrict the ranges to blocks where either significant frequencies could be visually identified or the range appeared to consist of nothing but noise. For example, the range 0.28–3.2 cycles d^{-1} contained two frequencies which could easily be identified by visual inspection, while the ranges on either side, namely 0.0–0.3 and 3.0-20.0 cycles d^{-1}, appeared to contain only noise.

Table 4. The frequency ranges used in the restricted range analysis together with the number of statistically significant frequencies reported.

Frequency Range	*Significant Frequencies*
0.0–0.3	0
0.28–3.2	2
3.0–20.0	0
20–25	2
25–30	11
30–35	16
35–40	0
40–60	0
60–75	1
Total	32

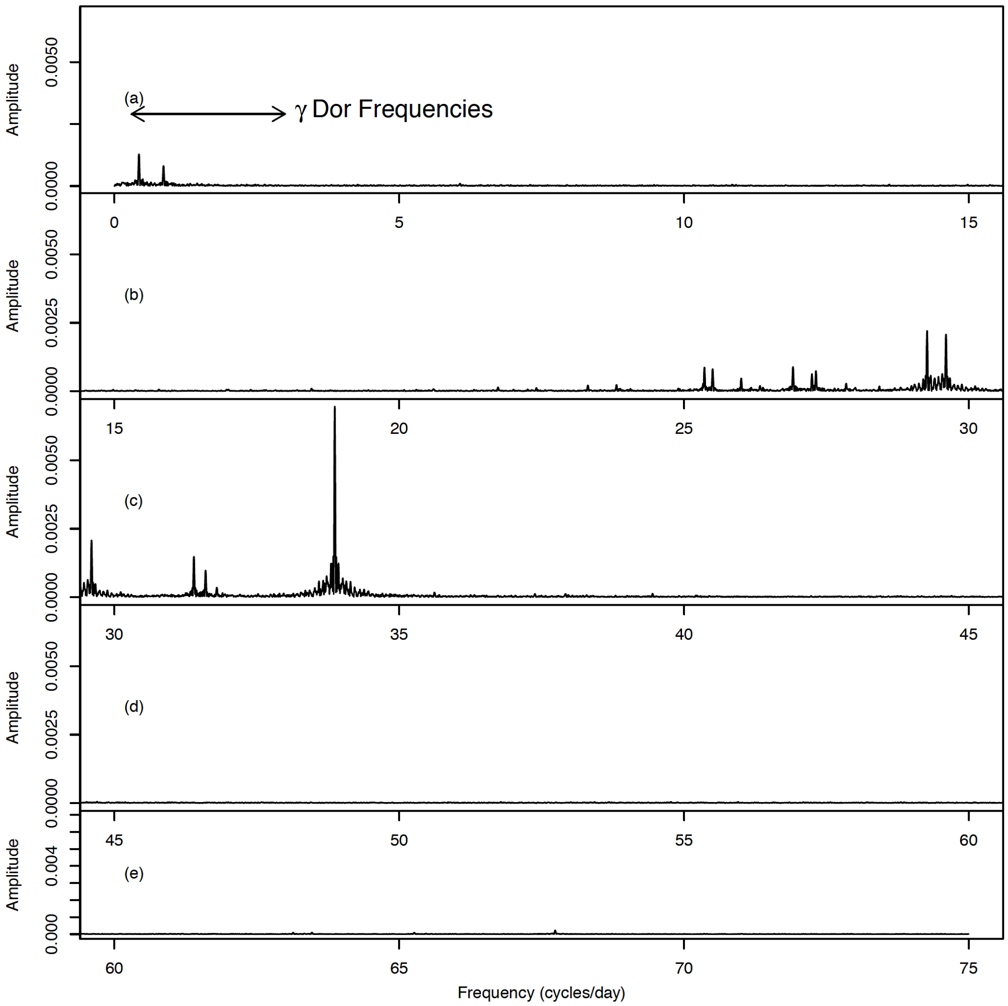

Figure 4. The Fourier periodogram of the complete TESS data for EE Cha (HD 104036) obtained using FAMIAS (Zima 2008). The five panels break the periodogram into 15 cycles d^{-1} segments with panel (a) covering the 0–15 cycles d^{-1} range, through to panel (e), which covers the 60–75 cycles d^{-1} range. The range of frequencies corresponding to the γ Doradus g-mode frequency range is marked in panel (a).

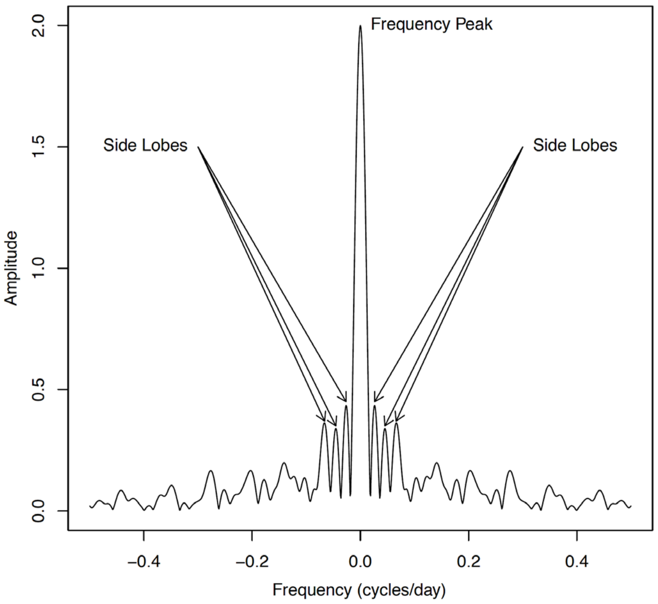

Figure 5. The spectral window of the complete TESS data obtained using FAMIAS (Zima 2008). The central peak has three clear side lobes.

Table 5. The frequency spacing and the relative height of the three main side lobes of the spectral window plotted in Figure 5. The height of the central frequency peak is normalised to one.

Side Lobe	*Frequency Spacing (cycles d^{-1})*	*Relative Height*
1	0.026404	0.2174
2	0.045264	0.1701
3	0.066010	0.1814

Table 6. The number of different types of statistically significant frequencies in the combined data set as reported by SigSpec (Reegen 2011), FAMIAS (Zima 2008) and using a restricted range analysis with SigSpec as described in the text.

Frequency Type	*SigSpec*	*FAMIAS*	*Restricted Range*
δ Scuti	479	82	30
γ Dor	60	7	2
Others	10	9	0
Total	549	98	32

The ranges in Table 4 were analyzed by SigSpec and the residuals from each lower frequency range were used as input into the next higher range. For example, the residuals from the 0.0–0.3 cycle d^{-1} range were used in the frequency analysis of the 0.28–3.2 cycles d^{-1} range, the residuals of which were then used in the 3.0–20.0 cycles d^{-1} range. The purpose of using the residuals rather than the original data set was two-fold. First, once all nine frequency ranges had been successively analyzed, the final set of residuals could be used to generate a periodogram for comparison against the original periodogram of the data set. Secondly, it was clear from initial investigations that sometimes a high peak in the periodogram outside the restricted frequency range being analyzed was either noticeably lowered or reduced to the level of the noise. The alternative, of using the original data set for each restricted range, was not investigated in detail so could perhaps be studied later.

User-written R code (R Core Team 2019) was used to plot each statistically significant frequency against the periodogram. The spectral window, generated by either SigSpec or FAMIAS as appropriate, was scaled by the height (amplitude) of the significant frequency and overplotted on the periodogram. A visual inspection was carried out to check if the identified statistically significant frequency matched an identifiable feature in the periodogram.

4. Results

Both FAMIAS (Zima 2008) and SigSpec (Reegen 2011) were used to obtain a periodogram of the data. Figure 4 plots the periodogram obtained using FAMIAS out to 75 cycles d^{-1}, which covers the range within which statistically significant frequencies were obtained. The highest significant frequency was 67.738957 cycles d^{-1}. In panel (a) of Figure 4 the range of g-mode frequencies, also known as γ Doradus frequencies, is marked. All other higher frequencies were considered to be p-mode or δ Scuti frequencies.

The TESS data had significant gaps caused by the operational requirements resulting from its 13.7-day orbital period. Data gaps can give rise to the presence of aliases which must be taken account of during any frequency analysis. Figure 5 presents a plot of the spectral window, which is the Fourier transform of a noiseless sinusoid sampled in the same way as the data; see Aerts and Kurtz (2010) section 5.3.3 for more details on the spectral window. Three strong side lobes were visible in the window. They are marked in Figure 5. Details of their frequency deviation from the main peak and their height relative to it after standardizing the peak to a height of one are given in Table 5. The evidence presented in the Figure and a close examination of the numerical data for the spectral window do not indicate a strong alias in the data at the inverse of the orbital period, that is, at (or near) 0.072993 cycle d^{-1}. However, the inverse of the orbital period lies quite close to the third side lobe of the spectral window and it is possible the two have been merged into an apparent single side lobe.

Because FAMIAS was limited to a maximum of 100 statistically significant frequencies a second frequency analysis was carried out using SigSpec (Reegen 2011), and the results from both FAMIAS and SigSpec are presented in Table 6. The ranges of frequencies classified as either δ Scuti or γ Doradus were those of Catelan and Smith (2015) Table 9.1, namely $0.3 \leq f < 3$ were classified as γ Doradus types and $f \geq 3$ cycles d^{-1} were classified as δ Scuti types. The remaining frequencies, for which $f < 0.3$, were classified as other. However, one should note that Grigahcène *et al.* (2010), in their Figure 2, showed that for hybrid γ Doradus/δ Scuti stars the γ Doradus and δ Scuti frequency ranges should not overlap. If we had taken their gap into account, which depends on a precise measure of the effective temperature, some of the frequencies classified as δ Scuti should perhaps be classified as other.

Figure 6 presents a scatter plot of the 549 statistically significant frequencies reported by SigSpec in the order in which they were identified. It is fairly easy to observe the gradual fanning out of frequencies from the two areas of the periodogram with highly significant frequencies, namely the 25–35 cycles d^{-1} and 0.4–0.9 cycle d^{-1} regions, into the adjacent frequency regions.

Of the 32 statistically significant frequency reported by the restricted range analysis, 13 of these had a problem when matched to the periodogram. There were two types of problems: firstly, the identified frequency was close to the local peak of the periodogram but did not match it and, secondly, there was no discernible feature in the periodogram at, or near, the location of the frequency. Examples of both of these problems are presented in Figure 7. The first is illustrated in panel (a) and the second in panel (b).

The periodogram of the residuals from the final stage of the restricted range analysis was plotted against the periodogram of the data to check if there appeared to be any clear peaks which had been missed by the restricted range analysis. A plot of both periodograms appears in Figure 8. From an analysis of the periodogram of the residuals and comparing the remaining peaks with the results of the unrestricted analysis, a further eight significant frequencies were identified; these are reported in Table 7. The frequencies F1 through F22 in Table 7 were

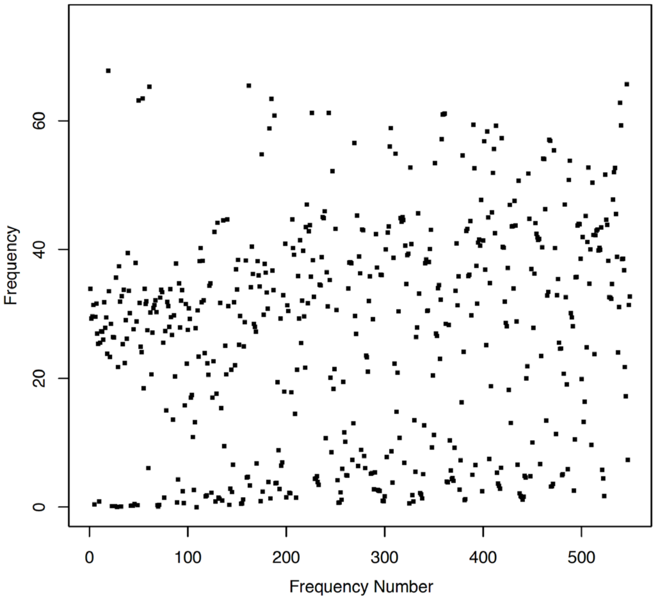

Figure 6. The statistically significant frequencies from the complete TESS data set in the order in which SigSpec (Reegen 2011) reported them.

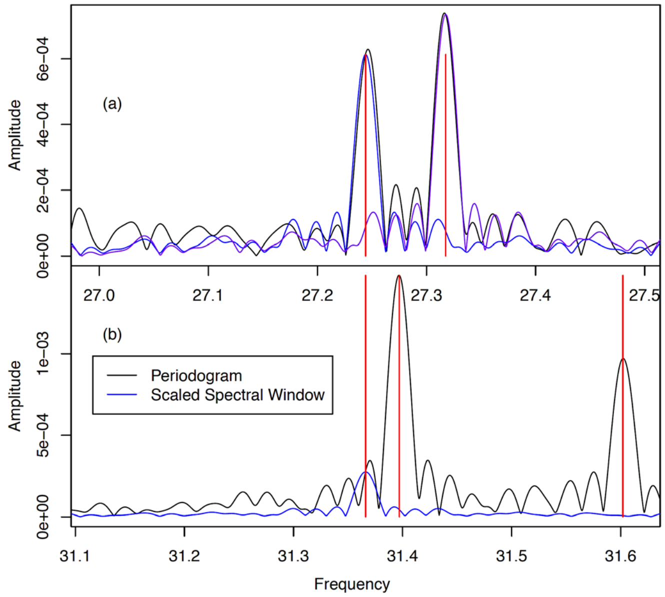

Figure 7. Examples of the two types of problems which arose in the restricted range frequency analysis. In both panels the periodogram is marked in black, the scaled spectral window in blue, and the locations of the significant frequencies in red. Panel (a) is an example of when the identified frequency did not match the location of the local peak in the periodogram. Panel (b) is an example of when the identified frequency could not be matched to any feature in the periodogram.

Table 7. The final list of significant frequencies.

Number	*Frequency*	*SNR*	*Number*	*Frequency*	*SNR*
F1	0.432322	29.19	F16	31.397066	64.55
F2	0.863226	18.86	F17	31.601901	42.91
F3	23.313647	21.40	F19	31.798934	15.23
F4	23.815548	23.65	F19	31.894335	6.57
F5	25.358788	57.76	F20	31.940864	4.45
F6	25.503446	57.41	F21	33.869470	323.41
F7	26.004749	27.95	F22	67.738708	47.92
F8	26.913886	54.10	F23	20.299375	7.15
F9	27.244179	31.67	F24	20.598099	8.48
F10	27.317593	38.04	F25	21.737048	13.68
F11	27.846068	14.32	F26	22.408476	12.18
F12	29.267407	96.72	F27	24.062921	7.47
F13	29.534648	46.91	F28	26.337816	11.29
F14	29.599931	97.35	F29	26.386373	11.20
F15	30.112743	4.87	F30	27.639601	5.44

Table 8. Pairs of frequencies of the form f, 2f.

f_1	$f_2 = 2f_1$	$2f_1 - f_2$	*Amplitude Ratio* f_1/f_2
0.432322	0.863226	0.001418	1.62
33.869470	67.738708	0.000232	31.53

identified by the restricted range analysis. Frequencies F23 through F30 were identified by visual inspection and comparison of the periodograms of the data and the residuals from the same restricted range analysis. All 30 frequencies were subject to a least squares fit in FAMIAS and the signal-to-noise ratios (SNR) reported in the final column were calculated by FAMIAS.

A search was made for frequency groupings of the form f, 2f, 3f... and only two were found. These are reported in Table 8 in which the third column gives a measure of how exact the 2:1 frequency ratio is. The final column is the ratio of the amplitudes of the two frequencies. A search was also made for regular frequency spacings such as doublets or triplets and two doublets were found. These are plotted in Figure 9.

5. Discussion

5.1. Simulated light curve

For the simulated light curve both the restricted and unrestricted frequency analysis recovered all 18 of the real frequencies. In the periodogram of the simulated light curve in Figure 1 the six sets of three frequencies are easily seen. Thus it is unsurprising that they were all recovered. The periodogram of the residuals from the restricted range analysis, plotted in red, show little remaining structure. While not shown in this paper, a plot of the periodogram of the residuals from the restricted and unrestricted frequency analyses showed only minor differences.

The eight-stage restricted analysis resulted in a modest reduction in the number of statistically significant frequencies reported in Table 3. Nevertheless, in both cases the number of spurious frequencies reported (27 for the restricted and 36 for the unrestricted) exceeded the number of real frequencies in the data. While raising the significance level would have eliminated some of the spurious frequencies, some were of such high significance—for example, the 22.456008 cycles d^{-1} frequency had a significance of 83.94—that not all spurious frequencies could be eliminated by this method.

Figure 2 gives us an indication of why spurious frequencies are unavoidable. Panel (a) of the Figure is of a frequency with two nearby spurious frequencies while panel (b) has a single significant frequency. In panel (b) the scaled spectral window almost completely obscures the data periodogram. Panel (b) shows that if the pulsation generates a sinusoid in the light curve, there should be no complicating spurious frequencies in its immediate neighborhood. In Panel (a) there are two very distinct deviations in the periodogram from the spectral window, both of relatively high significance (12.25 and 11.60, respectively). While both frequencies are required mathematically to describe the data, when interpreted in terms of a model of stellar pulsations, they would not correspond to any physical pulsation. Without the prior knowledge of the construction of this data set, one would almost certainly accept these frequencies as physically meaningful, and in one sense they are because they give information about the shape of the pulsation.

5.2. EE Cha Data

Attempting a frequency analysis of astronomical light curve data where multiple non-sinusoidal pulsations are present is extremely challenging, as previous literature and the results presented above and in Paper I show. The difference in the number statistically significant frequencies reported by SigSpec and FAMIAS in Table 6 is easily explained by the fact that FAMIAS is limited to 100 frequencies whereas SigSpec does not have this limitation. The difference in the number of reported statistically significant frequencies between the unrestricted and restricted range analysis is quite dramatic even though the analysis was carried out with the same software, namely SigSpec (Reegen 2011).

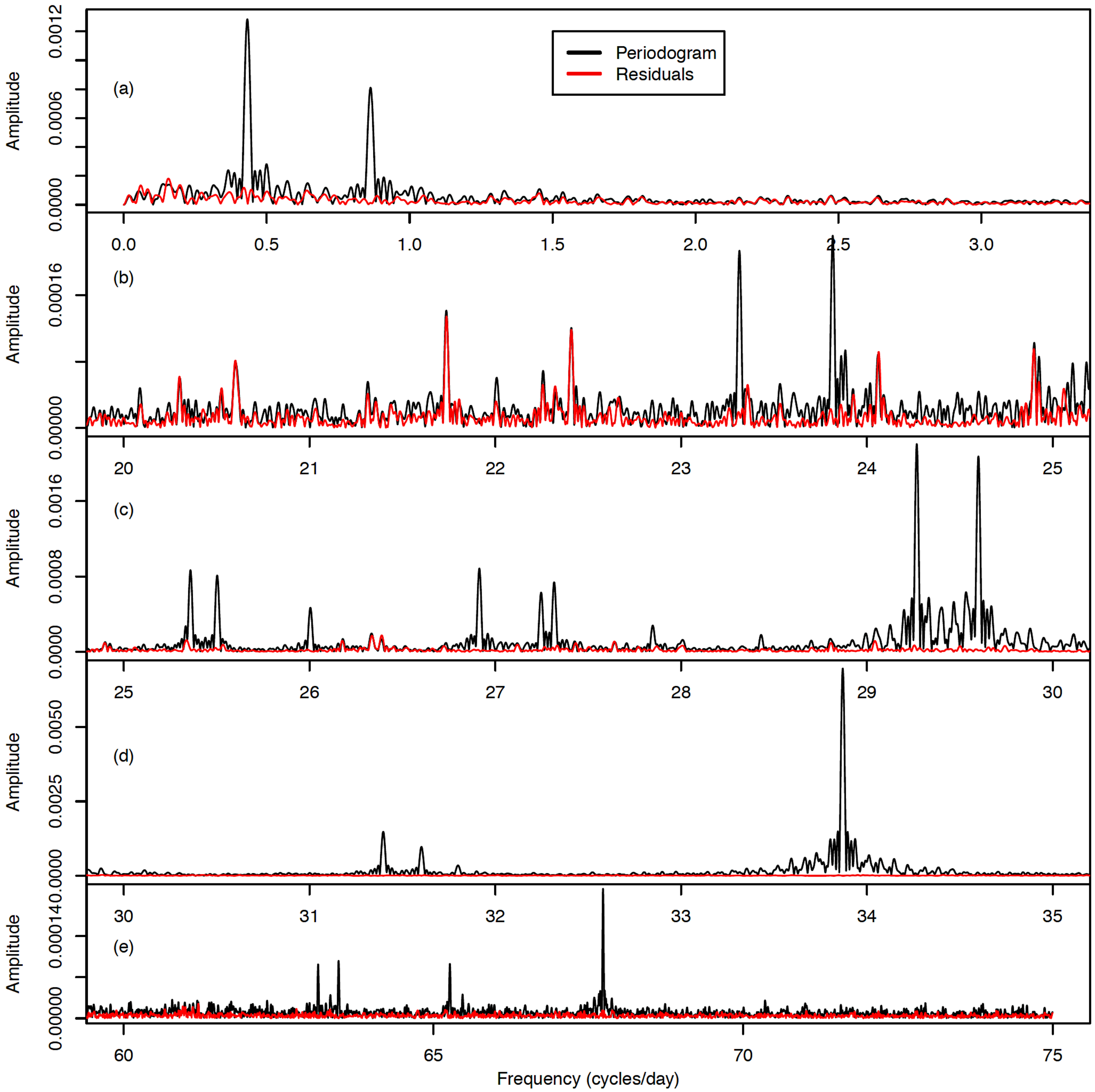

Figure 8. The periodogram of the full two-sector data set is in black while the periodogram of the residuals after the nine-stage restricted range analysis was run is in red. The vertical axis in each of the five panels is not to the same vertical scale.

Although the significance level used was the same in both cases, part of the difference may be because of what is considered signal and what is considered noise in the light curve. A problem familiar to users of FAMIAS (Zima 2008) is that often a frequency is first reported as statistically insignificant but after a few more cycles of pre-whitening it reaches statistical significance. Consider a light curve composed of 10 pulsation frequencies and some noise. After the first cycle of frequency analysis one frequency will have been identified as the strongest and the remaining nine will be grouped with the true noise as just noise. After the second pre-whitening cycle the second strongest frequency will be identified and the remaining eight will be grouped with the true noise as just noise. If the signal-to-noise ratio (SNR) is calculated at each stage, the SNR of the first frequency will increase with each subsequent cycle of pre-whitening and analysis. For example, with only the single 33.869470 cycles d^{-1} frequency included, FAMIAS reported its SNR as 267.80. If all of the frequencies from the restricted range analysis were included, its SNR rose to 323.99.

The periodogram of the residuals from the restricted range frequency analysis in Figure 8 clearly has a lot of remaining structure. Some of that will be artifacts from the analysis, as Balona (2014) and Paper I have shown, but some will likely be from unidentified physically meaningful but weak pulsations. Thus, two things must be done after running a restricted range frequency analysis. The first is to check every statistically

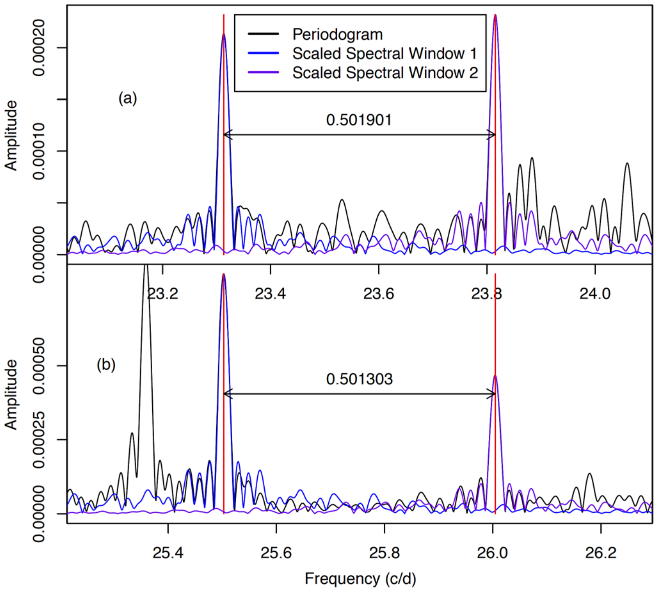

Figure 9. Two doublets with nearly identical spacing from the full two-sector data set. Panel (a) displays frequencies F3 and F4 in Table 7 and panel (b) displays frequencies F6 and F7.

significant frequency against the periodogram to ensure it corresponds to some identifiable feature. Second, the periodogram of the residuals must be examined carefully for evidence of physically meaningful pulsations which may have been missed.

Taking the first of these two steps, of the 32 statistically significant frequency reported by the restricted range analysis, 13 of these had a problem when matched to the periodogram. As illustrated in Figure 7, the two types of problems were, firstly, as in panel a, the identified frequency was close to the local peak of the periodogram but did not match it and, secondly, as in panel b, there was no discernible feature in the periodogram at, or near, the location of the significant frequency. There were four of the first type and nine of the second. At least some of both types appear to be caused by interference from a side lobe of a nearby stronger frequency. In all four cases where the periodogram peak was slightly displaced from the location of the identified frequency, either the second or third side lobe of a nearby strong peak was situated within the frequency span of the peak. Three of the four had significances above 10. The question is whether one should manually correct the reported frequency to match the location of the periodogram peak. This does not appear to be advisable because the side lobe and the real frequency were combined into a single peak in the periodogram. Software such as FAMIAS or SigSpec should be able to disentangle such merged features.

By contrast, all nine frequencies which did not match a discernible feature in the periodogram had significances of less than 7.5. There seems little reason to retain these for they appear to be artifacts of the pre-whitening process, something entirely expected.

Moving now to checking for missed frequencies, Figure 8 compares the periodogram of the residuals from the restricted range analysis (red) with the periodogram of the data (black). Not all of the periodogram is presented; the two long-frequency regions 3–20 and 35–60 cycles d^{-1} are omitted because they appeared to consist of nothing but noise. Panel (a) covers the γ Doradus frequency range and there appears to be no noticeable peaks in the residuals, from which we conclude that the two identified frequencies were all that there are in this region.

In panel b of Figure 8 there appear to be several peaks in the periodogram of both the full data set and in the residuals which do not appear to have been adequately modelled in the restricted range analysis. For example, the peaks at 21.737048 and 22.408476 cycles d^{-1} had significances of 104.78 and 89.64, respectively, in the unrestricted analysis. While not obvious at the vertical scale used in panel b, there are several peaks in the periodogram of the residuals that are larger than the same peaks in the periodogram of the data. This is the result of modelling a non-sinusoidal pulsation with a single sinusoid and some of the power from the pulsation leaking out into other parts of the periodogram in the pre-whitening process.

Similarly, in panel c there appear to be a few frequency peaks missed in the restricted range analysis. These missed frequencies in panels b and c are included as frequencies F23–F30 in Table 7.

In panel d of Figure 8 there appears to be no strong frequency in the residuals, indicating that in this frequency range the few frequencies identified during the restricted range frequency analysis were adequate to model the data.

In panel e of Figure 8 there are a number of peaks in the periodogram of the original data set that do not appear in the residuals, even though only a single statistically significant frequency in the 60–75 cycles d^{-1} range was identified at 67.738708 cycles d^{-1} then modelled and removed. It is likely that these other periodogram peaks are overtones from lower frequencies which, once these lower frequencies were modelled and removed, also removed these apparently strong peaks in the high frequency region.

Once the detailed frequency identification was complete, then the extracted frequencies could be analyzed for information they may provide on the structure of the star. Since this paper is primarily about frequency analysis, we only note two features of the identified frequencies. The first is that frequencies of the form f, 2f, 3f... often indicate an asymmetric pulsation which requires more than one frequency in the Fourier series to adequately model it. Table 8 presents two such groupings. This raises the question of whether the 0.863226 cycle d^{-1} is, in fact, real or the result of an asymmetry in the 0.432322-d^{-1} pulsation. Given the strength of the higher of these two frequencies we might have expected significant frequencies at 3f and 4f. Neither of these frequencies appeared in the unrestricted analysis and there is no evidence of an unmodelled pulsation in the periodogram of the residuals. This implies that the 0.863226 cycle-d^{-1} pulsation was physically meaningful.

The second pair in Table 8 is much more likely to be the result of slight asymmetry in the lower frequency, which is the strongest pulsation in the data. We did not search for a frequency of the form 3f, which would have had a frequency near 100 cycles d^{-1}. However, given the magnitude of the reduction in amplitude of 2f relative to 1f (31.5 to 1), a similar reduction in amplitude between 2f and 3f would have rendered the peak indistinguishable from noise even if it existed.

Figure 9 presents two doublets with nearly the same frequency spacing. The scale of the horizontal axes is the same in both panels. Rotational splitting of pulsation modes is expected to give rise to a multiplet with an odd number of frequencies. However, as Aerts and Kurtz (2010, p. 16) point out, not all members of the multiplet may be excited to the same amplitude and, consequently, not all members of the multiplet will be observable in the data. With a single published v sin i value of 93 km/s (Royer *et al.* 2002, 2007), the frequency spacing may well reflect the rotational period.

6. Conclusions and suggestions for further research

There appears to be no simple solution to the problem of separating the reported statistically significant frequencies into those which correspond to a pulsation and those which are mathematically required to describe the data (for example because of changes in the amplitude of a pulsation or asymmetric light curve shape) but do not correspond to a pulsation mode. The restricted range analysis proposed in Paper I has the advantage of being particularly simple to implement. Our results suggest the following approach is useful:

1. Run an unrestricted range frequency analysis followed by a restricted range analysis, dividing the frequency range into sub-ranges with visually obvious peaks and sub-ranges which appear to be only noise.
2. Compare all significant frequencies from the restricted range analysis against the data periodogram. Accept each one which matches a distinct feature within it, while making use of the scaled spectral window to examine the effects of a strong frequency on nearby periodogram peaks. Reject those frequencies which do not match any discernible feature in the periodogram.
3. Carefully examine the periodogram of the residuals from the restricted range analysis for unexplained peaks which also appear in the data periodogram. Check these against possible significant frequencies in the unrestricted analysis.
4. After obtaining a set of candidate frequencies, make a search for combination frequencies.

As pointed out above, step 2 is problematic because frequencies which are mathematically necessary to describe the data may have an apparently high significance and easily discernible periodogram feature while corresponding to no physical pulsation in the star of interest.

There are promising new methods proposed to distinguish between mathematically and physically meaningful pulsation frequencies, such as that proposed by Lares-Maritz *et al.* (2020). This and other methods need further research.

Looking towards the future, because EE Cha is a young δ Scuti with a relatively simple periodogram and is relatively bright (Mag 6.7 in V), it would benefit from an intensive spectroscopic observing campaign to attempt to do mode identification.

7. Acknowledgements

The author would like to thank the editor and an anonymous referee who commented on Paper I for valuable comments which helped to improve both papers.

The author would like to thank NASA for making the data from its Transiting Exoplanet Survey Satellite freely available and the TESS Asteroseismic Science Operations Center (TASOC) for operating their particular database of TESS photometry data.

The author would like to thank the American Association of Variable Star Observers for maintaining and making freely available the Variable Star Index (VSX).

This research has made use of the SIMBAD database, operated at CDS, Strasbourg, France.

References

Aerts, C, Christensen-Dalsgaard, J., and Kurtz, D. W. 2010, *Asteroseismology*, Springer Science + Business Media B. V., Dordrecht.

Balona, L. A. 2014, *Mon. Not. Roy. Astron. Soc.*, **439**, 3453.

Catelan, M., and Smith, H. A. 2015, *Pulsating Stars*, Wiley-VCH, Weinheim, Germany.

Gaia Collaboration, *et al.* 2020, *Astron. Astrophys.*, **649A**, 1 (doi:10.5270/esa-1ug).

Grigahcène, A., *et al.* 2010, *Astrophys. J., Lett.*, **713**, L192.

Kurtz, D., and Müller, M. 1999, *Mon. Not. Roy. Astron. Soc.*, **310**, 1071.

Lares-Maritz, M., Garrido, R., and Pascual-Granado, J. 2020, *Mon. Not. Roy. Astron. Soc.*, **498**, 1194.

Murphy, S. J., Lawson, W. A., and Bessell, M. B. 2013, *Mon. Not. Roy. Astron. Soc.*, **435**, 1325.

Poretti, E., *et al.* 2009, *Astron. Astrophys.*, **506**, 85.

R Core Team. 2019, R: A Language and Environment for Statistical Computing, R Foundation for Statistical Computing, Vienna, Austria (https://www.R-project.org).

Rea, B. 2022, *J. Amer. Assoc. Var. Star Obs.*, **50**, 8.

Reegen, P. 2011, *Commun. Asteroseismology*, **163**, 3.

Ricker, G. R., *et al.* 2014, *Proc. SPIE*, **9143**, id. 914320.

Royer, F., Gerbaldi, M., Faraggiana, R., and Gómez, A. E. 2002, *Astron. Astrophys.*, **381**, 105.

Royer, F., Zorec, J., and Gómez, A. E. 2007, *Astron. Astrophys.*, **463**, 671.

Uytterhoeven, K., *et al.* 2011, *Astron. Astrophys.*, **534**, A125.

Wenger, M., *et al.* 2000, *Astron. Astrophys., Suppl. Ser.*, **143**, 9.

Zima, W. 2008, *Commun. Asteroseismology*, **155**, 17.

BVI Observations of the Eclipsing Binary XZ Andromedae at the EKU Observatory

Marco Ciocca

Department of Physics, Geosciences, and Astronomy, Eastern Kentucky University, Richmond, KY 40475; marco.ciocca@eku.edu

Received January 23, 2022; revised April 4, 2022; accepted April 5, 2022

Abstract The eclipsing binary XZ Andromedae has been the subject of many observing campaigns, due to variability of its orbital period and the interesting mechanisms causing the change. We therefore observed this star during the period October–November 2021. We determined the current orbital period (P = 1.357308 (18) d), and using transformed standard BVI magnitudes, constructed a model of the eclipsing binary using the PHOEBE (Physics of Eclipsing Binaries) and Binary Maker 3 software packages to compare with results from previous studies. The model that best fit the data suggests that XZ And is a semidetached system with the secondary filling the Roche Lobe. The parameters fit of the primary (T_1 = 9393 K, mass M_1 = 2.1 solar masses, and radius R_1 = 2.2 solar radii) are indicative of a A1V main sequence star, while the secondary's parameters (T_2 = 5334, M_2 = 1.02, and R_2 = 2.40) point to a star in a more advanced evolutionary status.

1. Introduction

XZ And, R.A. = $01^h\ 56^m\ 51.52^s$, Dec. +42° 06' 02.2" (J 2000) (see Figure 1) is an eclipsing variable of the Algol type, that is, a more evolved, larger and cooler star with a hotter, younger companion. There is likelihood of mass transfer under these conditions and the ultimate evolution of the system will be one of a white dwarf orbiting the younger companion.

XZ And has been the subject of many observing campaigns, aiming at determining the eclipse period, its variation over time, and the mechanisms responsible for its variation. It was first reported as variable by Shapley (1923) with many other attempts at determination since then.

Blitzstein (1950, 1954) described the binary as a primary of spectral type A0 with a secondary of spectral type G4. Blitzstein (1954) reached the conclusion that the light between eclipses was not constant, thus suggesting a semidetached system, that the primary eclipse was due to occultation (this is an important aspect of our analysis), and that the depth and duration of the observed secondary eclipse could not be reconciled with the calculated light curve. Blitzstein provided two possible explanations: that the secondary eclipse is wider than the primary due to an elliptical orbit or that (verbatim) "the light in secondary eclipse is not that produced by an ordinary eclipse but is modified by rings or streams of gas."

Blitzstein observations were unfiltered. Reinhart (1967) performed a two-color photoelectric measurement and determined that both eclipses have the same duration and therefore eliminated the possibility of an elliptical orbit. Giuricin *et al.* (1980) concurred with the determination of the primary as A0 and concluded that the secondary instead be a G5. Demircan *et al.* (1995) performed another study on the period variation of XZ And (again identified as an evolved Algol system) by using additional data.

Demircan *et al.* determined that the Observed – Computed (O–C) diagram formed by the times of minimum light (ToM), and the orbital period of the system, could be explained in terms of the beat effect of two (or possibly three) cyclic variations differing in periods (P_1 = 137.5 yr, P_2 = 36.8 yr, and P_3 = 11.2 yr) and amplitudes. They examined three possible explanatory mechanisms: apsidal motion of the slightly elliptical orbit, light time effect due to additional objects in the system, and the period modulation due to magnetic activity cycle of cool secondary component star (Applegate 1989, 1992). They rejected the possibility of apsidal motion effect on the period variation, while they thought P_3 could be related to the cyclic magnetic activity of the secondary component. The third-body hypothesis required one or two under-luminous stars (with total mass of about 3 solar masses $M_\odot$) around the system. Their reported

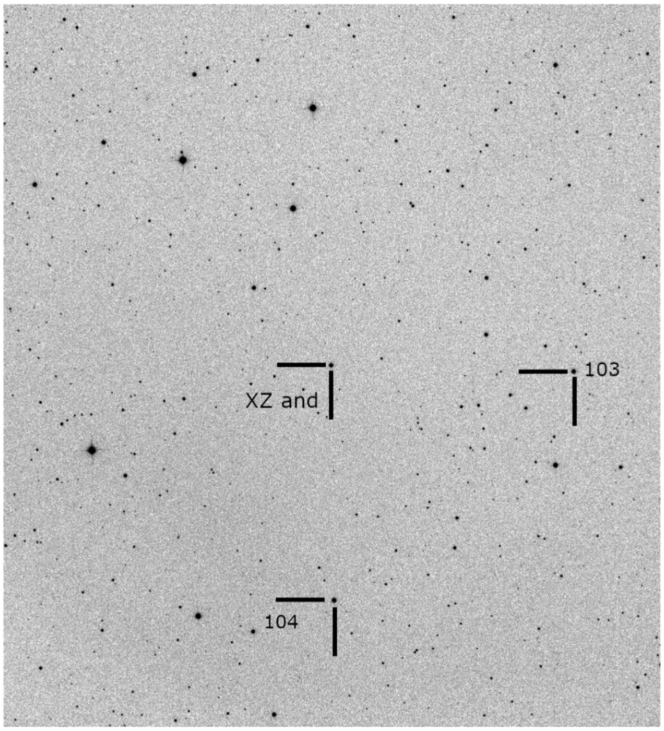

Figure 1. CCD frames (I_c Filter, 10 s integration time) showing the target star, comparison star, and check star. Star 104 (see Table 2 for its AUID designation) is the check star for the differential photometry of XZ And using VPHOT, while Star 103 is the comparison star. Scale: 1.90 arcseconds/pixel. Size (pixels): 1365 × 1365. Angular Size: 0° 43' 14" × 0° 43' 14". Position Angle (top of image): 86° 31' from north through east.

O–C diagram shows a good agreement with the third-body hypothesis.

2. Observations

2.1. Facilities

Eastern Kentucky University (EKU) Observatory has been described previously in Ciocca (2013). The telescope, however, is now an imaging Dall-Kirkham truss 17-inch telescope (IDK 17 from Planewave), with a Paramount ME II mount from Software Bisque. The instrument package now consists of a FLI 16803 Proline CCD, which has an array of 4096 × 4096 pixels, with 9-µm pixels, and is Anti-Blooming (ABG). The combination camera-telescope results in a field of view of 43 × 43 arcminutes, with an image scale of 1.90 arcsec/pixel when binning 3 × 3.

2.2. Telescope transformation parameters

We measured the transformation coefficients of the new scope-camera combination, as this allows converting the raw instrumental magnitudes to standard magnitudes, thus making comparisons with other measurements possible. This is done by using the software tools TRANSFORM GENERATOR TG (Myers 2014) and TRANSFORM APPLIER TA (Silvis 2015). TG and TA made the process much simpler (Ciocca 2016). Recently, TA has been integrated with the online photometry software VPHOT, also provided by AAVSO (AAVSO 2012). We generated the transformation parameters by imaging the standard field NGC 7790 (one of the suggested star fields in TG) during October 2021.

The transformation parameters for our BVR$_c$I$_c$ filter set (Table 1) show a system close to the "ideal" case, as all the Color Index coefficients are approximately equal to 1 and the Filter Band Coefficients are near zero.

3. Data Analysis

3.1. Orbital period determination

From October 11 to November 19, 2021, we observed XZ And via Johnson-Cousins BVI$_c$ filters. Data were not collected with R$_c$ as the standard stars available for the chart used (AAVSO chart X27525ALU, see also Figure 1) did not have any R$_c$ photometry available (see Table 2). Even though we had more standard stars available in the field of view, we limited the VPHOT sequence to one check and one comparison stars as to be able to use the TRANSFORM APPLIER routine, which is not yet capable of applying transform coefficient to ensemble photometry (see Figure 1 and Table 2).

Table 1. Transformation parameters for the EKU observatory (November 2021).

Transformation Parameters	*Value and Uncertainties*
TBV	1.029 ± 0.016
TBR	1.021 ± 0.015
TBI	1.07 ± 0.010
TRI	0.98 ± 0.012
TVI	0.996 ± 0.01
TB_BV	0.008 ± 0.023
TB_BR	0.005 ± 0.015
TB_BI	0.005 ± 0.011
TV_BV	–0.02 ± 0.014
TV_VR	–0.035 ± 0.0024
TR_VR	–0.043 ± 0.018
TR_RI	–0.045 ± 0.022
TI_RI	–0.034 ± 0.023
TV_VI	–0.018 ± 0.015
TI_VI	–0.015 ± 0.011
TR_VI	–0.023 ± 0.01

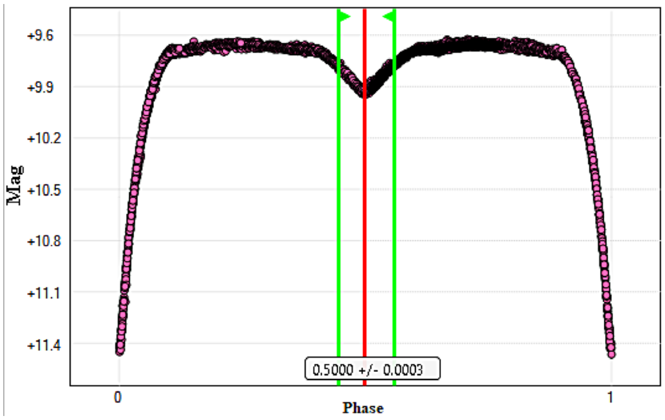

Figure 2. Phase plot of the transformed I$_c$ magnitudes (red dots). The green lines are used by PERANSO to demark the data used to determine the time of minimum of the secondary eclipse. The minimum is at the red line.

Calibration of the CCD frames was done using PIXINSIGHT (Pleiades Astrophoto 2022) while plate solving was performed using THE SKY X (Software Bisque 2018). The frames were then uploaded to, and the photometric results generated by VPHOT using the sequence shown in Table 2. After the differential photometry was complete, we uploaded the resulting observation files to the TRANSFORM APPLIER in VPHOT. This generated transformed magnitudes of XZ And.

We analyzed the transformed magnitudes via PERANSO (Vanmunster 2013). This allowed us the determination of the orbital period and the generation of phase diagrams, with one example shown in Figure 2.

The period determined using data we collected between October and November 2021 is T = 1.357308 ± 0.000018 d, in good agreement to the period reported by the AAVSO International Variable Star Index (VSX; Watson *et al.* 2014). The uncertainty quoted in our determination (0.000018 d = 1.56 s) is

Table 2. Sequence stars used (AAVSO chart C27525ALU).

AUID	*R.A. (2000)* *h m s*	*Dec. (2000)* *° ' "*	*Label*	*B*	*V*	*I$_c$*	*Comments*
000-BBD-311	01 55 46.68	+42 05 26.0	104	11.417 (0.1133)	10.447 (0.075)	8.319 (0.153)	Check Star
000-BBD-332	01 56 45.66	+42 18 26.2	103	10.861 (0.110)	10.346 (0.079)	9.596 (0.170)	Comp. Star

simply the standard error of the mean of the values obtained in Peranso for each filter and does not reflect the base line uncertainty of the computer time, which is less than 0.2 sec / day (we use time calibration routines). In Figure 2, the phase plot generated by Peranso, using the determined orbital period, shows the location of the secondary minimum. This occurs at phase 0.5000 ± 0.0003, consistent with a purely circular orbit.

3.2. Time of Minimum (ToM), O–C, and period variability

Yang (2013) published an extensive work on XZ And, in which ToM from several sources and several ToM measured directly by that author, were used to build a more extensive O–C diagram, and compare it with a new model. These are the conclusions: the O–C graph showed a parabolic trend with a quasi-cyclic variation, with a time period of $P_{mod} = 32.30 \pm 0.06$ yr and amplitude $A = 0.0368 \pm 0.0008$ day, respectively. The model reproduced the data very effectively (see Figure 2 in Yang's paper).

We constructed an O–C diagram as well, in which we used exclusively the ToM we were able to determine using the CCD data available in the AAVSO International Database (Table 3). Most of the data in the database use the Johnson V filter. Our own V data are in the database as well, but we also have included our own Johnson B and Cousins I filters data. All the determinations are of the primary eclipse.

Table 3. Time of Minima (TOM) for XZ And determined using CCD data in the AAVSO International Database.

HJD –240000	*Uncertainty (d)*	*Filter*	*HJD –240000*	*Uncertainty (d)*	*Filter*
50430.6020	0.002514	V	58050.4840	0.000051	V
51486.6005	0.002190	V	58058.6270	0.000183	V
53591.7900	0.001168	V	58073.5570	0.000053	V
53769.5960	0.000108	V	58100.7047	0.000076	B
54107.5660	0.000079	I	58100.7050	0.000108	I
54476.7510	0.001697	V	58100.7050	0.000173	V
54799.7890	0.000623	V	58100.7053	0.000181	B
54833.7200	0.000091	V	58111.5640	0.000058	V
54863.5800	0.000262	V	58374.8800	0.000043	V
55084.8178	0.000037	V	58392.5250	0.000067	V
55084.8180	0.000450	V	58396.5970	0.000049	V
55239.5490	0.000410	V	58415.6000	0.000106	V
55486.5740	0.000303	V	58456.3160	0.003142	V
55490.6460	0.000058	V	58464.4600	0.000056	V
55836.7520	0.000060	V	58479.3900	0.000080	V
55938.5470	0.000164	V	58494.3200	0.000054	V
56163.8550	0.001215	V	58712.8490	0.000058	V
56520.8210	0.000077	V	58825.5020	0.000095	V
56603.6150	0.000090	V	59130.8970	0.000070	V
56862.8560	0.001062	V	59167.5440	0.000085	V
57321.6200	0.000206	V	59186.5460	0.000077	V
57336.5500	0.000071	V	59426.7870	0.000117	V
57355.5520	0.000120	V	59498.7240	0.000469	I
57359.6240	0.000596	V	59498.7240	0.000549	V
57633.7960	0.000261	V	59498.7244	0.000515	B
57644.6560	0.001982	V	59506.8680	0.000342	I
57705.7320	0.000204	V	59506.8680	0.000398	V
57705.7330	0.001119	B	59506.8682	0.000394	B
57709.8040	0.000342	V	59509.5820	0.000265	I
57709.8049	0.000399	B	59509.5827	0.000454	B
57712.5180	0.001436	V	59509.5830	0.000351	V
57712.5200	0.000399	B	59524.5120	0.000529	V
57714.5560	0.001433	V	59524.5125	0.000380	B
57724.7378	0.000075	V	59524.5130	0.000416	I
57754.5940	0.000113	V	59525.8702	0.000278	B
58043.6990	0.000085	V	59525.8710	0.000487	I
58047.7710	0.000254	V	59525.8710	0.000203	V

We used as epoch the first ToM we measured in the AAVSO database, and the period determined analyzing all the CCD data available in the database. We have: epoch = 2450430.6020 (25) JD and period = 1.357290 (1) d. The resulting O–C diagram is shown in Figure 3.

It is noteworthy to indicate that, by using the CCD data (covering the period December 1996–2021) in the AAVSO International Database, we obtained (using Peranso) the period shown above to plot the O–C diagram. If we limit the data to more recent dates (December 2015–2021), the period (P) obtained is instead P = 1.357299 (2). This appears consistent with an overall lengthening of the orbital period of XZ And, and further reflected in our own determination (with October–December 2021 data, approximately 30 cycles only) of P = 1.357308 (18) d.

By fitting the last 1,000 cycles of our O–C diagram with linear fit (Figure 4), we obtained the correction to the period and Epoch used in the generation of the diagram, resulting in a new epoch = 2459525.797977 JD and new eriod P = 1.3573008 d. These results are in agreement with Bob Nelson's analysis of XZ And (Southwest Research Inst. 2022). Nelson used a much larger data set, with over 1,100 ToM determinations.

4. Modeling using PHOEBE and Binary Maker 3

Many other authors—Manzoori (2016), Yang (2013), Demircan *et al.* (1995), Giuricin *et al.* (1980)—have solved the light curves using the WD code, from Wilson and Devinney (1971) and Wilson and Van Hamme (2014).

In this work, we used PHOEBE 0.32a (Legacy version, released in 2017) and followed, initially, a step-by-step manual by Zasche (2016), written for version 0.31. The 0.32a version of PHOEBE is also based on the WD code but has been updated with Castelli and Kurucs (2004) model atmospheres and has a built-in table of limb darkening (dated 2010). The results of the fit are in Tables 4 and 5. Manzoori (2016) used PHOEBE 0.31.

After attempting some of the other choices (detached Binary, double contact etc.) with poor results, we modeled XZ And as a semi-detached system with the secondary filling its Roche lobe, a configuration typical for Algol-type eclipsing binaries (see Figure 5 for a 3-D model of the star) and used by both Yang (2013) and Manzoori (2016). The latter had access to radial velocity data and therefore was able to determine the mass ratio ($q = M_2 / M_1$) and the semimajor axis of the system A directly. We used those determinations, $q = 0.485 \pm 0.02$ and $A = 7.53 \pm 0.21$ in solar Radii respectively, as fixed input values for PHOEBE.

The primary spectral characterization of XZ And is reported as A1V by Manzoori (2016), based on the determination of Halbedel (1984). We therefore set the initial temperature of the Primary as 9500 K, as per Manzoori (2016), but we left this parameter as free for PHOEBE to fit. After many iterations, the fit settled on $T_1 = 9393$ K.

In the literature there is a large variation of the temperature of the cooler companion (and ensuing spectral class) ranging

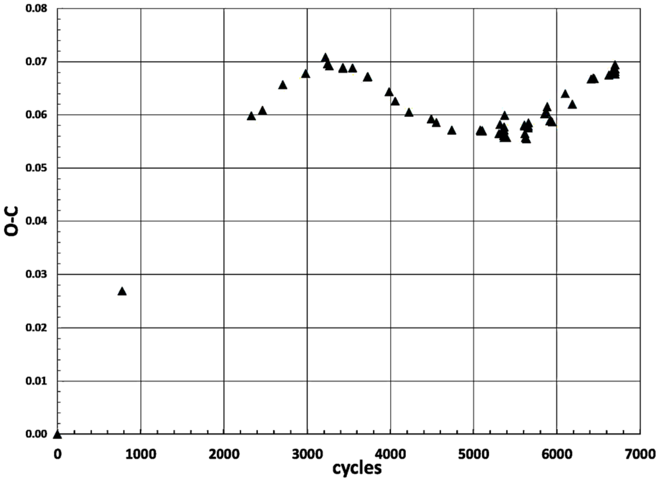

Figure 3. O–C diagram with Times of Minima from the AAVSO International Database.

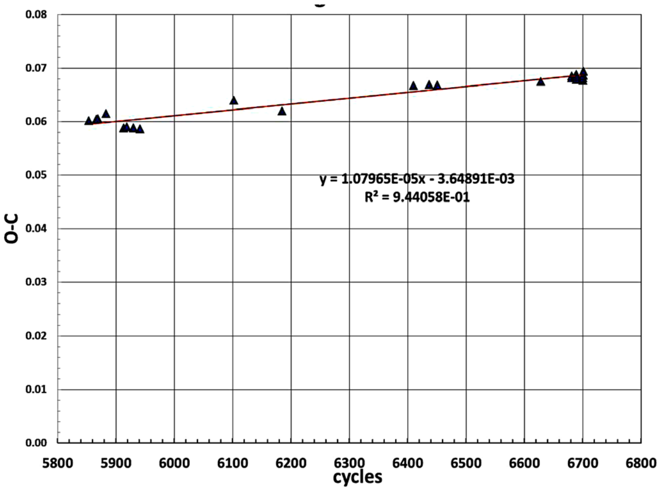

Figure 4. O–C diagram of the last 1,000 cycles to obtain correction to the period and the new epoch for XZ And.

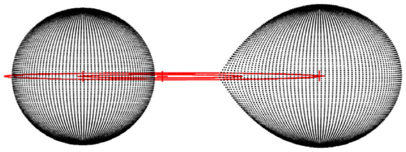

Phase 0.25, filled Roche Lobe

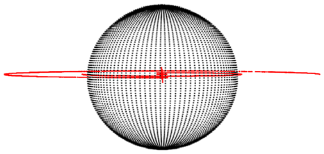

Primary Eclispe, Phase 0

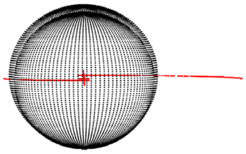

Secondary Eclipse, Phase 0.5

Figure 5. XZ And 3-d model generated by Binary Maker 3 using the parameters found in PHOEBE, showing the secondary filling its Roche Lobe, the Primary Eclipse, and the Secondary Eclipse.

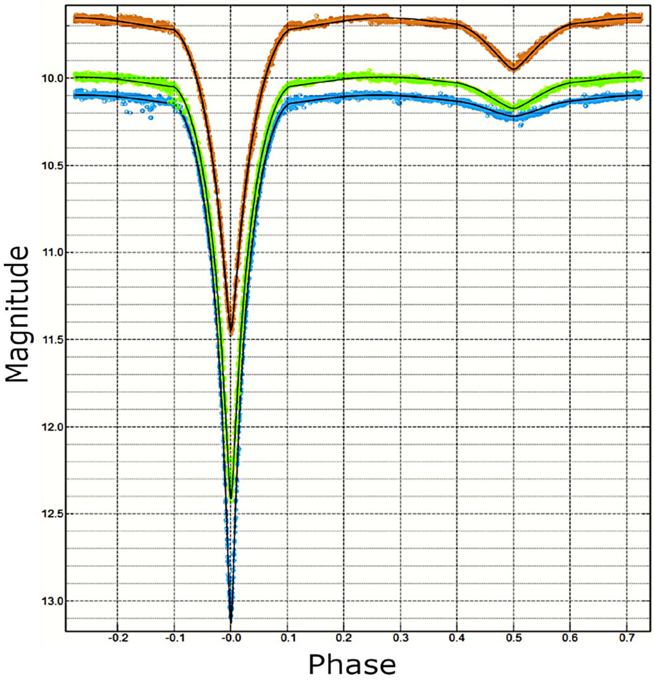

Figure 6. BVI observational magnitudes of XZ And with fit obtained using PHOEBE. Top to Bottom, I_c, V, and B filters. The fit is the solid line. Notice the differing depths of the primary and secondary eclipses as mentioned in the text.

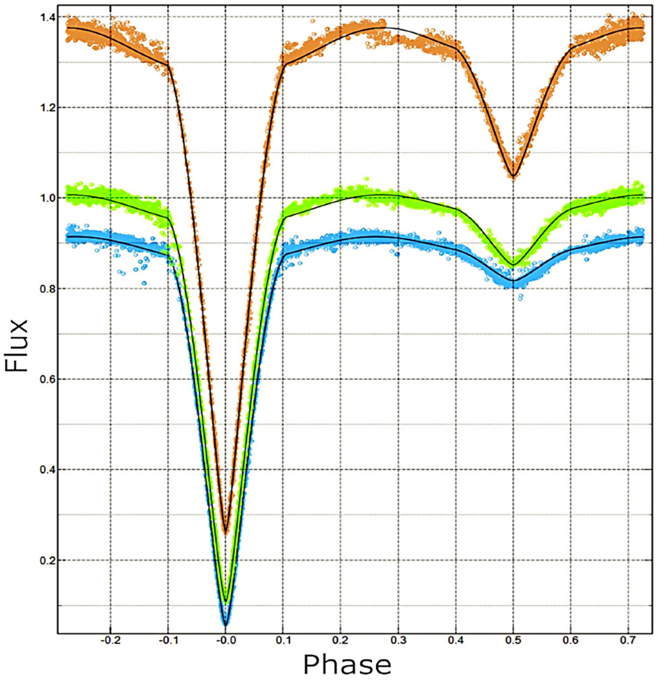

Figure 7. BVI observational fluxes of XZ And with fit obtained using PHOEBE. Top to Bottom, I_c, V, and B filters. The fit is the solid line. Notice the differing depths of the primary and secondary eclipses as mentioned in the text.

Table 4. Fit Parameters used and determined in PHOEBE.

Parameters	*This work*	*Manzoori (2016)*	*Yang (2013)*
T_0 HJD	2459498.723672	2423977.1915	1.424152.2546
P d	1.357308	1.357285	1.35727963
i °	88.34 ± .02	89.80 ± 0.04	88.4 ± 0.13
T_1 (K)	9393 ± 13	9500	9400
T_2 (K)	5337 ± 6	5100 ± 246	5094 ± 4
Ω_1	4.09 ± 0.01	4.55 ± 0.12	3.8347 ± 0.0024
Ω_2	2.85 ± 0.01	2.84	2.8255
q	0.485 ± 0.02 (Note 1)	0.485 ± 0.02	0.474 ± 0.0003
$(L_1/(L_1+L_2))$B	0.945 ± 0.01	0.869 ± 0.02 (Note 2)	0.9609 ± 0.0004
$(L_1/(L_1+L_2))$V	0.891 ± 0.01	—	0.9198 ± 0.0005
$(L_1/(L_1+L_2))$I	0.793 ± 0.01	—	0.8702 ± 0.0006 (Note 3)
$(L_2/(L_1+L_2))$B	0.055 ± .01	0.1310 ± 0.003 (Note 2)	—
$(L_2/(L_1+L_2))$V	0.109 ± 0.01	—	—
$(L_2/(L_1+L_2))$I	0.207 ± 0.01	—	—
(l_3)B	0.0032 ± 0.0005	0.004 ± 0.002 (Note 2)	—
(l_3)V	0.003 ± 0.001	—	—
(l_3)I	0.003 ± 0.001	—	—
e	0	$0.001 \pm 2.170 \times 10^{-4}$	—
F_1	1.980 ± 0.009	3.20 ± 0.011	—
F_2	1	1	—
(X_1)B	0.560	0.621 (Note 2)	Note 4
(X_2)B	0.861	0.622 (Note 2)	—
(X_1)V	0.476	—	—
(X_2)V	0.717	—	—
(X_1)I	0.315	—	—
(X_2)I	0.524	—	—
Number of Points	B = 3194, V = 2465, I = 3225	10277	B = 994, V = 989, R = 992
ALB 1	1.0	1.0	—
ALB 2	0.5	0.5	—
GBR 1	1.0	1.0	—
GBR 2	0.32	0.32	—
r_1 (pole)	0.276 ± 0.001	—	0.2958 ± 0.0002
r_1 (side)	0.297 ± 0.001	—	0.3018 ± 0.0002
r_1 (point)	0.306 ± 0.001	—	0.3102 ± 0.0003
r_1 (back)	0.303 ± 0.001	—	0.3070 ± 0.0002

Notes 1. Value adopted from Manzoori (2016). 2. Manzoori's data were obtained with a broadband filter (400–700 nm). 3. Yang used the R passband here. 4. Yang adopted a different Limb Darkening Law.

Table 5. Physical and orbital parameters, of XZ And.

Parameter	*This Work*	*Manzoori (2016)*	*Yang (2013)*
Semi-major axis A (in solar radii)	7.53 ± 0.21 (adopted from Manzoori)	7.53 ± 0.21	8.20
$M_{1\odot}$	2.10 ± 0.01	2.102 ± 0.010	2.15
$M_{2\odot}$	1.02 ± 0.01	1.017 ± 0.020	1.02
$R_{1\odot}$	2.20 ± 0.01	2.288 ± 0.042	2.30
$R_{2\odot}$	2.40 ± 0.01	2.401 ± 0.053	2.59

from 5094 K (Yang 2013) to 5500 K (Demircan *et al.* 1995) to 5470 K (Giuricin *et al.* 1980). In the work on XZ And by Manzoori (2016), the author's fit provided a value of 5100 ± 246 K.

In our data there are five primary eclipses. The primary eclipse has been described as an occultation (Blitzstein 1954), in which the cooler secondary completely obscures the hot primary. Considering also that the inclination of the system, as described by all previous published works as approximately 88–89 degrees, we assumed that during a primary eclipse the light is coming solely from the secondary star. We therefore used the color Index B–V at the minima of the light curve at the primary eclipse to give us an initial estimate of the temperature of the cooler star.

The weighted average of the B–V term at the minimum of all the primary eclipses in our data set is B–V = 0.67 ± 0.01 mag.

Making use of Ballesteros (2012), of the Sekiguchi and Fukugita (2000) fit, of the Galactic Dust Reddening and Extinction tool (https://irsa.ipac.caltech.edu/applications/DUST/), based on the work by Schlafly and Finkbeiner (2011), and other approximate formulae (Imaging the Universe Lab Manual (University of Iowa 2017)), we obtained an average value for T_{eff} of 5471 ± 100 K for the secondary. This is consistent with the spectral determination of the secondary as G5IV by Demircan *et al.* (1995). We therefore set this temperature as a starting point for the fit by PHOEBE, but we kept it too as a free parameter. For each PHOEBE iteration we interpolated the limb darkening coefficients tables available in PHOEBE to match the temperatures determination of the primary and secondary. After several cycles of this approach, and observing very small changes of those parameters, we set T_{eff1} and T_{eff2} at the values shown in Table 5. Therefore, the limb darkening coefficient shown correspond to these temperatures.

Demircan *et al.* (1995) and Manzoori (2016) accounted, in their solution, for the presence of a third body. Because of this, we also had PHOEBE fit the third light parameter, l_3, in the three passband, B, V, and I. The values we obtained are fairly small and converged to the values shown after many iterations.

Manzoori also obtained better results by modeling the rotation of the primary as non-synchronous with the orbital period. We followed suit and indeed obtained a better fit if we allowed the corresponding parameter F_1 to be fit by PHOEBE as well. We obtained the best results with $F_1 = 1.970 \pm 0.009$. Manzoori, with a much larger data set spanning a much larger period of time, obtained a best fit with F1 = 3.20 ± 0.011.

Another free parameter we used was the inclination i of the plane of the binary system.

Given the chosen temperatures (even if set as free parameters initially), we treated the primary as having a radiative atmosphere, while the secondary as convective. This was reflected in our choosing the albedo and gravity brightening parameters (ALB and GR) for the Primary as ALB1 = 1 and GR1 = 0.5 for the primary, while for the secondary we had ALB2 = 0.5 and GR2 = 0.32 respectively, which are the standard choices.

PHOEBE's fit is excellent, and it is shown in Figure 6 (Magnitudes) and Figure 7 (Fluxes), with the observations in the three filters. These phased plots use the orbital period and epoch, generated with PERANSO analysis, of the data we collected during October–November 2021 (HJD time = 2459498.723672, and T = 1.357308 d respectively), as opposed to the period determined over the last 1,000 cycles as shown in section 3.2 using the last 1,000 cycles of the O–C diagram.

The light change in secondary eclipse, when observed through I_c filter, appears deeper in than the one through the V filter which, in turn, is also deeper that the one in B (see Figure 6 and 7). This suggests that when the secondary is behind the primary star, there is little light lost at the B (and V) wavelengths, consistent with secondary being the cooler star.

Conversely, the primary eclipse is deeper in the B band than the V band and the V band is deeper than the I_c band (see Figures 6 and 7). This again suggests that during the primary eclipse the hotter star is behind the cooler one and more B wavelengths (and V as well) are lost. The PHOEBE fit accounts for this well. The light curves (in all the three filters) are never constant between eclipses, and therefore suggestive of the choice that XZ And is an Algol-type eclipsing binary, which is a semi-detached binary, in which the primary does not fill the Roche Lobe, while the secondary does so exactly. This can clearly be seen in the 3-d models, shown in Figure 5, which were generated in BINARY MAKER 3 (BM3; Bradstreet and Steelman 2004) using the PHOEBE results. Under these conditions, as shown by both Yang (2013) and Manzoori (2016), mass transfer from the secondary to the primary can and does occur and this explain the overall trend of increasing orbital period.

The agreement between our work and Manzoori (2016) is certainly expected given the fact that we used Manzoori's values for A and q, but this gives us more confidence in our model. It might be worth noting that, according to Pecaut and Mamajek (2013), a typical main sequence A1V has a mass $M_\odot = 2.05$, a radius of approximately $R_\odot = 2.14$, and a surface temperature T = 9300 K. These values are in very good agreement with the fit results, thus indicating that the primary in XZ And is indeed still on the main sequence, while the secondary is further along the evolutionary curve. From the above results, it seems likely that final evolutionary stage of XZ And will be of a main Sequence A star with a helium white dwarf, as the secondary is basically as massive as the Sun and losing mass, but with over twice the radius.

5. Conclusions

The orbital period of the eclipsing binary XZ And is continually evolving due to several mechanisms, which include mass transfer, period modulation due to third body, or bodies, as Demircan *et al.* (1995) suggested, and magnetic effects, as presented by Demircan *et al.* (1995), Yang (2013), and Manzoori (2016).

With the data from the AAVSO International Database, we generated an O–C diagram that seems to agree with the much more extensive dataset from Bob Nelson, albeit only for the last 7,000 cycles or so.

We were successful in using PHOEBE to model XZ And, and the results were in good agreement with previous efforts by Yang (2013) and Manzoori (2016). The fit of T = 9393 K for the primary seems to strengthen the case for the star to be classified as A1V spectral category. Our determination of the B–V value for the secondary agreed overall with the model as well.

The third light parameters we obtained are also in overall agreement with Manzoori (2016), thus indicating the definite possibility of a third body in the system.

XZ And is continuing to prove a very interesting subject. In the paper by Jetsu (2020), the author developed a method to study O–C diagrams of binary systems searching for invisible companions. In the case of XZ And, the author suggests that there are at least ten wide orbiting stars with periods ranging between 1.6 and 91.7 years. More mysteries remain to unravel on XZ And.

6. Acknowledgements

We acknowledge with thanks the variable star observations from the AAVSO International Database contributed by observers worldwide and used in this research. We also wish to thank Dr. M. Pitts and Dr. A. Blose for a careful reading of the manuscript, and Dr. David Bradstreet for considerable help with BM3. Many thanks are also given to the anonymous manuscript referee for his/her extremely helpful comments to improve this work.

References

AAVSO. 2012, VPhot AAVSO photometric software (https://www.aavso.org/vphot).

Applegate, J. H. 1989, *Astrophys. J.*, **337**, 865.

Applegate, J. H. 1992, *Astrophys. J.*, **385**, 621.

Ballesteros, F. J. 2012, *Europhys. Lett.*, **97**, 34008.

Blitzstein, W. 1950, *Astron. J.*, **55**, 165.

Blitzstein, W. 1954, *Astron. J.*, **59**, 251.

Bradstreet, D. H., and Steelman, D. P. 2004, Binary Maker 3, Contact Software (http://www.binarymaker.com).

Castelli, F., and Kurucz, R. L. 2004, arXiv:astro-ph/0405087v1.

Ciocca, M. 2013, *J. Amer. Assoc. Var. Star Obs.*, **41**, 134.

Ciocca, M. 2016, *J. Amer. Assoc. Var. Star Obs.*, **44**, 200.

Demircan, O., Akalin, A., Selam, S., Derman, E., and Mueyesseroglu, Z. 1995, *Astron. Astrophys., Suppl. Ser.*, **114**, 167.

Giuricin, G., Mardirossian, F., and Predolin, F. 1980, *Acta Astron.*, **30**, 561.

Halbedel, E. M. 1984, *Inf. Bull. Var. Stars*, No. 2549, 1.

Jetsu, L. 2020, arXiv:2006.00863v1 [astro-ph.SR].

Manzoori, D. 2016, *Astron. Lett.*, **42**, 329.

Myers, G. 2014, Transform Generator (TG) (https://www.aavso.org/tg).

Pecaut, M. J., and Mamajek, E. E. 2013, *Astrophys. J., Suppl. Ser.*, **208**, 9.

Pleiades Astrophoto, S.L. 2022, PixInsight (https://pixinsight.com/).

Reinhardt, M. W. 1967, *Astron. Nachr.*, **290**, 19.

Schlafly, E. F., and Finkbeiner, D. P. 2011, *Astrophys. J.*, **737**, 103.

Sekiguchi, M., and Fukugita, M. 2000, *Astron. J.*, **120**, 1072.

Shapley, H. 1923, *Bull. Harvard Coll. Obs.*, **790**, 1.

Silvis, G. 2015, Transform Applier (TA) (https://www.aavso.org/ta-release-notes).

Software Bisque. 2018, TheSkyX Professional Edition, 10.5.0 (https://www.bisque.com).

Southwest Research Institute (SwRI). 2022, Eclipsing Binaries (http://binaries.boulder.swri.edu/binaries/omc).

University of Iowa Department of Physics and Astronomy. 2017, Imaging the Universe Lab Manual (http://astro.physics.uiowa.edu/ITU/).

Vanmunster, T. 2013, light curve and period analysis software, Peranso v.2.50 (https://www.cbabelgium.com/peranso).

Watson, C., Henden, A. A., and Price, C. A. 2014, AAVSO International Variable Star Index VSX (Watson+, 2006–2014; https://www.aavso.org/vsx).

Wilson, R. E., and Devinney, E. J. 1971, *Astrophys. J.*, **166**, 605.

Wilson, R. E., and Van Hamme, W. 2014, *Astrophys. J.*, **780**, 151.

Yang, Y.-G. 2013, *New Astron.*, **25**, 109.

Zasche, P. 2016, *Open Eur. J. Var. Stars*, **176**. 10.

Spectral Classification of Algol C

Megan G. Frank
David G. Whelan
Jessica C. Junginger
Department of Physics, Austin College, Sherman, TX; dwhelan@austincollege.edu

Received April 28, 2022; revised May 12, 2022; accepted May 12, 2022

Abstract The spectral classification of Algol C, the third star in the Algol triple system, has long been a matter of some uncertainty. There is good reason to suspect that it should be a metallic-line A-type star, and one study in particular showed that this was so, but further studies have cast doubt on that assessment. We utilized a simple spectral subtraction method between spectra taken in and out of primary eclipse to reveal the light of Algol C in the absence of the light from the brightest star. Our resultant spectrum is well-matched to an F1 V spectroscopic standard and shows no evidence of metallic-line spectral anomalies. We note that this classification matches recent abundance determinations for this source.

1. Introduction

Algol (β Persei) is a hierarchical triple system in which Algols A and B are the eponymous eclipsing pair. Algol B, the less massive secondary, is physically large, filling its Roche lobe and losing mass to the primary. The orbital period of Algols A and B is a short 2.87 days. The third component of the system, Algol C, has an orbital period of 680 days around the binary pair (Zavala *et al.* 2010).

Algol A is by far the brightest star in the system, contributing $\gtrsim$94% of the light at visual wavelengths (Kolbas *et al.* 2015). Algol C is the next brightest, contributing $\gtrsim$5% of the system's light. The dimmest component of the system is Algol B, which contributes $\lesssim$0.8% of the system's light. During primary eclipse, the majority of Algol A is covered up by Algol B. This causes spectral absorption lines from Algol C to become prominent, allowing for identification of the star's spectral type.

The spectral type for Algol C seems uncertain from the literature. Hall (1939) claimed it was approximately an A5 V star, while Meltzer (1957) approximated F5 V based on absorption line ratios. Other spectral types (e.g., Struve and Sahade 1957) were approximate, and while many attempts were made to answer this simple question none could be more precise. Fletcher (1964) determined that Algol C was a metallic-line A-type (Am) star, specifically with a spectral type of kA4^{h}A9.5^{m}F0 for the spectral classes of the Ca II K line, hydrogen Balmer lines, and metal lines, respectively. The presented evidence for this spectral type included that the Sr II λ4077, λ4216, and Ca I λ4226 lines were all slightly strong for an A9.5 star, and that the Ca II K line was particularly weak, which is common for Am stars. The strengths of these lines relative to the Fe I lines, as well as a magnitude difference between Algols A and C ($\delta M_{ac} = 2.6$), were used as supporting evidence.

Physical considerations justify an Am designation for Algol C. Algol C is a very slowly-rotating star, with a rotational speed of $\approx$12 km s^{-1} (Kolbas *et al.* 2015). Meridional circulation is responsible for chemical mixing in A- and F-type stars that do not have convection zones near the surface, and the star must be rotating at $\gtrsim$90 km s^{-1} for this effect to take place (Charbonneau 1993). All the Am stars have slower rotation rates than this, though it should be noted that not all slowly-rotating A- and F-type stars are Am stars (Abt and Levy 1985). However, nearly all Am stars are part of close binaries in which the Am star is in synchronous rotation (Gray and Corbally 2009). Algol C is not in synchronous rotation (using the rotation speed from Kolbas *et al.* 2015), so other evidence is needed to confirm that Algol C is an Am star.

Richards *et al.* (1987) determined that the spectral type for Algol C is F 1 ± 1. They particularly noted that the Ca II K line was only marginally weak for the spectral type, contrary to Fletcher's (1964) findings. Richards *et al.* (1988) followed up with a temperature for Algol C of 7500 ± 500 K, consistent with a late A- or early F-type star. Later, Richards (1993) compared the metal line ratios for Algol C to four other stars (spectral types A7 V to F5 V) using Mn I λ4030, Fe I λ4046, Ca I λ4226, and Fe II λ4233. They showed that the metal line ratios for Algol C were consistent with an F1 or F2 spectral type, with the exception of the Calcium line, which was underabundant. However, their analysis of the Balmer line profiles suggested a temperature of 7500 K, which is too hot for an early F-type star but consistent with their earlier study. Their analysis of the Balmer lines therefore suggests an earlier spectral type than does their abundance analysis.

The most recent study of the metal abundances of Algol C is found in Kolbas *et al.* (2015). This work disentangles the spectra of the three components in the frequency domain, so that spectral absorption lines are perfectly preserved for each component's spectrum. They measured the abundances of twenty-two elements for Algol C and compared them to solar abundances and the abundances of chemically normal and Am-type stars from the Hyades open cluster study of Gebran *et al.* (2010). They show that Algol C has a roughly solar abundance for all elements measured, and of particular note is the fact that they do *not* see any underabundance of Calcium in its spectrum.

We present a spectrum of Algol C that we then use for spectral classification. Section 2 discusses the observations and data reduction, section 3 examines the methods used to isolate the spectrum of Algol C, section 4 presents the analysis of our final spectrum, and we conclude in section 5.

2. Observations and data reduction

Low-resolution spectra were obtained using a Lhires III long-slit spectrograph, built by Shelyak, on the Adams Observatory 24-inch f/8 telescope at Austin College. The CCD used to capture the spectra is an e2v 42–10 with 13.5 µm pixels. The spectrograph is in the Littrow configuration with a 35 µm slit, which measures 1.5" on the sky. We used a 1200 gr/mm grating for a dispersion of 0.54 Å/pixel. The resolution of the spectrograph is therefore 1.4 Å. Observations were taken between 2020 August 14 and 2020 October 13; a log of observations is shown in Table 1 with dates, times, number of spectra secured per observing session, the range in airmass, and the range of orbital phase of the Algol AB system at the time of the observations. Observation dates and times were chosen to observe the system at every tenth of the Algol AB orbital phase. Exposure time was 30 seconds per image.

Data were reduced using standard procedures written in Python. Science images were bias- and dark-subtracted, and flatfield-corrected using images taken with an integrated flat-field lamp. Each spectrum was extracted by first fitting a Gaussian curve to the dispersion profile to find its location and width. Pixel values within two standard deviations of the mean were summed, and sky emission was subtracted based on the average values of the sky on either side of the extraction window at each wavelength. The signal-to-noise ratio was computed at each wavelength using the CCD equation. Wavelength calibration was performed by manually identifying the positions of five absorption lines of known wavelength in air in the extracted spectrum and fitting the correlation between pixel number and wavelength value with a quadratic function. Rectified spectra were created by dividing by the continuum that was calculated by fitting a cubic spline between hand-picked continuum points.

Table 1. Observational log.

Date	*Time Range*	*No. of Spectra*	*Sec Z Range*	*Phase Range*
2020-08-14	08:32–09:08	3	1.344–1.223	0.31–0.32
2020-08-18	08:11–10:32	12	1.366–1.044	0.70–0.73
2020-08-20	08:13–10:06	12	1.326–1.063	0.40–0.43
2020-09-08	05:34–09:39	86	1.812–1.021	0.99–0.04
2020-09-18	06:21–08:01	14	1.317–1.078	0.49–0.51
2020-09-25	04:15–04:44	6	1.920–1.678	0.90
2020-09-26	06:57–08:15	10	1.131–1.030	0.28–0.30
2020-09-27	04:16–04:58	6	1.838–1.540	0.59–0.60
2020-10-06	07:07–08:57	9	1.057–1.012	0.77–0.80
2020-10-07	04:17–06:07	11	1.547–1.146	0.08–0.11
2020-10-13	05:04–06:15	10	1.247–1.088	0.19–0.20

3. Method of spectral subtraction

3.1. Method development

Spectral disentanglement in Fourier space has become a common method for isolating components of complex spectra (e.g., Hadrava 1995). But this method requires high spectral resolution, so that individual spectral absorption lines can be resolved and their components can be separated. Our resolution of 1.4 Å is far too large to resolve lines from Algol A and C, whose radial velocity difference is never more than 77 km/s (Kolbas *et al.* 2015).

A method for determining the spectral classification of companion stars in binary systems using low-resolution spectra was described in Griffin and Griffin (1986). One component of the binary is spectroscopically classified, and then the spectrum of a standard star of that class is subtracted from the spectrum of the binary. This should leave only light from the other component, which can then be classified in its own right.

The trouble is that Algol was long considered a B8 V spectroscopic standard in its own right (e.g., Cannon and Pickering 1918; Morgan *et al.* 1943), and is still used that way on occasion today (e.g., in the library of standard spectra for the expert classifying program MKCLASS; Gray and Corbally 2014). The most commonly used B8 V standard in the northern hemisphere today is a high rotation-rate star, 18 Tau (Garrison and Gray 1994; Gray and Corbally 2009), whose absorption lines are significantly wider than are Algol's. This would present serious issues when subtracting the two spectra. The other accepted standard, HR 9050, has narrower lines but is only visible from more southern latitudes. Therefore we do not have a suitable standard star with which to perform a spectral subtraction.

Our solution is to subtract a scaled spectrum of Algol taken when it is out of eclipse from a spectrum of Algol when it is in primary eclipse. This is tantamount to removing the light from Algol A, leaving only the light from Algols B and C, because Algol A is by far the brightest star in the system (see section 1; what little light from Algol B that will remain in this final spectrum should be negligible because it is so dim). Representative rectified spectra of Algol taken in and out of eclipse are shown in Figure 1, labeled with the orbital phases at which they were observed. Several differences between the two spectra reveal tantalizing facts about the spectrum of Algol C. These include the stronger Ca II K line, the weaker He I λ4026 line, the stronger metal lines throughout the spectrum, and the change in the ratio of the He I λ4471 and Mg II λ4481 lines.

Subtracting a scaled spectrum of Algol A from the spectrum taken during primary eclipse requires that we determine the scale factor that correctly represents the contribution of Algol A to the total light of the spectrum. We will show some algebra that suggests the range of possible scale values, and we will also show the effect of choosing different scale factors on the final spectrum.

But first we must confront the major issue of how to treat the spectral continuum. Figure 2 illustrates what happens when we subtract continuum-rectified spectra. The subtracted spectra were those shown in Figure 1 and they were scaled appropriately before they were subtracted. This procedure should have resulted in a spectrum that effectively only included light from Algol C. When we compare the subtracted spectrum of "Algol C" to an F0 V spectral standard, however, we see that the strengths of the metal lines in the Algol spectrum vary with wavelength, when compared with the standard, appearing weakest at shorter wavelengths. This makes it appear as if "Algol C" has a spectral type that is earlier than F0 at shorter wavelengths, but later than F0 at longer wavelengths!

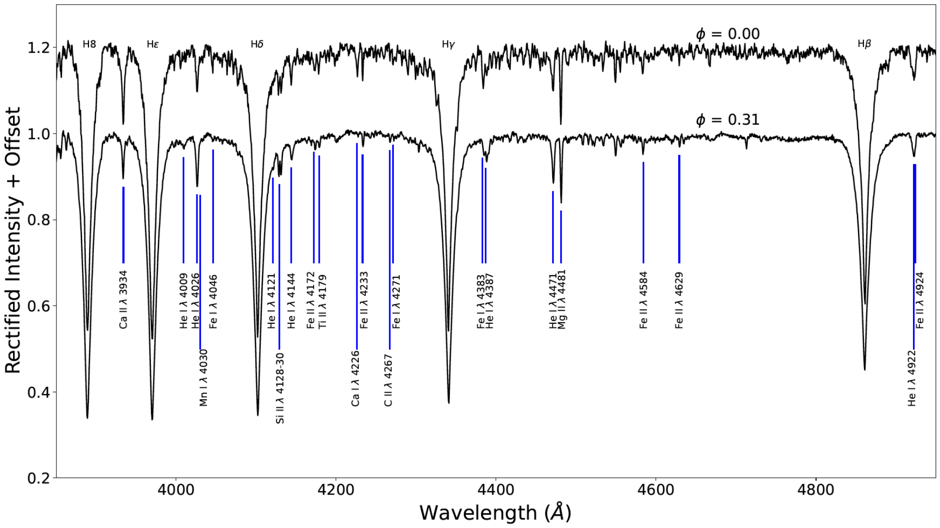

Figure 1. Rectified spectra of Algol taken during primary eclipse (φ = 0.00) and at a phase angle out of eclipse (φ = 0.31), offset by 0.2 unit for clarity. Numerous absorption lines useful in spectrally classifying B-, A-, and F-type stars are labeled.

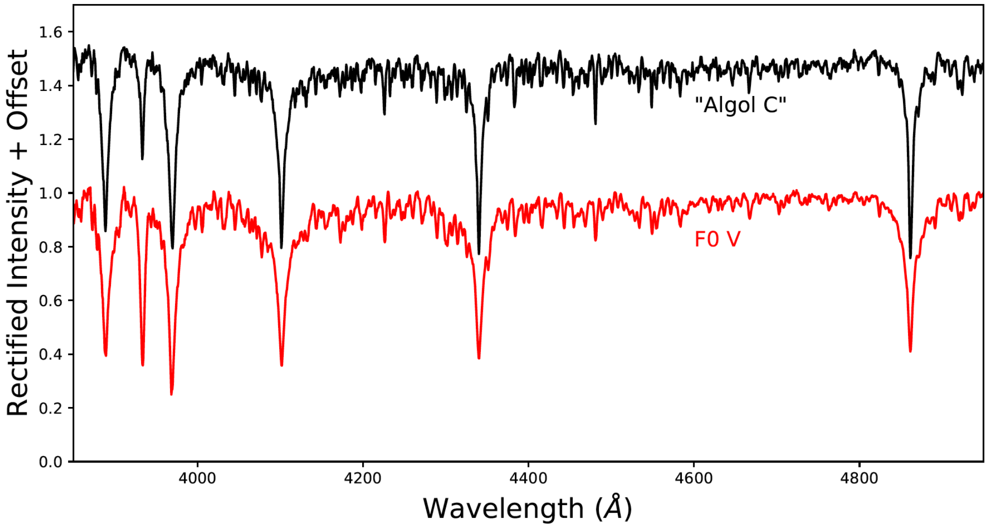

Figure 2. This spectrum of "Algol C" (top) was created by subtracting the rectified spectra shown in Figure 1. The standard star spectrum is that of F0 V spectral standard HD 23585 (bottom).

The ultimate reason for the line strength's apparent function with wavelength is that the slopes of the two spectra are different. During primary eclipse a majority of Algol A's light is being blocked by Algol B, greatly reducing the contribution of Algol A to the overall spectrum. This not only affects the strengths of the lines in the spectrum taken during primary eclipse (as illustrated in Figure 1) but also the shape of the continuum, because the cooler stars now contribute more to the overall light of the spectrum.

3.2. The finalized method

We must therefore subtract un-rectified spectra. An extracted, a background-subtracted but otherwise uncalibrated spectrum possesses a continuum that is determined by the starlight extincted by the Earth's atmosphere, and altered according to the spectral response of our instrumentation. Without detailed knowledge concerning the atmospheric extinction or the spectral response function, these factors cannot be removed accurately. But observing Algol in and out of eclipse at similar airmass allows us to assume that the atmospheric extinction is constant. We must also assume that the spectral response is the same for each spectrum.

Given these constraints, we chose spectra taken near phase angle φ = 0.31 at an airmass of sec z = 1.30, to subtract from spectra taken at φ = 0.00 (sec z = 1.45). We averaged ten individual spectra taken at each phase to increase the signal-to-noise ratio, so that the subtracted spectrum would show absorption lines into the ultraviolet, where the spectrum is lowest signal-to-noise. Figure 3 shows the two spectra, normalized so that they overlap near 4400 Å. These are the same spectra that were first shown in Figure 1, but now with their continua. The spectrum from φ = 0.31 exhibits more light in the ultraviolet than does the spectrum from φ = 0.00. This is expected, since the majority of the UV light from Algol comes from Algol A, which is being blocked during primary eclipse.

Now we must estimate the scale factor by which the φ = 0.31 spectrum will be multiplied. Our spectral range is fairly close to the bandwidth of the Johnson B-band, so we begin by using the $\Delta m_B \approx 1.2$ that is shown in Kim (1989) for primary eclipse. This magnitude difference equates to a flux ratio $F_{eclipse} / F_{total} \approx 0.33$.

The total flux in the B-band is composed of light from stars A, B, and C; i.e., $F_{total} = F_A + F_B + F_C$. The observed flux during primary eclipse can be given by $F_{eclipse} \approx 0.33\,F_{total} = Y F_A + F_B + F_C$, where Y is the fraction of the flux still visible from star A, representing how much light from star A remains during primary eclipse. The contribution of light from star A during primary eclipse to the total light during primary eclipse we call our scale factor SF and is written:

$$SF = \frac{YF_A}{Y\,F_A + F_B + F_C} \tag{1}$$

which is reminiscent of the algebra used by Glushneva and Esipov (1968) to find the infrared spectrum of Algol C. This scale factor SF is applied to one spectrum before subtracting it from another, to properly remove light from Algol A in the spectrum. We assume that the φ = 0.31 spectrum is entirely that of Algol A because that star contributes ~95% of the total light of the system at these wavelengths, and that the φ = 0.00 spectrum is that of Algols A, B, and C combined. This means that the scale factor is applied to the φ = 0.31 spectrum before it is subtracted from the φ = 0.00 spectrum.

Determining the scale factor SF therefore depends on knowing the fractional fluxes of each star in the system. The photometric study by Kim (1989) suggested that the fraction of light from stars A, B, and C in the B-band is {0.854, 0.040, 0.106}, respectively, whereas the spectroscopic study of Kolbas *et al.* (2015) suggested fractions in the same waveband of {0.943, 0.008, 0.049}. Various other authors have calculated fractions somewhere between these two sets of values. This provides us with a rough range of possible fractional fluxes. Setting $F_A = 0.85$ on the low end of this range from Kim (1989), then Y = 0.21 (using $F_{eclipse} \approx 0.33\,F_{total} = Y\,F_A + F_B + F_C$ from above), and we determine a value SF = 0.54. For $F_A = 0.95$ on the high end of this range from Kolbas *et al.* (2015), we compute Y = 0.29 and SF = 0.85.

The choice of the scale factor will have a serious impact on the final interpretation of the spectrum of Algol C. Figure 4 shows spectra of Algol C that were computed with scale factors ranging from 0.55 to 0.85, in increments of 0.05, bracketing the most likely set of values as determined in the previous paragraph. Each spectrum is plotted with an F1V standard star spectrum overplotted for comparison. Changing the scale factor varies several aspects of the spectrum. Most notable is that the strengths of the metal lines are correlated to the scale factor value. The effect of this correlation is most pronounced at shorter wavelengths, and the Ca II K line is extremely sensitive. The depth of the Balmer lines is also correlated with scale factor, but this effect is only noticeable from scale factors of about 0.70 and above. The widths of the Balmer line wings is the most noticeable feature in the spectrum that is *anti*-correlated with the scale factor because the lines become narrower as the scale factor is increased.

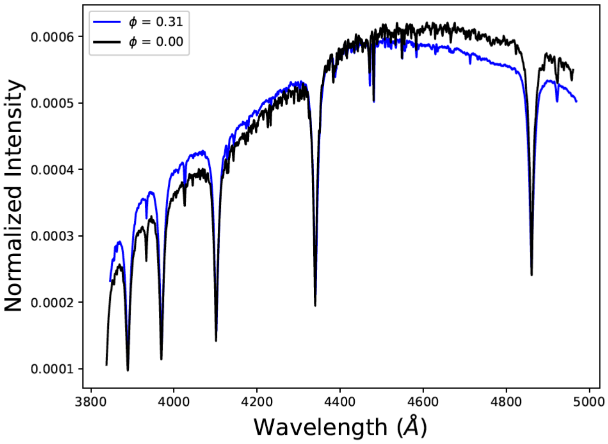

Figure 3. Extracted spectra plotted in ADUs taken at primary eclipse (labeled φ = 0.00) and outside of eclipse (labeled φ = 0.31), normalized.

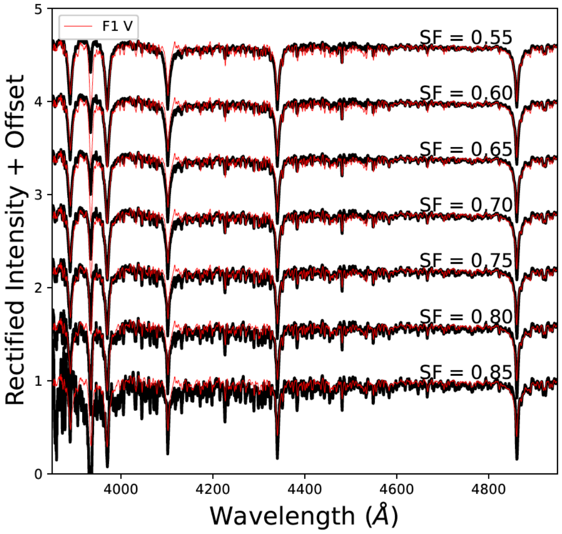

Figure 4. The two spectra shown in Figure 3 are subtracted after the φ = 0.31 spectrum is scaled by the scale factor SF; the results of subtraction for SF values ranging from 0.55 to 0.85 are shown plotted against an F1 V spectral standard.

For the purposes of this investigation, it was decided that an iterative approach was best, whereby a scale factor is applied and then the resultant spectrum is compared to standard star spectra. The comparison is then used to inform a change to the scale factor, after which the procedure is performed over again. When comparing the spectrum of Algol C to the standards, it was further decided that the Balmer lines alone would be used to judge the scale factor choice. This was decided for two reasons. First, the fact that the Balmer line depths and line widths behave oppositely to the scale factor (line depths increase with scale factor while line widths decrease) means that it is possible to find a unique fit to a standard star spectrum using Balmer lines alone. Second, by relying solely on the Balmer lines to determine spectral type we are able to test whether Algol C is an Am star without inviting circular logic into our result, whereby the metal lines are used to judge whether the scale factor choice is optimized. Such logic would only return a result that we were intending to find from the outset.

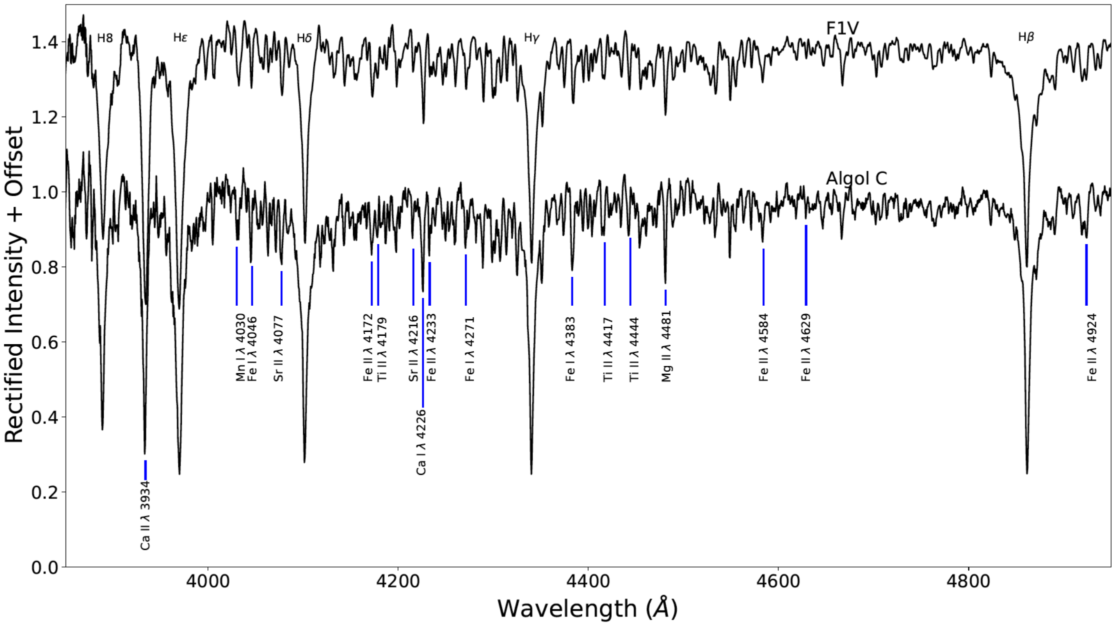

Figure 5. The final spectrum of Algol C (bottom) compared to an F1 V comparison spectrum (top). Numerous lines useful in classifying F-type stars are shown.

4. Analysis of the Algol C spectrum

Figure 5 shows the final spectrum for Algol C. We used a scale factor of SF = 0.76, corresponding to a fraction of the flux still visible from star A during primary eclipse of Y = 0.27.

Notably, we do not see any spectral characteristics that would be considered unique to the spectrum of Algol B. This includes the strengths of the Cr I λ4254 and Fe I lines at λ4250 and λ4260, as well as the Mn I λ4030, all of which would be much stronger if Algol B were contributing substantially to the subtracted spectrum. This was not a surprise: Algol B is a K2 IV star and, being red, is not expected to contribute much light to the ultraviolet-blue portion of the spectrum, where we are studying. The disentangled spectrum of Algol B exhibited in Kolbas *et al.* (2015) shows very weak spectral lines in this wavelength range, so we should not expect much contribution from this source. We ignore Algol B for the remainder of our analysis.

The metal lines in the spectrum of Algol C all appear narrow, consistent with its slow rotation rate. The F1 V spectral standard, 37 UMa, with a rotational speed of 87 km s^{-1} (Garcia Lopez *et al.* 1993), has similarly narrow lines. Since the resolution of our spectra is 1.4 Å ≈ 100 km s^{-1}, the width of the lines in both spectra is set by the instrument profile without additional Doppler broadening due to rotation. This is helpful in our analysis, because it allows us to directly compare the spectra shown without having to make corrections for line depths due to different stellar rotation speeds.

The spectrum of Algol C showcases hydrogen Balmer lines that are consistent with an F1 V spectral classification. The metallic line spectrum also appears to be consistent with this spectral type—the strong absorption lines labeled as well as the weaker lines generally—making allowances for the slightly noisier spectrum of Algol C. Most notably when looking for characteristics of Am stars, the Ca II K and Ca I λ4226 lines do not appear weak, and the Sr II λ4077 and λ4216 lines are not strong for the metallic-line spectral type.

The evidence from the literature that suggests Algol C is an Am star requires a closer look. Fletcher (1964) claimed that the Ca II K line was five spectral classes earlier than the Balmer lines, which would be consistent with expectations for Am stars generally. They also claimed that the metal lines were half a spectral type later than were the hydrogen lines, specifically noting that the lines Sr II λ4077, λ4216 and Ca I λ4226 were all slightly strong. This, however, does not make sense for the spectrum from an Am star. The strength of the Ca I λ4226 line is usually weak compared to the metal line spectrum, though not as weak as the Ca II K line. The Sr II lines, however, are usually stronger (later) than even the metal line spectrum (Gray and Corbally 2009). It would therefore appear that Fletcher (1964) made a mistake. Considering the weak Ca II K line in our "Algol C" spectrum from Figure 2, we suspect it is possible that their fault was in the treatment of the spectral continuum.

Richards (1993) showed evidence for a low Calcium abundance in their spectrum of Algol C. But it also appears that they did not fully trust their abundance analysis, because they classify the star as type F1 V in their Table 1 while referring to it as a "marginal Am star" in the text. They label its spectral classification F1 V again in Richards *et al.* (2012) without further explanation. When we additionally consider that the Calcium abundance determined by Kolbas *et al.* (2015) was normal, it seems increasingly clear that the current result is the correct one, and that Algol C is an F1 V star.

We would like to exhaust all possibilities before concluding. Perhaps the spectrum of Algol C has changed since Fletcher's (1964) observations. This is an intriguing thought, since Richards (1993) showed evidence of a low calcium abundance for Algol C, but not to the extreme that Fletcher's results implied. Such a finding would be reasonable if Algol C were gradually transitioning from an Am star to a normal star over the course of the last sixty years.

However, it seems unlikely that the spectrum has changed significantly over the past sixty years; Am stars identified in the early spectroscopic literature remain so today. An example is the prototypical Am star 63 Tau, which was first identified as a chemically peculiar star in Titus and Morgan (1940) and as an Am star in Morgan *et al.* (1943), where the Am class was codified. The Am designation for 63 Tau has remained since, with only minor adjustments (e.g., Abt and Morrell 1995).

5. Conclusion

We have used a spectral subtraction technique to classify Algol C. We have observed the Algol system in and out of primary eclipse and, having scaled the spectra to one another appropriately, were able to recover a spectrum for Algol C without contamination from Algol A. Our result is that Algol C has the spectrum of an F1 V star; most notably, we see no sign that it possesses the qualities of a metallic-line star. Our result confirms a recent chemical abundance analysis.

References

Abt, H. A., and Levy, S. G. 1985, *Astrophys. J., Suppl. Ser.*, **59**, 229.

Abt, H. A., and Morrell, N. I. 1995, *Astrophys. J., Suppl. Ser.*, **99**, 135.

Cannon, A. J., and Pickering, E. C. 1918, *Ann. Harvard Coll. Obs.*, **91**, 1.

Charbonneau, P. 1993, in *Peculiar versus Normal Phenomena in A-type and Related Stars*, eds. M. M. Dworetsky, F. Castelli, R. Faraggiana, IAU Colloq. 138, Astronomical Society of the Pacific, San Francisco, CA, 474.

Fletcher, E. S. 1964, *Astron. J.*, **69**, 357.

Garcia Lopez, R. J., Rebolo, R., Beckman, J. E., and McKeith, C. D. 1993, *Astron. Astrophys.*, **273**, 482.

Garrison, R. F., and Gray, R. O. 1994, *Astron. J.*, **107**, 1556.

Gebran, M., Vick, M., Monier, R., and Fossati, L. 2010, *Astron. Astrophys.*, **523**, A71.

Glushneva, I. N., and Esipov, V. F. 1968, *Soviet Ast.*, **11**, 828.

Gray, R. O., and Corbally, C. J. 2009, *Stellar Spectral Classification*, Princeton University Press, Princeton, NJ.

Gray, R. O., and Corbally, C. J. 2014, *Astron. J.*, **147**, 80.

Griffin, R., and Griffin, R. 1986, *J. Astrophys. Astron.*, **7**, 195.

Hadrava, P. 1995, *Astron. Astrophys., Suppl. Ser.*, **114**, 393.

Hall, J. S. 1939, *Astrophys. J.*, **90**, 449.

Kim, H.-I. 1989, *Astrophys. J.*, **342**, 1061.

Kolbas, V., *et al.* 2015, *Mon. Not. Roy. Astron. Soc.*, **451**, 4150.S

Meltzer, A. S. 1957, *Astrophys. J.*, **125**, 359.

Morgan, W. W., Keenan, P. C., and Kellman, E. 1943, *An Atlas of Stellar Spectra, with an Outline of Spectral Classification*, The University of Chicago press, Chicago.

Richards, M. T. 1993, *Astrophys. J., Suppl. Ser.*, **86**, 255.

Richards, M. T., Agafonov, M. I., and Sharova, O. I. 2012, *Astrophys. J.*, **760**, 8.

Richards, M. T., Bolton, C. T., and Mochnacki, S. W. 1987, *Bull. Amer. Astron. Soc.*, **19**, 1036.

Richards, M. T., Mochnacki, S. W., and Bolton, C. T. 1988, *Astron. J.*, **96**, 326.

Struve, O., and Sahade, J. 1957, *Publ. Astron. Soc. Pacific*, **69**, 41.

Titus, J., and Morgan, W. W. 1940, *Astrophys. J.*, **92**, 256.

Zavala, R. T., Hummel, C. A., Boboltz, D. A., Ojha, R., Shaffer, D. B., Tycner, C., Richards, M. T., and Hutter, D. J. 2010, *Astrophys. J., Lett.*, **715**, L44.

Recent Maxima of 78 Short Period Pulsating Stars

Gerard Samolyk
P.O. Box 20677, Greenfield, WI 53220; gsamolyk@wi.rr.com

Received January 21, 2022; accepted January 21, 2022

Abstract This paper contains times of maxima for 78 short period pulsating stars (primarily RR Lyrae and δ Scuti stars). These times of maxima represent the CCD observations received by the AAVSO Short Period Pulsator (SPP) Section in 2021.

1. Recent observations

Table 1 contains times of maxima calculated from CCD observations made by participants in the AAVSO's Short Period Pulsator (SPP) Section. This list will be web-archived and made available through the AAVSO ftp site at:

ftp:ftp.aavso.org/public/datasets/gsamj501spp78.txt .

The error estimate is included. RR Lyr stars in this list, along with data from earlier AAVSO publications, are included in the GEOS database at:

http://rr-lyr.irap.omp.eu/dbrr/ .

This database does not include δ Scuti stars. These observations were reduced by the writer using the Peranso program (Vanmunster 2007). Column F indicates the filter used. A "C" indicates a clear filter.

The linear elements in the *General Catalogue of Variable Stars* (GCVS; Kholopov *et al.* 1985) were used to compute the O–C values for most stars. For a few exceptions where the GCVS elements are missing or are in significant error, light elements from another source are used: V799 Aur, V377 Boo, V876 Cep, V873 Her, and KP Lyn (AAVSO VSX site; Watson *et al.* 2014)); VY CrB (Antipin 1996); DG Hya (Samolyk 2010); V2416 Cyg (Samolyk 2018); and V355 Cam and GO Hya (GEOS database (2021)).

References

Antipin, S. V. 1996, *Inf. Bull. Var. Stars*, No. 4343, 1.
Groupe Européen d'Observation Stellaire (GEOS). 2021, GEOS RR Lyr Database, (http://rr-lyr.irap.omp.eu/dbrr/index.php).
Kholopov, P. N., *et al.* 1985, *General Catalogue of Variable Stars*, 4th ed., Moscow.
Samolyk, G. 2010, *J. Amer. Assoc. Var. Star Obs.*, **38**, 12.
Samolyk, G. 2018, *J. Amer. Assoc. Var. Star Obs.*, **46**, 70.
Vanmunster, T. 2021, light curve and period analysis software, Peranso v.2.50 (http://www.cbabelgium.com/peranso).
Watson, C., Henden, A. A., and Price, C. A. 2014, AAVSO International Variable Star Index VSX (Watson+, 2006–2014; https://www.aavso.org/vsx).

Table 1. Recent times of maxima of stars in the AAVSO Short Period Pulsator program.

Star	JD (max) Hel. 2400000 +	Cycle	O–C (day)	F	Observer	Error (day)
SW And	59213.3831	92885	-0.5355	V	T. Arranz	0.0009
SW And	59214.2671	92887	-0.5360	V	T. Arranz	0.0008
SW And	59221.3426	92903	-0.5370	V	T. Arranz	0.0007
SW And	59229.3019	92921	-0.5387	V	T. Arranz	0.0009
SW And	59233.2828	92930	-0.5383	V	T. Arranz	0.0008
SW And	59244.3371	92955	-0.5410	V	T. Arranz	0.0008
SW And	59502.6198	93539	-0.5495	V	G. Samolyk	0.0008
SW And	59503.5037	93541	-0.5502	V	T. Arranz	0.0007
SW And	59512.3483	93561	-0.5512	V	T. Arranz	0.0006
SW And	59527.3854	93595	-0.5516	V	T. Arranz	0.0007
SW And	59531.3653	93604	-0.5522	V	T. Arranz	0.0007
SW And	59566.3037	93683	-0.5539	V	T. Arranz	0.0007
XX And	59462.6981	28191	0.2961	V	G. Samolyk	0.0014
AC And	59441.6324	15383	0.4745	V	G. Samolyk	0.0021
AC And	59443.7486	15386	0.4570	V	G. Samolyk	0.0016
AC And	59446.7504	15390	0.6138	V	G. Samolyk	0.0018
AC And	59510.4398	15480	0.2916	V	T. Arranz	0.0024
AC And	59528.3972	15505	0.4680	V	T. Arranz	0.0023
AC And	59553.3777	15540	0.5551	V	T. Arranz	0.0017
AT And	59446.7692	27724	0.0042	V	G. Samolyk	0.0016
AT And	59503.5153	27816	-0.0059	V	T. Arranz	0.0016
AT And	59513.3853	27832	-0.0065	V	T. Arranz	0.0009
DM And	59568.4120	37835	0.2132	V	T. Arranz	0.0007
GM And	59468.8379	47863	0.0458	V	K. Menzies	0.0012
SW Aqr	59459.6867	74814	0.0015	V	G. Samolyk	0.0007
SW Aqr	59479.4359	74857	0.0007	V	T. Arranz	0.0008
SW Aqr	59514.3441	74933	0.0018	V	T. Arranz	0.0007
TZ Aqr	59505.6250	38440	0.0161	V	G. Samolyk	0.0018
YZ Aqr	59465.7277	43667	0.0884	V	G. Samolyk	0.0018
AA Aqr	59514.5928	63667	-0.1982	V	G. Samolyk	0.0017
AA Aqr	59549.2965	63724	-0.2012	V	T. Arranz	0.0005
BO Aqr	59521.6227	25792	0.2430	V	G. Samolyk	0.0016
BR Aqr	59488.6838	45349	-0.2433	V	G. Samolyk	0.0011
CY Aqr	59465.6402	412154	0.0177	V	G. Samolyk	0.0004
CY Aqr	59465.7007	412155	0.0172	V	G. Samolyk	0.0003
CY Aqr	59465.7618	412156	0.0173	V	G. Samolyk	0.0003
CY Aqr	59465.8228	412157	0.0173	V	G. Samolyk	0.0003
CY Aqr	59465.8838	412158	0.0172	V	G. Samolyk	0.0004
CY Aqr	59468.7529	412205	0.0175	V	G. Samolyk	0.0004
CY Aqr	59468.8138	412206	0.0174	V	G. Samolyk	0.0004
CY Aqr	59468.8753	412207	0.0178	V	G. Samolyk	0.0004
CY Aqr	59474.6734	412302	0.0173	V	G. Samolyk	0.0003
CY Aqr	59474.7346	412303	0.0175	V	G. Samolyk	0.0004
CY Aqr	59474.7956	412304	0.0174	V	G. Samolyk	0.0004
CY Aqr	59474.8565	412305	0.0173	V	G. Samolyk	0.0004
CY Aqr	59495.3045	412640	0.0174	V	T. Arranz	0.0003
CY Aqr	59495.3661	412641	0.0180	V	T. Arranz	0.0004
CY Aqr	59495.4265	412642	0.0174	V	T. Arranz	0.0002
CY Aqr	59495.4875	412643	0.0173	V	T. Arranz	0.0003
RV Ari	59468.7981	262555	-0.0057	V	G. Samolyk	0.0006
RV Ari	59468.8926	262556	-0.0043	V	G. Samolyk	0.0011
RV Ari	59476.8109	262641	-0.0019	V	G. Samolyk	0.0012
RV Ari	59476.9069	262642	0.0010	V	G. Samolyk	0.0007
RV Ari	59484.8249	262727	0.0031	V	G. Samolyk	0.0007
RV Ari	59484.9084	262728	-0.0065	V	G. Samolyk	0.0005
RV Ari	59504.7521	262941	0.0008	V	G. Samolyk	0.0008
RV Ari	59504.8383	262942	-0.0061	V	G. Samolyk	0.0006
RV Ari	59504.9313	262943	-0.0062	V	G. Samolyk	0.0009
RV Ari	59506.7050	262962	-0.0020	V	G. Samolyk	0.0006
RV Ari	59506.7926	262963	-0.0075	V	G. Samolyk	0.0007
RV Ari	59506.8910	262964	-0.0022	V	G. Samolyk	0.0011
RV Ari	59521.6956	263123	-0.0050	V	G. Samolyk	0.0009
RV Ari	59521.7951	263124	0.0014	V	G. Samolyk	0.0007
RV Ari	59521.8832	263125	-0.0037	V	G. Samolyk	0.0006
RV Ari	59528.5860	263197	-0.0061	V	G. Samolyk	0.0007
RV Ari	59528.6821	263198	-0.0031	V	G. Samolyk	0.0011
RV Ari	59528.7792	263199	0.0008	V	G. Samolyk	0.0009
RV Ari	59540.5978	263326	-0.0078	V	G. Samolyk	0.0004
RV Ari	59540.6943	263327	-0.0045	V	G. Samolyk	0.0009
RV Ari	59540.7965	263328	0.0046	V	G. Samolyk	0.0011
RV Ari	59540.8796	263329	-0.0054	V	G. Samolyk	0.0005
RV Ari	59546.6515	263391	-0.0075	V	G. Samolyk	0.0006
RV Ari	59546.7547	263392	0.0026	V	G. Samolyk	0.0011
TZ Aur	59242.6410	100441	0.0186	V	G. Samolyk	0.0010
TZ Aur	59283.3741	100545	0.0175	V	T. Arranz	0.0008
TZ Aur	59523.8624	101159	0.0176	V	G. Samolyk	0.0008
BH Aur	59269.4021	36216	0.0119	V	T. Arranz	0.0008
BH Aur	59293.5749	36269	0.0119	V	K. Menzies	0.0011
BH Aur	59518.8844	36763	0.0131	V	G. Samolyk	0.0015
V799 Aur	59244.2968	66270	0.0072	V	T. Arranz	0.0005
V799 Aur	59244.3712	66271	0.0055	V	T. Arranz	0.0005
V799 Aur	59273.3651	66652	0.0062	V	T. Arranz	0.0004
V799 Aur	59273.4410	66653	0.0060	V	T. Arranz	0.0004
V799 Aur	59273.5181	66654	0.0070	V	T. Arranz	0.0005
RS Boo	59327.6616	46529	-0.0329	V	G. Samolyk	0.0008
RS Boo	59347.6555	46582	-0.0379	V	G. Samolyk	0.0009
RS Boo	59351.4326	46592	-0.0342	V	T. Arranz	0.0009
RS Boo	59360.4853	46616	-0.0377	V	T. Arranz	0.0009
RS Boo	59368.4103	46637	-0.0368	V	T. Arranz	0.0008
RS Boo	59371.4307	46645	-0.0351	V	T. Arranz	0.0008
RS Boo	59394.4435	46706	-0.0400	V	T. Arranz	0.0008
ST Boo	59321.8223	64504	0.0978	V	G. Samolyk	0.0019
ST Boo	59340.4959	64534	0.1027	V	T. Arranz	0.0009
ST Boo	59355.4440	64558	0.1158	V	T. Arranz	0.0012
ST Boo	59360.4264	64566	0.1199	V	T. Arranz	0.0010
ST Boo	59373.4968	64587	0.1222	V	T. Arranz	0.0008
ST Boo	59393.4127	64619	0.1248	V	T. Arranz	0.0007
ST Boo	59406.4809	64640	0.1249	V	T. Arranz	0.0009
SW Boo	59238.9138	32457	0.5723	V	K. Menzies	0.0009
SW Boo	59289.7570	32556	0.5762	V	K. Menzies	0.0009
SW Boo	59348.8161	32671	0.5795	V	K. Menzies	0.0009
SW Boo	59354.4657	32682	0.5803	V	T. Arranz	0.0010
SW Boo	59371.4126	32715	0.5808	V	T. Arranz	0.0009
SZ Boo	59292.8034	60542	0.0161	V	G. Samolyk	0.0015
SZ Boo	59398.4106	60744	0.0137	V	T. Arranz	0.0012
TV Boo	59342.4988	111124	0.1375	V	T. Arranz	0.0011
TV Boo	59343.4366	111127	0.1376	V	T. Arranz	0.0012
TV Boo	59352.5031	111156	0.1399	V	T. Arranz	0.0012
TV Boo	59353.4366	111159	0.1357	V	T. Arranz	0.0014
TV Boo	59358.4125	111175	0.1107	V	T. Arranz	0.0012
TV Boo	59367.4768	111204	0.1107	V	T. Arranz	0.0009
TV Boo	59368.4200	111207	0.1163	V	T. Arranz	0.0016
TV Boo	59372.5088	111220	0.1418	V	T. Arranz	0.0014
TV Boo	59373.4249	111223	0.1202	V	T. Arranz	0.0016
TV Boo	59393.4301	111287	0.1216	V	T. Arranz	0.0018
TV Boo	59398.4250	111303	0.1156	V	T. Arranz	0.0015
TV Boo	59403.4292	111319	0.1188	V	T. Arranz	0.0017
TV Boo	59408.4251	111335	0.1138	V	T. Arranz	0.0009
TW Boo	59293.8145	60876	-0.1138	V	G. Samolyk	0.0011
TW Boo	59353.4267	60988	-0.1162	V	T. Arranz	0.0010
TW Boo	59361.4111	61003	-0.1159	V	T. Arranz	0.0009
UU Boo	59302.7417	50814	0.3734	V	G. Samolyk	0.0012
UU Boo	59369.4551	50960	0.3764	V	T. Arranz	0.0007
UU Boo	59390.4744	51006	0.3774	V	T. Arranz	0.0007
UY Boo	59327.7742	26875	0.8493	V	G. Samolyk	0.0014
UY Boo	59341.4390	26896	0.8465	V	T. Arranz	0.0008
UY Boo	59354.4548	26916	0.8456	V	T. Arranz	0.0008
V377 Boo	59355.4234	3386	0.0002	V	T. Arranz	0.0007
V377 Boo	59355.5136	3387	-0.0004	V	T. Arranz	0.0008
V377 Boo	59365.4014	3496	0.0001	V	T. Arranz	0.0004

Table continued on following pages

Table 1. Recent times of maxima of stars in the AAVSO Short Period Pulsator program, cont.

Star	*JD (max) Hel. 2400000 +*	*Cycle*	*O–C (day)*	*F*	*Observer*	*Error (day)*
V377 Boo	59365.4922	3497	0.0003	V	T. Arranz	0.0005
UY Cam	59238.7119	88651	-0.0976	V	K. Menzies	0.0041
UY Cam	59287.5810	88834	-0.0972	V	K. Menzies	0.0095
UY Cam	59518.8422	89700	-0.0947	V	G. Samolyk	0.0025
UY Cam	59526.8563	89730	-0.0919	V	G. Samolyk	0.0029
V355 Cam	59266.2641	35130	0.0335	V	A. Beck	0.0028
V355 Cam	59266.2681	35130	0.0375	I	A. Beck	0.0017
V355 Cam	59266.4821	35131	0.0330	V	A. Beck	0.0052
V355 Cam	59266.4877	35131	0.0386	I	A. Beck	0.0014
RW Cnc	59287.4696	36058	0.2541	V	T. Arranz	0.0014
RW Cnc	59321.3975	36120	0.2556	V	T. Arranz	0.0014
TT Cnc	59289.3925	34333	0.1172	V	T. Arranz	0.0012
TT Cnc	59537.8945	34774	0.1381	V	G. Samolyk	0.0011
RV Cap	59414.8275	57023	-0.1412	V	G. Samolyk	0.0007
RV Cap	59476.6101	57161	-0.1473	V	G. Samolyk	0.0011
V876 Cep	59469.5710	46116	-0.0508	V	T. Arranz	0.0014
RR Cet	59466.8549	47530	0.0234	V	G. Samolyk	0.0012
RR Cet	59502.7989	47595	0.0206	V	G. Samolyk	0.0013
RV Cet	59555.6492	32791	0.2784	V	G. Samolyk	0.0015
TY Cet	59504.7982	24956	0.0001	V	G. Samolyk	0.0033
UU Cet	59560.5206	30280	-0.1881	V	G. Samolyk	0.0019
S Com	58942.6649	31177	-0.1144	TG	G. Conrad	0.0017
VY CrB	59468.5766	38216	-0.1982	V	K. Menzies	0.0009
XX Cyg	59334.6622	110327	0.0044	V	G. Samolyk	0.0005
XX Cyg	59370.6718	110594	0.0050	V	G. Samolyk	0.0005
XX Cyg	59370.8062	110595	0.0045	V	G. Samolyk	0.0005
XX Cyg	59397.6444	110794	0.0046	V	G. Samolyk	0.0005
XX Cyg	59397.7795	110795	0.0048	V	G. Samolyk	0.0008
XX Cyg	59440.6666	111113	0.0048	V	G. Samolyk	0.0006
XX Cyg	59464.6726	111291	0.0048	V	K. Menzies	0.0004
XZ Cyg	59352.7363	32636	-2.9249	V	G. Samolyk	0.0011
XZ Cyg	59366.7261	32666	-2.9361	V	G. Samolyk	0.0012
XZ Cyg	59381.6578	32698	-2.9388	V	G. Samolyk	0.0009
XZ Cyg	59409.6599	32758	-2.9387	V	G. Samolyk	0.0009
XZ Cyg	59414.7922	32769	-2.9401	V	G. Samolyk	0.0012
XZ Cyg	59421.7860	32784	-2.9468	V	G. Samolyk	0.0009
XZ Cyg	59428.7844	32799	-2.9489	V	G. Samolyk	0.0012
XZ Cyg	59433.4504	32809	-2.9499	V	T. Arranz	0.0006
XZ Cyg	59440.4539	32824	-2.9469	V	T. Arranz	0.0006
XZ Cyg	59442.7900	32829	-2.9443	V	G. Samolyk	0.0014
XZ Cyg	59443.7183	32831	-2.9494	V	G. Samolyk	0.0012
XZ Cyg	59444.6534	32833	-2.9477	V	G. Samolyk	0.0012
XZ Cyg	59446.5231	32837	-2.9448	V	T. Arranz	0.0009
XZ Cyg	59448.3867	32841	-2.9480	V	T. Arranz	0.0007
XZ Cyg	59461.4553	32869	-2.9470	V	T. Arranz	0.0006
XZ Cyg	59462.3881	32871	-2.9476	V	T. Arranz	0.0005
XZ Cyg	59469.3839	32886	-2.9523	V	T. Arranz	0.0005
XZ Cyg	59476.3787	32901	-2.9580	V	T. Arranz	0.0006
XZ Cyg	59512.3145	32978	-2.9581	V	T. Arranz	0.0005
XZ Cyg	59526.3089	33008	-2.9647	V	T. Arranz	0.0007
XZ Cyg	59540.2953	33038	-2.9793	V	T. Arranz	0.0006
DM Cyg	59366.8291	39976	0.0997	V	G. Samolyk	0.0009
DM Cyg	59382.7853	40014	0.1013	V	G. Samolyk	0.0009
DM Cyg	59429.8100	40126	0.1016	V	G. Samolyk	0.0014
DM Cyg	59432.7502	40133	0.1028	TG	G. Conrad	0.0015
DM Cyg	59463.3991	40206	0.1019	V	T. Arranz	0.0009
DM Cyg	59486.4924	40261	0.1029	V	T. Arranz	0.0008
DM Cyg	59492.3678	40275	0.1003	V	T. Arranz	0.0009
DM Cyg	59510.4251	40318	0.1036	V	T. Arranz	0.0009
DM Cyg	59513.3619	40325	0.1014	V	T. Arranz	0.0008
DM Cyg	59529.3189	40363	0.1037	V	T. Arranz	0.0008
DM Cyg	59537.2964	40382	0.1039	V	T. Arranz	0.0008
V2416 Cyg	59334.7008	102382	0.0034	V	G. Samolyk	0.0015
V2416 Cyg	59370.6340	103025	-0.0004	V	G. Samolyk	0.0018
V2416 Cyg	59370.6913	103026	0.0010	V	G. Samolyk	0.0014
V2416 Cyg	59370.7461	103027	-0.0002	V	G. Samolyk	0.0018
V2416 Cyg	59370.8032	103028	0.0010	V	G. Samolyk	0.0014
V2416 Cyg	59370.8604	103029	0.0024	V	G. Samolyk	0.0016
V2416 Cyg	59397.6272	103508	-0.0020	V	G. Samolyk	0.0015
V2416 Cyg	59397.6836	103509	-0.0015	V	G. Samolyk	0.0015
V2416 Cyg	59397.7408	103510	-0.0002	V	G. Samolyk	0.0016
V2416 Cyg	59397.8525	103512	-0.0002	V	G. Samolyk	0.0018
V2416 Cyg	59440.6086	104277	0.0002	V	G. Samolyk	0.0012
V2416 Cyg	59440.6623	104278	-0.0019	V	G. Samolyk	0.0017
V2416 Cyg	59464.6413	104707	0.0004	V	K. Menzies	0.0014
V2416 Cyg	59464.6981	104708	0.0014	V	K. Menzies	0.0014
RW Dra	59317.7816	45020	0.2673	V	G. Samolyk	0.0016
RW Dra	59376.7255	45153	0.3032	V	G. Samolyk	0.0017
RW Dra	59400.6153	45207	0.2755	V	T. Arranz	0.0012
RW Dra	59402.3860	45211	0.2745	V	T. Arranz	0.0015
RW Dra	59408.6071	45225	0.2948	V	T. Arranz	0.0010
RW Dra	59409.4965	45227	0.2983	V	T. Arranz	0.0009
RW Dra	59413.4925	45236	0.3081	V	T. Arranz	0.0009
RW Dra	59417.4824	45245	0.3117	V	T. Arranz	0.0007
XZ Dra	59364.7320	36593	-0.0967	V	G. Samolyk	0.0011
XZ Dra	59429.5423	36729	-0.0900	V	T. Arranz	0.0011
XZ Dra	59442.4038	36756	-0.0939	V	T. Arranz	0.0008
XZ Dra	59450.4990	36773	-0.0992	V	T. Arranz	0.0008
XZ Dra	59451.4520	36775	-0.0992	V	T. Arranz	0.0009
XZ Dra	59461.4606	36796	-0.0970	V	T. Arranz	0.0005
XZ Dra	59462.4158	36798	-0.0948	V	T. Arranz	0.0009
XZ Dra	59494.3359	36865	-0.1000	V	T. Arranz	0.0009
SV Eri	59506.8396	33558	1.1510	V	G. Samolyk	0.0019
RR Gem	59247.7992	45031	-0.6994	V	G. Samolyk	0.0008
RR Gem	59248.5938	45033	-0.6994	V	G. Samolyk	0.0007
RR Gem	59288.3276	45133	-0.6967	V	T. Arranz	0.0007
RR Gem	59299.4456	45161	-0.7034	V	T. Arranz	0.0007
RR Gem	59311.3678	45191	-0.7005	V	T. Arranz	0.0007
RR Gem	59519.9472	45716	-0.7092	V	G. Samolyk	0.0008
TW Her	59303.8271	94491	-0.0203	V	K. Menzies	0.0008
TW Her	59371.7589	94661	-0.0205	V	G. Samolyk	0.0006
TW Her	59383.7471	94691	-0.0203	V	K. Menzies	0.0006
TW Her	59400.5294	94733	-0.0213	V	T. Arranz	0.0006
TW Her	59402.5287	94738	-0.0200	V	T. Arranz	0.0002
VX Her	59346.8585	82562	-0.1150	V	G. Samolyk	0.0011
VX Her	59378.7339	82632	-0.1157	V	G. Samolyk	0.0009
VX Her	59399.6817	82678	-0.1150	V	G. Samolyk	0.0011
VX Her	59412.4296	82706	-0.1176	V	T. Arranz	0.0006
VZ Her	59348.7540	51234	0.0969	V	G. Samolyk	0.0008
VZ Her	59381.7793	51309	0.0976	V	G. Samolyk	0.0008
AR Her	59321.7801	38016	-1.1513	V	G. Samolyk	0.0009
AR Her	59327.8726	38029	-1.1692	V	G. Samolyk	0.0012
AR Her	59346.6990	38069	-1.1439	V	G. Samolyk	0.0011
AR Her	59352.8080	38082	-1.1453	V	G. Samolyk	0.0012
AR Her	59368.7402	38116	-1.1940	V	G. Samolyk	0.0011
AR Her	59375.8323	38131	-1.1524	V	G. Samolyk	0.0018
AR Her	59382.8798	38146	-1.1553	V	G. Samolyk	0.0015
AR Her	59389.4466	38160	-1.1689	V	T. Arranz	0.0007
AR Her	59390.3836	38162	-1.1719	V	T. Arranz	0.0008
AR Her	59397.4142	38177	-1.1918	V	T. Arranz	0.0011
AR Her	59403.5189	38190	-1.1974	V	T. Arranz	0.0014
AR Her	59404.4808	38192	-1.1756	V	T. Arranz	0.0013
AR Her	59405.4351	38194	-1.1613	V	T. Arranz	0.0016
AR Her	59409.6881	38203	-1.1386	V	G. Samolyk	0.0016
AR Her	59413.4306	38211	-1.1563	V	T. Arranz	0.0009
DL Her	59346.7603	35729	0.0603	V	K. Menzies	0.0011
DL Her	59399.4231	35818	0.0682	V	T. Arranz	0.0013
DY Her	59294.9142	173957	-0.0366	V	G. Samolyk	0.0006
DY Her	59347.8265	174313	-0.0370	V	G. Samolyk	0.0005
DY Her	59357.7847	174380	-0.0371	V	G. Samolyk	0.0004

Table continued on next page

Table 1. Recent times of maxima of stars in the AAVSO Short Period Pulsator program, cont.

Star	*JD (max) Hel. 2400000 +*	*Cycle*	*O–C (day)*	*F*	*Observer*	*Error (day)*
DY Her	59379.6343	174527	-0.0363	V	G. Samolyk	0.0007
DY Her	59379.7825	174528	-0.0368	V	G. Samolyk	0.0007
DY Her	59385.4300	174566	-0.0373	V	T. Arranz	0.0005
DY Her	59395.3887	174633	-0.0369	V	T. Arranz	0.0005
DY Her	59397.6181	174648	-0.0369	V	G. Samolyk	0.0009
LS Her	59399.6456	136021	0.0031	V	G. Samolyk	0.0026
LS Her	59451.5653	136246	-0.0090	V	K. Menzies	0.0022
V873 Her	59405.4792	52674	-0.0504	V	L. Corp	0.0015
SZ Hya	59247.7569	34563	-0.2888	V	G. Samolyk	0.0013
SZ Hya	59300.4059	34661	-0.2894	V	T. Arranz	0.0011
SZ Hya	59303.6274	34667	-0.2913	V	G. Samolyk	0.0011
UU Hya	59302.6830	37841	0.0359	V	G. Samolyk	0.0016
DG Hya	59307.6046	9192	0.0407	V	G. Samolyk	0.0019
DG Hya	59308.3567	9193	0.0386	V	T. Arranz	0.0014
DH Hya	59288.3856	57489	0.1241	V	T. Arranz	0.0007
GO Hya	59294.6660	7500	-0.0030	V	G. Samolyk	0.0029
RR Leo	59248.7973	35264	0.1980	V	G. Samolyk	0.0008
RR Leo	59286.7978	35348	0.1974	V	G. Samolyk	0.0007
RR Leo	59338.3739	35462	0.2007	V	T. Arranz	0.0006
SS Leo	59302.6406	27974	-0.1183	V	G. Samolyk	0.0015
SS Leo	59311.4067	27988	-0.1210	V	T. Arranz	0.0011
ST Leo	59245.8877	65531	-0.0195	V	K. Menzies	0.0012
ST Leo	59303.7236	65652	-0.0197	V	G. Samolyk	0.0009
TV Leo	59292.7626	33070	0.1371	V	G. Samolyk	0.0016
WW Leo	59242.8263	40409	0.0578	V	G. Samolyk	0.0029
WW Leo	59310.3486	40521	0.0614	V	T. Arranz	0.0014
AA Leo	59303.6780	32919	-0.1240	V	G. Samolyk	0.0015
U Lep	59560.7309	31314	0.0392	V	G. Samolyk	0.0009
SZ Lyn	59221.6586	175030	0.0333	TG	G. Conrad	0.0009
SZ Lyn	59298.4386	175667	0.0326	V	T. Arranz	0.0006
SZ Lyn	59537.8242	177653	0.0358	V	G. Samolyk	0.0006
SZ Lyn	59537.9438	177654	0.0349	V	G. Samolyk	0.0006
SZ Lyn	59554.7009	177793	0.0376	TG	G. Conrad	0.0018
SZ Lyn	59570.7307	177926	0.0363	V	G. Samolyk	0.0007
SZ Lyn	59570.8514	177927	0.0364	V	G. Samolyk	0.0008
KP Lyn	59235.6969	66260	-0.0283	TG	G. Conrad	0.0009
RR Lyr	59364.7105	29005	-0.7082	V	G. Samolyk	0.0010
RR Lyr	59422.5190	29107	-0.7202	V	T. Arranz	0.0010
RZ Lyr	59364.6793	35563	-0.0566	V	G. Samolyk	0.0013
RZ Lyr	59424.4842	35680	-0.0671	V	T. Arranz	0.0007
CX Lyr	59484.5791	42834	1.8443	V	K. Menzies	0.0039
AV Peg	59375.8524	39924	0.2169	V	G. Samolyk	0.0009
AV Peg	59420.7480	40039	0.2194	V	G. Samolyk	0.0008
AV Peg	59489.4564	40215	0.2218	V	T. Arranz	0.0007
BH Peg	59421.8121	31290	-0.1389	V	G. Samolyk	0.0018
BH Peg	59462.8235	31354	-0.1510	V	G. Samolyk	0.0015
DY Peg	59464.6283	205174	-0.0222	V	G. Samolyk	0.0006
DY Peg	59464.7014	205175	-0.0220	V	G. Samolyk	0.0004
DY Peg	59464.7736	205176	-0.0227	V	G. Samolyk	0.0004
DY Peg	59464.8466	205177	-0.0227	V	G. Samolyk	0.0005
DY Peg	59474.5464	205310	-0.0221	V	G. Samolyk	0.0006
DY Peg	59474.6185	205311	-0.0229	V	G. Samolyk	0.0006
DY Peg	59474.6922	205312	-0.0221	V	G. Samolyk	0.0005
DY Peg	59474.7652	205313	-0.0220	V	G. Samolyk	0.0005
DY Peg	59559.2867	206472	-0.0221	V	T. Arranz	0.0004
GV Peg	59495.6382	25714	0.2322	V	K. Menzies	0.0021
DF Ser	59328.6975	67663	0.1123	V	K. Menzies	0.0009
DF Ser	59409.6898	67848	0.1125	V	G. Samolyk	0.0009
RV UMa	59242.8940	30268	0.1429	V	G. Samolyk	0.0013
RV UMa	59308.8870	30409	0.1395	V	K. Menzies	0.0014
RV UMa	59352.4201	30502	0.1430	V	T. Arranz	0.0007
RV UMa	59359.4411	30517	0.1431	V	T. Arranz	0.0009
RV UMa	59367.3937	30534	0.1387	V	T. Arranz	0.0008
RV UMa	59374.4128	30549	0.1369	V	T. Arranz	0.0009
RV UMa	59389.3899	30581	0.1360	V	T. Arranz	0.0011
AE UMa	59300.4055	275481	0.0032	V	T. Arranz	0.0006
AE UMa	59300.4868	275482	-0.0015	V	T. Arranz	0.0004

Recent Minima of 227 Eclipsing Binary Stars

Gerard Samolyk
P.O. Box 20677, Greenfield, WI 53220; gsamolyk@wi.rr.com

Received February 24, 2022; accepted February 24. 2022

Abstract This paper continues the publication of times of minima for eclipsing binary stars. Times of minima were determined from observations received by the AAVSO Eclipsing Binaries Section from August 2021 through January 2022 and are presented.

1. Recent observations

The accompanying list (Table 1) contains times of minima calculated for 227 variables calculated from recent CCD observations made by participants in the AAVSO's eclipsing binary program. These observations were reduced by the observers or the writer using the method of Kwee and van Worden (1956).

The linear elements in the *General Catalogue of Variable Stars* (GCVS; Kholopov *et al.* 1985) were used to compute the O–C values for most stars. For a few exceptions where the GCVS elements are missing or are in significant error, light elements from another source are used: CD Cam (Baldwin and Samolyk 2007), AC CMi (Samolyk 2008), CW Cas (Samolyk 1992), DK Hya (Samolyk 1990), EF Ori (Baldwin and Samolyk 2005), GU Ori (Samolyk 1985).

The light elements used for QX And, EK Aqr, V409 Aql, V889 Aql, VY Cet, LS Del, MR Del, GR Psc, CU Tau, V1123 Tau, V1223 Tau, and V1128 Tau are from Kreiner (2004).

The light elements used for BN Ari, MZ Del, V470 Hya, ET Leo, V740 Per, VZ Psc, ET Psc, V1130 Tau, V1332 Tau, V1370 Tau, and BV Tri are from Paschke (2014).

The light elements used for V731 Cep, and V407 Peg are from Nelson (2014).

The light elements used for V868 Mon are from Watson *et al.* (2014).

The standard error is included when available. Column F indicates the filter used; a "C" indicates a clear filter.

This list will be web-archived and made available through the AAVSO ftp site at:

ftp://ftp.aavso.org/public/datasets/gsamj501eb227.txt .

This list, along with the eclipsing binary data from earlier AAVSO publications, is also included in the Lichtenknecker Database administrated by the Bundesdeutsche Arbeitsgemeinschäft für Veranderliche Sterne e. V. (BAV) at: http://www.bav-astro.de/LkDB/index.php?lang=en (Frank and Lichtenknecker 1987).

References

Baldwin, M. E., and Samolyk, G. 2005, *Observed Minima Timings of Eclipsing Binaries No. 10*, AAVSO, Cambridge, MA.

Baldwin, M. E., and Samolyk, G. 2007, *Observed Minima Timings of Eclipsing Binaries No. 12*, AAVSO, Cambridge, MA.

Frank, P., and Lichtenknecker, D. 1987, *BAV Mitt.*, No. 47, 1.

Kreiner, J. M. 2004, *Acta Astron.*, **54**, 207 (http://www.as.up.krakow.pl/ephem/).

Kholopov, P. N., *et al.* 1985, *General Catalogue of Variable Stars*, 4th ed., Moscow.

Kwee, K. K., and van Woerden, H. 1956, *Bull. Astron. Inst. Netherlands*, **12**, 327.

Nelson, R. 2014, Eclipsing Binary O–C Files (http://www.aavso.org/bob-nelsons-o-c-files).

Paschke, A. 2014, "O–C Gateway" (http://var.astro.cz/ocgate/).

Samolyk, G. 1985, *J. Amer. Assoc. Var. Star Obs.*, **14**, 12.

Samolyk, G. 1990, *J. Amer. Assoc. Var. Star Obs.*, **19**, 5.

Samolyk, G. 1992, *J. Amer. Assoc. Var. Star Obs.*, **21**, 34.

Samolyk, G. 2008, *J. Amer. Assoc. Var. Star Obs.*, **36**, 171.

Watson, C., Henden, A. A., and Price, C. A. 2014, AAVSO International Variable Star Index VSX (Watson+, 2006–2014; https://www.aavso.org/vsx).

Table 1. Recent times of minima of stars in the AAVSO eclipsing binary program.

Star	*JD (min) Hel. 2400000 +*	*Cycle*	*O–C (day)*	*F*	*Observer*	*Standard Error (day)*
RT And	59549.3845	29268	–0.0135	V	T. Arranz	0.0001
RT And	59574.5428	29308	–0.0124	V	G. Samolyk	0.0001
TW And	59514.6492	4971	–0.0708	V	G. Samolyk	0.0001
UU And	59521.6829	12024	0.1198	V	G. Samolyk	0.0002
UU And	59548.4368	12042	0.1204	V	T. Arranz	0.0001
WZ And	59514.6149	26798	0.0925	V	G. Samolyk	0.0002
WZ And	59588.3538	26904	0.0917	V	T. Arranz	0.0002
XZ And	59441.7172	26129	0.2089	V	L. Hazel	0.0003
XZ And	59592.3772	26240	0.2110	V	T. Arranz	0.0001
AB And	59464.7779	70370	–0.0520	V	K. Menzies	0.0001
AB And	59500.2891	70477	–0.0532	V	T. Arranz	0.0002
AB And	59500.4551	70477.5	–0.0532	V	T. Arranz	0.0001
AB And	59504.4372	70489.5	–0.0538	V	L. Corp	0.0003
AB And	59511.5742	70511	–0.0525	V	G. Samolyk	0.0001
AB And	59511.7384	70511.5	–0.0542	V	G. Samolyk	0.0001
AB And	59514.3941	70519.5	–0.0537	V	X. Miret	0.0002
AB And	59528.3338	70561.5	–0.0534	V	T. Arranz	0.0001
AB And	59528.5017	70562	–0.0515	V	T. Arranz	0.0001
AB And	59534.4753	70580	–0.0519	V	K. Menzies	0.0002
AD And	59440.7955	20724.5	–0.0710	V	G. Samolyk	0.0002
AD And	59580.3403	20866	–0.0729	V	T. Arranz	0.0002
BD And	59444.8488	52889	0.0091	V	G. Samolyk	0.0002
BD And	59504.5645	53018	0.0104	V	G. Samolyk	0.0001
BD And	59532.3399	53078	0.0116	V	T. Arranz	0.0001
BX And	59459.8434	37585	–0.1194	V	G. Samolyk	0.0001
BX And	59555.6304	37742	–0.1205	V	G. Samolyk	0.0002
BX And	59598.3375	37812	–0.1214	V	T. Arranz	0.0001
CN And	59504.4451	38737	–0.1767	V	L. Corp	0.0004
DS And	59428.8056	23044	0.0048	V	G. Samolyk	0.0002
DS And	59519.7528	23134	0.0053	V	G. Samolyk	0.0001
DS And	59578.3636	23192	0.0060	V	T. Arranz	0.0002
EP And	59591.3246	41951	0.0868	V	T. Arranz	0.0001
QR And	59559.3518	35975	0.1822	V	T. Arranz	0.0004
QX And	59428.8492	16810.5	0.0078	V	G. Samolyk	0.0005
QX And	59519.7354	17031	0.0101	V	G. Samolyk	0.0004
QX And	59594.3383	17212	0.0098	V	T. Arranz	0.0003
RY Aqr	59457.7376	9475	–0.1545	V	L. Hazel	0.0006
RY Aqr	59459.7004	9476	–0.1584	V	L. Hazel	0.0003
RY Aqr	59477.3994	9485	–0.1587	V	T. Arranz	0.0001
CX Aqr	59464.7315	41388	0.0197	V	G. Samolyk	0.0001
CX Aqr	59496.4223	41445	0.0192	V	T. Arranz	0.0001
CX Aqr	59545.3489	41533	0.0191	V	T. Arranz	0.0001
CZ Aqr	59506.6197	18702	–0.0746	V	G. Samolyk	0.0002
CZ Aqr	59546.3061	18748	–0.0749	V	T. Arranz	0.0001
EK Aqr	59488.7257	22799.5	0.0466	V	G. Samolyk	0.0006
XZ Aql	59498.4052	8225	0.1805	V	T. Arranz	0.0001
XZ Aql	59515.5176	8233	0.1794	V	L. Hazel	0.0006
FK Aql	59459.5895	2647	–0.0640	V	L. Hazel	0.0006
KP Aql	59476.6044	5666	–0.0262	V	G. Samolyk	0.0002
OO Aql	59435.4661	41086.5	0.0790	V	L. Corp	0.0001
OO Aql	59443.5748	41102.5	0.0791	V	T. Arranz	0.0001
OO Aql	59486.6510	41187.5	0.0783	V	G. Samolyk	0.0002
V337 Aql	59433.4105	2669	–0.0389	V	T. Arranz	0.0008
V346 Aql	59436.5199	15834	–0.0158	V	T. Arranz	0.0001
V409 Aql	59437.4178	3385	–0.0149	V	T. Arranz	0.0002
V417 Aql	59076.6961	43391	0.0333	C	G. Frey	0.0002
V889 Aql	59453.5492	624.5	–1.6086	V	T. Arranz	0.0004
RX Ari	59465.8103	20461	0.0630	V	K. Menzies	0.0009
RX Ari	59528.6157	20522	0.0612	V	G. Samolyk	0.0001
RX Ari	59588.3328	20580	0.0600	V	T. Arranz	0.0003
SS Ari	59464.8502	50338	–0.4506	V	K. Menzies	0.0003
SS Ari	59464.8514	50338	–0.4494	V	G. Samolyk	0.0002
SS Ari	59568.3754	50593	–0.4538	V	T. Arranz	0.0001
SS Ari	59582.5851	50628	–0.4539	V	G. Samolyk	0.0001
BN Ari	59594.3508	26952	–0.0482	V	T. Arranz	0.0001
RY Aur	59209.6818	7676	0.0175	V	G. Samolyk	0.0002
RY Aur	59506.7464	7785	0.0145	V	G. Samolyk	0.0002
TT Aur	59531.7197	28730	–0.0132	TG	G. Conrad	0.0009
AP Aur	59504.9319	29965	1.8738	V	G. Samolyk	0.0002
CL Aur	59519.6997	21338	0.1880	V	G. Samolyk	0.0001
EM Aur	59488.8833	15641	–1.1415	V	G. Samolyk	0.0005
EM Aur	59606.4032	15705.5	–1.1395	V	T. Arranz	0.0003
EP Aur	59528.7836	56208	0.0239	V	G. Samolyk	0.0002
EP Aur	59547.6907	56240	0.0188	TG	G. Conrad	0.0009
EP Aur	59582.5636	56299	0.0222	V	G. Samolyk	0.0003
HP Aur	59522.8516	11784	0.0734	V	K. Menzies	0.0001
VW Boo	59367.6864	82362	–0.3160	V	L. Hazel	0.0005
VW Boo	59611.9280	83075.5	–0.3235	V	K. Menzies	0.0005
Y Cam	59546.7630	5017	0.5178	V	G. Samolyk	0.0003
SV Cam	59589.6908	28656	0.0631	TG	G. Conrad	0.0003
AO Cam	59542.6654	21347.5	–0.0292	V	L. Hazel	0.0006
AO Cam	59609.3031	21549.5	–0.0317	V	T. Arranz	0.0002
CD Cam	59518.8291	8841	–0.0226	V	G. Samolyk	0.0006
CD Cam	59526.8504	8851.5	–0.0252	V	G. Samolyk	0.0005
TZ CMa	59540.8494	16959	–0.2343	V	G. Samolyk	0.0002
XZ CMi	59523.9201	29508	0.0077	V	G. Samolyk	0.0001
AC CMi	59540.8865	8720	0.0066	V	G. Samolyk	0.0002
AK CMi	59565.8683	29094	–0.0256	V	G. Samolyk	0.0001
RW Cap	59459.6860	4951	–0.8461	V	G. Samolyk	0.0002
RW Cap	59500.3931	4963	–0.8484	V	T. Arranz	0.0003
TY Cap	59476.4414	10315	0.1047	V	T. Arranz	0.0003
RZ Cas	59449.7628	13595	0.0735	V	G. Samolyk	0.0002
RZ Cas	59473.6673	13615	0.0731	TG	G. Conrad	0.0004
RZ Cas	59473.6674	13615	0.0732	V	G. Samolyk	0.0002
TW Cas	59565.3713	12292	0.0254	V	T. Arranz	0.0001
ZZ Cas	59465.7816	20931	0.0230	V	K. Menzies	0.0002
AB Cas	59465.6512	12255	0.1501	V	G. Samolyk	0.0001
AB Cas	59473.8530	12261	0.1506	V	L. Hazel	0.0003
AB Cas	59502.5569	12282	0.1502	V	G. Samolyk	0.0001
AX Cas	59561.2840	51526	–0.1318	V	T. Arranz	0.0002
BZ Cas	59548.4085	14132	0.3597	V	T. Arranz	0.0001
CW Cas	59433.7471	55828.5	–0.1423	V	K. Menzies	0.0001
CW Cas	59476.6316	55963	–0.1450	V	G. Samolyk	0.0002
CW Cas	59511.5471	56072.5	–0.1451	V	G. Samolyk	0.0001
CW Cas	59511.7058	56073	–0.1459	V	G. Samolyk	0.0002
CW Cas	59537.3746	56153.5	–0.1456	V	T. Arranz	0.0001
DZ Cas	59465.8063	39536	–0.2240	V	G. Samolyk	0.0003
DZ Cas	59595.3139	39701	–0.2235	V	T. Arranz	0.0003
GR Cas	59527.6586	3519	–0.0010	V	L. Hazel	0.0006
IR Cas	59439.7463	25086	0.0184	V	L. Hazel	0.0003
IR Cas	59473.7810	25136	0.0188	V	L. Hazel	0.0006
IR Cas	59534.3618	25225	0.0186	V	T. Arranz	0.0003
IS Cas	59505.6551	16687	0.0747	V	G. Samolyk	0.0001
IT Cas	59518.6707	7893	0.0730	V	G. Samolyk	0.0002
IT Cas	59530.3610	7896	0.0734	V	T. Arranz	0.0001
KR Cas	59598.3324	9086	–0.1665	V	T. Arranz	0.0002
MM Cas	59474.6217	20780	0.1321	V	L. Hazel	0.0006
MM Cas	59518.6405	20818	0.1290	V	G. Samolyk	0.0003
MM Cas	59531.3829	20829	0.1283	V	T. Arranz	0.0001
MT Cas	59515.7360	10389.5	–0.0097	V	L. Hazel	0.0006
MW Cas	59515.7673	62752.5	–0.0010	V	L. Hazel	0.0006
OR Cas	59482.7776	12260	–0.0357	V	L. Hazel	0.0006
OR Cas	59536.3429	12303	–0.0359	V	T. Arranz	0.0001
OX Cas	59466.8205	7310	0.0898	V	L. Hazel	0.0006
OX Cas	59476.7749	7314	0.0869	V	G. Samolyk	0.0005
PV Cas	59473.7902	10995	–0.0303	V	G. Samolyk	0.0003
V364 Cas	59525.4024	16326	–0.0238	V	T. Arranz	0.0002
V375 Cas	59523.6055	16887	0.3097	V	G. Samolyk	0.0004
V375 Cas	59566.3382	16916	0.3142	V	T. Arranz	0.0002
V380 Cas	59457.8130	24912	–0.0770	V	G. Samolyk	0.0002
U Cep	59442.7914	5977	0.2434	V	G. Samolyk	0.0003
U Cep	59502.6236	6001	0.2425	V	G. Samolyk	0.0006

Table continued on following pages

Table 1. Recent times of minima of stars in the AAVSO eclipsing binary program (cont.).

Star	JD (min) Hel. 2400000 +	Cycle	O–C (day)	F	Observer	Standard Error (day)
U Cep	59507.6141	6003	0.2469	V	L. Hazel	0.0003
SU Cep	59465.4837	36765	0.0073	V	T. Arranz	0.0002
SU Cep	59503.3416	36807	0.0063	V	T. Arranz	0.0001
SU Cep	59519.5678	36825	0.0073	V	G. Samolyk	0.0001
WZ Cep	59504.5641	75373	–0.2322	V	G. Samolyk	0.0003
XX Cep	59506.5641	6275	0.0375	V	G. Samolyk	0.0002
XX Cep	59548.6348	6293	0.0363	V	K. Menzies	0.0002
XX Cep	59567.3361	6301	0.0390	V	T. Arranz	0.0001
DK Cep	59466.6921	26246	0.0297	V	L. Hazel	0.0006
DK Cep	59473.5912	26253	0.0275	V	G. Samolyk	0.0001
DK Cep	59485.4223	26265	0.0277	V	T. Arranz	0.0001
DK Cep	59486.4077	26266	0.0272	V	T. Arranz	0.0001
DL Cep	59540.3380	15697	0.0697	V	T. Arranz	0.0002
DL Cep	59548.4914	15702	0.0707	V	K. Menzies	0.0003
EG Cep	59477.6667	31000	0.0075	V	K. Menzies	0.0003
GI Cep	59466.6243	1756	0.0076	V	L. Hazel	0.0006
GW Cep	59439.8107	66037.5	0.0428	V	L. Hazel	0.0006
NW Cep	59469.5572	655	–0.0108	V	T. Arranz	0.0001
V731 Cep	59600.3247	594	–0.3903	V	T. Arranz	0.0001
SS Cet	59560.6898	5753	0.0769	V	G. Samolyk	0.0001
SS Cet	59596.3781	5765	0.0775	V	T. Arranz	0.0001
TT Cet	59519.7272	55507	–0.0902	V	G. Samolyk	0.0001
TT Cet	59567.3506	55605	–0.0906	V	T. Arranz	0.0001
TW Cet	59540.6956	54181	–0.0352	V	G. Samolyk	0.0003
TW Cet	59559.3896	54240	–0.0355	V	T. Arranz	0.0001
TX Cet	59606.3509	22304	0.0157	V	T. Arranz	0.0002
VY Cet	59600.2931	20833	–0.0128	V	T. Arranz	0.0001
SW Cyg	59437.4081	3842	–0.3905	V	T. Arranz	0.0003
SW Cyg	59446.5556	3844	–0.3892	V	T. Arranz	0.0003
SW Cyg	59455.7043	3846	–0.3868	V	L. Hazel	0.0003
UW Cyg	59432.5303	4562	0.0341	V	T. Arranz	0.0001
UW Cyg	59439.4312	4564	0.0335	V	T. Arranz	0.0001
WW Cyg	59428.6767	5742	0.1611	V	G. Samolyk	0.0001
WW Cyg	59468.4900	5754	0.1612	V	T. Arranz	0.0001
WW Cyg	59488.3969	5760	0.1615	V	T. Arranz	0.0001
WW Cyg	59511.6196	5767	0.1598	V	L. Hazel	0.0006
ZZ Cyg	59436.4497	22965	–0.0838	V	T. Arranz	0.0001
ZZ Cyg	59449.6506	22986	–0.0839	V	G. Samolyk	0.0001
ZZ Cyg	59497.4259	23062	–0.0834	V	T. Arranz	0.0001
AE Cyg	59489.4188	15377	–0.0015	V	T. Arranz	0.0001
BO Cyg	59451.6556	13099	0.0698	V	L. Hazel	0.0006
CG Cyg	59457.6203	31740	0.0829	V	G. Samolyk	0.0001
CG Cyg	59474.6617	31767	0.0835	V	G. Samolyk	0.0001
DK Cyg	59464.6243	45603	0.1393	V	G. Samolyk	0.0001
DK Cyg	59468.3904	45611	0.1399	V	T. Arranz	0.0001
DK Cyg	59501.3377	45681	0.1389	V	T. Arranz	0.0001
DL Cyg	59501.4261	3191	0.1561	V	T. Arranz	0.0009
DL Cyg	59530.4042	3197	0.1518	V	T. Arranz	0.0005
DO Cyg	59451.6061	8751	–0.0605	V	L. Hazel	0.0006
KV Cyg	59442.5470	10558	0.0636	V	T. Arranz	0.0001
KV Cyg	59479.4534	10571	0.0631	V	T. Arranz	0.0003
V346 Cyg	59457.4968	8665	0.2083	V	T. Arranz	0.0002
V387 Cyg	59429.7938	49086	0.0179	V	G. Samolyk	0.0001
V387 Cyg	59487.4469	49176	0.0173	V	T. Arranz	0.0001
V387 Cyg	59514.3522	49218	0.0176	V	T. Arranz	0.0001
V388 Cyg	59429.4467	20344	–0.1434	V	T. Arranz	0.0007
V388 Cyg	59503.3215	20430	–0.1458	V	T. Arranz	0.0001
V401 Cyg	59442.4103	26783	0.1080	V	T. Arranz	0.0001
V445 Cyg	59455.6784	9913	0.3376	V	L. Hazel	0.0006
V445 Cyg	59457.6223	9914	0.3337	V	L. Hazel	0.0006
V445 Cyg	59463.4648	9917	0.3330	V	T. Arranz	0.0003
V456 Cyg	59449.4252	16313	0.0538	V	T. Arranz	0.0005
V466 Cyg	59435.4723	22033.5	0.0074	V	T. Arranz	0.0001
V466 Cyg	59451.4757	22045	0.0078	V	T. Arranz	0.0001
V477 Cyg	59477.5148	6514	–0.0459	V	T. Arranz	0.0002
V836 Cyg	59447.4763	22335	0.0245	V	T. Arranz	0.0001
V1034 Cyg	59453.5018	16905	0.0242	V	T. Arranz	0.0001
W Del	59486.6603	3362	0.0026	V	G. Samolyk	0.0001
W Del	59491.4664	3363	0.0026	V	T. Arranz	0.0001
TT Del	59441.4426	4949	–0.1443	V	T. Arranz	0.0001
TT Del	59487.3816	4965	–0.1432	V	T. Arranz	0.0001
TY Del	59474.5061	13865	0.0868	V	T. Arranz	0.0001
TY Del	59492.3733	13880	0.0871	V	T. Arranz	0.0002
YY Del	59434.4301	20773	0.0138	V	T. Arranz	0.0001
YY Del	59488.3607	20841	0.0142	V	T. Arranz	0.0001
FZ Del	59449.4633	35910	–0.0302	V	T. Arranz	0.0001
LS Del	59440.4447	19074.5	–0.0121	V	L. Corp	0.0005
MR Del	59454.4284	13330	–0.0133	V	L. Corp	0.0005
MZ Del	59440.3930	14923	–0.0526	V	L. Corp	0.0006
UZ Dra	59445.4848	5481	0.0033	V	T. Arranz	0.0001
S Equ	59464.6371	4909	0.0940	V	L. Hazel	0.0003
S Equ	59488.6890	4916	0.0932	V	G. Samolyk	0.0001
TZ Eri	59609.4613	6598	0.3795	V	T. Arranz	0.0001
YY Eri	59488.8599	55699.5	0.1725	V	G. Samolyk	0.0002
YY Eri	59607.3294	56068	0.1714	V	T. Arranz	0.0001
SX Gem	59542.7155	29638	–0.0550	V	L. Hazel	0.0006
WW Gem	59486.8877	27066	0.0382	V	G. Samolyk	0.0003
AF Gem	59582.8630	26072	–0.0692	V	G. Samolyk	0.0001
AL Gem	59521.8939	23860	0.1106	V	G. Samolyk	0.0001
AZ Gem	59306.3240	33101	0.0965	R	J. Coliac	0.0004
AZ Gem	59306.3241	33101	0.0966	B	J. Coliac	0.0011
AZ Gem	59306.3247	33101	0.0972	V	J. Coliac	0.0006
AZ Gem	59306.3254	33101	0.0979	I	J. Coliac	0.0006
AZ Gem	59307.3297	33102	0.0960	V	J. Coliac	0.0011
AZ Gem	59307.3304	33102	0.0967	B	J. Coliac	0.0004
AZ Gem	59307.3307	33102	0.0970	R	J. Coliac	0.0004
AZ Gem	59307.3315	33102	0.0978	I	J. Coliac	0.0007
RX Her	59443.4690	14772	–0.0005	V	T. Arranz	0.0003
SZ Her	59439.4732	21483	–0.0373	V	T. Arranz	0.0001
WY Hya	59574.9067	26541.5	0.0447	V	G. Samolyk	0.0001
DK Hya	59574.9285	32057	–0.0014	V	G. Samolyk	0.0002
FG Hya	59595.4730	44618.5	–0.1754	V	L. Corp	0.0006
V470 Hya	59574.9448	17383.5	0.0053	V	G. Samolyk	0.0008
SW Lac	59435.4179	44151	–0.0783	V	L. Corp	0.0001
SW Lac	59496.3535	44341	–0.0796	V	T. Arranz	0.0001
SW Lac	59496.5137	44341.5	–0.0798	V	T. Arranz	0.0001
SW Lac	59543.4981	44488	–0.0810	V	K. Menzies	0.0002
VX Lac	59469.8162	13226	0.0899	V	K. Menzies	0.0001
VX Lac	59494.5295	13249	0.0898	V	T. Arranz	0.0001
VX Lac	59523.5406	13276	0.0896	V	G. Samolyk	0.0001
AW Lac	59459.6624	28731	0.2228	V	G. Samolyk	0.0003
AW Lac	59498.5189	28765	0.2224	V	T. Arranz	0.0001
CM Lac	59529.3396	20255	–0.0048	V	T. Arranz	0.0001
CO Lac	59444.6426	20691.5	–0.0167	V	G. Samolyk	0.0001
CO Lac	59477.8297	20713	0.0130	V	K. Menzies	0.0002
CO Lac	59499.4198	20727	0.0121	V	T. Arranz	0.0002
DG Lac	59511.3581	6799	–0.2536	V	T. Arranz	0.0001
EM Lac	59429.7271	54403	0.1573	V	L. Hazel	0.0006
EP Lac	59429.7470	12765	–0.4523	V	L. Hazel	0.0009
EP Lac	59464.6847	12782	–0.4636	V	L. Hazel	0.0009
PP Lac	59466.7957	34578	–0.0565	V	L. Hazel	0.0003
PP Lac	59477.6249	34605	–0.0587	V	L. Hazel	0.0006
ET Leo	59602.4682	32041.5	0.0021	V	L. Corp	0.0009
Z Lep	59570.7857	32350	–0.2055	V	G. Samolyk	0.0002
Z Lep	59582.7106	32362	–0.2052	V	G. Samolyk	0.0002
RR Lep	59518.8415	31834	–0.0555	V	G. Samolyk	0.0008
RR Lep	59610.3891	31934	–0.0507	V	T. Arranz	0.0001
RY Lyn	59574.8913	11629	–0.0272	V	G. Samolyk	0.0002
RV Lyr	59515.6056	3887	–0.3331	V	L. Hazel	0.0009
UZ Lyr	59457.4243	8337	–0.0577	V	T. Arranz	0.0001
EW Lyr	59464.6081	16916	0.3128	V	G. Samolyk	0.0001
FL Lyr	59445.4864	9744	–0.0026	V	T. Arranz	0.0001

Table continued on following pages

Table 1. Recent times of minima of stars in the AAVSO eclipsing binary program (cont.)

Star	*JD (min) Hel. 2400000 +*	*Cycle*	*O–C (day)*	*F*	*Observer*	*Standard Error (day)*
FL Lyr	59519.5438	9778	–0.0024	V	G. Samolyk	0.0001
β Lyr	59376.04	802.5	2.88	B	G. Samolyk	0.02
β Lyr	59376.04	802.5	2.88	V	G. Samolyk	0.02
β Lyr	59376.15	802.5	2.99	R	G. Samolyk	0.03
β Lyr	59382.51	803	2.88	B	G. Samolyk	0.02
β Lyr	59382.51	803	2.88	V	G. Samolyk	0.02
β Lyr	59382.52	803	2.89	R	G. Samolyk	0.02
RU Mon	59574.7521	4974.5	–0.7765	V	G. Samolyk	0.0002
BB Mon	59565.8137	44881	–0.0039	V	G. Samolyk	0.0001
EP Mon	59519.9105	23196	0.0231	V	G. Samolyk	0.0002
V868 Mon	59595.4870	9173	0.0659	V	L. Corp	0.0005
V839 Oph	59457.6378	46477	0.3494	V	G. Samolyk	0.0001
EF Ori	59519.8965	4427	0.0109	V	G. Samolyk	0.0004
EQ Ori	59546.7354	16098	–0.0332	V	G. Samolyk	0.0001
EQ Ori	59604.3550	16131	–0.0335	V	T. Arranz	0.0001
ER Ori	59526.8133	42277.5	0.1598	V	G. Samolyk	0.0001
ET Ori	59523.8892	34534	–0.0038	V	G. Samolyk	0.0001
FH Ori	59526.8373	15632	–0.4828	V	G. Samolyk	0.0003
FL Ori	59521.8302	9139	0.0422	V	G. Samolyk	0.0002
FR Ori	59544.7688	35874	0.0501	V	G. Samolyk	0.0001
FZ Ori	59574.7167	38877	–0.0206	V	G. Samolyk	0.0002
GU Ori	59519.8947	34949.5	–0.0739	V	G. Samolyk	0.0002
GU Ori	59574.7300	35066	–0.0729	V	G. Samolyk	0.0003
U Peg	59428.8127	61148.5	–0.1784	V	G. Samolyk	0.0001
U Peg	59464.7915	61244.5	–0.1786	V	G. Samolyk	0.0001
U Peg	59500.5822	61340	–0.1795	V	T. Arranz	0.0001
U Peg	59511.4511	61369	–0.1793	V	L. Corp	0.0002
U Peg	59518.5716	61388	–0.1796	V	G. Samolyk	0.0001
U Peg	59537.3114	61438	–0.1789	V	X. Miret	0.0002
U Peg	59590.5293	61580	–0.1799	V	G. Samolyk	0.0001
TY Peg	59477.7135	6153	–0.5002	V	L. Hazel	0.0006
TY Peg	59499.3671	6160	–0.4921	V	T. Arranz	0.0001
UX Peg	59473.6994	12332	0.0036	V	G. Samolyk	0.0002
UX Peg	59504.5918	12352	0.0036	V	G. Samolyk	0.0002
UX Peg	59532.3954	12370	0.0041	V	T. Arranz	0.0001
AQ Peg	59505.5958	3295	0.5743	V	G. Samolyk	0.0005
BB Peg	59495.4223	43516	–0.0365	V	T. Arranz	0.0001
BB Peg	59511.3281	43560	–0.0368	V	T. Arranz	0.0001
BB Peg	59511.5084	43560.5	–0.0372	V	T. Arranz	0.0001
BG Peg	59462.6526	7135	–2.5226	V	G. Samolyk	0.0003
BG Peg	59515.3682	7162	–2.5304	V	T. Arranz	0.0003
BX Peg	59498.3558	54572	–0.1452	V	T. Arranz	0.0001
BX Peg	59498.4971	54572.5	–0.1441	V	T. Arranz	0.0002
BX Peg	59507.3293	54604	–0.1452	V	T. Arranz	0.0001
BX Peg	59512.3770	54622	–0.1450	V	X. Miret	0.0002
DI Peg	59502.6011	20098	0.0191	V	G. Samolyk	0.0001
DI Peg	59525.3795	20130	0.0193	V	T. Arranz	0.0001
EU Peg	59509.4062	35400	0.0456	V	T. Arranz	0.0002
GP Peg	59428.6635	18645	–0.0602	V	G. Samolyk	0.0004
GP Peg	59459.8834	18677	–0.0601	V	G. Samolyk	0.0002
GP Peg	59511.5909	18730	–0.0604	V	G. Samolyk	0.0001
GP Peg	59520.3713	18739	–0.0605	V	T. Arranz	0.0001
KW Peg	59498.3874	13890	0.2461	V	T. Arranz	0.0002
V407 Peg	59496.3749	4029	0.0017	V	L. Corp	0.0005
Z Per	59540.5968	4542	–0.3928	V	G. Samolyk	0.0001
Z Per	59580.3270	4555	–0.3946	V	T. Arranz	0.0001
RT Per	59474.8531	30726	0.1206	V	G. Samolyk	0.0001
RT Per	59590.3722	30862	0.1212	V	T. Arranz	0.0001
RT Per	59600.5653	30874	0.1215	V	G. Samolyk	0.0001
RV Per	59474.8327	8831	0.0074	V	L. Hazel	0.0006
RV Per	59581.4026	8885	0.0087	V	T. Arranz	0.0001
ST Per	59587.3214	6476	0.3255	V	T. Arranz	0.0001
XZ Per	59474.8055	13865	–0.0790	V	L. Hazel	0.0006
XZ Per	59504.7474	13891	–0.0796	V	G. Samolyk	0.0001
XZ Per	59608.3927	13981	–0.0814	V	T. Arranz	0.0001
IT Per	59486.8630	19628	–0.0529	V	G. Samolyk	0.0005
IU Per	59449.8237	16147	0.0034	V	G. Samolyk	0.0002
IU Per	59590.3757	16311	0.0033	V	T. Arranz	0.0002
KW Per	59506.9207	18365	0.0201	V	G. Samolyk	0.0001
KW Per	59595.3898	18460	0.0196	V	T. Arranz	0.0001
V432 Per	59449.8004	73325.5	0.0296	V	G. Samolyk	0.0002
V432 Per	59560.5774	73670	0.0440	V	G. Samolyk	0.0001
V432 Per	59564.4102	73682	0.0186	V	T. Arranz	0.0002
V740 Per	59596.3376	21977	–0.0014	V	T. Arranz	0.0001
V740 Per	59609.3939	22012	–0.0016	V	T. Arranz	0.0001
V873 Per	59514.4648	27614.5	–0.0340	C	J. Coliac	0.0001
V873 Per	59514.6126	27615	–0.0336	C	J. Coliac	0.0001
V873 Per	59601.3129	27909	–0.0351	V	T. Arranz	0.0001
V873 Per	59601.4590	27909.5	–0.0364	V	T. Arranz	0.0001
β Per	59579.6342	4861	0.1545	V	S. Dvorak	0.0001
Y Psc	59519.5959	3687	–0.0280	V	G. Samolyk	0.0001
Y Psc	59538.4250	3692	–0.0278	V	T. Arranz	0.0003
RV Psc	59461.8103	63323	–0.0703	V	K. Menzies	0.0002
RV Psc	59583.4113	63542.5	–0.0704	V	T. Arranz	0.0001
UV Psc	59593.3438	18799	–0.0238	V	T. Arranz	0.0001
VZ Psc	59454.4413	59796	0.0052	V	L. Corp	0.0004
VZ Psc	59536.3417	60109.5	0.0008	V	T. Arranz	0.0003
VZ Psc	59536.4756	60110	0.0041	V	T. Arranz	0.0005
ET Psc	59511.4047	15670	–0.0050	V	L. Corp	0.0005
GR Psc	59602.3432	16456	–0.0092	V	T. Arranz	0.0001
U Sge	59435.5114	12514	0.0297	V	T. Arranz	0.0001
RW Tau	59505.9203	4992	–0.3110	V	G. Samolyk	0.0001
RZ Tau	59505.8277	52515	0.1038	V	G. Samolyk	0.0001
TY Tau	59599.3239	35649	0.2827	V	T. Arranz	0.0001
WY Tau	59588.6067	32026	0.0682	V	K. Menzies	0.0001
WY Tau	59607.3106	32053	0.0676	V	T. Arranz	0.0002
AC Tau	59582.7124	6825	0.2177	V	G. Samolyk	0.0003
AC Tau	59611.3209	6839	0.2192	V	T. Arranz	0.0001
AH Tau	59603.3957	85792	–0.0003	V	T. Arranz	0.0002
AQ Tau	59528.8398	24569	0.5204	V	G. Samolyk	0.0003
AQ Tau	59599.3633	24627	0.5215	V	T. Arranz	0.0003
AQ Tau	59606.6567	24633	0.5195	V	K. Menzies	0.0003
CT Tau	59523.7484	21174	–0.0754	V	G. Samolyk	0.0002
CT Tau	59606.4358	21298	–0.0749	V	T. Arranz	0.0001
CT Tau	59608.4357	21301	–0.0755	V	T. Arranz	0.0001
CU Tau	59587.3092	17180	–0.0695	V	X. Miret	0.0003
CU Tau	59603.3957	17219	–0.0712	V	T. Arranz	0.0001
EQ Tau	59466.8636	56404.5	–0.0517	V	G. Samolyk	0.0001
EQ Tau	59473.8604	56425	–0.0526	V	G. Samolyk	0.0001
EQ Tau	59574.5578	56720	–0.0530	V	G. Samolyk	0.0003
EQ Tau	59592.3084	56772	–0.0525	V	T. Arranz	0.0001
EQ Tau	59610.5695	56825.5	–0.0536	V	K. Menzies	0.0001
V781 Tau	59602.4573	45599	–0.0478	V	L. Corp	0.0002
V781 Tau	59605.3889	45607.5	–0.0479	V	T. Arranz	0.0002
V1123 Tau	59606.3588	17768	0.0236	V	L. Corp	0.0004
V1128 Tau	59567.5004	23143.5	–0.0086	V	L. Corp	0.0004
V1130 Tau	59567.4410	13853.5	0.0041	V	L. Corp	0.0004
V1223 Tau	59603.3783	16420	0.0027	V	T. Arranz	0.0001
V1332 Tau	59604.3457	21770	0.0289	V	T. Arranz	0.0003
V1332 Tau	59610.4608	21792.5	0.0279	V	T. Arranz	0.0002
V1370 Tau	59605.3816	27536	0.0145	V	T. Arranz	0.0001
V Tri	59484.8161	59826	–0.0051	V	K. Menzies	0.0005
V Tri	59581.3750	59991	–0.0051	V	T. Arranz	0.0001
X Tri	59457.8445	17452	–0.1088	V	G. Samolyk	0.0001
X Tri	59578.3128	17576	–0.1109	V	T. Arranz	0.0001
RS Tri	59593.3517	11343	–0.0564	V	T. Arranz	0.0001
RV Tri	59474.8998	17835	–0.0499	V	G. Samolyk	0.0001
RV Tri	59611.3114	18016	–0.0519	V	T. Arranz	0.0001
BV Tri	59611.3691	11354	0.0139	V	T. Arranz	0.0008
RS Vul	59441.4225	5948	0.0230	V	T. Arranz	0.0005
XZ Vul	59431.7553	4369	0.6066	V	L. Hazel	0.0006
AW Vul	59447.5187	16321	–0.0398	V	T. Arranz	0.0001

Table continued on next page

Table 1. Recent times of minima of stars in the AAVSO eclipsing binary program (cont.)

Star	*JD (min) Hel. 2400000 +*	*Cycle*	*O–C (day)*	*F*	*Observer*	*Standard Error (day)*
AX Vul	59462.5583	7215	–0.0422	V	T. Arranz	0.0001
AX Vul	59468.6325	7218	–0.0425	V	L. Hazel	0.0003
AY Vul	59444.4500	6947	–0.1949	V	T. Arranz	0.0001
AY Vul	59485.4552	6964	–0.2013	V	T. Arranz	0.0001
BE Vul	59434.4303	12450	0.1015	V	T. Arranz	0.0001
BO Vul	59528.6054	12097	–0.0029	V	G. Samolyk	0.0001
BS Vul	59473.6101	34040	–0.0367	V	G. Samolyk	0.0003
BT Vul	59441.5643	21065	0.0063	V	T. Arranz	0.0001
BT Vul	59474.6583	21094	0.0055	V	L. Hazel	0.0006
BT Vul	59506.6134	21122	0.0070	V	G. Samolyk	0.0003
BU Vul	59444.4977	45538	0.0115	V	T. Arranz	0.0001
BU Vul	59448.4803	45545	0.0111	V	T. Arranz	0.0001
BU Vul	59449.6181	45547	0.0109	V	G. Samolyk	0.0001
BU Vul	59523.5875	45677	0.0112	V	G. Samolyk	0.0001
CD Vul	59432.5608	19209	–0.0019	V	T. Arranz	0.0001
CD Vul	59469.4828	19263	–0.0021	V	T. Arranz	0.0001
CD Vul	59488.6279	19291	–0.0019	V	G. Samolyk	0.0001
ER Vul	59464.3409	27621	0.0219	V	L. Corp	0.0009

NOTES